

GENERAL INSTRUCTIONS FOR COMPLETING SF 298

The Report Documentation Page (RDP) is used in announcing and cataloging reports. It is important that this information be consistent with the rest of the report, particularly the cover and title page. Instructions for filling in each block of the form follow. It is important to *stay within the lines* to meet *optical scanning requirements*.

Block 1. Agency Use Only (Leave blank).

Block 2. Report Date. Full publication date including day, month, and year, if available (e.g. 1 Jan 88). Must cite at least the year.

Block 3. Type of Report and Dates Covered. State whether report is interim, final, etc. If applicable, enter inclusive report dates (e.g. 10 Jun 87 - 30 Jun 88).

Block 4. Title and Subtitle. A title is taken from the part of the report that provides the most meaningful and complete information. When a report is prepared in more than one volume, repeat the primary title, add volume number, and include subtitle for the specific volume. On classified documents enter the title classification in parentheses.

Block 5. Funding Numbers. To include contract and grant numbers; may include program element number(s), project number(s), task number(s), and work unit number(s). Use the following labels:

C - Contract	PR - Project
G - Grant	TA - Task
PE - Program Element	WU - Work Unit Accession No.

Block 6. Author(s). Name(s) of person(s) responsible for writing the report, performing the research, or credited with the content of the report. If editor or compiler, this should follow the name(s).

Block 7. Performing Organization Name(s) and Address(es). Self-explanatory.

Block 8. Performing Organization Report Number. Enter the unique alphanumeric report number(s) assigned by the organization performing the report.

Block 9. Sponsoring/Monitoring Agency Name(s) and Address(es). Self-explanatory.

Block 10. Sponsoring/Monitoring Agency Report Number. (If known)

Block 11. Supplementary Notes. Enter information not included elsewhere such as: Prepared in cooperation with...; Trans. of...; To be published in.... When a report is revised, include a statement whether the new report supersedes or supplements the older report.

Block 12a. Distribution/Availability Statement. Denotes public availability or limitations. Cite any availability to the public. Enter additional limitations or special markings in all capitals (e.g. NOFORN, REL, ITAR).

DOD - See DoDD 5230.24, "Distribution Statements on Technical Documents."

DOE - See authorities.

NASA - See Handbook NHB 2200.2.

NTIS - Leave blank.

Block 12b. Distribution Code.

DOD - Leave blank.

DOE - Enter DOE distribution categories from the Standard Distribution for Unclassified Scientific and Technical Reports.

NASA - Leave blank.

NTIS - Leave blank.

Block 13. Abstract. Include a brief (*Maximum 200 words*) factual summary of the most significant information contained in the report.

Block 14. Subject Terms. Keywords or phrases identifying major subjects in the report.

Block 15. Number of Pages. Enter the total number of pages.

Block 16. Price Code. Enter appropriate price code (*NTIS only*).

Blocks 17. - 19. Security Classifications. Self-explanatory. Enter U.S. Security Classification in accordance with U.S. Security Regulations (i.e., UNCLASSIFIED). If form contains classified information, stamp classification on the top and bottom of the page.

Block 20. Limitation of Abstract. This block must be completed to assign a limitation to the abstract. Enter either UL (unlimited) or SAR (same as report). An entry in this block is necessary if the abstract is to be limited. If blank, the abstract is assumed to be unlimited.

QUASI-OPTICAL CONSTRAINED LENS
AMPLIFIERS

by

JON S. H. SCHOENBERG

B. S., Cornell University, 1985

M. S., Northeastern University, 1989

A thesis submitted to the
Faculty of the Graduate School of the
University of Colorado in partial fulfillment
of the requirements for the degree of
Doctor of Philosophy

Department of Electrical and Computer Engineering

1995

Accession For	
NTIS CRA&I	<input checked="checked" type="checkbox"/>
DTIC TAB	<input type="checkbox"/>
Unannounced	<input type="checkbox"/>
Justification _____	
By _____	
Distribution /	
Availability Codes	
Dist	Avail and/or Special
A-1	

This thesis for the Doctor of Philosophy degree by

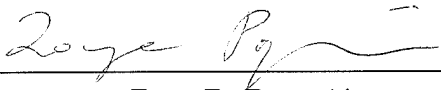
Jon S. H. Schoenberg

has been approved for the

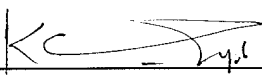
Department of

Electrical and Computer Engineering

by



Zoya B. Popović



K. C. Gupta

Date 08/30/95

Schoenberg, Jon S. H. (Ph. D., Electrical Engineering)

Quasi-Optical Constrained Lens Amplifiers

Thesis directed by Associate Professor Zoya B. Popović

A major goal in the field of quasi-optics is to increase the power available from solid-state sources by combining the power of individual devices in free-space, as demonstrated with grid oscillators and grid amplifiers. Grid amplifiers and most amplifier arrays require a plane-wave feed, provided by a far-field source or at the beam waist of a dielectric lens pair. These feed approaches add considerable loss and size, which is usually greater than the quasi-optical amplifier gain. In addition, grid amplifiers require external polarizers for stability, further increasing size and complexity. This thesis describes using constrained lens theory in the design of quasi-optical amplifier arrays with a focal-point feed, improving the power coupling between the feed and the amplifier for increased gain. Feed and aperture arrays of elements, input/output isolation and stability, amplifier circuitry, delay lines and bias distribution are all contained on a single planar substrate, making monolithic circuit integration possible. Measured results of *X*-band transmission lenses and a low noise receive lens are presented, including absolute power gain up to 13 dB, noise figure as low as 1.7 dB, beam scanning to $\pm 30^\circ$, beam forming and beam switching of multiple sources, and multiple-level quasi-optical power combining. The design and performance of millimeter-wave power combining amplifier arrays is described, including a *Ka*-Band hybrid array with 1 watt output power, and a *V*-Band 36-element monolithic array with a 5-dB on/off ratio.

DEDICATION

I dedicate this work to my parents, to whom I am forever indebted for their love, understanding and guidance throughout my childhood, maturation, educational and professional experiences. I also dedicate this work to my girlfriend and companion, Jen Kelly, for her patience and sense of humor throughout the preparation of this thesis.

ACKNOWLEDGMENTS

The contributions of ideas, time, and resources from many colleagues, organizations, friends and family made my journey through graduate school, culminating in the presentation of this thesis, possible. First, I wish to thank my thesis advisor, Professor Zoya Popović, for her wealth of ideas and endless foresight and energy. Zoya treated me with great respect, allowing me to pursue my own ideas while providing the laboratory and office facilities, funding, and undergraduate assistants needed. Next, the numerous contributions and friendship of fellow students are very much appreciated. Tom Mader and Scott Bundy provided leadership and learned knowledge as the senior students when I started my studies. It was a great experience writing journal articles and presenting conference papers with them. Wayne Shiroma consistently exemplified the purpose for pursuing my studies. He strives for excellence in teaching, is dedicated to the mission, and provides selfless leadership of the highest character. I would not have been prepared for the preliminary exams without his tireless efforts. Jonathan Dixon was instrumental in providing knowledge and reassurance on countless occasions whenever I needed help on the work stations. Jon has cheerfully directed the *V*-band array project through its numerous difficulties, and I thank him for his good sense of humor. Undergraduate assistants Boyd Shaw and Michael Forman provided many hours of effort building arrays and their various components that challenged their patience and dexterity. I enjoyed their inquisitiveness and appreciated the many times they corrected my errors. New graduate students Eric Bryerton and

Stein Hollung provided invaluable help in wrapping up details during the final hectic months of preparing this thesis.

This work was supported in part by the U.S. Army Research Office, the National Science Foundation under a Presidential Faculty Fellow Award and the Research Experience for Undergraduates Program. I thank David Wait at NIST for use of the low-noise preamplifier, Gerald Johnson and Gary O'Dell of Lockheed Martin-Denver for use of the TWT amplifier and V -band measurement facilities, Dr. Sander Weinreb and Scott Duncan at Lockheed Martin-Baltimore for the V -band array fabrication, and John Hubert and Terry Duffield at Lockheed Martin-Orlando for the opportunity to design and verify our ideas at Ka -band.

I thank Colonel Alan Klayton, Professor and Head of the Department of Electrical and Computer Engineering at the U.S. Air Force Academy, for entrusting me to pursue graduate work at the University of Colorado. Through the Air Force Institute of Technology Civilian Institution Program, he made my educational experience possible. I look forward to my future service teaching on his staff. In the near-term, I look forward to serving with Dan McGrath at Phillips Laboratory, whose invention of the microstrip constrained lens and discussions with him motivated this work.

Finally, I thank my parents for their support, understanding and enthusiasm throughout this most rewarding experience.

CONTENTS

CHAPTER

1	INTRODUCTION AND BACKGROUND	1
1.1	The Requirement for Quasi-Optics	1
1.2	Background	7
1.3	Organization of the Thesis	15
2	FEED EFFICIENCY OF QUASI-OPTICAL AMPLIFIERS . .	18
2.1	Motivation	18
2.2	Active Quasi-Optical Arrays	23
2.3	Plane-Wave Fed Transmission Wave Amplifier Array . . .	26
2.3.1	Amplifier Unit Cell	27
2.3.2	Array Performance	32
2.4	Power Amplifier Power Added Efficiency	37
3	CONSTRAINED LENS THEORY	40
3.1	Motivation	40
3.2	Background	43
3.3	Constrained Lenses	48
3.4	Planar Constrained Lens	56
3.5	Other Functions	63
3.6	Conclusion	63
4	THEORETICAL BACKGROUND FOR PASSIVE ANTENNA ARRAYS	66
4.1	Motivation	66

4.2	Grating Lobe Formation and Suppression	75
4.3	Bandwidth Considerations	81
4.4	Quasi-TEM Transmission Line Delay Lines	83
4.4.1	Microstrip Delay Lines	85
4.4.2	Coplanar Waveguide	89
4.5	Conclusion	92
5	MICROSTRIP PATCH LENS AMPLIFIER ARRAYS	94
5.1	Motivation	94
5.2	Linear 7-Element Lens Amplifier Array	95
5.3	Two-Dimensional Lens Amplifier	102
5.4	Two-Level Power Combining	108
5.4.1	Grid Oscillator Feed Design	109
5.4.2	Two-Level Power Combiner Performance	110
5.4.3	Beamforming	117
5.5	Conclusion	120
6	BROADBAND RADIATORS	122
6.1	Motivation	122
6.2	Microstrip Patch	123
6.3	Broadband Quasi-Microstrip Antenna	132
6.4	Slot Antennas	135
6.4.1	Introduction	135
6.4.2	Motivation	136
6.4.3	Theory	137
6.4.4	Results	143
6.5	Conclusion	148

7	LOW NOISE CONSTRAINED LENS AMPLIFIER	149
7.1	Motivation	149
7.2	Theory of Noise Added by a Linear Amplifier	150
7.2.1	Noise Received from the Far Field	151
7.2.2	Background Noise Bypassing the Array	154
7.2.3	Noise Contributed by the Amplifiers	155
7.2.4	Noise Measurement Procedure	156
7.3	Slot-Slot Low Noise Lens Amplifier	160
7.4	Conclusion	168
8	QUASI-OPTICAL MILLIMETER-WAVE AMPLIFIER ARRAYS	171
8.1	Motivation	171
8.2	Slot-Slot Ka-Band Hybrid Array	172
8.2.1	Introduction	172
8.2.2	Amplifier Design	172
8.2.3	Measurement and Results	175
8.2.4	Conclusion	177
8.3	Patch-Slot 60-GHz Monolithic Array	177
8.3.1	Return Loss Measurement	180
8.3.2	Transmission Gain Measurement	181
8.3.3	Reflection-Gain Measurement	183
8.3.4	Conclusion	183
9	CONCLUSION AND FUTURE WORK	185
	BIBLIOGRAPHY	190

FIGURES

FIGURE

1.1	Continuous-wave power handling capacity from a variety of vacuum devices and solid-state devices.	2
1.2	Corporate combiner employing cascaded stages of two-way combiners.	4
1.3	Theoretical combining efficiency of a corporate structure . . .	5
1.4	Categories of Quasi-Optical Power Combiners	8
1.5	Topology and side view of the bar-grid oscillator.	9
2.1	General spherical coordinate system used to describe the fields around an aperture antenna centered at the origin.	19
2.2	General corporate feed structure of a passive phased array. .	23
2.3	A general quasi-optical array amplifier.	25
2.4	A 24-element patch-patch quasi-optical transmission wave amplifier.	28
2.5	Planar transmission-wave amplifier unit cells	29
2.6	Free-space measurement system for quasi-optical amplifiers .	31
2.7	Gain contributed by the MESFET amplifier in the polarization-preserving unit cell.	32
2.8	Feed methods for quasi-optical amplifiers	35
2.9	Measurement arrangement for grid amplifiers	36
2.10	Saturation curves for a single-cell free-space amplifier	38

3.1 Schematic layout of an amplifier unit cell used in a constrained lens amplifier.	41
3.2 General layout of a constrained lens amplifier.	42
3.3 Microwave devices analogous to optics.	44
3.4 An artificial lens comprised of a stack of parallel plate waveguides	46
3.5 An input and output element pair of the bootlace aerial by Gent.	47
3.6 General layout of a constrained lens.	49
3.7 Geometry of the Rotman (trifocal) lens.	50
3.8 General layout of a three- dimensional lens.	52
3.9 A cross-section of the three-dimensional geometry used for quadrufocal lenses.	53
3.10 Normalized RMS path length error comparison between the quadrufocal lens and the ϕ -symmetric lens.	56
3.11 Layout of an input-output patch pair similar to that used in the constrained lens of McGrath.	57
3.12 Geometry used in the planar linear constrained lens for determining the path length equality conditions.	58
3.13 Exact focus occurs at points P_1 and P_2 on a sphere of radius F . When fed at other points on the sphere, a path length error will occur.	59
3.14 The corrected focal distance $G(\theta)$ for effective beamsteering with minimum path length error.	61
3.15 Calculated focal arc for the two dimensional lens amplifier . .	62

3.16	Constrained structures for various functions.	64
4.1	Generalized array coordinate system and geometry.	67
4.2	Projection in the xy plane for planar arrays showing the derivation of the normalized directional cosines u and v	68
4.3	Linear, periodic array with inter-element spacing d_x	71
4.4	Planar, periodic two-dimensional array	72
4.5	Planar, periodic two-dimensional array with a triangular lattice. .	73
4.6	Grating lobe node coordinates for rectangular and triangular periodic array lattices	78
4.7	E -plane beamsteering plot of a triangular-lattice array com- pared to a rectangular-lattice array.	80
4.8	Cross-section of TEM transmission lines used in the delay lines of lens amplifiers.	84
4.9	The effective dielectric constant of the microstrip transmis- sion line used in the patch-patch constrained lens amplifier array.	88
4.10	Effective dielectric constant detail for the $100\ \Omega$ microstrip line. .	89
5.1	The 7-element lens amplifier array with focal-point feed. . . .	95
5.2	Topology of an amplifier unit cell used in the patch-patch linear and two-dimensional lens array.	96
5.3	Measured frequency response of the linear 7-element lens am- plifier.	99
5.4	Measured beamsteering performance of the linear 7-element lens amplifier array.	100

5.5	Measured beamsteering performance when the lens is fed along the focal arc.	101
5.6	Theoretical 7-element linear lens radiation patterns for beam- steering.	102
5.7	The 24-element two-dimensional lens amplifier array.	103
5.8	Measured <i>s</i> -parameters of the single-stage PHEMT amplifier used in the two-dimensional lens amplifier array.	104
5.9	Absolute power gain (or loss) of the lens amplifier as a func- tion of the number of elements biased.	106
5.10	Measured absolute power gain as a function of frequency for the 24-element planar lens amplifier.	107
5.11	A 28-element grid oscillator	110
5.12	Measured antenna patterns for the 24-element lens amplifier array fed by the grid oscillator at the focal point.	111
5.13	Measured <i>E</i> -plane pattern for the 24-element lens amplifier array fed by a horn at the focal point.	112
5.14	Theoretical 24-element lens array factor with frequency-dependent radiation pattern of output patches.	113
5.15	Measured beamsteering <i>E</i> -plane pattern for the 24-element lens amplifier fed by the grid oscillator.	114
5.16	Measured beamsteering <i>H</i> -plane pattern for the 24-element lens amplifier fed by the grid oscillator.	115
5.17	Theoretical <i>E</i> -plane beamsteering patterns of the 24-element lens array.	116

5.18 Theoretical H -plane beamsteering patterns of the 24-element lens array.	117
5.19 A patch antenna lens amplifier with a dual grid-oscillator focal feed point.	118
5.20 Measured normalized beamforming lens amplifier radiation patterns.	119
5.21 Measured gain compression and corresponding radiation patterns of the lens amplifier.	120
6.1 Non-Radiating-Edge (NRE) microstrip-fed patch antenna. . .	124
6.2 The measured return loss of the NRE patch compared to multiport network model (MNM) simulation and moment-method solution.	125
6.3 Measured radiation patterns of the output patch with matching stub and drain bias line.	127
6.4 Measured and modeled input return loss of the input-side patch. .	128
6.5 Improved two-dimensional lens amplifier gain	130
6.6 Method of moments simulation of a 7-element array of patches showing the magnitude of mutual coupling between elements. .	131
6.7 The geometry of an N -element quasi-microstrip antenna. . .	133
6.8 The slot antenna analyzed using the quasi-full wave analysis. .	139
6.9 The complementary/dual structure of the structure in the sandwich CPW line.	142
6.10 The slot antennas designed and simulated using the procedure outlined in the text.	144

6.11	Folded slot return loss comparison between simulation and measurement.	145
6.12	Radiation patterns of the center-fed folded slot at 10 GHz. . .	146
6.13	Return loss of the 100- Ω anti-resonant slot used in the low noise amplifier array.	147
6.14	Radiation patterns of the off-center-fed slot at 10 GHz. . . .	148
7.1	Noise figure measurement setup for evaluating the low noise lens amplifier.	150
7.2	Experimental procedure for determining the noise figure of an amplifier unit cell in free space.	158
7.3	Measurement scheme for determining the noise figure of the lens amplifier array.	159
7.4	A single cell of an <i>X</i> -band slot-slot CPW-based low-noise amplifier array with two-stage low noise amplifier.	160
7.5	Measured <i>s</i> -parameters of the two-stage CPW LNA design for the lens array.	161
7.6	Measured and simulated noise figure and associated gain of a single cell of the low noise amplifier array.	162
7.7	A 24-element two-dimensional CPW low noise amplifier lens array.	165
7.8	Measured absolute power gain as a function of frequency for the low noise amplifier lens array.	166
7.9	Measured gain and noise figure of the 24-element CPW LNA with folded slot input and off-center-fed output slot.	167

7.10	Measured radiation patterns for the E - and H -plane of the 24-element low noise lens amplifier array.	168
7.11	The theoretical H -plane array factor multiplied by measured folded slot pattern compared to the theoretical array factor. .	169
8.1	Layout of the amplifier unit cell for the V -Band amplifier. . .	174
8.2	A single cell of a V -Band patch-slot amplifier array.	178
8.3	Free-space measurement system for evaluating the array at the reference plane.	179
8.4	Measured input return loss of the V -Band array.	181
8.5	Measured transmission-through gain results of the V -Band amplifier.	182
8.6	Measured reflection-mode frequency response for the V -band amplifier array.	184
9.1	Cascaded lens amplifiers in communication-link and $2F$ con- figurations.	186
9.2	Transmit-Receive lens shown with a grid oscillator source/mixer, linear-to-circular polarizer, and isolator in a quasi-optical sys- tem.	188

TABLES

TABLE

2.1	Comparison of quasi-optical amplifiers with various feed mechanisms.	37
2.2	Measured gain, power and efficiency of the 24-MESFET array at 10 GHz for an input power of 64 mW (2.7 mW/device) and a constant total drain current of 1 Amp.	39
5.1	Element and delay line data for the 7-element linear lens amplifier array	98
5.2	Element and delay line data for the 24-element two-dimensional lens amplifier array	105
6.1	Dimensions of the Microstrip Patch Antennas	124
7.1	Element and delay line data for the 24-element two-dimensional CPW LNA lens amplifier array	164

CHAPTER 1

INTRODUCTION AND BACKGROUND

1.1 The Requirement for Quasi-Optics

As the demands placed on the electromagnetic spectrum continue to increase by civilian and military users, the development of millimeter-wave systems has become an area of growing interest. The millimeter-wave spectrum corresponds to the frequencies between 30 GHz and 300 GHz. This frequency range has a wide variety of applications in communication, radar, radiometry, remote sensing, radio astronomy, plasma diagnostics, and spectroscopy [1]–[4]. The shorter wavelengths at these frequencies generally allow for the use of smaller and lighter components than their microwave counterparts. This is especially important in military and space-borne applications where size and weight are a prime concern. Atmospheric attenuation of millimeter waves is lower than optical wavelengths in the “transmission window” spectrum that lies between water vapor and oxygen absorption peaks, where millimeter-wave cameras and radar systems are effective in penetrating clouds, smoke, and haze unlike their optical counterparts [1]. Wireless Local Area Networks (LANs) are being developed at 60 GHz, where the high atmospheric attenuation enables good isolation between separate networks [5]. Millimeter-wave systems also provide broader bandwidth and higher resolution for radar, imaging, and communications systems compared to their microwave counterparts.

The lack of reliable, inexpensive high-power sources has been an obstacle in developing millimeter-wave systems. As shown in Figure 1.1, vacuum devices produce significantly greater power than their solid-state counterparts. Electron tubes such as klystrons and gridded tubes can generate several kilowatts of RF power in the microwave spectrum [6],[7]. Gyrotrons can produce tens of kilowatts in the millimeter-wave spectrum, and Travelling-Wave Tubes (TWTs) are capable of 100 watts at 100 GHz [8]–[10]. The size and weight of the required high voltage DC power supplies increase the cost and degrade the usefulness of space-borne and military systems using vacuum devices. Electron tubes are costly, have limited lifetimes, and systems relying on them are subject

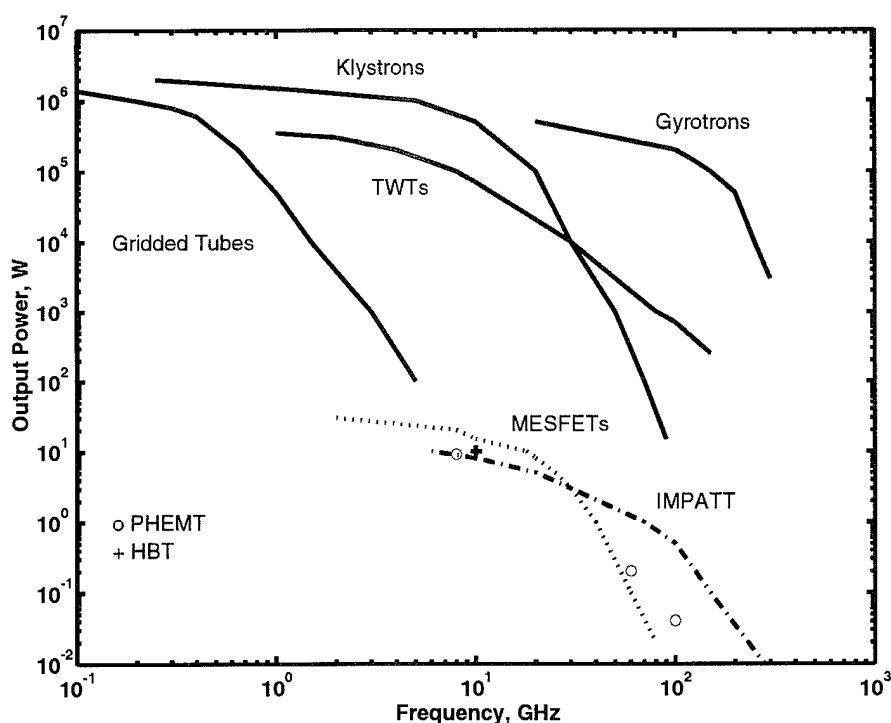


Figure 1.1. Continuous-Wave power handling capacity from a variety of vacuum devices (solid lines) and solid-state devices (dashed lines and symbols). Data adapted from Hieslmair [8] and Slegler [10].

to catastrophic failure. Solid-state devices offer improved reliability, decreased size and weight, and require low-voltage power supply [11],[12]. Therefore, it would be advantageous to use solid-state devices to attain medium and high power at microwave and millimeter-wave frequencies.

However, solid-state devices have limited power generating capability at millimeter waves. IMPATT diodes can produce several watts at 100 GHz, but the noise generated by the avalanche multiplication process limits their usefulness. Gunn diodes offer better noise performance, but generate only a few hundred milliwatts at 100 GHz [8],[10]. Two terminal devices also suffer from low DC-to-RF conversion efficiency, thus generating unwanted heat that must be dissipated with large, heavy heat sinking. Three-terminal devices such as MESFETs, Pseudomorphic High Electron Mobility Transistors (PHEMTs), Heterojunction Bipolar Transistors (HBTs), and Heterojunction Field Effect Transistors (HFETs) offer better DC-to-RF conversion efficiency and high gain. At X-band, the output power per device is currently up to 33 dBm for HBTs [13], 39 dBm for PHEMTs [14], and 40 dBm for HFETs [15]. To achieve high power levels, these high power field effect devices use large gate peripheries approaching 16 millimeters per device, but this approach is untenable at millimeter waves due to parasitic gate capacitance and gate transit delay effects. Along with the $1/f^2$ reduction in device power with frequency, output power of millimeter-wave devices is much lower. For PHEMTs, output power of 22 dBm at 57 GHz with a power added efficiency of 20% has been the highest demonstrated [16]. High-power solid-state millimeter-wave sources will require power combining of several devices to achieve the power levels currently available at microwave frequencies.

To overcome the limited power output of solid-state devices at millimeter waves, power combining techniques must be employed. A review of microwave and millimeter-wave power-combining techniques may be found in [17],[18]. Both the complexity of coherently combining the power of hundreds of devices and the associated losses prohibit the use of conventional passive circuit combiners. Scaled-down microwave techniques such as resonant cavities and waveguide power combiners [19] have been used at millimeter waves. However, resonant cavities and waveguides must be scaled down in size to prevent over-moding, thus limiting the number of devices used and increasing the machining precision used in their manufacture. Conductor losses in the cavity and waveguide walls become more severe at millimeter waves. Combiners using resonant cavities or waveguide couplers accommodate a limited number (up to a few tens) of devices, making large scale power combining impractical.

A very common combiner used both at the integrated-circuit level and the component level is the corporate combiner shown in Figure 1.2. The output

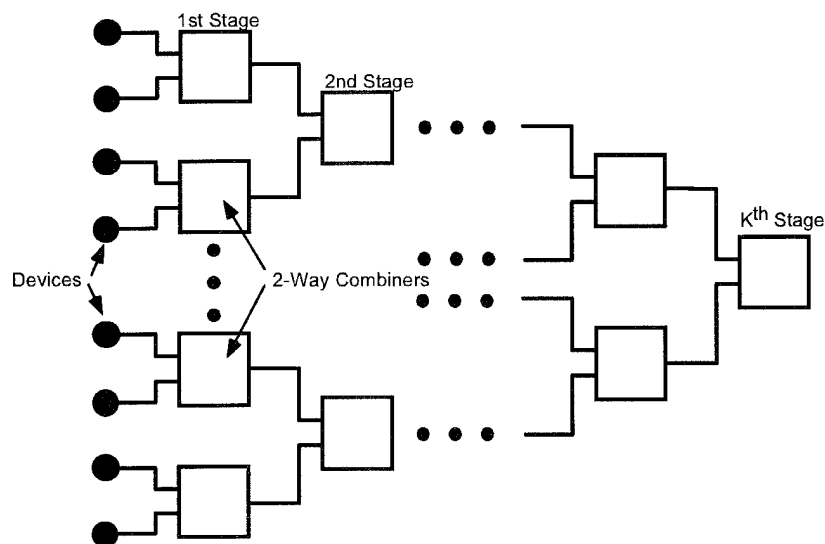


Figure 1.2. Corporate combiner employing cascaded stages of two-way combiners such as hybrid or Wilkinson couplers.

power from each device are successively added using two-way combiners, such as hybrid couplers. The number of individual devices combined is $N = 2^K$, where K is the number of stages. The net output power is $P_{out} = P_o 2^K L^K$ where P_o is the output power of each individual device and L is the insertion loss of each combiner. The combiner efficiency, $\eta = L^K$, is dependent on amplitude and phase matching at each stage, how well balanced each combiner is, and conductor losses. Figure 1.3 illustrates the effect of combiner efficiency on the corporate power combiner, showing that the combiner efficiency can become unacceptably low for a large number of devices even for a modest insertion loss per stage.

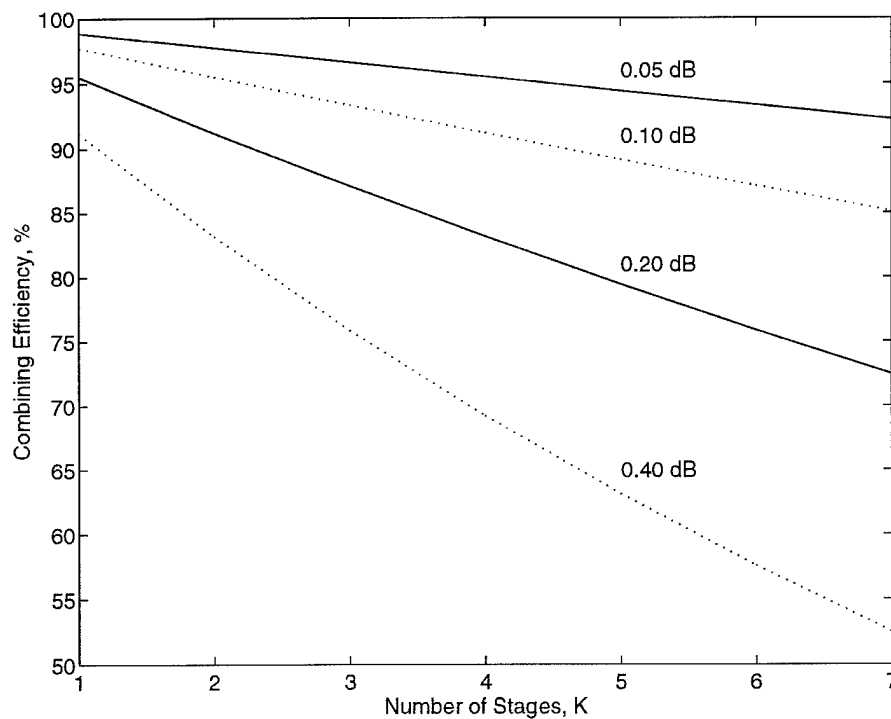


Figure 1.3. Theoretical combining efficiency of a corporate structure for various levels of insertion loss L for each two-way combiner.

An approach which overcomes the limitations and obstacles of the aforementioned power combining techniques involves combining the outputs of many devices in free space. The basic idea behind free-space power-combining is to coherently combine the output power of a large number, perhaps hundreds or even thousands, of solid-state devices in free space. Mink first suggested using an array of millimeter wave devices as a “gain medium” within a Fabry-Perot resonator as a means of large-scale power combining [20]. Since the power is combined in free space, losses and dispersion associated with waveguide walls and distributed feed networks are eliminated. Power can be distributed over a larger number of devices than in a waveguide cavity because the quasi-optical power-combining structure can be many wavelengths across. The term *quasi-optical* is used to describe power combining that uses traditionally optical techniques and devices. Quasi-optical devices such as Fabry-Perot resonators, grids, and polarizers have their optical analogues. Optical techniques such as reflection, focusing, and polarization isolation or rotation are utilized in quasi-optical devices. However, the operating wavelength is comparable to the size of most quasi-optical devices, so diffraction plays an important role and the quality factors of quasi-optical resonators are lower than their optical counterparts.

Mink’s classic 1986 paper [20] is credited with generating the significant amount of research interest in the quasi-optical power-combining (QOPC) field seen today. Since then, researchers at several universities and corporations have been developing quasi-optical power combiners. Several excellent review articles discuss the variety of quasi-optical power-combining techniques studied to date [21],[22]. A special issue of the IEEE Transactions on Microwave

Theory and Techniques has also been dedicated to this subject, as are two technical sessions at the 1994 and 1995 IEEE International Microwave Theory and Techniques Symposium.

1.2 Background

Quasi-optical power-combining techniques can essentially be categorized into three distinct areas. The QOPC categories are illustrated in Figure 1.4 as (a) wave-beam resonators, (b) active grids, and (c) active antenna arrays. Beam-wave resonators use Fabry-Perot resonant cavities in which the output power of several independently-biased and tuned oscillators are combined in free space. This type of resonator was first demonstrated by Wandinger and Nalbandian in [23], and varies only slightly from that studied by Mink [20]. Additional work in oscillators utilizing open-cavity resonators may be found in [24]–[28]. An active grid consists of a periodic metal pattern loaded with active devices, where the spacing between individual elements is a small fraction of a free-space wavelength, as shown in Figure 1.4(b). A number of both grid oscillators [29]–[35] and grid amplifiers [36]–[38] have been demonstrated. An active array consists of a standard antenna array in which the individual elements are driven by active devices as shown in Figure 1.4(c). Unlike the grid structure, the inter-element spacing is on the order of a half-wavelength or larger, and the array elements may be either periodically spaced or arbitrarily spaced across the array surface. A number of both amplifier [39]–[46] and oscillator [47]–[60] arrays have been demonstrated, using a variety of different antenna elements and devices. In all three of these power-combining techniques, a wide variety of solid-state devices can be used, including two-terminal such as Gunn, IMPATT, or tunnelling diodes, and three-terminal devices such as MESFETs,

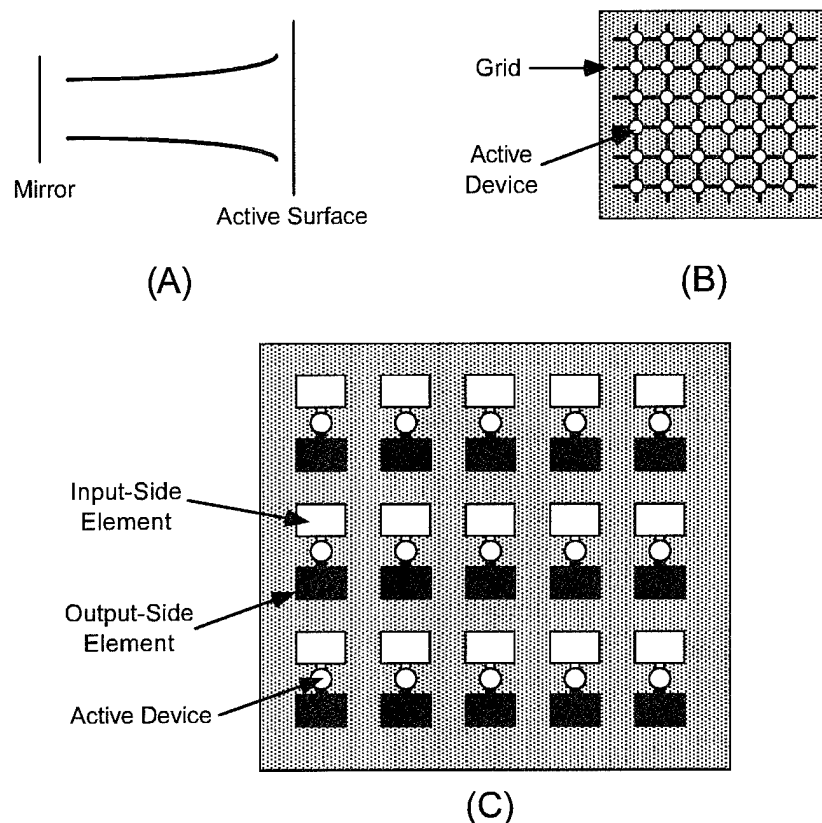


Figure 1.4. Categories of quasi-optical power combiners: (a) Beam-wave combiners utilizing a Fabry-Perot resonator; (b) Grid topology with active devices; (c) Quasi-optical arrays with input and output elements.

PHEMTs, or HBTs.

The first successful active grid devices were oscillators. The first grid oscillator was demonstrated by Popović, Kim, and Rutledge in 1988 [61]. This structure consists of a 5×5 array of GaAs MESFETs loading a periodic metal pattern printed on a grounded dielectric substrate. The gate and drain terminals of the device are connected to radiating leads in a manner similar to the bar-grid oscillator topology illustrated in Figure 1.5(a). However, this first grid oscillator required vias for source ground connection through the substrate a ground plane affixed to the back-side of the grid substrate. The ground plane acts as a feedback mirror for the grid, but since it is affixed to the substrate,

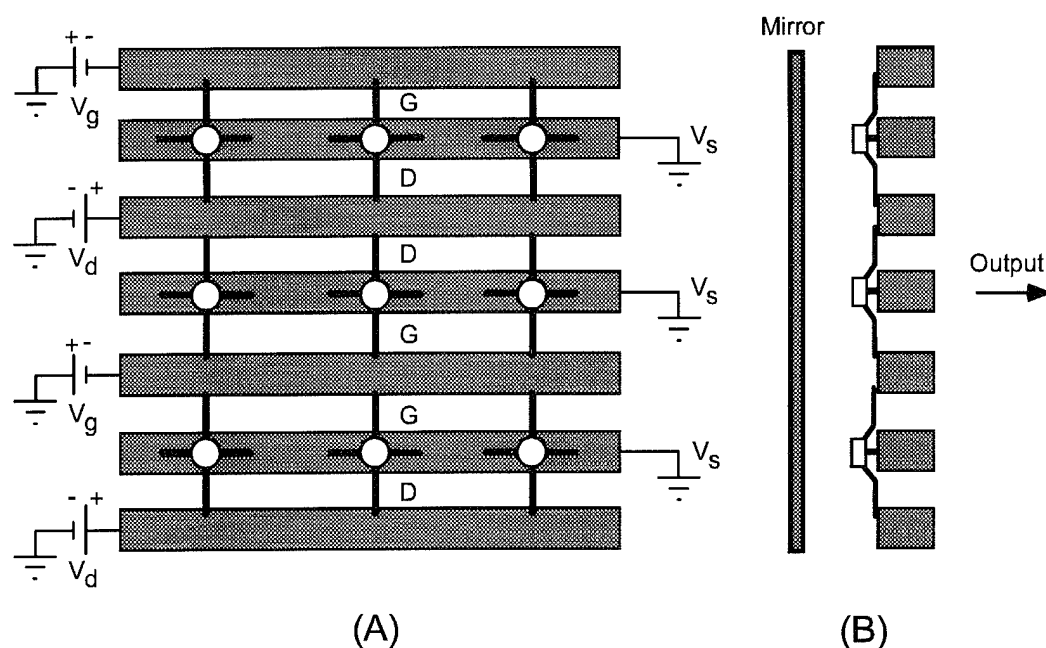


Figure 1.5. (a) Topology of the bar-grid oscillator. Horizontal metal bars provide source connection and heat-sinking for the MESFETs, enforce TEM boundary conditions between unit cells, and provide a waveguide transition to free-space. (b) Side view of the bar-grid oscillator with mirror forming a Fabry-Perot resonator.

the frequency of oscillation cannot be tuned with mirror position. A coherent oscillation frequency of 9.7 GHz with a few hundred milliwatts of power was observed when this grid was biased on.

The bar-grid oscillator was developed to eliminate the need for vias by making all device terminals coplanar [62]. In this structure, a series of parallel, horizontal metal bars are periodically loaded with MESFETs, as shown in Figure 1.5. The gate and drain leads of the devices are connected to the vertical radiating elements between the bars, and the source leads are connected to the bars. The bars form parallel plates to reinforce the desired TEM boundary conditions at the top and bottom edges of the unit cell (electric-field walls),

and simultaneously provide the bias and the heat sink for the devices. Symmetry of the current distribution on neighboring sets of gate and drain leads enforces magnetic-field wall boundary conditions between the vertical edges of the unit cells. The bar-grid oscillator may be placed in a Fabry-Perot cavity as illustrated in Figure 1.5(b), where the distance between the grid surface and the mirror may be used to adjust the mode or frequency of oscillation. This bar-grid oscillator operated at 3.1 GHz with an effective radiated power (ERP) of 3 watts.

Since the primary goal is to develop a high-power source at millimeter-wave frequencies using solid-state devices, a design compatible with monolithic fabrication techniques is desired. This led to a planar grid oscillator similar in topology to Figure 1.5(a), where the metal bars of the bar-grid oscillator are replaced by printed strips on a dielectric substrate, and all of the device terminals are on the same planar surface [29]. In this case, the drains and gates are connected to the vertical radiating leads and the sources are connected directly to the horizontal bias lines. A 10×10 array was fabricated and an oscillation frequency of 5.0 GHz was observed with 21 watts ERP. A number of other grid oscillators similar in nature have been studied [30]–[35], with the highest obtained output power of 10 watts and ERP of 660 watts [35].

Planar grid oscillators are very compact sources. Most employ a grid of thin dipole strips with a three-terminal active device feeding the dipole gap. Thin metal-strip grids can be adequately modelled using the EMF theory because the currents induced or generated along the dipole strips are well confined and easily predicted [30],[63]. Feedback between the output and input of each device causes them to oscillate, and mutual coupling between devices creates

synchronized oscillation in frequency and phase across the grid. It was shown by Bundy, Mader, and Popović that improved locking bandwidth and increased output power was possible by changing the shape of the periodic metal grid pattern from a dipole grid to a bowtie-shaped grid for a grid of MESFET oscillators [64],[65]. In addition, they placed a grid of varactor diodes behind the MESFET grid in order to change the feedback capacitance that couples the MESFETs, thus controlling the frequency of oscillation with the varactor voltage. This voltage-controlled oscillator provided a wider tuning bandwidth using bowtie grids than by using a comparable dipole grid. However, the frequency of oscillation could no longer be adequately predicted using EMF because the currents on the bowtie-shaped grids were more difficult to predict. Therefore, Bundy developed a full-wave analysis based using the method of moments to solve for the currents along an arbitrarily-shaped metal grid structure [66]. The theory assumes a periodic planar structure that is infinite in extent and uniform in phase so that simple boundary conditions may be applied to a unit cell of the grid. Once the current on the grid is known for an assumed voltage across a narrow gap (where the device is attached to the grid), a driving point impedance can be determined. The driving point impedance may then be converted into s -parameters, thus providing the ability to design the grid oscillator for operation at a specific frequency for a specific device using network analysis [67],[68]. The theory can model grids placed on both sides of a dielectric, and may include the effect of additional feedback provided by a mirror for improved locking and unidirectional radiation. The theory has been extended to include the effect of a partially reflective, frequency selective front reflector mirror for selection of a particular mode [69]. Bundy's model

allows for the design of grid oscillators for incorporation into a quasi-optical system for multiple-level power combining [70]–[72].

Quasi-optical oscillator antenna arrays have been widely studied for power combining [47]–[60]. Of particular note is the report of an FET oscillator element equipped with two patch antennas by Birkeland and Itoh [53]. One is used for reception of an injection signal and the other for radiating the oscillator output power. The circuit layout uses a microstrip coupler to provide feedback for oscillation. The injection-locking bandwidth was found to be 270 MHz. The authors report an *isotropic gain* of 46.5 dB at 6 GHz for the oscillator array. They define the isotropic gain as the ratio of the array's output power to the injection signal power level at the array input. This figure of merit neglects the injection signal power at the source since the loss due to diffraction between the source and the array input is not taken into account. Furthermore, it is questionable to consider gain as a figure of merit for oscillators, since the oscillation cannot be sustained without an input signal within the injection-locking bandwidth that is at or above some minimum threshold power. In addition, the output power is not a linear function of input power.

The oscillator arrays reported by Liao and York [55],[56] using varactor-tuned patches to adjust the free-running oscillation frequency of the oscillators. The nominal oscillation frequency was 8.45 GHz with 150 MHz of tuning bandwidth. Beam-scanning capability to 20° was demonstrated by adjusting the free-running oscillation frequency of the end element in a linear array. Since the oscillators are coupled in free-space, a phase shift is imparted on each successive element in the array. A 61° phase shift between neighboring elements was achieved, or a total of over 500° of phase shift as imparted across the ten

element linear array.

A large number of quasi-optical oscillators have been demonstrated, while quasi-optical amplifier development lagged because isolation between input and output, and therefore stability, is difficult to achieve in a planar structure. The first quasi-optical amplifier was a grid structure very similar to the grid oscillator structure, but with orthogonally polarized input and output dipoles in the grid to achieve isolation, and with a differential transistor pair [36]. External polarizers were required to stabilize the amplifiers, and a uniform phase front was required for the feed. A far-field source provided the uniform phase front feed, but this contributes a feed loss which is larger than this grid amplifier's gain, as well as other amplifiers demonstrated to date [42]. Since this first demonstration of a quasi-optical amplifier, amplifier grids with more elements have been developed for more output power [37],[38]. To reduce feed loss, these grids were tested in the beam waist of a dielectric lens pair, though these additional elements add complexity and may produce aberrations.

Later, an approach for quasi-optical amplifiers employing active arrays similar to standard phased arrays was developed. Each cell of the array has its own separate input and output antenna elements interconnected by a dedicated amplifier, forming a free-space amplifier [39]–[46]. Isolation may be achieved within the array amplifier, thus eliminating the need for external polarizers and allowing for polarization flexibility between input and output [42],[73]. Since the antenna elements are resonant structures, they are much larger than the elements employed in grids. In addition, amplifier matching circuitry and resistive feedback stabilization networks consume much more array area than grid-embedded devices. Therefore, active array amplifiers have a

lower density of amplifiers than grids, and thus may have lower power density for comparable devices. Again, these arrays require a planar wave feed, which, if provided from the far-field, represents a large system loss.

The array power combiner, with its discrete input and output antenna arrays, lends itself to lens focussing techniques to increase the efficiency of the amplifier and overcome the losses due to diffraction, as demonstrated in [74]–[75]. These active arrays may be fed from a focal point very close to their input side, reducing the losses due to diffraction. The array uses delay lines so that the received spherical wave is converted into a collimated beam at the output. Low-dispersion microstrip delay lines provide the proper time delay at the array surface to enable its refractive properties. The major emphasis of this thesis is to demonstrate that the discrete lensing concept, referred to as *constrained* lensing, is applicable to QOPC amplifier arrays for improved combiner gain. These active lens power combiner arrays have the added features of beamforming and beamsteering without the use of phase shifters.

Other quasi-optical components have been demonstrated as well. Several grid mixers have been fabricated [76]–[80]. The grid mixer presented in [79] consists of a planar array of Schottky diodes. When two different plane waves are incident on the grid (an RF and an LO signal), the mixer diodes generate a signal at the difference frequency, and this low-frequency IF signal is seen across the entire mixer grid. Phase-shifter grids have been studied in [81]–[83]. In [82], an array of Schottky diodes is used to change the phase of the surface's reflection coefficient by varying the DC bias on the devices. Two of these phase-shifter grids were also used for beamsteering [81],[83]. Multiplier grids have been demonstrated in [84]–[87]. In these cases, the diode array

generates a plane wave at a harmonic frequency of the incident plane wave. Grid switches have also been presented [88]–[90]. In [90], the forward bias on an array of PIN diodes is used to vary the reflectance and transmittance of this variable impedance surface. With such a wide variety of quasi-optical components present in the literature, the demonstration of a full system based on a number of quasi-optical devices should be possible in the near future.

Device failure with grid arrays has been studied [29],[37] by removing bias from various elements in the grid and measuring the resulting output power. Both studies showed that grids can suffer a 10% device failure rate with about a 1 dB loss in radiated power. Therefore, quasi-optical power combiners offer *graceful degradation* if device failures occur.

1.3 Organization of the Thesis

This thesis introduces the application of constrained lens theory, based on geometrical optics principles, to quasi-optical array amplifiers. Some of the motivation for using free-space power-combining techniques, as well as previous work in quasi-optics, are given in Chapter 1.

Chapter 2 describes feed mechanisms used in quasi-optical amplifiers, and describes some early work on a quasi-optical array amplifier, where input and output arrays of microstrip patches are interconnected with MESFET amplifiers to form an active array on a planar dielectric substrate. This planar transmission-wave amplifier was the first quasi-optical amplifier to integrate stabilization on the substrate so that external devices, such as polarizers, were unnecessary for device stability. This early work showed that providing a plane wave feed from a far-field source introduces losses in the feed that the amplifier was unable to overcome. This motivated the pursuit of a focal-point feed design

to reduce feed losses and obtain quasi-optical amplifiers with insertion gain.

In Chapter 3, the principles of geometric optics are applied to the theory of constrained lenses. Several constrained lenses are presented, leading to a design which is planar and thus applicable to monolithic integration. Since quasi-TEM delay lines are used in the lens, a discussion of their dispersive effects will be provided once array theory is presented. Chapter 4 discusses array theory, and presents a development of idealizing the arrangement of array elements to reduce sidelobes in arrays where the elements are spaced relatively far apart.

Experimental verification of the constrained lens theory applied to active arrays is shown in Chapter 5. Results of both a linear and a two-dimensional power-combining transmission-wave lens amplifier using patch antennas are shown. The two-dimensional lens array provides a significantly improved insertion gain over previous quasi-optical amplifiers, and it generates a significant effective radiated power from relatively small number of single-stage solid-state amplifiers. In addition, beamforming, beamsteering, and beam-switching experimental results are shown to illustrate the practical usefulness of the lens amplifier arrays. Two-level power combining with a grid oscillator specifically designed to feed the lens amplifier is demonstrated.

The patch antennas employed in our first quasi-optical amplifiers lend themselves to planar, monolithic amplifiers. However, they have a high quality factor and thus the bandwidth of our amplifier arrays is limited. Chapter 6 explores the modeling of broader-band antenna elements, in particular the anti-resonant slot antenna, and presents data on measured results compared to theory.

In addition to power combining for high-power, high gain transmitters, the active array concept can be applied to receivers. In this case the advantage in using quasi-optical active arrays is an increase in dynamic range by a factor of $10 \log N$, where N is the number of array elements. In Chapter 7, the theory of noise analysis is applied to our free-space measurements. An array with a two-stage amplifier optimized for low noise performance and wideband operation is presented.

Chapter 8 presents our preliminary work on millimeter-wave amplifier arrays. Although constrained lensing is not applied to these arrays, these quasi-optical amplifier arrays extend the high power performance and high frequency operation of quasi-optical power combiners, and demonstrates large-scale monolithic integration of active antennas.

Finally, Chapter 9 gives a summary of the thesis with concluding remarks and suggestions for future work. Since quasi-optical power combiners applicable for communication systems are new areas of research, there is a wide variety of possible topics.

CHAPTER 2

FEED EFFICIENCY OF QUASI-OPTICAL AMPLIFIERS

2.1 Motivation

A fundamental consideration for designers of microwave and millimeter-wave arrays is to determine how much power needs to be delivered to the end user, or load. In accordance with the principle of power conservation, the power density in watts/square meter from an isotropic antenna radiating at a distance R is given by

$$S = \frac{P_{\text{rad}}}{4\pi R^2} \quad (2.1)$$

where P_{rad} is the total radiated power in watts, and the power density S is shown here as a scalar. Figure 2.1 illustrates the spherical coordinate system used to describe the fields around an aperture antenna centered at the origin. If the antenna has a directional pattern with power density $S(\theta, \phi)$, the antenna pattern directive gain $D(\theta, \phi)$ is defined so that the power density at some distant spherical surface a distance R from the origin is

$$S(\theta, \phi) = \frac{P_{\text{rad}} D(\theta, \phi)}{4\pi R^2} \quad (2.2)$$

and

$$D(\theta, \phi) = \frac{4\pi R^2 S(\theta, \phi)}{P_{\text{rad}}} \quad (2.3)$$

or

$$D(\theta, \phi) = \frac{4\pi S(\theta, \phi)}{\int_{\Omega} S(\theta, \phi) d\Omega} \quad (2.4)$$

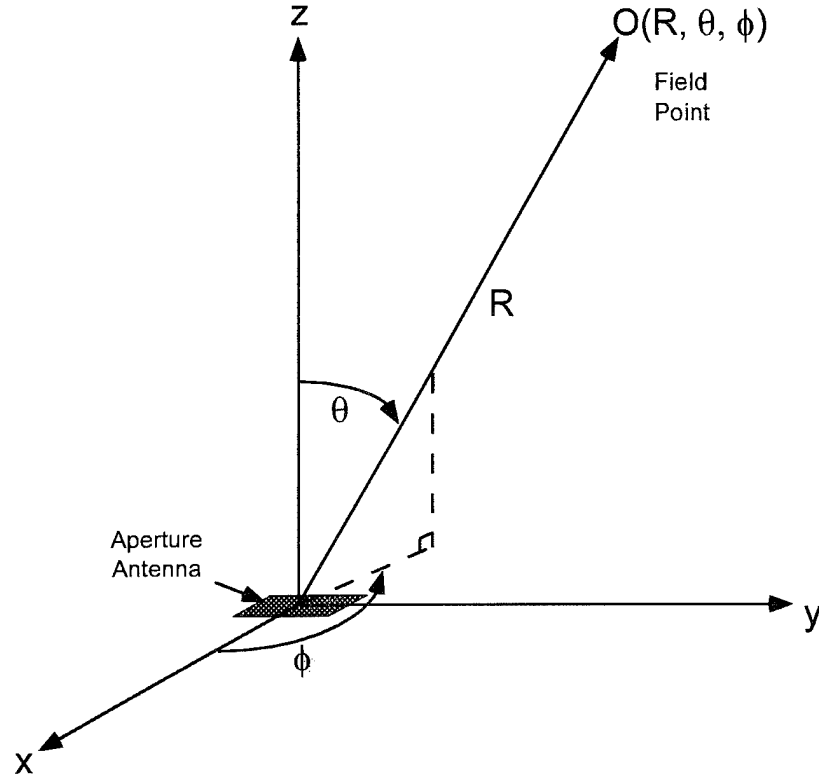


Figure 2.1. General spherical coordinate system used to describe the fields around an aperture antenna centered at the origin.

where the integral is over a sphere. In the most general case it is

$$\int_{\Omega} S(\theta, \phi) d\Omega = \int_0^{2\pi} d\phi \int_0^{\pi} S(\theta, \phi) \sin \theta d\theta. \quad (2.5)$$

Eq. 2.4 is the definition of the directive gain function and implies that the power density is the total in both polarizations (i.e. in the desired or *copolarized* direction, and the orthogonal or *cross-polarized* direction). The directivity D_o is defined as the maximum value of the directive gain function, or $D_o = \max [D(\theta, \phi)]$. The radiated power is less than the input power P_{in} by an efficiency factor ϵ_L , which accounts for circuit losses, and by the reflected signal power

$$P_{rad} = \epsilon_L P_{in} (1 - |\Gamma|^2), \quad (2.6)$$

where Γ is the antenna reflection coefficient measured at the feed transmission line. The power density in the far field can thus be written in terms of a gain function $G(\theta, \phi)$ by modifying Eq. 2.2 as

$$S(\theta, \phi) = \frac{P_{\text{rad}}}{4\pi R^2} G(\theta, \phi), \quad (2.7)$$

where

$$G(\theta, \phi) = \epsilon_L (1 - |\Gamma|^2) D(\theta, \phi). \quad (2.8)$$

The peak value of the gain distribution G_o is often called the gain, where $G_o = \max[G(\theta, \phi)]$.

In practice, the maximum theoretical directivity of a planar aperture is achieved for uniform amplitude and phase illumination of the aperture, and is given as

$$D_u = \frac{4\pi}{\lambda^2} A_p \quad (2.9)$$

for an aperture with a physical area A_p at wavelength λ . One may consider that a receiving antenna immersed in an incident wave receives power roughly proportional to the amount of energy it intercepts. This leads to the concept of an effective area A_e for an antenna. If the polarization of the receiving antenna is the same as that of the incident wave, then the received power is given by

$$P_r = A_e S(\theta, \phi). \quad (2.10)$$

The maximum value of the effective area is related to the directivity D_o by [91]

$$A_{e,\text{max}} = \frac{\lambda^2}{4\pi} D_o. \quad (2.11)$$

A practical value of the effective aperture needs to account for reflection, dissipative loss, and polarization match. For the case of matched polarization,

$$A_e = \frac{\lambda^2}{4\pi} D_o \epsilon_{ER} (1 - |\Gamma|^2) = \frac{\lambda^2}{4\pi} G_R \quad (2.12)$$

where ϵ_{ER} is the loss efficiency, due to dissipative and aperture illumination losses, for the receiving antenna. Thus, by Eqs. 2.10–2.12, the total power received by the antenna is

$$P_r = SA_e = S \frac{\lambda^2}{4\pi} G_R. \quad (2.13)$$

In the case of a planar aperture array with a large number of elements, it is also convenient to define a term called *aperture efficiency* ϵ_A , which relates the array's directivity D_o to the directivity for an aperture of the same physical area that is uniformly illuminated in amplitude and phase, or D_u , by the relation

$$D_o = \epsilon_A D_u. \quad (2.14)$$

Or, in terms of the maximum effective area of the antenna array $A_{e,\max}$ and its physical area A_p ,

$$A_{e,\max} = \epsilon_A A_p. \quad (2.15)$$

Thus, the effective area is a measure of how effectively the planar array makes use of its physical area in comparison to a uniformly illuminated aperture of the same size. Therefore, the maximum gain G_o of a planar aperture array may be written as

$$G_o = \epsilon_L \cdot \epsilon_A (1 - |\Gamma|^2) D_u = \epsilon_L (1 - |\Gamma|^2) D_o. \quad (2.16)$$

The concept of an antenna aperture becomes meaningless for an array with only a few elements or a one-dimensional (linear) array of elements, and one must either use the general equation, Eq. 2.4, or rely on the element pattern gain to evaluate the array directivity and gain, as will be shown in Chapter 4.

Finally, a polarization match between the incident field and the receiving elements in an array must be matched for maximum gain. Otherwise, a polarization loss ϵ_P will result between the polarization of the incident wavefront

and the receiving elements' polarization unit vectors $\hat{\rho}_w$ and $\hat{\rho}_a$, respectively. Consider a wave traveling in the z direction with electric field components

$$\bar{E} = \hat{x}E_x e^{-j(kz+\phi_x)} + \hat{y}E_y e^{-j(kz+\phi_y)}. \quad (2.17)$$

The unit polarization vector of the incident wave is defined as

$$\hat{\rho}_w = \frac{\hat{x}E_x + \hat{y}E_y}{(E_x^2 + E_y^2)^{\frac{1}{2}}} e^{-j(\phi_x + \phi_y)}. \quad (2.18)$$

The polarization unit vector of the antenna elements is defined according to the wave it excites or optimally receives. A receiving antenna has its effective aperture modified by the polarization loss factor ϵ_P as

$$\epsilon_P = |\hat{\rho}_a \cdot \hat{\rho}_w^*|^2. \quad (2.19)$$

Linearly polarized antennas may excite (or receive) fields oriented in the direction orthogonal to its intended polarization. The extent to which an antenna does this is defined as the cross-polarization ratio. The electric field in Eq. (2.17) is circularly polarized if $E_x = E_y$ and $\phi_x = \phi_y + \left(\frac{1}{2} + 2n\right)\pi$ for any integer n .

The total power received by the antenna at its feedline is thus

$$P_r = S \frac{\lambda^2}{4\pi} D_o \epsilon_L \cdot \epsilon_A \cdot \epsilon_P (1 - |\Gamma|^2) = S \frac{\lambda^2}{4\pi} \epsilon_P G_R \quad (2.20)$$

or in terms of the physical area, using Eqs. (2.11–2.15), the total power received is

$$P_r = S \epsilon_L \cdot \epsilon_A \cdot \epsilon_P (1 - |\Gamma|^2) A_p = S A_e. \quad (2.21)$$

Therefore, the effective area of the antenna array may be reduced by resistive losses in the antenna, aperture efficiency, polarization mismatch, and feedline mismatch.

2.2 Active Quasi-Optical Arrays

The quasi-optical active arrays consist of an array of input elements, each element connected to its own amplifier. Each amplifier processes the signal, routes the signal to its own output element, where each radiator contributes to the power and pattern of the output array.

In a large, planar, two-dimensional passive receiver array with a conventional corporate power collection network, the power collected by each antenna element in the array is added coherently, as shown in Figure 2.2. In this configuration, if the signal received by each element in the array is of equal amplitude and phase, then the total power collected by the combiner is

$$P_r = N A_e S(\theta, \phi) \quad (2.22)$$

for N elements in the array, assuming that the combiner is lossless and phase-

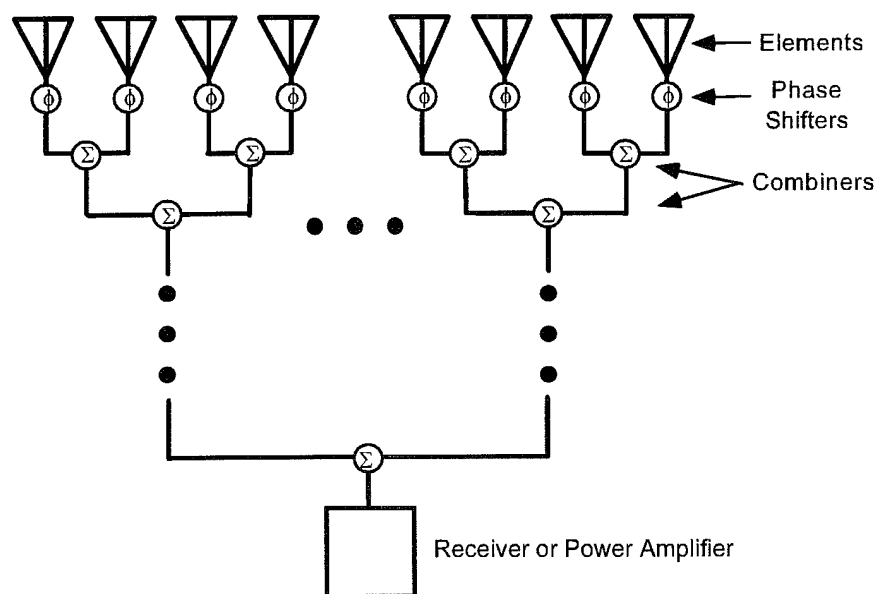


Figure 2.2. General corporate feed structure of a passive phased array. Phase shifters are used at each element for array beamsteering control. The array may be used for transmitting or receiving, depending on the functionality of the device at the corporate port.

matched. For a periodic, planar two-dimensional arrangement of identical elements in the array, a relationship between the physical array area A_p and the number of array elements N is obtained in terms of the cell area,

$$A_p = N A_{\text{CELL}} \quad (2.23)$$

where A_{CELL} is the area of a grid occupied by a single element in the array. The maximum directivity of the array, assuming uniform amplitude and phase across the elements, in this case is

$$D_u = \frac{4\pi}{\lambda^2} N A_{\text{CELL}}. \quad (2.24)$$

Considering the aperture efficiency ϵ_A , the actual directivity for a large aperture array is

$$D_o = \epsilon_A \frac{4\pi}{\lambda^2} A_p. \quad (2.25)$$

However, in the case of a quasi-optical active array, the input elements are not combined in any manner, as shown in Figure 2.3. Rather, each input element independently feeds its own amplifier through a short length of transmission line. Therefore, the power coupled into each amplifier from its respective element can be considered independently of any other element, provided there is no coupling between input antennas. In Chapter 6, we model mutual coupling among elements in an array representative of our quasi-optical power-combining lenses using patch antennas. The maximum coupling between elements is -25 dB for uniform amplitude and phase illumination, so power collection expressions for individual antenna elements are a good approximation. The total power collected by the input surface is simply the sum of the power collected by the elements. For uniform amplitude illumination across all of the

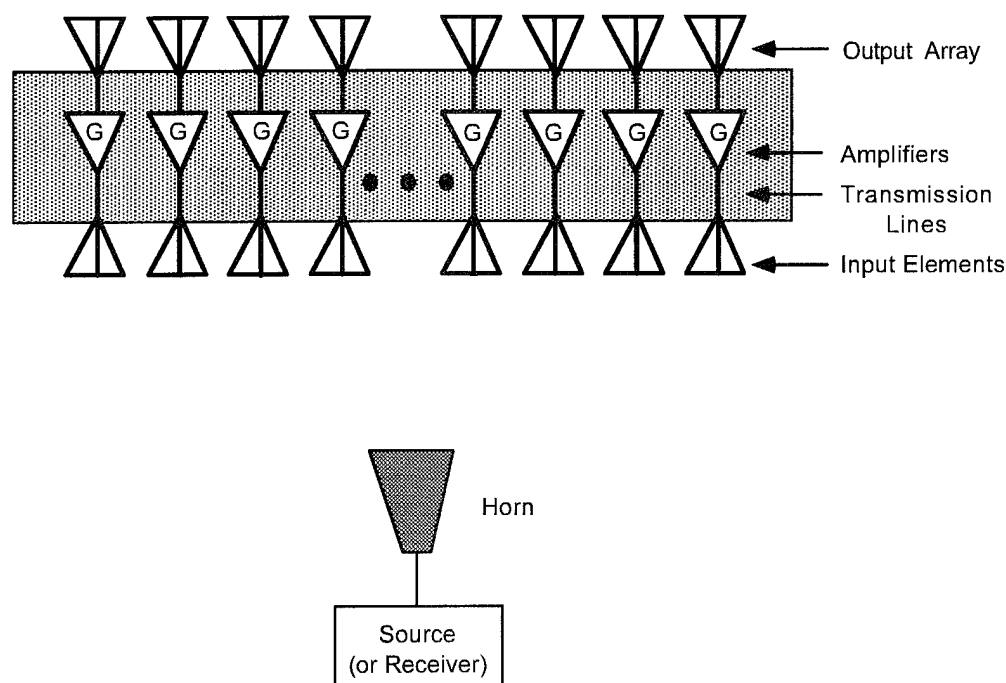


Figure 2.3. A general quasi-optical array amplifier. Power combining occurs in free-space, removing sources of loss and dispersion found in a corporate feed structure.

input elements, the total input power is the product of the number of input elements and the input power of an individual element.

The amplifiers in the quasi-optical power combiner are assumed to have identical amplitude and phase response. The high device uniformity achievable in monolithic microwave integrated circuit (MMIC) fabrication is making this assumption realizable for multi-element arrays built on an integrated circuit. The output of each amplifier is routed through a transmission line to their respective output elements. The lengths of these transmission lines may be used to provide the proper phase relationship between the output elements for power combining in free space. The lengths of these lines as a function of element position in the array is a critical design factor in quasi-optical lens amplifiers, and will be discussed in Chapter 3.

At the output plane, the output elements radiate the power from their respective amplifiers into free space. Under the proper phase relationship among the output signals, the power of the elements constructively combine in free space. The combined power may be collected by a horn antenna, or it may be directed in a particular direction (or multiple directions) for use in a communication or radar system. Because a phase and amplitude relationship among the output elements is present at the output surface, an array factor describes the output pattern of the array's electric field in the far field. The array factor significantly increases the effective radiated power (ERP) in a desired direction while reducing it in other directions, and will be described in Chapter 4.

The generalized quasi-optical power-combining amplifier configuration of Figure 2.3 is utilized in several quasi-optical amplifiers described below. These amplifiers are either grid or array topologies.

2.3 Plane-Wave Fed Transmission Wave Amplifier Array

The first plane-wave amplifier was demonstrated under the direction of David Rutledge at Caltech in 1991 [36],[92]. The amplifier is a 5×5 grid loaded with a two-MESFET differential amplifier in each of the grid's 25 cells. Gate and drain leads of each differential amplifier are connected to vertically and horizontally oriented metal strips, respectively, that form the grid. Since the input and output waves are linearly polarized and orthogonal to each other, external polarizers are necessary to maintain device stability. The plane wave feed assures uniform phase across the grid, so the output of all grid cells add coherently in free space using the same power combining technique as was employed earlier in a 100 element MESFET oscillator [29]. The grid period

is about two-tenths of a free-space wavelength, and the entire grid area is 64 cm^2 .

Later, our group at the University of Colorado developed a MESFET patch antenna amplifier array in which the input and output wave polarizations may be arbitrarily selected [42]. This amplifier, shown in Figure 2.4, has an array of rectangular patch antennas on input and output sides of the substrate. Each common-source MESFET amplifier is coupled and matched to its input and output patch elements with microstrip lines. A substrate via connects the output of each amplifier to its output patch printed on the opposite side of the substrate. Alternating ground planes effectively isolate input and output sections of the amplifying structure. The ground planes are connected by vias periodically spaced at quarter-wavelength intervals. High impedance gate and drain bias lines run through the voltage nulls of the patches on input and output surfaces, respectively.

2.3.1 Amplifier Unit Cell

To confirm the concept of using this active array topology for power combining, an individual amplifier unit cell using a packaged Avantek ATF-13484 GaAs MESFET was built on a teflon substrate with relative permittivity $\epsilon_r = 2.2$ and dielectric thickness $h = 0.508 \text{ mm}$. To save space, minimize parasitics, and maximize bandwidth, a single microstrip transmission line matches the radiating-edge impedance of the patch to the MESFET. The patch antennas were designed using a multi-port network model analysis and synthesis program [93], and are fed at the center of their radiating edges. The resonant input impedance of the patch is 140Ω . The use of a frequency-dependent one-port equivalent circuit for the patch during the design process was essential

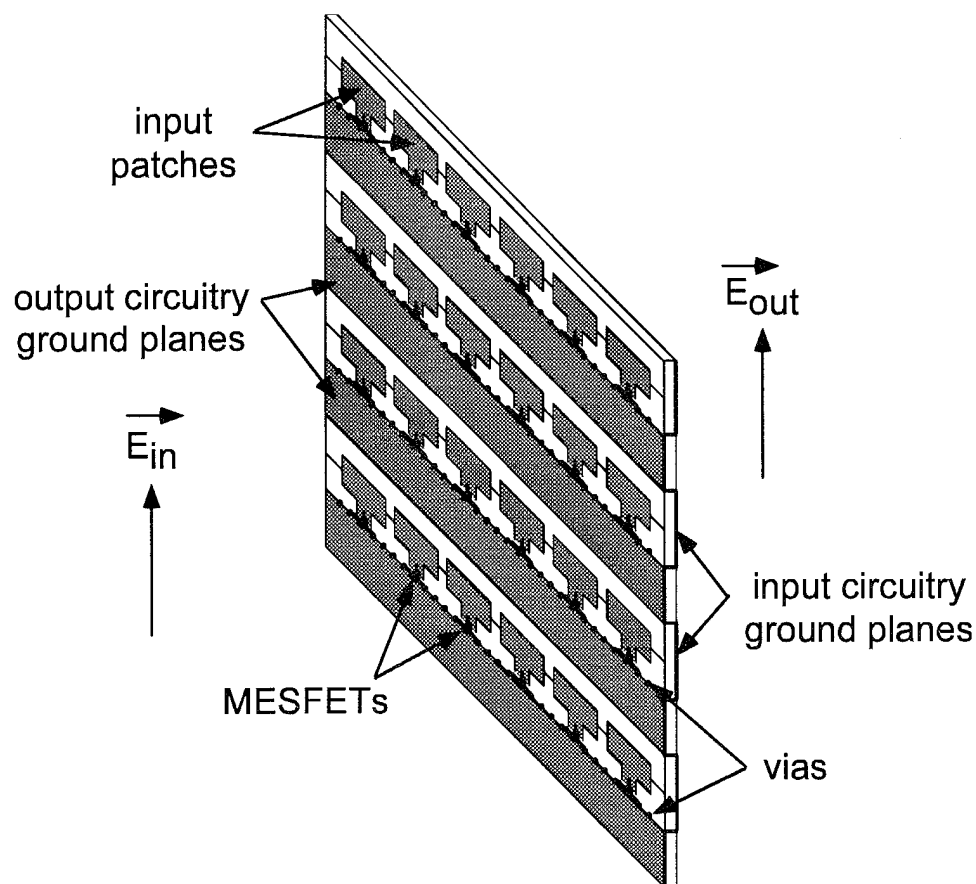


Figure 2.4. A 24-element patch-patch quasi-optical transmission wave amplifier.

for analyzing the stability of the amplifier. A bilateral design at 10 GHz was performed with a $100\ \Omega$ stabilizing resistor between the gate and source of the MESFET. The DC and RF voltages across the gate-to-source terminals of the MESFET are smaller in magnitude than across the drain-to-source terminals, so degradation of efficiency and heat dissipation due to the stabilization resistor is minimized. The design is stable and the maximum gain contributed by the MESFET amplifier is 8.4 dB at 10 GHz. The final design of the amplifier unit cell is shown in Figure 2.5(a). The polarization of input and output waves in this unit cell are linear and copolarized. Therefore, polarization is

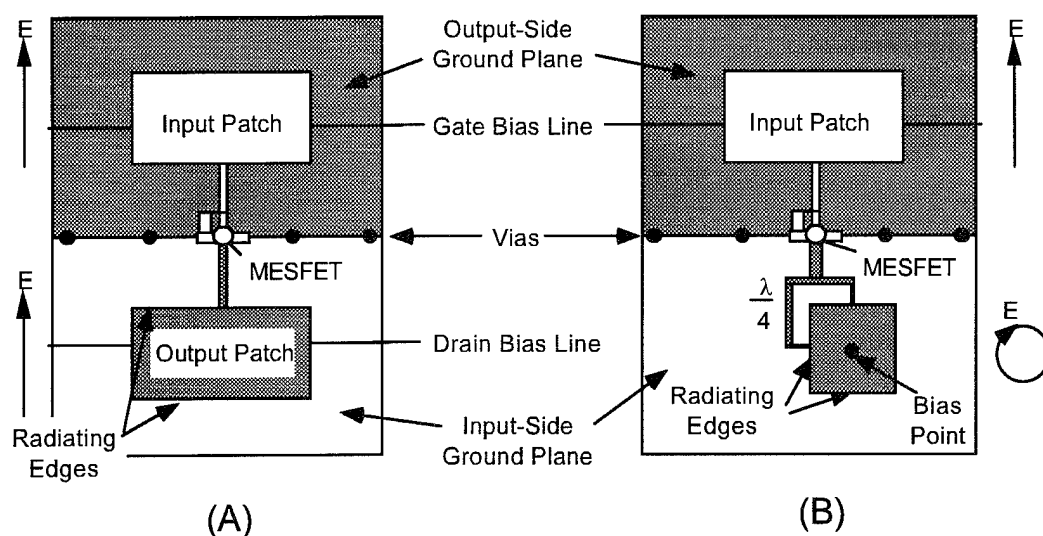


Figure 2.5. Planar transmission-wave amplifier unit cells for (a) linear polarization for input and output; (b) linear polarization input and circular polarization output.

preserved between input and output while maintaining stability because of the alternating ground-plane isolation.

The ground-plane isolation structure of the amplifier unit cell provides the flexibility to arbitrarily select the polarities of the input and output waves without affecting stability. An amplifier unit cell with a linearly polarized input and a circularly polarized output patch was designed as illustrated in Figure 2.5(b). The output square patch is fed on two adjacent edges with a $300\text{-}\Omega$ edge impedance and a 90° separation in phase between the two feeds. The drain bias of the MESFET is provided through a via to the output patch at its voltage null.

A free-space measurement technique determines the gain contributed by the MESFET, as well as determining the frequency response of the transmission amplifier under test. Our technique uses a known gain value of the patch element and, in the case of the array, the theoretical directivity of the

array with uniform amplitude and phase at each element. Figure 2.6 shows the experimental setup in which an absorbing screen at the device plane prevents diffraction path measurement error. Standard gain horns G_1 and G_2 are connected to an HP 83640A synthesized sweeper and HP71500A/HP70820A microwave transition analyzer (MTA), respectively. The MTA enables us to measure power received across a frequency range. First, a free space power measurement is performed without the device under test, which determines the path loss between the horns and is recorded as P_c . Then the free-space transmission amplifier is placed between the horns, and the received power is recorded as P_r . The ratio between these two measured powers P' is then given as

$$P' = \frac{P_r}{P_c} = G_{\text{in}} G_{\text{out}} G_{\text{active}} \frac{(r_1 + r_2)^2}{r_1^2 \cdot r_2^2} \left(\frac{\lambda_o}{4\pi} \right)^2 \quad (2.26)$$

where G_{in} and G_{out} are the effective input and output antenna gains of the transmission amplifier, G_{active} is the gain added by the MESFET amplifier, and r_1 and r_2 are the distances from the horn antennas to the device under test. Distances r_1 and r_2 are selected to be in the far field of both the horns and the transmission amplifier. Once P' is measured, the only unknown parameter in Eq. (2.26) is G_{active} , which is expected to be the same regardless of array size. The active gain of the single-MESFET polarization-preserving patch amplifier unit cell was measured over a frequency range of 9 to 11 GHz, and the “biased on” result is plotted as a solid line in Figure 2.7. When the MESFET is biased at cutoff, a condition referred to as “biased off,” little power will be transferred through the amplifier because the alternating ground planes provide good input-to-output isolation. When the MESFET is biased on ($V_{DS} = 2.5\text{V}$, $I_{DS} = 20\text{mA}$), a maximum gain G_{active} of 7.1 dB is measured at 10 GHz.

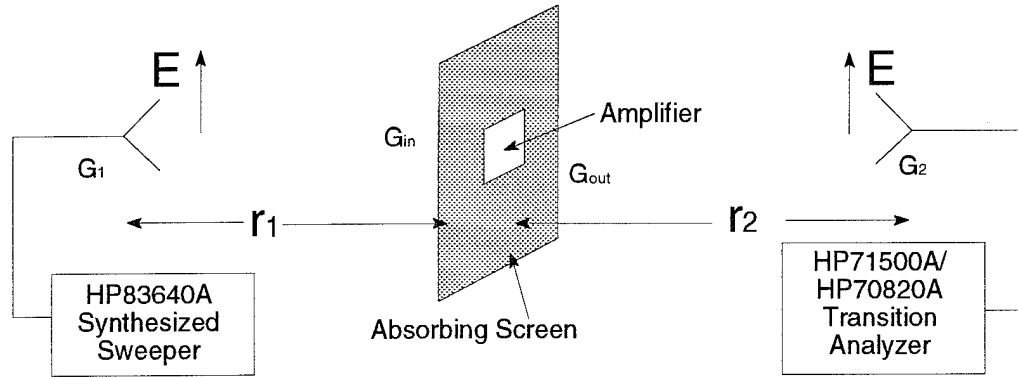


Figure 2.6. Free-space measurement system for quasi-optical amplifiers. The absorbing screen reduces the diffraction-path signal, which can be significant for the polarization-preserving amplifier measurement.

The measurement was performed in the far-field of the standard-gain horns at a distance $r_1 = r_2 = 60$ cm, referring to Figure 2.6 above. The frequency-dependent gain of the patch antennas, calculated from a multiport network model [93] of the patch and experimentally verified at 10 GHz, is used for G_{in} and G_{out} in Eq.(2.26).

One can deduce from the values of G_{active} , r_1 , r_2 and Eq.(2.26) that P' , which is the insertion gain (or loss) of the amplifier, is -23.9 dB. Thus, the unit cell amplifier is an attenuator when considering the feed and receiver as part of the system. The narrowband behavior of the transmission amplifier is due mainly to feedline mismatch with the patch away from the center frequency due to the highly resonant nature of the patch antennas. The measured cross-polarization ratio is 23.4 dB.

Using the same measurement methodology, the gain of the rectangular-to-circularly polarized amplifier cell was evaluated. An amplifier added gain G_{active} of 6.8 dB and an output axial ratio of 0.3 dB were measured at 10 GHz.

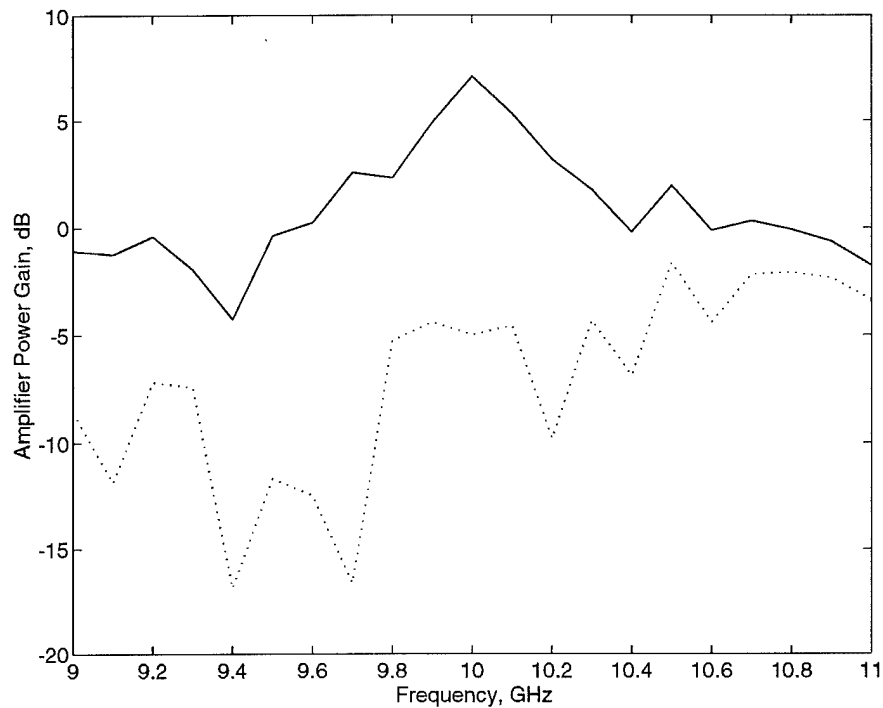


Figure 2.7. Gain contributed by the MESFET amplifier in the polarization-preserving, linearly polarized unit cell. The solid line is the measured biased-on gain, and the dotted line is the measured transmission characteristics when biased off.

The bandwidth of the circularly-polarized output amplifier was narrower than its linearly polarized counterpart because axial ratio degradation is a more sensitive bandwidth limitation than the input match.

2.3.2 Array Performance

The 24 elements of this array are arranged in a 4×6 periodic rectangular lattice. The horizontal spacing between elements is $2\lambda_o/3$ in the horizontal direction and the vertical spacing between elements is $4\lambda_o/3$. The large vertical spacing is required to accommodate the ground plane isolation, and could be reduced by using a substrate with higher dielectric permittivity. It is assumed

that the inter-element spacing is large enough so that the individual amplifier cells do not parasitically couple to one another. The measured gain of the array is 21 dB higher than that of the amplifier unit cell. Therefore, the insertion gain of the array is $-23.9 \text{ dB (unit cell)} + 21 \text{ dB} = -2.9 \text{ dB}$ and thus the array exhibits insertion loss.

The single biggest factor of the insertion loss is diffraction loss in the amplifier feed. The array's diameter is $D = 6\lambda_o$, thus requiring an approximate far-field distance of $2D^2/\lambda_o = 2.1$ meters at 10 GHz to provide a plane wave feed. The standard gain horn illuminating the array has a gain $G_T = 15 \text{ dB}$, a 3-dB E -plane beamwidth of 31° and an H -plane beamwidth of 28° . If each element in the array could capture all of the power incident on its physical area (i.e. $\epsilon_A = 1$), such that $A_p = A_e$, then we can define a directivity for each cell in a uniformly-spaced array for the broadside direction as

$$D_{\text{CELL}} = \frac{4\pi}{\lambda_o^2} d_x d_y \quad (2.27)$$

where d_x and d_y are the horizontal and vertical spacing between element centers. For now, assume that the unit cell radiation efficiency and array aperture efficiency are both unity. Then the gain of the array at its input is

$$G_r = N D_{\text{CELL}} \quad (2.28)$$

for N cells in the array. For the 24-element array with the inter-element spacing described above, the gain $G_r = 24.3 \text{ dB}$. The Friis transmission relation,

$$\frac{P_r}{P_T} = G_r G_T \left(\frac{\lambda_o}{4\pi R} \right)^2 \quad (2.29)$$

may be employed to illustrate the power loss of the free-space feed placed in the far-field of the array. Illuminating the array at the design frequency in

the broadside direction with a standard gain horn at the far-field range of 2.1 meters, the array captures only 1.1 % of the source power. This represents a feed loss of -19.6 dB due to diffraction from the far-field source, as illustrated in Figure 2.8(a).

The first quasi-optical amplifier, described above, employed this far-field feed with polarizers for isolation of input and output waves as shown in Figure 2.9 [36]. The 5×5 grid of differential-pair MESFET amplifiers covered a 64 cm^2 area. The grid amplifier was fed at a range of 50 cm, and the investigators assumed that the effective array area equals the physical area. Substituting

$$G_{in} = G_{out} = \frac{4\pi}{\lambda_o^2} A_p \quad (2.30)$$

into Eq.2.26, setting $r_1 = r_2$, and rearranging results in an equation for the active gain contributed by the amplifiers:

$$G_{\text{active}} = \frac{P_r}{P_c} \left(\frac{\lambda r}{2A_p} \right)^2. \quad (2.31)$$

Using this equation, Rutledge reported a peak gain G_{active} of 11 dB at 3.3 GHz. However, the device exhibited an insertion loss $P' = 0.1$ dB. So although the paper reported gain, in reality the device has little use as a stand-alone power combiner fed in the far-field. The purpose of the work presented in this thesis is to overcome the insertion loss problem and develop quasi-optical power combiners with absolute power gain.

To capture more of the feed power, dielectric lenses with an aperture much greater than that of the amplifier array may be oriented as shown in Figure 2.8(b). The distance between the lenses, assuming they are identical, is approximately twice the focal length. The active array is placed at the beam waist, where the wavefront is planar. However, the amplitude distribution

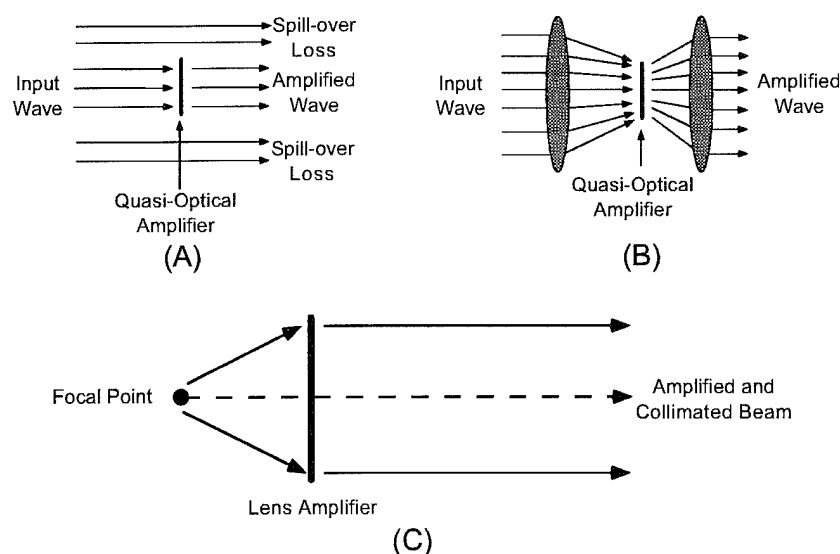


Figure 2.8. Feed methods for quasi-optical amplifiers: (a) Plane wave feed from a source in the far-field; (b) Feed at the beam waist of a dielectric lens pair; (c) Focal point feed of a lens amplifier.

is Gaussian in the transverse direction, leading to an unintentional amplitude taper for the amplifier array. As will be shown in a later chapter, the amplitude taper will modify the output-side pattern of amplifier arrays. Dielectric lenses add weight, size and complexity to the quasi-optical system. If lenses with a shorter focal length to diameter ratio (F/D) are used to reduce system size, the system is more difficult to align and prone to aberrations.

Rutledge *et al* used the dielectric lens feed in a second grid amplifier utilizing HBTs [37]. This amplifier consists of a 10×10 grid of differential-pair amplifiers covering a 64 cm^2 area. Again, the input and output printed dipoles are orthogonally polarized to one another, and are very short with respect to wavelength – only $0.10\lambda_o$. Input and output isolation is provided with external polarizers to maintain amplifier stability. The dielectric lenses used have a focal length of 46 cm and a diameter of 30 cm, and the beam waist spot size is 10 cm. The power calibration was performed with a square aperture in an

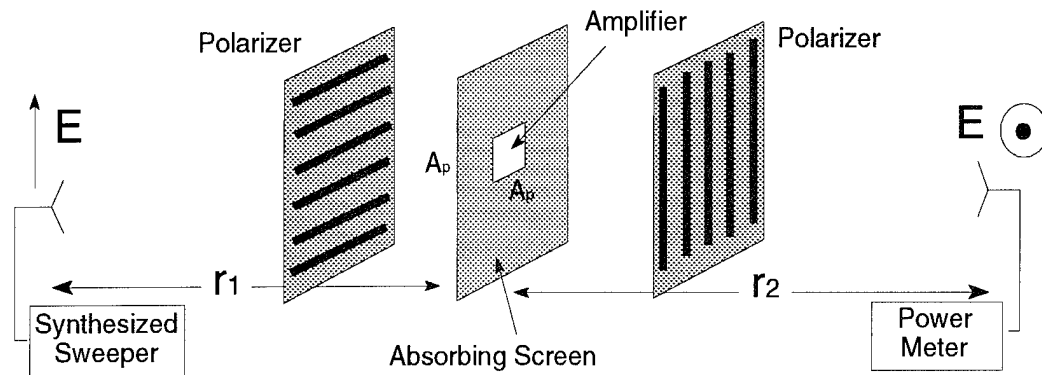


Figure 2.9. Measurement arrangement for grid amplifiers. External polarizers with orthogonal orientation isolate input and output waves for stability.

absorbing screen placed at the beam waist. The square aperture and the grid amplifier are the same size, so that insertion gain may be determined simply by filling the screen's aperture with the grid amplifier. Assuming that no power is lost in the dielectric lens to waveguide horn transitions, the resulting insertion gain was 10 dB at 10 GHz with a 3-dB bandwidth of 1 GHz. A comparison to the far-field feed was performed at a range $r_1 = r_2 = 90$ cm, resulting in a peak insertion gain of 3.5 dB at 10 GHz. Employing the dielectric lens feed improved the system insertion loss of the grid amplifier by 6.5 dB.

This thesis reports the theory, design, and results of quasi-optical transmission wave amplifier arrays that use a novel scheme of focusing using delay lines and element positioning on the array's substrate. These amplifiers demonstrate the very desirable quality of producing *absolute* power gain without the requirement for external polarizers and lenses. What is meant by *absolute* is an increase in the effective radiated power (ERP) of a source due to using the quasi-optical amplifier in a free-space power measurement .

The results of these amplifiers are tabulated in Table 2.1 for comparison. It is obvious that the amplifier grids and arrays that are fed from the far-field suffer from feed loss since the absolute gain of the array is much lower than the active gain. The dielectric lens and the focal point feed significantly reduce the feed loss, thus greatly improving the absolute power gain.

Table 2.1. Comparison of quasi-optical amplifiers with various feed mechanisms.

Quasi-optical amp	Feed Type	f (GHz)	G_{active} (dB)	G_{absolute} (dB)
Mader [42]	Far-field	10.0	7.1	-2.9
Rutledge [36]	Far-field	3.3	11.0	-0.1
Rutledge [37]	Far-field	10.0	10.0	3.5
Rutledge [37]	Diel Lens	10.0	10.0	10.0
Schoenberg [75]	Focal Pt	9.75	9.5	8.1
Schoenberg [75]	Focal Pt	10.0	18.5	13.0

2.4 Power Amplifier Power Added Efficiency

The polarization-preserving 24-MESFET patch array shown above in Figure 2.4 was designed for maximum gain at a bias point of 20 mA and 2 V per device. The s -parameters at a higher bias point (40 mA and 4 V per device) are practically identical, except for an increase in $|S_{21}|$. Since, to a first approximation, only this parameter changes (decreases) when a MESFET is saturated, the design for a saturated class-A amplifier at the high bias point should be approximately the same as the low-bias point linear design.

First a single cell was measured between two polarization-aligned 16-dB gain horn antennas, placed in the far field of the active antenna as illustrated above in Figure 2.6. The horns were connected to a HP71500A Transition Analyzer, used to measure the power saturation curves of the unit cell at several bias points. In Figure 2.10, these saturation curves are plotted for a

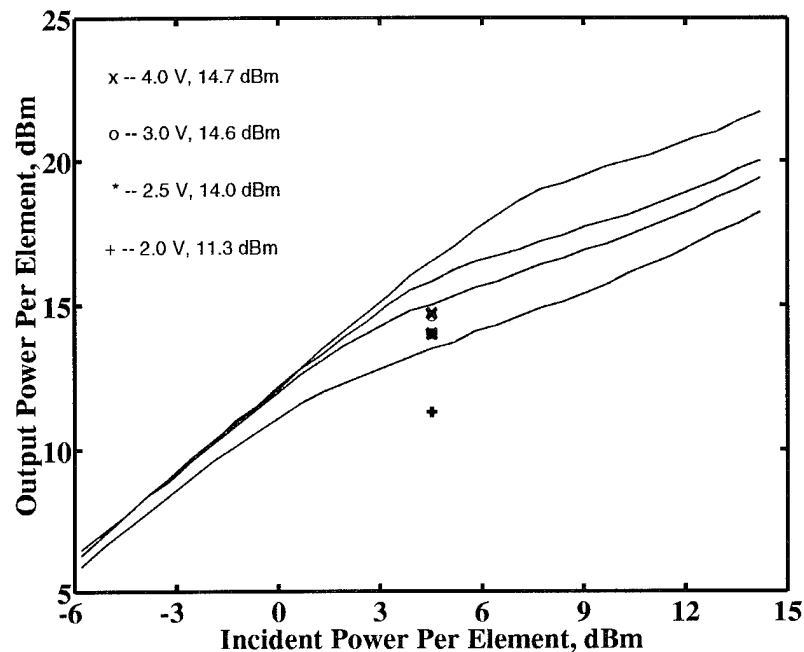


Figure 2.10. Saturation curves for a single-cell free-space amplifier with a constant drain current and several drain bias voltages. The superimposed symbols represent measured array power levels, divided by the number of elements ($N = 24$).

unit cell. Then the array was tested in the setup, which required increasing the range from the horns to the array to 2.1 meters. A 10 W Travelling Wave Tube (TWT) amplifier was connected between the frequency sweeper and the feed horn to drive the entire array into saturation from this range. The TWT amplifier provided a total input power to the array of 64 mW (2.7 mW/device) at 10 GHz. The entire array results are superimposed on the curves. The average power per element in the array is slightly lower than that of a single element tested alone, which means that the array combining is lower than in an ideal, uniformly illuminated array. The on/off ratio was 10 dB. With a constant input power and total array drain current of 1 A, the output power was measured for several drain-bias voltage points, and the results are given in

Table 2.2. For obtaining the values in Table 2.2, the 10 GHz patch gain of 5.5 dB was used. For this low-cost class-A amplifier, an output power of 0.7 W with 21 % power-added efficiency was measured at 10 GHz for an DC power of 3 Watts.

Table 2.2. Measured gain, power and efficiency of the 24-MESFET array at 10 GHz for an input power of 64 mW (2.7 mW/device) and a constant total drain current of 1 Amp.

V_{DC}	Gain	Power Out	η_{Drain}	$\eta_{Power-Added}$
2.0 V	8.6 dB	0.3 W	16 %	13 %
2.5 V	9.7 dB	0.6 W	24 %	22 %
3.0 V	10.3 dB	0.7 W	23 %	21 %
4.0 V	10.4 dB	0.7 W	18 %	16 %

CHAPTER 3

CONSTRAINED LENS THEORY

3.1 Motivation

In the previous chapter, quasi-optical power-combining (QOPC) amplifiers were shown to exhibit poor insertion gain (or have overall insertion loss) unless the energy from the source is efficiently coupled into the amplifier. Dielectric lenses were shown to greatly improve the feed efficiency for QOPC amplifiers, but the increased system complexity, size, and weight may make such an arrangement undesirable. Mortazawi suggested that the system gain could be increased simply by placing the quasi-optical amplifier between two waveguide horns placed in close proximity [44]. However, this would violate the plane-wave feed condition necessary for the array to coherently combine, and severe standing wave conditions are possible between the array surface and the horns.

To preserve the proper phase relationship among elements in a QOPC array that is fed from the array's near field, geometric optics principles may be employed. The non-uniform phase front input into the QOPC array will require the designer to vary certain parameters of each element pair of the array, such as the elements' positions or delay-line length connecting the element pair. The theory of constrained lenses, demonstrated for passive lens arrays [94]–[96], may be employed for active arrays. The theory of constrained lenses developed in this chapter provides the expressions needed to develop a transmission-wave

amplifier array that may be fed from a single focal point or multiple focal points which are placed in close proximity to the input-side of the array. The constrained lens array receives a spherical wave, processes the signal at each element, and re-radiates an amplified collimated beam. The signal processing of each amplifier cell is schematically shown in Figure 3.1. Any type of antenna(s)

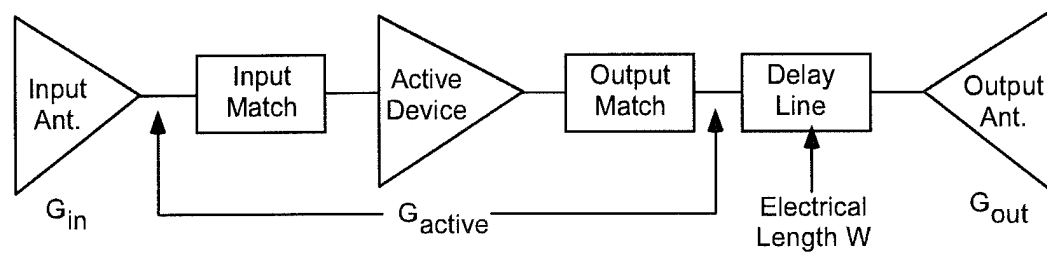


Figure 3.1. Schematic layout of an amplifier unit cell used in a constrained lens amplifier.

may be selected for input and output elements, and the choice is made based on the substrate choice and area available, desired frequency bandwidth, and desired element and array radiation patterns. The amplifier's input and output matching networks may be optimized for a particular performance goal, such as low noise, high gain, wide bandwidth, or high efficiency. The delay line is formed from low-dispersion transmission lines, such as coplanar waveguide or high-impedance microstrip.

In addition to serving as a free-space power combiner, the constrained lens amplifier may also perform beamsteering, beamforming, and beamswitching over a wide scan angle range with a relatively small cluster of feed horns [97]. As illustrated in Figure 3.2, the feed may be provided by any one horn in the cluster to produce a single beam in a particular direction, or the horns may simultaneously feed the array for multiple beam forming. These functions

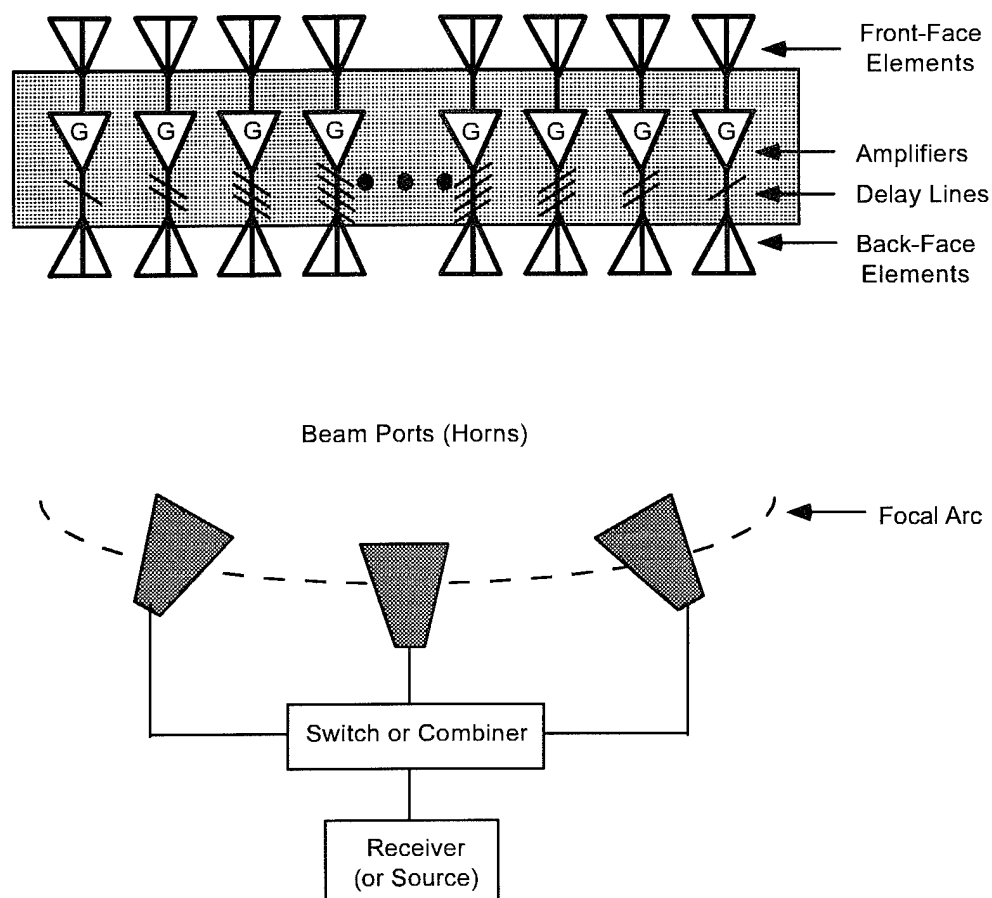


Figure 3.2. General layout of a constrained lens amplifier. Beamsteering and multiple beam forming capability is provided by horns placed along the focal arc of the lens.

are necessary for active array applications in airborne satellite communication terminals and satellite cross links [98]. Such application currently calls for extremely high frequency (EHF) phased array development in the 20–60 GHz frequency range using active transmit–receive (T/R) modules with phase shifters at each element in the array. The small physical dimensions at EHF lead to several unexpected difficulties not encountered at microwaves. For instance, a 4000-element phased array at 40 GHz has an aperture of only 24×24 cm², yet there needs to be RF distribution, phase control, and DC power distribution lines to all elements – tasks that approaches a total of 36,000 lines

[98]. A QOPC constrained lens amplifier array could conceivably replace the conventional phased array approach at millimeter-wave frequencies. *X*-band QOPC lens arrays demonstrated in Chapters 5 and 7 distribute and combine the RF signal in free space, perform beam scanning with a cluster of feed horns, and distribute DC power simply with a minimum of distribution lines.

3.2 Background

The use of reflectors and dielectric lenses for applications in the visible and near-infrared spectra is well understood using geometrical optics principles and is chronicled in several classic texts, for example Born and Wolf [99]. Geometrical optics principles have also been applied successfully to microwave and millimeter-wave design problems involving such devices as planar or curved reflectors, and dielectric lenses possessing constant or space-variable refractive indices. Whether the application is for optics or microwaves, the postulates upon which ray-tracing techniques are based must remain inviolate. Hence, the medium's refractive index or surface curvature comprising the device must be a slowly varying function of spacial coordinate compared to the wavelength of operation. Reflectors and lenses are widely used as collimating elements in microwave and millimeter-wave antennas [100],[101]. Typical examples of these devices, whose design may be based on geometrical optics, is shown in Figure 3.3. The devices shown here bear a strong kinship to certain lightwave optics analogues, although it will be shown that the control over amplitude, phase, and polarization may give much greater freedom to the designer of such transmitting or receiving devices. The curvature of the reflector is the one degree of freedom available in their design. Reflector antennas exhibit low reflection loss and no internal losses, have no chromatic aberration, and may be perforated

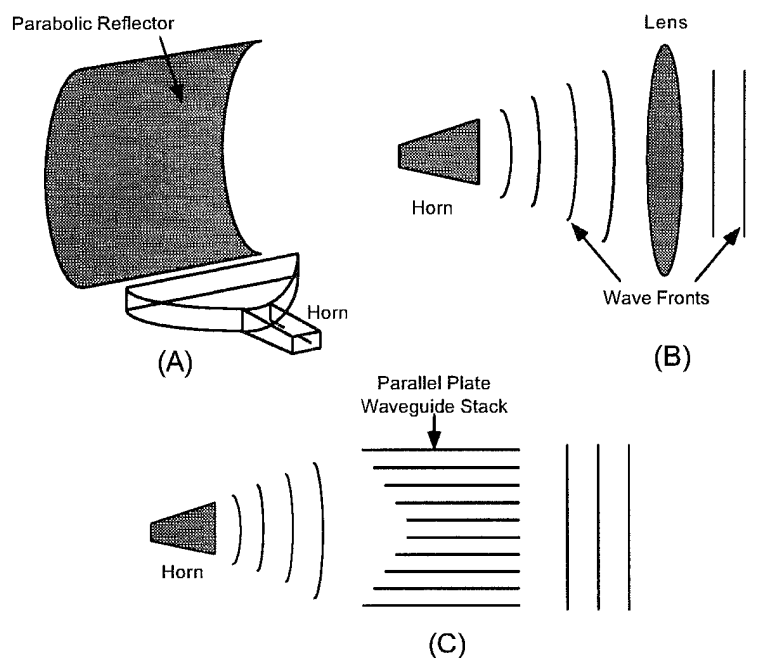


Figure 3.3. Microwave devices analogous to optics: (a) Reflector antenna with horn feed; (b) Dielectric Lens; (c) Artificial lens composed of a stack of parallel plate waveguides.

into a grid pattern to reduce weight and wind loads. However, typical feeds such as primary horns or line sources block a considerable portion of the reflector aperture unless sophisticated multiple-reflector feeds are employed, such as a cassegrainian mirror [102].

The earliest work in microwave antenna design using geometrical optics was done during World War II for enhancing the detection and tracking functions of early radar systems. This work concentrated on the use of artificial dielectrics and metal parallel-plate configurations [103]. Shown in Figure 3.4(a), the metal plate lens, made up of a stack of parallel-plate waveguides, imitates a dielectric with a curved surface for collimation. First described as “metal plate dielectrics” [104], it was not until later that the device was perceived as an array structure. Since the phase velocity of parallel plate

waveguide is faster than that of free space, a stack of waveguides open at both ends appears electrically as a dielectric with an index of refraction less than unity. The open ends of the waveguides allow a TEM wave to be coupled between free-space and the waveguide. A wave travelling through the guide is *constrained* to that waveguide path length between the input and output. For a stack of thin metal plates spaced distance a apart as shown in Figure 3.4, the index of refraction inside the guide is [103]

$$n = \sqrt{1 - (\lambda_o/2a)^2} \quad (3.1)$$

for a wave polarized parallel to the plates. The metal parallel-plate structure in Figure 3.4(a) imitates the focusing properties of the homogeneous plano-convex dielectric lens in Figure 3.4(b). A wave normally incident on the front face will not be refracted since that face is flat. The wave propagates through the parallel-plate stack to the curved back face. With its refractive index less than unity, the parallel plates refract rays at the curved interface, allowing the waveguide stack to focus the rays in the plane parallel to the plates. Because this lens can focus in just one plane with only the wave component polarized parallel to the plates, it requires a line source feed and has limited utility. To obtain dual-plane scan capability, rows of vertical parallel plates were combined with a stack of horizontal plates, resulting in a lattice of rectangular waveguides. Since the phase velocity of rectangular waveguide is always faster than free space, a lens using rectangular waveguides is thinnest in the center and grows progressively thicker toward its edge. This structure, known as the “egg crate” lens, focuses in both transverse planes down to one perfect focal point, and may be scanned to wide angles along two perpendicular focal lines [105].

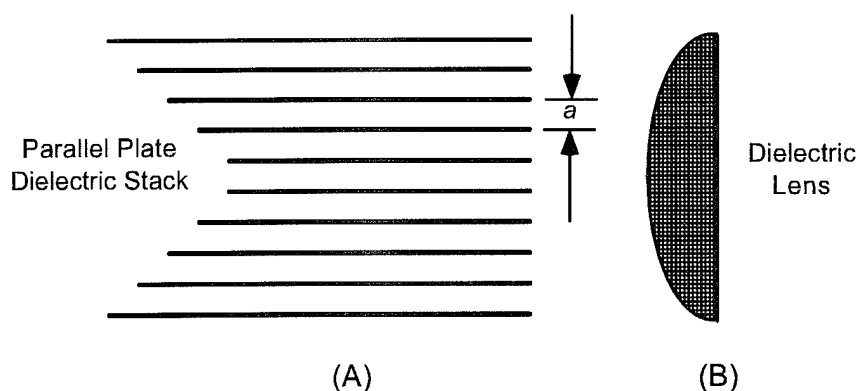


Figure 3.4. An artificial lens comprised of a stack of parallel plate waveguides is shown in (a), with the analogous plano-convex dielectric lens shown in (b).

An egg crate lens is a large and heavy structure, and dispersion in the waveguides tends to limit the bandwidth. To reduce weight and reduce the effect due to waveguide velocity variation with frequency, *zoning* or *stepping* of the lens surface may be employed [106]. Zoning reduces the length of transmission medium between two adjacent “zones” by exactly 360° at the design frequency. However, zoning increases sidelobe levels due to shadowing between zones. Natural homogeneous dielectrics are commonly used to avoid the dispersive effects seen in metal waveguide lenses, but again zoning is employed in large apertures to reduce weight. The index of refraction of homogeneous dielectrics at microwave frequencies is always greater than unity, leading to the convex lens shape seen in Figure 3.4.

With Gent’s introduction of the “Bootlace Aerial” in 1957 [107], the perception of microwave lenses changed from merely a convenient refractive medium to that of an antenna array. His experimental lens was made of pairs of folded dipole radiators separated by a ground screen and interconnected by parallel wire transmission line, or “twin lead”, as illustrated in Figure 3.5. Since the transmission lines were longest near the lens center and progressively

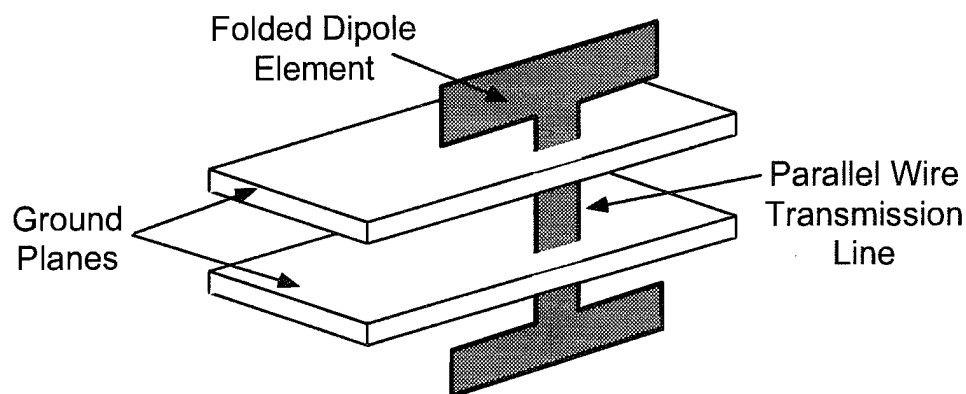


Figure 3.5. An input and output element pair of the bootlace aerial by Gent. Elements are folded dipoles fashioned out of twin lead, shorted at the ends. The delay line connecting input and output elements is twin lead.

shorter toward its edge, an incident wave from a feed suspended behind the lens would be delayed near the center relative to the edges, or be collimated. The importance of the bootlace aerial was to demonstrate that the delay lines in a constrained lens need not be made of waveguides. Numerous delay lines connecting pairs of any of several types of radiators could result in a lens. Possibly the most important capability of the new lens was for very broadband operation since it could use nondispersive transmission lines, like coax or twin lead, for the delay lines. The discussion in Chapter 4 will show that planar, open transmission media like microstrip and coplanar waveguide are low-dispersive media suitable for delay lines. The bandwidth limitation for our active lens amplifiers is the radiating elements used on the input and output surfaces of our transmission amplifiers as shown in Chapter 5 (the input match of the amplifiers is wider than the patch antenna VSWR match). Chapter 6 will introduce some wideband elements which are used in a receive lens array (detailed in Chapter 7) to considerably improve the bandwidth of the lens amplifier.

3.3 Constrained Lenses

Gent's bootlace aerial lens only embodied a single design degree of freedom in its design – the length of the parallel-wire transmission line, which varied as a quadratic function of radius in the plane of either lens face. However, as depicted in Figure 3.6, there are four design variables available in constrained lens design:

- (1) the shape of the input or back surface (that closest to the feed)
- (2) the shape of the output or front surface (the aperture)
- (3) the relative position of the elements comprising the pair on the two surfaces, and
- (4) the length of transmission line joining the element pair.

The first two features are incorporated into the metal plate lens shown in Figure 3.4. Degree of freedom (4) is not independently variable in this case since the length of the waveguides is dictated by the shape of the lens faces. Feature (3) would be difficult to achieve in a waveguide lens, but has been applied in some very useful lens designs.

Although Gent both alluded to the possibility of multiple-focal point lens design by incorporating the lens variables listed above, it was Rotman [108] who was the first to show a solution to the path length equality conditions necessary to produce three perfect focal points. His solution results in expressions for the back face element locations and transmission line lengths for the two-dimensional geometry shown in Figure 3.7. Using Fermat's Principle for the path length equality condition, it may be shown that three focal points may be simultaneously satisfied with the given lens geometry. These three focal points include one located on the optical axis at a distance G from the back face

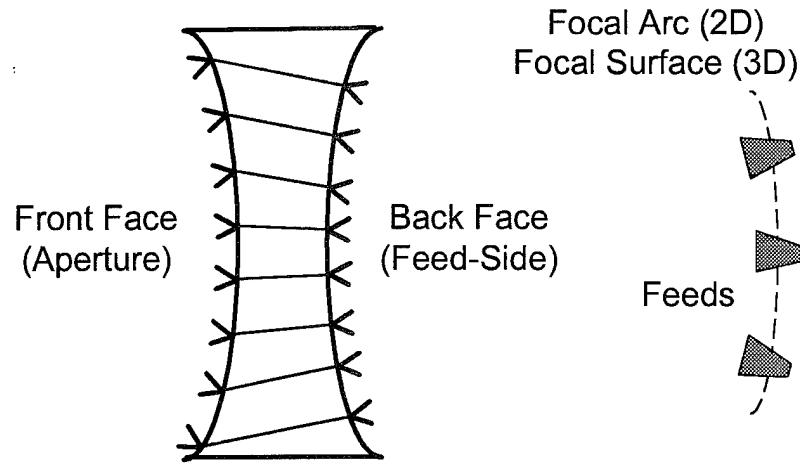


Figure 3.6. General layout of a constrained lens. Input and output surfaces may be curved or flat, and are populated with elements. Each front-face element is connected to its corresponding back-face element with a delay line. Multiple feeds may illuminate the lens at various scan angles along the focal arc or focal surface.

and two at symmetric points $(y, z) = (\pm F \sin \alpha, -F \cos \alpha)$. The path length conditions for the upper, on-axis, and lower focal points are, respectively

$$R_1 + W = F + W_o + N \sin \alpha \quad (3.2)$$

$$R_o + W = G + W_o \quad (3.3)$$

$$R_2 + W = F + W_o - N \sin \alpha \quad (3.4)$$

where

$$R_1^2 = (F \cos \alpha - Z)^2 + (Y + F \sin \alpha)^2$$

$$R_2^2 = (F \cos \alpha - Z)^2 + (Y - F \sin \alpha)^2$$

$$R_o^2 = (G - Z)^2 + Y^2.$$

Here, N represents the y -coordinate of the aperture element, which is not the same as that of the feed side element, Y . This lateral displacement between front and back faces is one of the three degrees of freedom. The other two

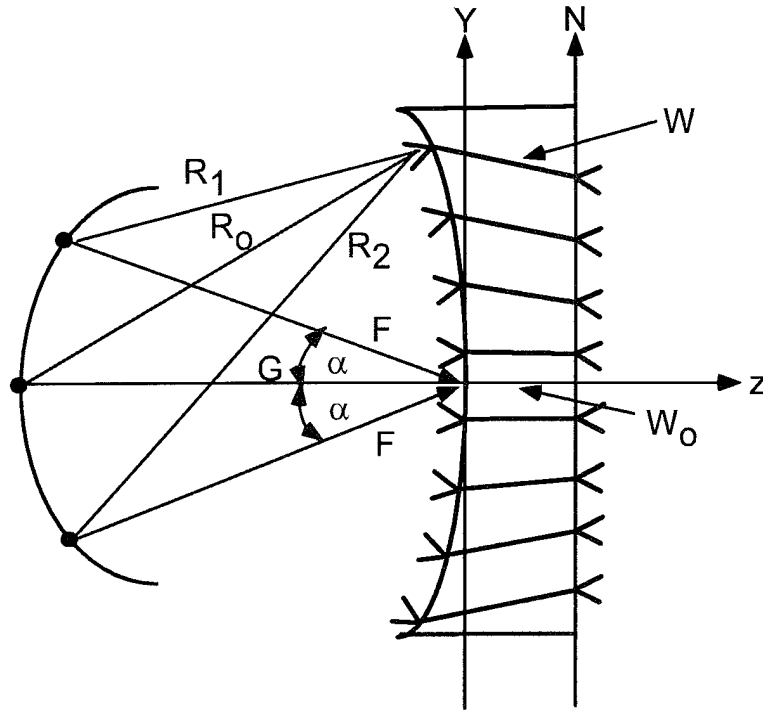


Figure 3.7. Geometry of the Rotman (trifocal) lens used in the solution. The Rotman lens scans in one plane only.

are the back face shape, defined by Z , and the delay line lengths W . The line length W_o is an arbitrary length required for practical considerations of spanning the distance between the lens faces. The details of the derivation, given in Rotman and Turner [108], result in the following coefficients of the quadratic equation $a\omega^2 + b\omega + c = 0$:

$$a = 1 - \eta^2 - \left(\frac{g-1}{g - \cos \alpha} \right)^2 \quad (3.5)$$

$$b = 2g \frac{g-1}{g - \cos \alpha} - \eta^2 \sin^2 \alpha \frac{g-1}{(g - \cos \alpha)^2} + 2\eta^2 - 2g \quad (3.6)$$

$$c = g \frac{\eta^2 \sin^2 \alpha}{g - \cos \alpha} - \frac{\eta^4 \sin^4 \alpha}{4(g - \cos \alpha)^2} - \eta^2 \quad (3.7)$$

where $\omega = (W - W_o)/F$. In the above, $g = G/F$ and $\eta = N/F$. Once ω is obtained from Eqs. (3.5–3.7), the normalized back face (feed side) element

coordinates (y_b, z_b) are found from

$$y_b = \frac{Y}{F} = \eta(1 - \omega) \quad (3.8)$$

$$z_b^2 + 2gz_b + (y_b^2 - \omega^2 + 2g\omega) = 0 \quad (3.9)$$

where $z_b = Z/F$. The normalized element locations on the front face (aperture side) are $(y_f, z_f) = (N/F, Z_o/F)$ where Z_o is a constant for a flat surface, and N is the inter-element period of a linear array. The solutions for $(W - W_o)$ are the electrical lengths of the delay lines joining the front and back face elements. Quite often, a Rotman lens is used as a multiple-beam antenna. Several feeds on the focal arc will transmit or receive simultaneously, and their beams are added in a power combiner. They may be amplitude weighted to synthesize a shaped beam or a low-sidelobe beam. It should be noted that the Rotman lens, whether employing a parallel-plate waveguide or a printed-circuit delay structure between input and output beam ports, is a two-dimensional structure restricted to beamforming and beamsteering in only one plane [109].

The most challenging application of constrained lenses is for two-axis scanning antennas. The goal is to use an array of feeds distributed over a paraboloid surface, or *focal surface*, behind the back face of the lens to form beams in all directions over a large, conical region. Switching between feeds will accomplish scanning in both the azimuth and elevation planes. The general layout of such an antenna is illustrated by Figure 3.8, which is a three-dimensional structure in contrast to the Rotman lens. The general design procedure for three-dimensional bootlace lenses is no different than for two-dimensional lenses. Path-length equality is enforced for the selected foci to determine the element locations and delay line lengths, and an optimum focal surface is found to establish the beam port positions. The three-dimensional

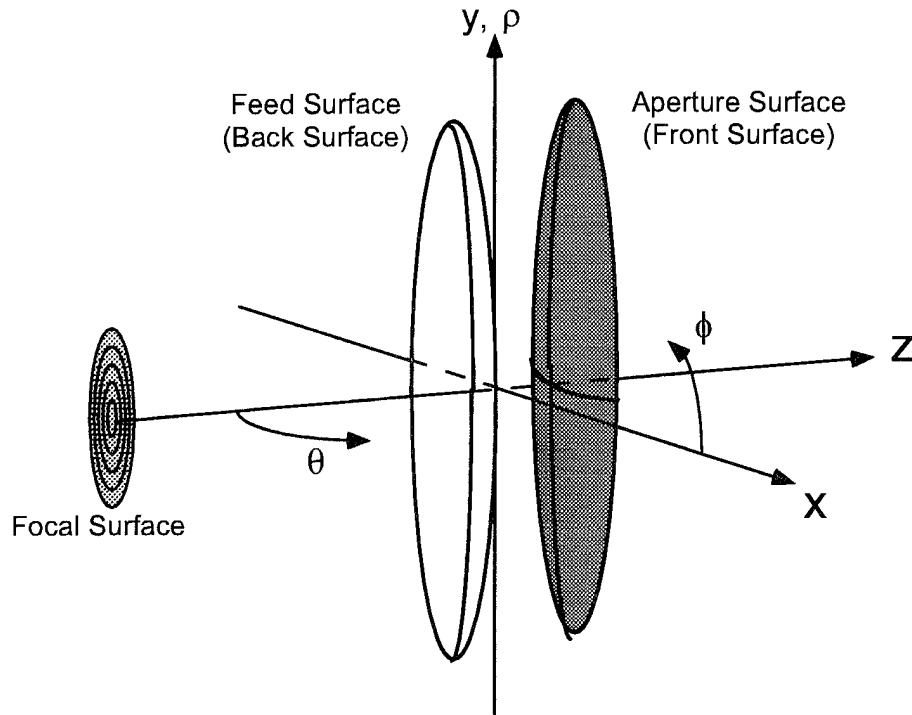


Figure 3.8. General layout of a three-dimensional lens. Input and output surfaces may be complex contours. The lens may be fed from a set of focal points for perfect focus or a focal surface for near-perfect focus.

design may be symmetrical in ϕ , as reported by Cornbleet [110], in which the focal surface is ϕ -symmetric. Alternatively, the design may have up to four perfect foci as reported by Rao [111], who chose to place them on a straight line, and Rappaport and Zaghloul [112], who oriented them on a circle. In both quadrufocal treatments, the four foci are all in the same ϕ -plane, so scanning in the orthogonal plane suffers as a result. Referring to the quadrufocal lens geometry in Figure 3.9, Cornbleet's ϕ -symmetric equations for two pairs of symmetrically placed foci at angles $\pm\alpha$ and $\pm\beta$ are

$$\frac{R_4 - R_1}{\sin \alpha} = \frac{R_3 - R_2}{\sin \beta} \quad (3.10)$$

which is a single relation between the back surface element coordinates ρ_b and z_b and thus describes the contour over which these elements are placed. The

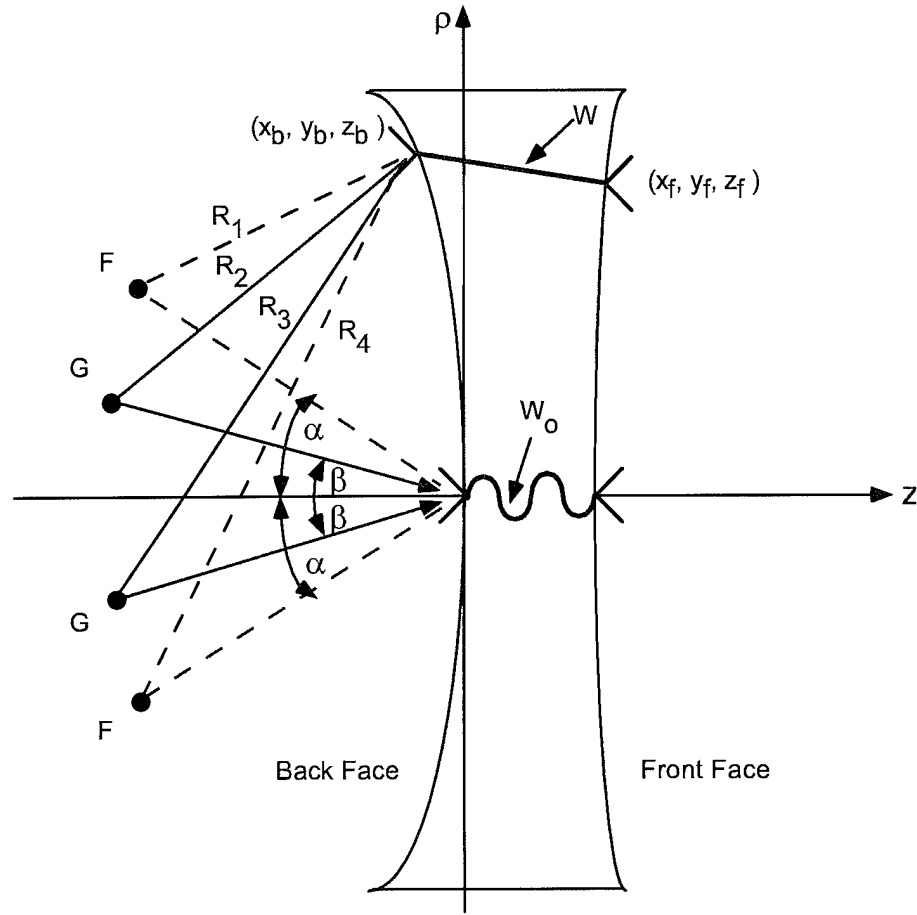


Figure 3.9. A cross-section of the three-dimensional geometry used for quadrifocal lenses. The ϕ -symmetric design of Cornbleet and the quadrifocal designs of Rappaport and Zaghloul [112] and the line-focus design of Rao [111] use this geometry.

front surface element coordinates ρ_f and z_f are obtained from the solution of the equations

$$z_f = \frac{w_o + (R_2 + R_3 - 2G) - (R_1 + R_4 - 2F)}{2(\cos \beta - \cos \alpha)} \quad (3.11)$$

$$\rho_f = \frac{R_4 - R_1}{2 \sin \alpha}. \quad (3.12)$$

The electrical line length connecting the back surface element to its corresponding front surface element is

$$w = \frac{w_o + \cos \alpha (R_2 + R_3 - 2G) - \cos \beta (R_1 + R_4 - 2F)}{2(\cos \beta - \cos \alpha)}. \quad (3.13)$$

A completely general lens design based upon Eqs. (3.10-3.13) may result in complicated front and back surface contours, and element-pair relative positioning and delay-line lengths that are difficult to achieve. Rappaport and Zaghloul [112] derived a case with a circular focal arc (i.e. $G = F$) and a planar front surface with four perfect foci. Their design procedure provides the freedom to place the aperture side elements on a planar surface at coordinates $(x_f, y_f, 0)$. This design freedom provides the opportunity to design the aperture side array to conform with desired antenna array performance requirements.

The design equations for the back surface element coordinates are

$$z_b = -x_f^2 \frac{\cos \beta + \cos \alpha}{2F} \quad (3.14)$$

$$x_b = x_f \sqrt{1 + \frac{1}{F^2 - x_f^2} \left[y_f^2 - x_f^2 \cos \alpha \cos \beta + x_f^4 \left(\frac{\cos \alpha + \cos \beta}{2F} \right)^2 \right]} \quad (3.15)$$

$$y_b = y_f \quad (3.16)$$

and the delay line length expression is

$$w = F \left(1 - \frac{x_b}{x_f} \right). \quad (3.17)$$

The design imposes the condition $y_b = y_f$ since, according to the authors, "scan angles α and β are in the xz plane," and so "there is no need to distort the mapping in the y -direction." This statement is true only in the $\phi = 0^\circ$ or $\phi = 180^\circ$ planes, and the quadrifocal design of Rappaport and Zaghloul suffers from significant path length error in other scan planes.

In either the ϕ -symmetric or quadrufocal cases above, the path length equality condition for an arbitrary feed point at a radial distance H from the origin and angles θ_h, ϕ_h is $H + s = R + w$ and the path length error is

$$\Delta l = H + s - (R + w), \quad (3.18)$$

where R is the distance from the feed to a back face element, and

$$s = x_f \sin \theta_h \cos \phi_h + y_f \sin \theta_h \sin \phi_h + z_f. \quad (3.19)$$

A comparison of the path length error for the ϕ -symmetric to the quadrufocal cases is performed in the following way. For both cases the focal length is $F = 6.0\lambda_o$, $D = 4.5\lambda_o$ and half-wavelength spacing between elements, resulting in 100-element arrays with an $F/D = 1.33$. For the ϕ -symmetric case, the interior pair of focal points are at $G = 5.5\lambda_o$. For both cases, the exterior pair of focal points subtend an angle $\alpha = 20^\circ$ and the interior pair subtend an angle $\beta = 10^\circ$. A computer routine was written to determine the element locations on the front and back faces of the lens, as well as the feed distance as a function of angle for minimum error. Figure 3.10 shows the results of the simulation comparing the quadrufocal lens at various feed angles (θ, ϕ) to the ϕ -symmetric over the same range of θ for a given ϕ . As expected, the quadrufocal lens performs better in the $\phi = 0^\circ$, or xz plane than in the orthogonal plane, with minimum error at focus angles α and β . The ϕ -symmetric lens case, plotted as the dotted line in the figure, exhibits lower path length error than the quadrufocal lens for scan angles $(\theta < 15^\circ, \phi = 15^\circ)$, and is comparable for angles $\theta > 15^\circ$. The ϕ -symmetric lens clearly has lower focusing error than the quadrufocal lens for scan planes $\phi > 30^\circ$. Since the ϕ -symmetric lens performs more consistently over all scan planes in ϕ , the

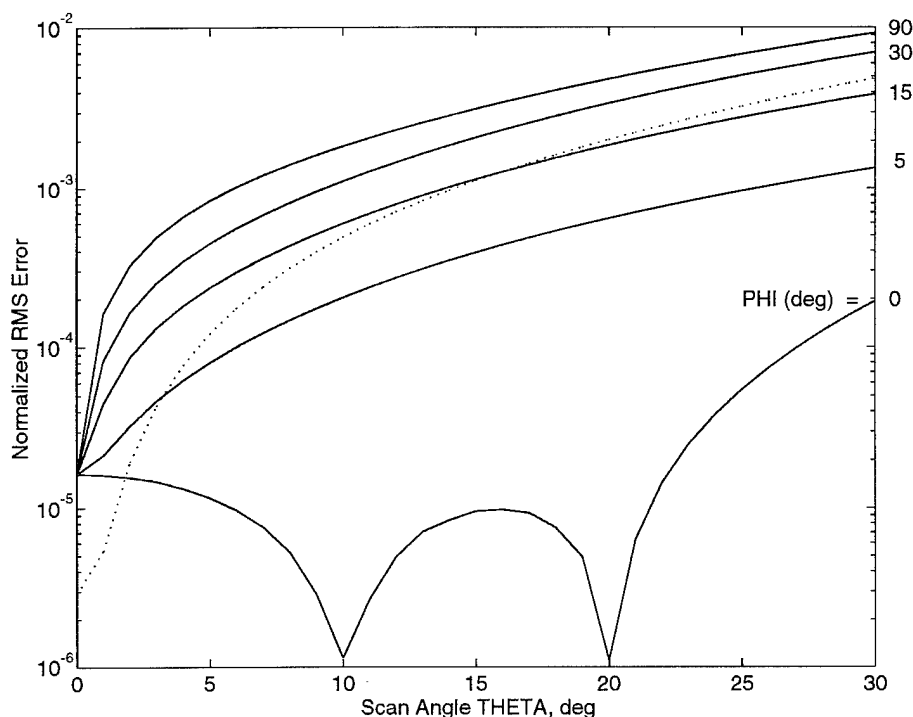


Figure 3.10. Normalized RMS path length error comparison between the quadrufocal lens (solid line) and the ϕ -symmetric lens (dotted line). The quadrufocal lens errors increase with increased scan plane ϕ , while the errors are independent of ϕ for the ϕ -symmetric case.

planar constrained lens equations developed for two-dimensional arrays below will consider the ϕ -symmetric case only.

3.4 Planar Constrained Lens

In spite of their wide angle scanning characteristics, lenses with four degrees of freedom are difficult to build. At least one face must be curved, with radiators placed in precise locations with transmission lines connecting the two surfaces. In addition, as bandwidth requirements increase, necessitating higher frequency of operation, either hybrid or monolithic microwave integrated circuit (MMIC) techniques may be used for lens fabrication. These fabrication

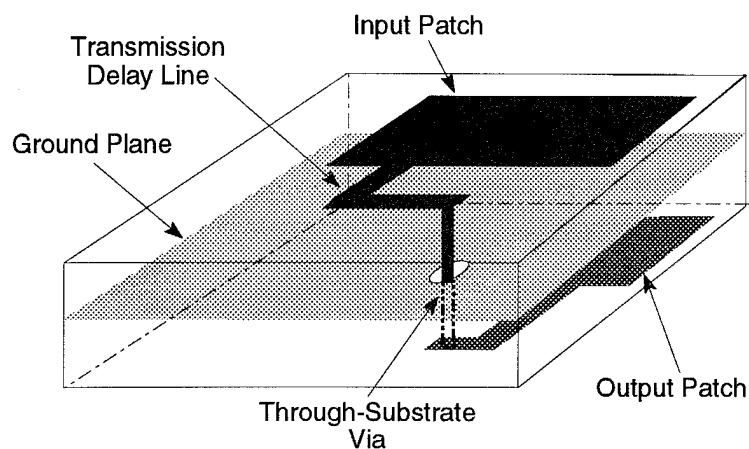


Figure 3.11. Layout of an input-output patch pair similar to that used in the constrained lens of McGrath. The central ground plane provides isolation to both input and output elements and completes the microstrip transmission medium. A through-substrate via connects the elements.

techniques are inherently planar, so a lens design with two interconnected planar printed circuit arrays is most applicable. McGrath [94],[95] proposed using arrays of printed microstrip patch antennas as shown in Figure 3.11. Front-side and back-side arrays have a common ground plane sandwiched between the two layers of dielectric. Delay lines are made with microstrip transmission lines and their meandered pattern is mirrored on both lens surfaces. The microstrip lines from the corresponding front and back side elements are connected together with either a feed-through pin [94] or with a coupling slot defined in the central ground plane [95]. With the constraints that both back side and front side surfaces are planar, the only design degrees of freedom available for this lens are the relative position of the feed side element with respect to its aperture side element, and the transmission line length connecting them.

To develop the lens equation for this case, first consider a planar linear

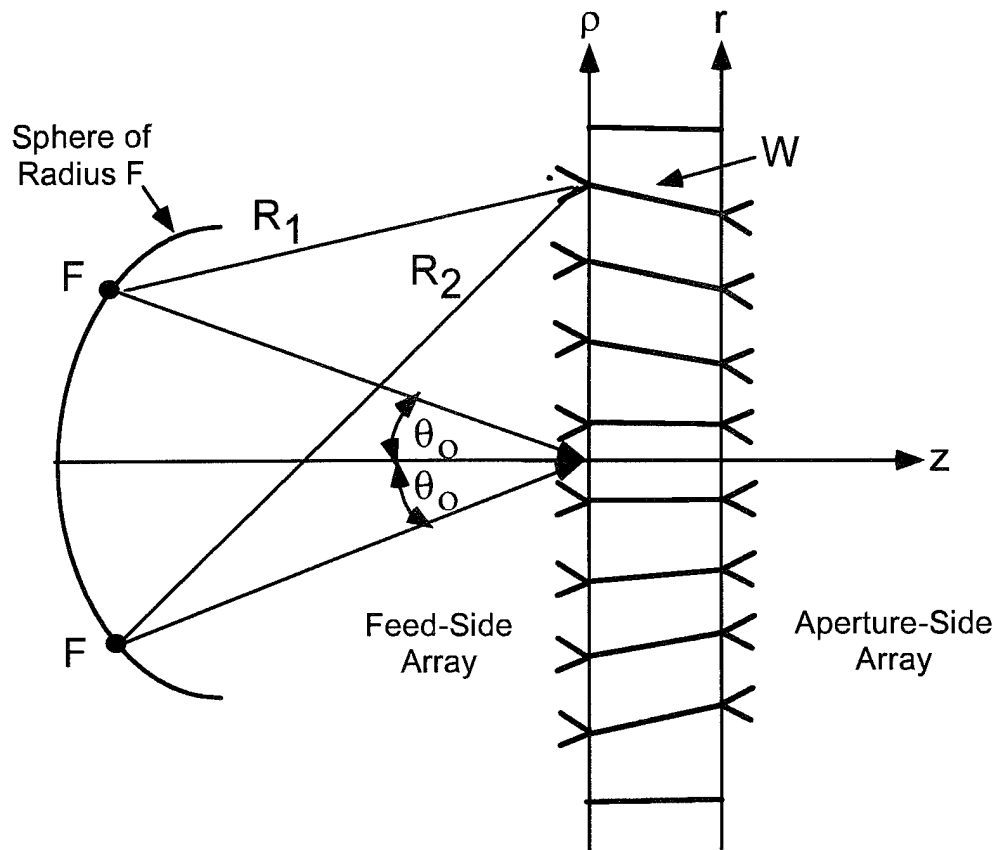


Figure 3.12. Geometry used in the planar linear constrained lens for determining the path length equality conditions.

array geometry as shown in Figure 3.12. Following [94], the relative location of the back side elements to the front side elements is

$$\rho = r \left[\frac{F^2 - r^2 \sin^2 \theta_o}{F^2 - r^2} \right]^{\frac{1}{2}} \quad (3.20)$$

where ρ and r are the distances from the lens center to the back side and front side elements, respectively, F is the focal length, and θ_o is the focal point angle.

The expression for the electrical line length, W , is

$$W = F + W_o - \frac{1}{2} \left[F^2 + \rho^2 - 2\rho F \sin \theta_o \right]^{\frac{1}{2}} - \frac{1}{2} \left[F^2 + \rho^2 + 2\rho F \sin \theta_o \right]^{\frac{1}{2}} \quad (3.21)$$

where W_o is an arbitrary constant electrical length. The aperture-side inter-element spacing is uniform, and thus the feed-side element coordinates are a

function of its corresponding aperture-side element position. The electrical length required for the delay line is also a function of distance away from the lens center, with the longest delay line required for the center element. Electrical line length may be converted into microstrip phase delay for microstrip-based lens designs. The delay line length is maximum at lens center and decreases away from the lens axis.

Since the lens is no longer fed at its focal point at angles other than 0° , lens defocusing due to path length errors in its feed reduces the output power of the lens. Consider the diagram in Figure 3.13, in which the lens has perfect focal points at positions P_1 and P_2 along a sphere of radius F and focal angle θ_o . The path length equality condition from focal point P_1 requires

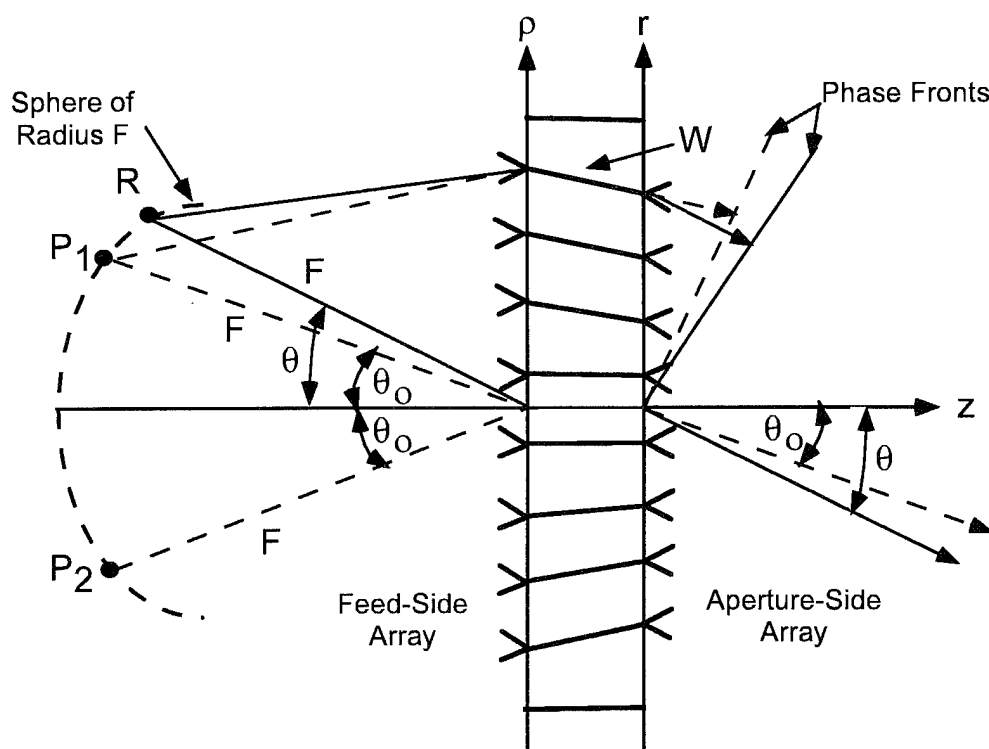


Figure 3.13. Exact focus occurs at points P_1 and P_2 on a sphere of radius F . When fed at other points on the sphere, a path length error will occur.

$$\sqrt{F^2 + \rho^2 - 2F\rho \sin \theta_o} + r \sin \theta_o + W = F + W_o. \quad (3.22)$$

The path length equality condition from an arbitrary feed point R along the sphere subtending an angle θ from the optical axis is of the same form as Eq. (3.22) with θ replacing θ_o and is

$$\sqrt{F^2 + \rho^2 - 2F\rho \sin \theta} + r \sin \theta + W = F + W_o \quad (3.23)$$

The path length error Δl at point R is the difference in the path length expressions Eqs. (3.23) and (3.22) for points R and P_1 , respectively. Subtracting the two expressions and assuming that the focal point is on-axis ($\theta_o = 0$), we obtain:

$$\Delta l = \sqrt{F^2 + \rho^2 - 2F\rho \sin \theta} + r \sin \theta - \sqrt{F^2 + \rho^2}. \quad (3.24)$$

A feed location G can be chosen at a distance different than F to minimize the peak error for any scan angle θ . Since the maximum path-length error occurs at the maximum value of r (at the aperture edge), set r to half the aperture diameter, or $r_{\max} = \frac{1}{2}D$. Defining the variable $\alpha = \sin^{-1}(\frac{r_{\max}}{F})$ and using Eq. (5.1), the path length error becomes

$$\Delta l = G - F = \sqrt{G^2 - 2FG \tan \alpha \sin \theta + F^2 \tan^2 \alpha} + F \sin \alpha \sin \theta - F \sec \alpha. \quad (3.25)$$

Rearranging Eq. (3.25) and squaring both sides results in a solution for $G(\theta)$:

$$G(\theta) = F \left[1 + \frac{\sin^2 \alpha \sin^2 \theta}{2(1 - \sec \alpha)(1 + \sin \alpha \sin \theta)} \right]. \quad (3.26)$$

Figure 3.14 illustrates the corrected distance, $G(\theta)$, as a function of feed angle for the lens. The focal arc minimizes defocusing errors as a function of angle and is instrumental in beamforming at angles other than the focal point angle θ_o as will be shown in Chapter 5. Figure 3.15 shows the calculated focal arc for

$F/D = 2.0$, which is the ratio used in the power-combining transmission lens amplifier arrays in Chapter 5, and $F/D = 1.2$, which is the ratio used in the low noise receiver array in Chapter 7. These focal arcs will be the feed location for the lens amplifiers when performing beamsteering and beamforming.

For a two-dimensional planar lens array, the ϕ -symmetric approach for element placement and delay line lengths will be taken due to its merits discussed in the previous section. The output element polar coordinates with respect to the lens axis are (r, ϕ_e) , and the input element coordinates are (ρ, ϕ_e) , where the radial distance ρ is given by a modified form of Eq. (5.1) as

$$\rho = r \left[\frac{F^2 - r^2 \sin^2 \theta_o \cos^2 \phi_e}{F^2 - r^2} \right]^{\frac{1}{2}}. \quad (3.27)$$

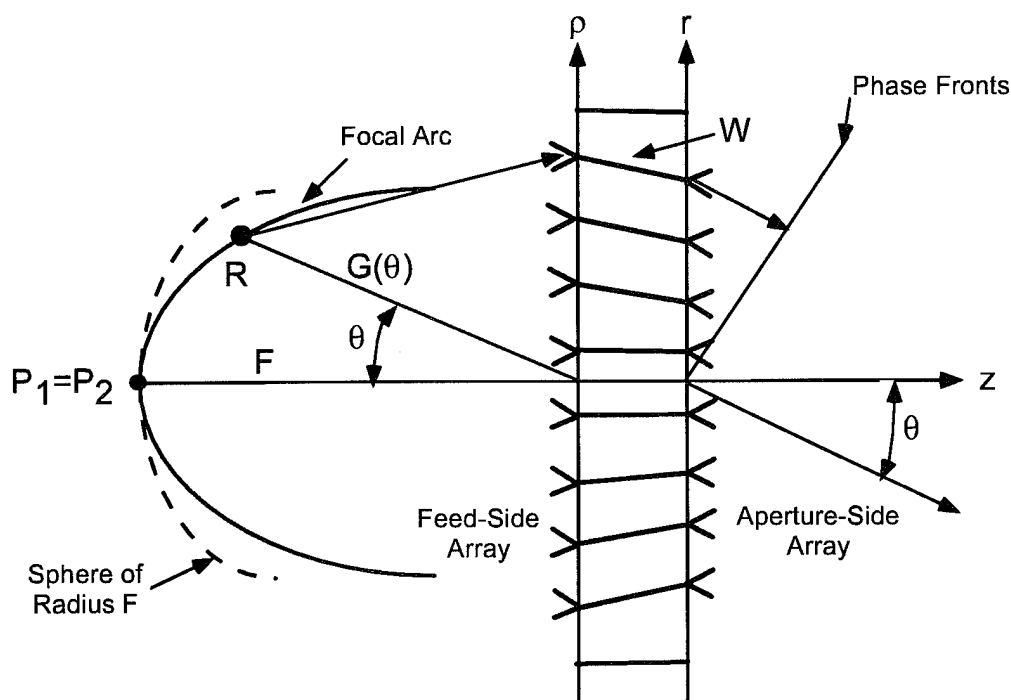


Figure 3.14. The corrected focal distance $G(\theta)$ for effective beamsteering with minimum path length error.

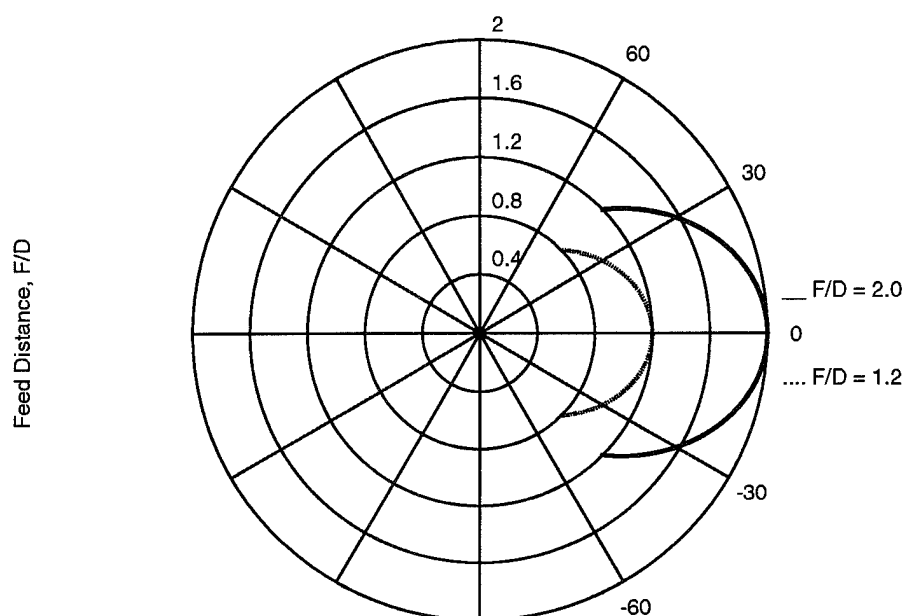


Figure 3.15. Calculated focal arc for the two-dimensional lens amplifier arrays discussed in Chapters 5 and 7, where the F/D ratio is 2.0 and 1.2, respectively.

The line length connecting input elements to output elements is similarly modified from Eq. (5.2):

$$W = F + W_o - \frac{1}{2} \left[F^2 + \rho^2 - 2\rho F \sin \theta_o \cos \phi_e \right]^{\frac{1}{2}} - \frac{1}{2} \left[F^2 + \rho^2 + 2\rho F \sin \theta_o \cos \phi_e \right]^{\frac{1}{2}}. \quad (3.28)$$

The planar lens equations of McGrath [94] have been used to calculate the delay line lengths of the lenses shown in Chapters 5 and 7. For the linear lens array in Chapter 5, Eqs. (5.1) and (5.2) are used to determine the input element locations and the electrical delay line lengths connecting input elements to their corresponding output elements, respectively. For the two-dimensional lens amplifiers in Chapters 5 and 7, Eqs. (5.3) and (5.4) are used instead for a

ϕ -symmetric design. For the linear lens, Eq. (3.26) was used to calculate the focal arc from which to feed the lens at the optimum distance. For the two-dimensional lenses, the focal arc equation is symmetrical in ϕ , so a focal surface may be defined. The measured results of the linear and two-dimensional lenses show outstanding beamsteering and beam forming capabilities when fed from the focal arc or focal surface. The two-dimensional lens amplifiers demonstrate insertion gain and on/off isolation ratio performance that far exceeds the far field-fed quasi-optical amplifiers discussed in Chapter 2. Thus, the application of geometrical optics principles to quasi-optical power combiners is a valid method towards making practical amplifiers for high power microwave and millimeter-wave sources.

3.5 Other Functions

The constrained lens concept may be applied to provide amplification as well as other functions for QOPC arrays. As illustrated in Figure 3.16, reflect arrays, polarization rotations, and amplitude or phase taper across the array may be performed. Several of these functions may be combined in a QOPC array, as demonstrated in the active arrays in Chapters 5 and 7.

3.6 Conclusion

The constrained lens theory developed in this chapter will be applied to planar lens amplifier arrays in Chapter 5 and 7, in which an amplifier circuit is embedded in the delay line network connecting input and output elements. These amplifier arrays demonstrate absolute power gain because the feed may be placed in the array's near field, thereby reducing loss due to diffraction. In addition, these arrays demonstrate the added features of beamforming and

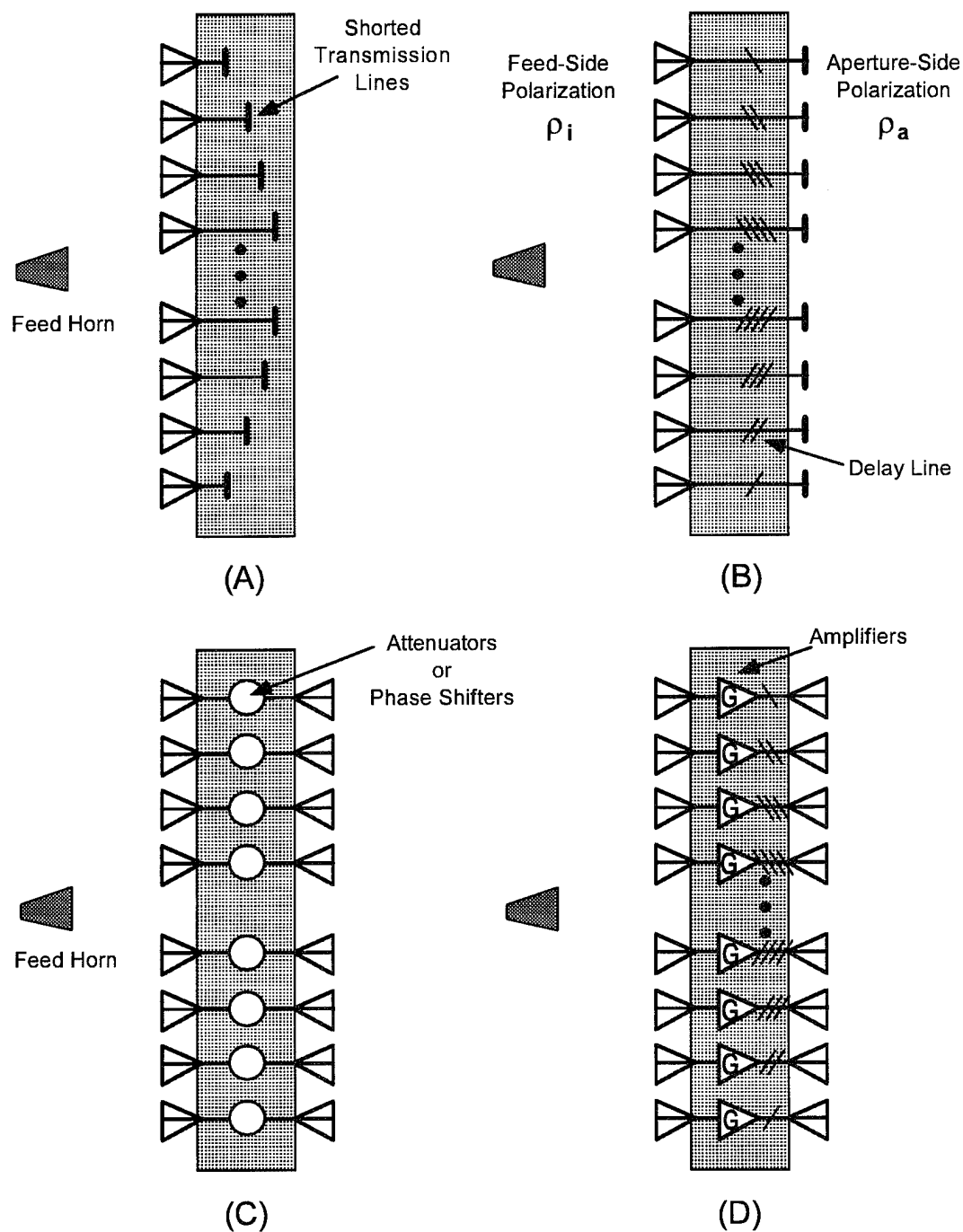


Figure 3.16. Constrained structures for various functions: (a) Reflect array; (b) Polarization rotation array; (c) Amplitude or phase taper array; (d) Active amplifier array.

beamsteering that constrained lenses offer for multiple-level quasi-optical power combiners that may use these lens amplifiers as either the final stage/radiator for transmission or receive array/front end for reception.

CHAPTER 4

THEORETICAL BACKGROUND FOR PASSIVE ANTENNA ARRAYS

4.1 Motivation

The present efforts into the research and development of quasi-optical arrays stems from the need for high power microwave and millimeter-wave sources that are reliable, lightweight, compact, and easily scalable. Arrays may be extended in two or three dimensions for a given output power requirement. Arrays may be conformal, though the arrays we have studied are planar, fabricated on a thin, flat copper-coated dielectric sheet. Therefore, the transmission medium connecting elements in a corporate feed network or used as delay lines in a constrained lens is quasi-TEM, such as microstrip or coplanar waveguide. These open transmission media are subject to dispersion at high frequencies, which will be examined in this chapter. Many of the properties of practical array antennas are apparent from a detailed consideration of idealized arrays. For such a general array of radiators as shown in the Figure 4.1, the electric field is given by the sum of radiated fields of each of the array's elements.

Each element at position (x_i, y_i, z_i) is excited by a complex weighting a_i and radiates with a vector element pattern $f_i(\theta, \phi)$ so that the total radiated field is given by

$$\overline{E}(\mathbf{r}) = K \sum_i \overline{f}_i(\theta, \phi) a_i \frac{e^{-jk|\mathbf{r}-\mathbf{r}_i|}}{|\mathbf{r}-\mathbf{r}_i|} \quad (4.1)$$

where K is a complex constant, $k = \frac{2\pi}{\lambda}$ is the free-space wave number at the

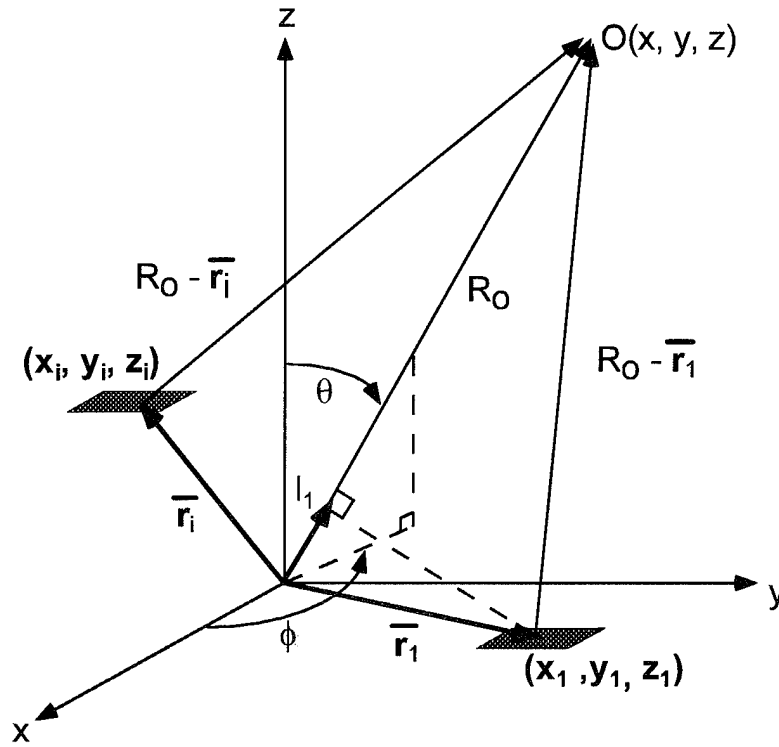


Figure 4.1: Generalized array coordinate system and geometry.

frequency of interest, and the distance from the field point to the position of the i^{th} element is

$$|\bar{\mathbf{r}} - \bar{\mathbf{r}}_i| = \sqrt{(x - x_i)^2 + (y - y_i)^2 + (z - z_i)^2}. \quad (4.2)$$

In the far field, this term can be approximated by

$$|\bar{\mathbf{r}} - \bar{\mathbf{r}}_i| \approx R_0 - \bar{\mathbf{r}}_i \cdot \hat{\boldsymbol{\rho}} \quad (4.3)$$

where

$$\bar{\mathbf{r}}_i = \hat{\mathbf{x}}x_i + \hat{\mathbf{y}}y_i + \hat{\mathbf{z}}z_i, \quad (4.4)$$

$$\hat{\boldsymbol{\rho}} = \hat{\mathbf{x}}u + \hat{\mathbf{y}}v + \hat{\mathbf{z}}\cos\theta, \quad (4.5)$$

and the projection of the field point onto the xy plane, called the directional

cosines, are

$$u = \sin \theta \cos \phi \quad (4.6)$$

$$v = \sin \theta \sin \phi$$

at all angles (θ, ϕ) in the spherical coordinate system. The directional cosines are derived as shown in Figure 4.2. The total field, assuming the far-field

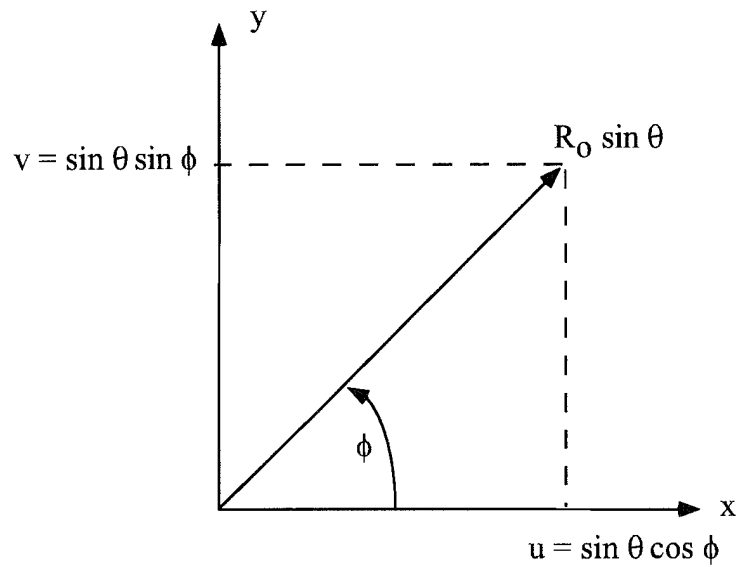


Figure 4.2. Projection in the xy plane for planar arrays showing the derivation of the normalized directional cosines u and v .

criterion is satisfied, is

$$\overline{E}(\overline{\mathbf{r}}) = K \frac{e^{-jkR_o}}{R_o} \sum_i \overline{f}_i(\theta, \phi) a_i e^{+jk\overline{\mathbf{r}}_i \cdot \hat{\mathbf{p}}}. \quad (4.7)$$

The vector element patterns \overline{f}_i are different in general due to mutual coupling among the elements and interaction between the elements and the array edge. For purposes of these discussions it is assumed that the element patterns are alike in an idealized array. This array may be used to form a beam at some desired radiation angle in space (θ_o, ϕ_o) . An element excitation that is applicable

for all frequencies is

$$a_i = |a_i| e^{-jk\bar{\mathbf{r}}_i \cdot \hat{\boldsymbol{\rho}}_o} = |a_i| e^{-jkl_i} \quad (4.8)$$

with ρ_o given by Eq. (4.6) using θ_o and ϕ_o in the directional cosine expressions. As shown in Figure 4.1, l_i is an electrical distance that is independent of frequency and that the product kl_i is a phase delay for the i^{th} element at frequency f . At the desired radiation angle (θ_o, ϕ_o) , the fully collimated beam field strength is a simple vector summation of the element patterns weighted by their amplitudes $|a_i|$,

$$\bar{E}(\bar{\mathbf{r}}) = K \frac{e^{-jkR_o}}{R_o} \sum_i \bar{f}_i(\theta_o, \phi_o) |a_i| \quad (4.9)$$

at which angle the largest possible value of the field $E(\mathbf{r})$ occurs for any value of R_o in the far-field if all of the element patterns f_i are equal and isotropic. Selecting the element excitation of Eq. (4.8) is understood intuitively by considering that the projected distance to the observer at (R_o, θ_o, ϕ_o) is different for each array element by the length l_i in Figure 4.1.

Removal of this path length difference will cause the contributions from each element to add in-phase in the far field. The envelope of the coefficients $|a_i|$ is the array illumination, and is the primary determinant of the radiated sidelobe levels. Applying signals of the form of Eq. (4.8) is called true time delay steering because the phase of the excitation signals exactly compensates for the time delay of a signal travelling the projected distances l_i . Time delay steering results in a fully collimated beam at all frequencies, but it requires dispersion-free delay lines for wideband coverage and relatively long delay lines for large apertures.

In the case that an array is steered with phase shifters, there will be some fixed frequency f_o , with wavelength λ_o and wavenumber $k_o = 2\pi/\lambda_o =$

$2\pi f_o/c$ where a phase weighting can be substituted for true time delay steering.

In such a case, the weighting coefficients a_i are

$$a_i = |a_i| e^{-j\frac{2\pi}{c} f_o \bar{\mathbf{r}}_i \cdot \hat{\boldsymbol{\rho}}_o} \quad (4.10)$$

so that the electric field in the far-field becomes the frequency dependent expression

$$\bar{E}(\bar{\mathbf{r}}) = K \frac{e^{-jkR_o}}{R_o} \sum_i \bar{f}_i(\theta, \phi) |a_i| e^{+j\frac{2\pi}{c} \bar{\mathbf{r}}_i \cdot (f\hat{\boldsymbol{\rho}} - f_o\hat{\boldsymbol{\rho}}_o)}. \quad (4.11)$$

Eq. (4.11) represents exact collimation at the desired angle (θ_o, ϕ_o) only at the fixed frequency $f = f_o$. For all other frequencies, the maximum electric field will occur at an angle other than the desired angle (θ_o, ϕ_o) resulting in a condition called beam squint. Beam squint may impose a greater bandwidth limit than antenna element bandwidth for phase-steered array using phase shifters to scan the beam [113]. Therefore, for higher-bandwidth requirements, it is more desirable to collimate an array's beam using time delay steering rather than using phase steering.

Our research, as well as the great preponderance of work, is performed on planar, periodic arrays because they are easily produced in planar form using hybrid or monolithic fabrication techniques. If we consider a planar periodic array arranged on a line, say along the x -axis with an inter-element spacing d_x as shown in Figure 4.3, the position vector r_m for the m^{th} element is

$$\bar{\mathbf{r}}_m = \hat{\mathbf{x}} m d_x, \quad (4.12)$$

where

$$\begin{aligned} m &= 0, \pm 1, \pm 2, \dots, \pm \frac{N_x - 1}{2} && \text{for } N_x \text{ odd} \\ &= \pm \frac{1}{2}, \pm \frac{3}{2}, \dots, \pm \frac{N_x - 1}{2} && \text{for } N_x \text{ even.} \end{aligned}$$

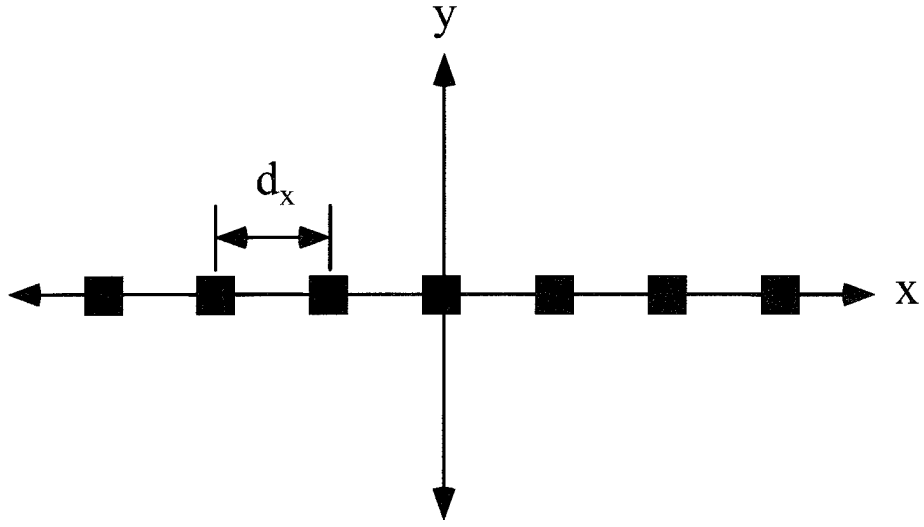


Figure 4.3: Linear, periodic array with inter-element spacing d_x .

The directional cosine is simply $u_o = \cos \theta_o$ for the linear array, so the steering excitation is

$$a_m = |a_m| e^{-jk_o m d_x u_o} \quad (4.13)$$

and the resulting electric field in the far-field is

$$\overline{E}(\bar{r}) = K \frac{e^{-jk R_o}}{R_o} \sum_m \overline{f}_m(\theta, \phi) |a_m| e^{+j m d_x (k u - k_o u_o)}. \quad (4.14)$$

A planar periodic array in two dimensions on the $z = 0$ plane with x -directed and y -directed inter-element spacing d_x and d_y , respectively, is shown in Figure 4.4. If the integer n is defined in a manner similar to m , the position vector \mathbf{r}_i for the i^{th} element becomes

$$\overline{\mathbf{r}}_{mn} = \hat{\mathbf{x}} m d_x + \hat{\mathbf{y}} n d_y \quad (4.15)$$

with steering excitation

$$a_{mn} = |a_{mn}| e^{-jk_o (m d_x u_o + n d_y v_o)}. \quad (4.16)$$

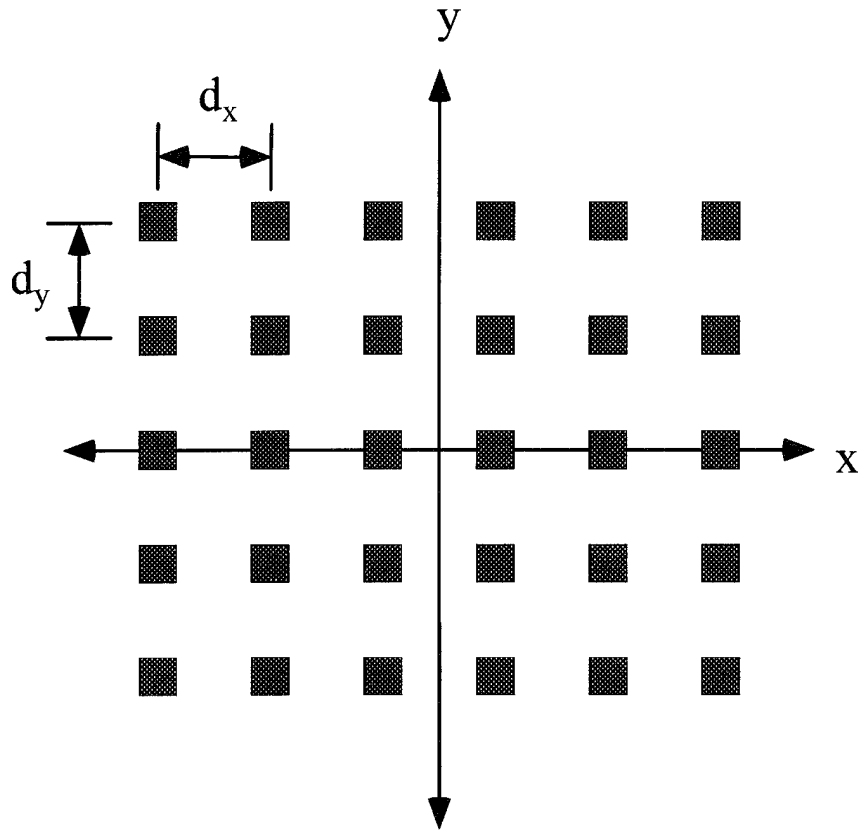


Figure 4.4. Planar, periodic two-dimensional array with inter-element spacing d_x and d_y in the x - and y -directions, respectively. A rectangular lattice geometry is shown.

The resulting far-field pattern for the planar two-dimensional periodic array is

$$\overline{E}(\bar{r}) = K \frac{e^{-jkR_o}}{R_o} \sum_m \sum_n \overline{f_{mn}}(\theta, \phi) |a_{mn}| e^{+j[m d_x (k u - k_o u_o) + n d_y (k v - k_o v_o)]}. \quad (4.17)$$

For reasons of element density or grating lobe suppression, it is sometimes desirable to displace certain rows of a planar, two dimensional array by some distance $\Delta_x(n)$. If we consider an array illustrated in Figure 4.5, with each row displaced by $\Delta_x(n)$, the element coordinates (x_m, y_n) are

$$\begin{aligned} x_m &= m d_x + \Delta_x(n) \\ y_n &= n d_y. \end{aligned} \quad (4.18)$$

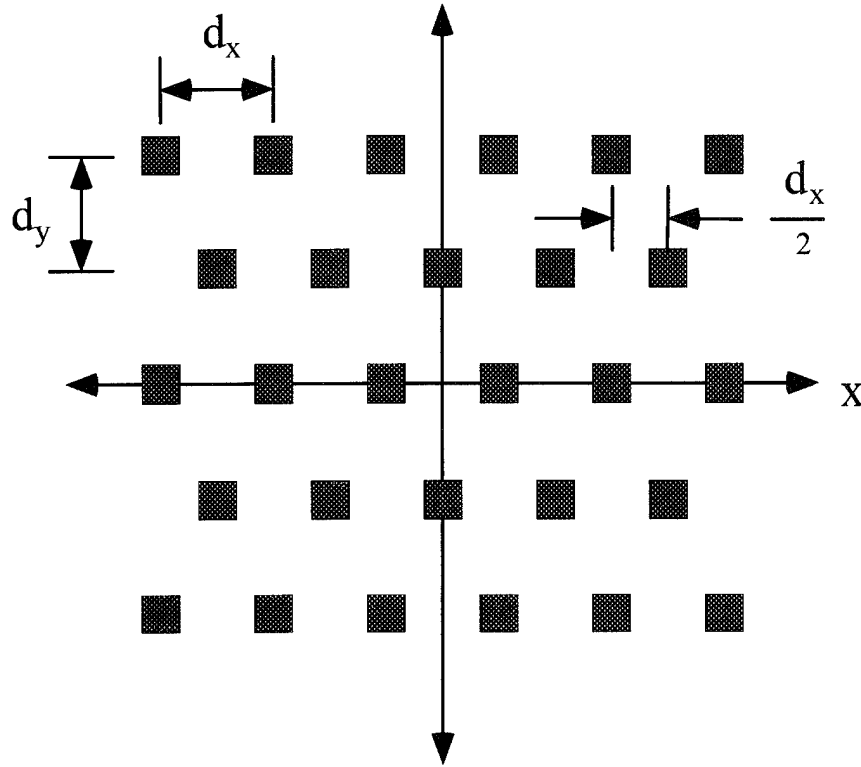


Figure 4.5. Planar, periodic two-dimensional array with a triangular lattice. Every other row is displaced by a distance $\frac{d_x}{2}$ in the x -direction.

where m and n are both defined as in Eq. (4.12) above, and N_x and N_y are the number of elements in the longest row or column, respectively. The normalized far field electric field for this planar array with displaced rows is given by

$$\overline{E_{norm}} = \frac{1}{N_x N_y} \sum_{m=0}^{N_x-1} \sum_{n=0}^{N_y-1} \overline{f_{mn}}(\theta, \phi) a_{mn} e^{+jk(mud_x + u\Delta_x(n) + nvdy)}. \quad (4.19)$$

The excitation required to form a beam at the desired position (θ_o, ϕ_o) at fixed frequency f_o is

$$a_{mn} = |a_{mn}| e^{-jk_o[u_o(md_x + \Delta_x(n)) + v_o nd_y]}. \quad (4.20)$$

If the amplitude illumination $|a_{mn}|$ is a separable distribution in x and y so that $|a_{mn}| = |a_m| \cdot |a_n|$, and the element pattern is also separable, so that

$$\overline{f}(\theta, \phi) = \overline{f_x}(u) \overline{f_y}(v), \quad (4.21)$$

then the normalized field pattern can be written in the following form:

$$\begin{aligned}
 \overline{E_{\text{norm}}} &= \frac{\overline{f_x(u)}}{N_x} \sum_{m=0}^{N_x-1} |a_m| e^{+j(ku-k_o u_o)md_x} \\
 &\quad \cdot \frac{\overline{f_y(v)}}{N_y} \sum_{n=0}^{N_y-1} |a_n| e^{+j(kv-k_o v_o)nd_y + j(ku-k_o u_o)\Delta_x(n)} \\
 &= E_x(u)E_y(u, v).
 \end{aligned} \tag{4.22}$$

Generally, this pattern is not separable, but can be for certain cases of $\Delta_x(n)$. First, consider the case of the rectangular-lattice array, where $\Delta_x(n) = 0$ for all rows. Assume that the array is uniformly illuminated, and performing the series expansions of the summations in Eq. (4.22) will yield the resulting form of the equation,

$$\begin{aligned}
 \overline{E_{\text{norm}}} &= \overline{f_x(u)} \left[\frac{\sin \left[N_x \pi d_x \left(\frac{u}{\lambda} - \frac{u_o}{\lambda_o} \right) \right]}{N_x \sin \left[\pi d_x \left(\frac{u}{\lambda} - \frac{u_o}{\lambda_o} \right) \right]} \right] \\
 &\quad \cdot \overline{f_y(v)} \left[\frac{\sin \left[N_y \pi d_y \left(\frac{v}{\lambda} - \frac{v_o}{\lambda_o} \right) \right]}{N_y \sin \left[\pi d_y \left(\frac{v}{\lambda} - \frac{v_o}{\lambda_o} \right) \right]} \right].
 \end{aligned} \tag{4.23}$$

The above equations have assumed a phase-steered excitation. In a later section, it will be shown that the transmission lines used for the lens delay lines are low-dispersion, so beam squint or chromatic aberrations are not a frequency limit. Therefore, the expressions above are changed to true time-delayed collimation by substituting $k = \frac{2\pi}{\lambda}$ for the phase-steered term, $k_o = \frac{2\pi}{\lambda_o}$. For clarity, Eq. (4.23) becomes

$$\begin{aligned}
 \overline{E_{\text{norm}}} &= \overline{f_x(u)} \left[\frac{\sin [N_x \pi d_x (u - u_o) / \lambda]}{N_x \sin [\pi d_x (u - u_o) / \lambda]} \right] \\
 &\quad \cdot \overline{f_y(v)} \left[\frac{\sin [N_y \pi d_y (v - v_o) / \lambda]}{N_y \sin [\pi d_y (v - v_o) / \lambda]} \right]
 \end{aligned} \tag{4.24}$$

for true time delay steering, which is the type of collimation considered below.

4.2 Grating Lobe Formation and Suppression

In Eq. (4.24), the field has principal maxima at discrete values of directional cosines u_p and v_q , in which p and q are integers, given by the expressions

$$\begin{aligned} u_p &= u_o + p \frac{\lambda}{d_x} \\ v_q &= v_o + q \frac{\lambda}{d_y}. \end{aligned} \quad (4.25)$$

An infinite number of values of u_p and v_q will produce principal maxima in directional cosine space. However, to limit our consideration to *visible space* corresponding to real angles of θ and ϕ [114], the integers p and q are limited to principal maxima such that $|u_p| \leq 1$ and $|v_q| \leq 1$. Therefore, not all combinations of p and q values correspond to real angles of radiation. An angle θ_{pq} associated with principal maxima may be defined by [113]

$$\cos \theta_{pq} = \left(1 - u_p^2 - v_q^2\right)^{\frac{1}{2}}. \quad (4.26)$$

Real values of θ_{pq} correspond to principal maxima that are radiated, which constrain the values of the directional cosines u_p and v_q of the grating lobes to be within a unit circle centered at the origin of the uv plane, or

$$u_p^2 + v_q^2 \leq 1. \quad (4.27)$$

When $p = q = 0$ and $\lambda = \lambda_o$, this maximum field, designated as the principal lobe or main lobe, is at the desired angle (θ_o, ϕ_o) . If p and/or q are non-zero integers, and the directional cosine condition above is met, then these maxima, referred to as grating lobes, will appear if the conditions

$$\begin{aligned} \frac{d_x}{\lambda} &\geq \frac{1}{|u_o| + 1} \\ \frac{d_y}{\lambda} &\geq \frac{1}{|v_o| + 1} \end{aligned} \quad (4.28)$$

are met, respectively. Therefore, if the array is scanned to endfire, so that the desired directional cosines $|u_o|$ or $|v_o|$ approach unity, then the inter-element spacing must be less than one-half wavelength to prevent grating lobe formation in visible space. Conversely, as the inter-element spacing approaches the wavelength of operation, then the maximum scan angle (θ_o, ϕ_o) allowed before the onset of grating lobes approaches the broadside angle. For a given array inter-element spacing, grating lobe formation places an upper-frequency bound on the array for a specified maximum scan angle if grating lobes are not desired in the field pattern.

An alternate choice to the rectangular lattice is the triangular lattice, which consists of displacing every other row by $\Delta_x(n) = \frac{d_x}{2}$ as shown in Figure 4.5. This configuration introduces a different periodicity into the v -plane, and the resulting function $E_y(u_p, v)$ reduces to a different expression at the grating lobe positions $p = \pm 1, \pm 3$, and so forth compared to the grating lobe positions $p = \pm 2, \pm 4, \dots$. The triangular-lattice element coordinates (x_m, y_n) are

$$(x_m, y_n) = \left(m \frac{d_x}{2}, n d_y \right) \quad (4.29)$$

for $(m+n) = \text{odd}$ and $m, n = 0, \pm 1, \pm 2, \dots$. The grating-lobe directional cosine coordinates in the uv plane for this triangular lattice are

$$\begin{aligned} u_p &= u_o + p \frac{\lambda}{d_x} & \text{and} & & v_q &= v_o + q \frac{\lambda}{d_y} & \text{for } p \text{ even,} \\ u_p &= u_o + p \frac{\lambda}{d_x} & \text{and} & & v_q &= v_o \frac{\lambda}{\lambda_o} + \left(q - \frac{1}{2} \right) \frac{\lambda}{d_y} & \text{for } p \text{ odd.} \end{aligned} \quad (4.30)$$

The resulting function $\overline{E}_y(u_p, v)$ for the odd- p grating lobe locations $p = \pm 1, \pm 3, \pm 5$, and so on is:

$$\overline{E}_y(u_p, v) = \frac{\overline{f}_y(v)}{N_y} \sum_{n=0}^{N_y-1} |a_n| e^{+jk(v-v_o)nd_y + jk(u_p-u_o)\frac{d_x}{2}}. \quad (4.31)$$

If the array is uniformly illuminated and isotropic so that $|a_n|$ is unity, then a series expansion of this expression will yield the following form:

$$\overline{E}_y(u_p, v) = \overline{f}_y(v) \left[\frac{\sin [N_y \pi d_y (v - v_o) / \lambda]}{N_y \cos [\pi d_y (v - v_o) / \lambda]} \right]. \quad (4.32)$$

The zeroes of this function occur when

$$\pi \frac{d_y}{\lambda} (v - v_o) = \pi q,$$

or

$$(v - v_o) = q \frac{\lambda}{d_y}. \quad (4.33)$$

The principal maxima value of unity of Eq. (4.32) occurs when

$$\pi \frac{d_y}{\lambda} (v - v_o) = \pm \pi(0.5 + q),$$

or at

$$(v - v_o) = \pm(0.5 + q) \frac{\lambda}{d_y}. \quad (4.34)$$

At even-integer lobe locations $p = 0, \pm 2, \pm 4, \dots$, the function $\overline{E}_y(u_p, v)$ is simply

$$\overline{E}_y(u_p, v) = \frac{\overline{f}_y(v)}{N_y} \sum_{n=0}^{N_y-1} |a_n| e^{+jk(v-v_o)nd_y}. \quad (4.35)$$

Again, if the array is uniformly illuminated and isotropic so that $|a_n|$ is unity, then the series expansion yields the familiar form, with no grating lobe suppression:

$$\overline{E}_y(u_p, v) = \overline{f}_y(v) \left[\frac{\sin [N_y \pi d_y (v - v_o) / \lambda]}{N_y \sin [\pi d_y (v - v_o) / \lambda]} \right]. \quad (4.36)$$

The principal maxima value of unity for Eq. (4.36) occurs when

$$\pi \frac{d_y}{\lambda} (v - v_o) = \pi q,$$

or

$$(v - v_o) = q \frac{\lambda}{d_y}. \quad (4.37)$$

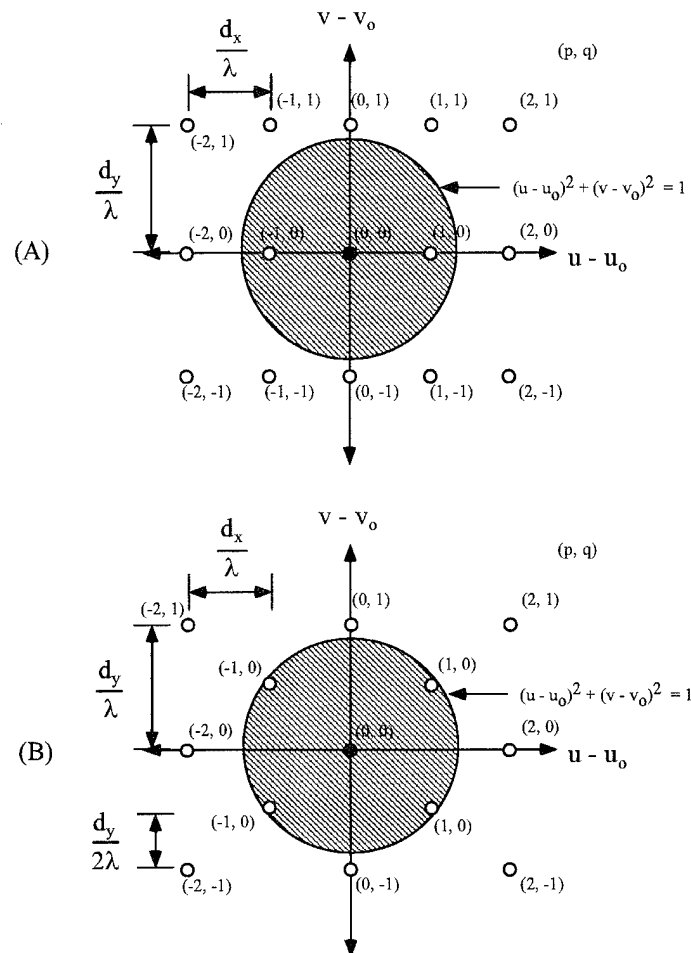


Figure 4.6. Grating lobe node coordinates for (a) a rectangular periodic array lattice and (b) a triangular periodic array lattice.

Grating lobes may form at these principal maxima locations.

Figure 4.6 shows the grating lobe plot for rectangular and triangular-lattice arrays. Each point represents a principal maximum in the field. The centered dark point represents the main lobe, while the white points show the locations of the grating lobes. The shaded circle represents the locus of points within which the grating lobes will radiate in visible space. Figure 4.6(a) is the grating lobe plot for a rectangular-lattice array. Two grating lobe nodes fall within the unit circle in the figure at an angle where $u - u_0 \approx 0.6$ along

the $u - u_o$ axis. If the triangular lattice is employed, then the odd- p grating lobe nodes are moved towards the edge of the shaded circle, as shown in Figure 4.6(b). The triangular lattice thus suppresses the odd- p grating lobes, in this case along the u axis by splitting each lobe node into two lobes and moving each out to a relatively wide angle, where they are reduced by the element pattern $\overline{f}_y(v)$. The triangular lattice does not alter the even grating lobes at all. This capability of selectively modifying a chosen grating lobe represents an additional degree of freedom that is useful in the array design.

To illustrate the advantage of using a triangular grid for grating lobe suppression, consider a 6×5 rectangular array with inter-element period $d_x = d_y = 0.75\lambda_o$ in an arrangement shown in Figure 4.4 above. If the elements of the array are uniformly illuminated and isotropic, a scan angle of only 15° in either E - or H -planes will produce a grating lobe, illustrated as the dash-dot line in Figure 4.7. To improve the scan performance, a triangular lattice similar to that in Figure 4.5 above may be selected. For comparison purposes, the same inter-element period is used, but the second and fourth rows of the array have only 5 elements and these rows are offset by $d_x/2$ with respect to their neighboring rows. The pattern of this 28-element triangular-lattice array may be scanned to 50° in the E -plane without grating lobe formation as shown in Figure 4.7 as the solid line. Therefore, the triangular grid offers improved scan performance for a given inter-element spacing.

Conversely, the triangular grid array allows substantially wider inter-element spacings for a given scan angle requirement than that of the rectangular lattice. For example, consider the hypothetical requirement for a main lobe scan angle of 60° from broadside for every plane of scan without grating lobe

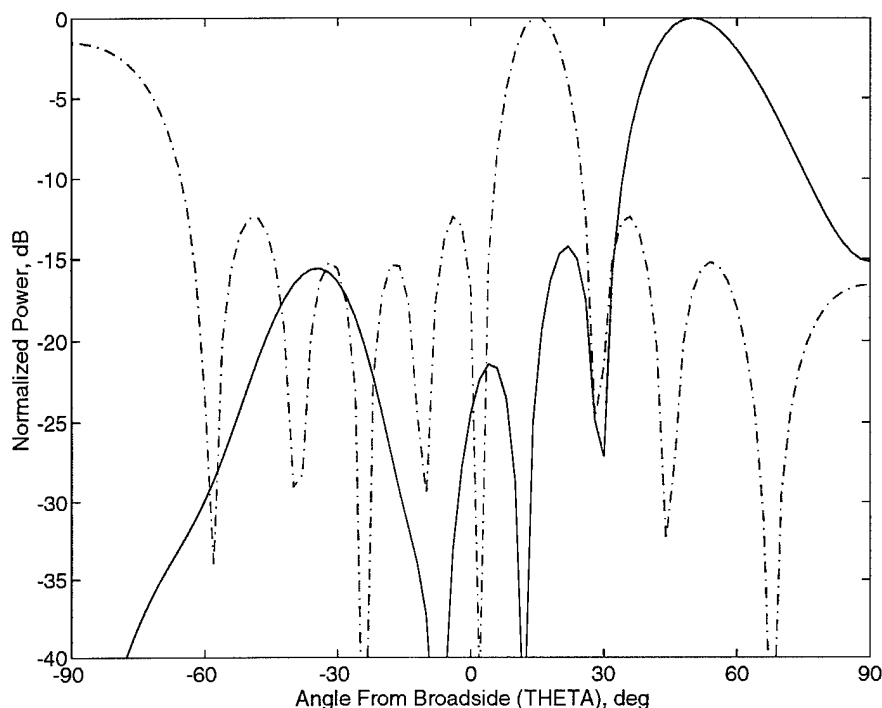


Figure 4.7. *E*-plane beamsteering plot of a triangular-lattice array (solid line) compared to a rectangular-lattice array (dot-dashed line) for the same inter-element period $d_x = d_y = 0.75\lambda_o$.

formation. In directional cosine space, this requires $|u_o|, |v_o| \leq \sin 60^\circ = 0.866$. From Eq. (4.28), we require a square lattice to have an inter-element spacing of $d_x = d_y = 0.536\lambda$. Hence, the area occupied per element location is $d_x \cdot d_y = (0.536\lambda)^2 = 0.287\lambda^2$. For an equilateral-triangular lattice, the requirement is satisfied by

$$\frac{\lambda}{d_y} = \frac{\lambda}{\sqrt{3}d_x} = 1.866 \quad \text{or} \quad d_y = 0.536\lambda, d_x = 0.309\lambda.$$

Since the elements are located only at every other value of (m, n) , the area per element is $2d_x d_y = 2(0.536)(0.309) = 0.332\lambda^2$. For the same amount of grating-lobe suppression, the number of elements saved using the triangular lattice over the rectangular lattice is about 14%. The relaxation of the area

requirements for the triangular lattice is employed in our active lens amplifier arrays to accommodate the space required for the amplifier circuits and delay lines, as will become evident in Chapters 5 and 7.

4.3 Bandwidth Considerations

The bandwidth of scanned array antennas depends upon the characteristics of the components used in the array. The type of elements, feed networks, and the mechanism used to determine the phase relationship between elements in the array may all contribute to bandwidth limitations. One set of components may dominate the bandwidth constraints of the array, or they may be comparable. A discussion on the bandwidth limitations due to the radiating elements is presented in Chapter 6. Since our lens array uses a free-space feed, bandwidth limitations due to the array feed are not considered.

As mentioned above, a popular method of scanning arrays is with constant-phase-type phase shifters. The phase shift is independent of frequency. A phase-steered array will establish the desired scan angle (θ_o, ϕ_o) only at one frequency f_o . For example, at the center frequency f_o the steering excitation is given by

$$a_{mn} = |a_{mn}| e^{-j \frac{2\pi}{c} f_o (m d_x u_o + n d_y v_o)} \quad (4.38)$$

but the inter-element phase required for the desired scan angle at some other frequency f_1 is

$$a_{mn} = |a_{mn}| e^{-j \frac{2\pi}{c} f_1 (m d_x u_o + n d_y v_o)}. \quad (4.39)$$

Since the phase distribution is designed to remain fixed independent of frequency, the array becomes phased to receive at a different incidence angle

(θ_1, ϕ_1) . For a fixed scan plane in ϕ , the amount of beam squint with frequency is given by the following relationship [115]:

$$f_1 \sin \theta_1 = f_o \sin \theta_o \quad (4.40)$$

For a small change in frequency, Eq. (4.40) shows that the change in scan angle is given by

$$\Delta\theta_o(\text{radians}) = -\frac{\Delta f}{f_o} \tan \theta_o. \quad (4.41)$$

Eq. (4.41) shows that the amount of beam squint depends upon the original scan angle as well as on the percent frequency change. At the broadside angle ($\theta_o = 0^\circ$), there is no beam squint scanning regardless of the amount of change in frequency. When the desired scan angle increases, the amount of beam squint increases for a given frequency variation. Therefore, the bandwidth limitation of an array steered with constant-phase-type phase shifters must be specified in terms of the desired maximum scan angle θ_o and some maximum squint angle $\Delta\theta_{o,\max}$. For instance, if the maximum scan angle desired is $\pm 60^\circ$, and the maximum allowable beam squint angle is $\pm 1^\circ$, then the bandwidth $\frac{\Delta f}{f_o}$ is only about 1%. Thus if $\theta_{o,\max} = \pm 60^\circ$, and $\Delta\theta_{o,\max}$ is defined in degrees, then the approximate relationship to bandwidth is:

$$\Delta\theta_{o,\max}(\text{degrees}) \simeq \frac{\Delta f}{f_o}(\text{percent})$$

The extent to which one specifies the maximum allowable squint angle may be dependent on the beam width of the main lobe or the resolution of the measurement system that would detect the squint.

In order to maintain the proper phase relationship over all frequencies, we must enforce the condition

$$a_{mn} = |a_{mn}| e^{-jk(md_x u_o + nd_y v_o)} = |a_{mn}| e^{-jkl_{mn}}. \quad (4.42)$$

Here, $-jkl_{mn}$ is the phase delay excitation required for the mn^{th} element in the array that is steered to the desired angle (θ_o, ϕ_o) . The electrical delay length l_{mn} may be related to a time delay ΔT_{mn} in a transmission medium with a phase velocity $\nu(f)$ that may be frequency dependent by

$$l_{mn} = \nu(f)\Delta T_{mn} = \frac{c}{\epsilon_{\text{eff}}(f)}\Delta T_{mn}. \quad (4.43)$$

An ideal TEM transmission medium is dispersionless and will have an effective dielectric constant ϵ_{eff} that is independent of frequency, yielding a frequency invariant electrical delay length l_{mn} . Such a delay mechanism is called true-time delay beamsteering. However, the planar arrays we have fabricated utilize either microstrip or coplanar waveguide (CPW) for delay lines and amplifier matching networks, which are quasi-TEM media that exhibit some dispersion. Analysis of the dispersive properties of these lines employed in the delay networks of the active constrained lenses will yield an error in the delay as a function of frequency, which in turn will set a frequency limit on the lens array due to the time-delay network.

4.4 Quasi-TEM Transmission Line Delay Lines

An important part of every array is the feed, which is usually made in some transmission-line medium and adds dispersion and loss. In our case, even though the transmission-line feed is eliminated, they are needed for delay lines and in the amplifier circuits. The open microstrip and coplanar waveguide (CPW) transmission medium used for the delay lines in our lens arrays are shown in Figure 4.8. The cross section of these lines consist of a substrate region with a homogeneous permittivity $\epsilon = \epsilon_r \epsilon_o$, and the remaining area is air. Following the development of Kuester [116], we may consider that the

propagation constant for a lossless, forward travelling quasi-TEM mode is

$$\gamma = j\beta = j\omega\sqrt{l_s c_s} = j\omega\sqrt{\mu\epsilon} \quad (4.44)$$

where l_s and c_s are the static inductance and capacitance per unit length of line.

The characteristic impedance for the medium operating in the TEM regime is

$$Z_c = \sqrt{\frac{l_s}{c_s}} = \sqrt{\frac{\mu}{\epsilon}}. \quad (4.45)$$

The substrate used in our delay lines is nonmagnetic, so $\mu = \mu_o$ for the entire waveguide. The value of c_s is dependent on the effective permittivity of the medium. For instance, if the quasi-TEM line conductor configuration remains unchanged, but cross section is completely filled with the homogeneous dielectric of the substrate, then the static capacitance may be considered as $c_s = C(\epsilon_r)$. Likewise, $c_s = C(1)$ for an air-filled cross section, and $c_s = C(\epsilon_{\text{eff}})$ for the actual transmission line. The value of l_s of the quasi-TEM line remains the same regardless of the dielectric(s) filling the cross section since ϵ has no effect on the static line inductance. Therefore, by Eqs.(4.44) and (4.45), $l_s = \frac{\mu_o \epsilon_o}{C(1)}$ for the air-filled line, and the propagation constant for the quasi-TEM mode may be expressed as

$$\beta \approx k_o \sqrt{\frac{C(\epsilon_r)}{C(1)}} \quad (4.46)$$

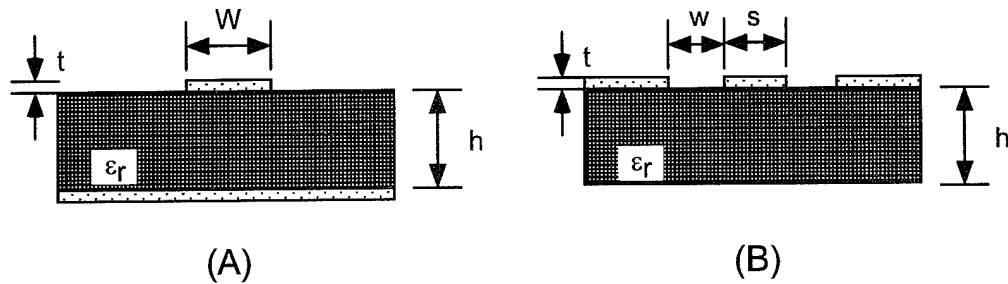


Figure 4.8. Cross-section of TEM transmission lines used in the delay lines of lens amplifiers: (a) microstrip; (b) unshielded coplanar waveguide (CPW).

and its characteristic line impedance is

$$Z_c(\epsilon_r) = Z_c(1) \sqrt{\frac{C(1)}{C(\epsilon_r)}}. \quad (4.47)$$

Here, $k_o = \sqrt{\mu_o \epsilon_o}$ and $Z_c(1)$ is the characteristic impedance of the corresponding air-filled line. Equations (4.46) and (4.47) imply that an effective dielectric constant ϵ_{eff} for the quasi-TEM mode may be defined as

$$\epsilon_{\text{eff}} = \frac{C(\epsilon_r)}{C(1)} \quad (4.48)$$

so that its propagation constant is

$$\beta \approx k_o \sqrt{\epsilon_{\text{eff}}} \quad (4.49)$$

and its characteristic line impedance is

$$Z_c(\epsilon_r) = \frac{Z_c(1)}{\sqrt{\epsilon_{\text{eff}}}}. \quad (4.50)$$

The transmission line cross-section homogeneously filled with a medium with relative permittivity ϵ_{eff} and permeability μ_o would have the same propagation constant and characteristic impedance as those given by Eqs.(4.49) and (4.50). Therefore, expressions for $C(\epsilon_r)$ as a function of ϵ_r are all that is required to characterize the quasi-TEM mode.

4.4.1 Microstrip Delay Lines

The patch-patch lens amplifier array uses microstrip transmission lines for the delay lines. The lens is fabricated on a planar dielectric sheet of Arlon 917 with relative permittivity $\epsilon_r = 2.17$, dielectric thickness $h = 0.787$ mm, loss tangent $\delta = 0.0009$, and copper metallization thickness $t = 17$ μm . The cross section of the microstrip transmission line is shown in Figure

4.8(a). Using the design-based formulae for determining the strip width W for a desired characteristic impedance Z_c , we have [116]

$$\frac{W}{h} = \frac{1}{K} \sqrt{\frac{8\pi^2(\epsilon_r + 1)}{\epsilon_r} + 64Kr_\epsilon} \quad (4.51)$$

where

$$K = \exp \left[\frac{4\pi Z_c}{\eta_o} \sqrt{\frac{\epsilon_r + 1}{2}} \right] - 1 \quad (4.52)$$

and

$$r_\epsilon \simeq \sqrt{0.4052 + \frac{0.5160}{\epsilon_r} + \frac{0.0788}{\epsilon_r^2}}. \quad (4.53)$$

These microstrip impedance formulae yield a stripwidth of $W = 0.71$ mm ($\frac{W}{h}$ ratio of 0.90) for the desired characteristic impedance of 100Ω on the Arlon dielectric. The approximate formulation for $C(\epsilon_r)$ of an open microstrip line for arbitrary $\frac{W}{h}$ is

$$C_{\text{micr}}(\epsilon_r) \simeq \frac{2\pi\epsilon_o(\epsilon_r + 1)}{\ln \left\{ 1 + \frac{32h}{W} \left[\frac{h}{W} r_\epsilon^2 + \sqrt{\left(\frac{h}{W} r_\epsilon^2 \right)^2 + \left(\frac{\pi(\epsilon_r + 1)}{16\epsilon_r} \right)^2} \right] \right\}}. \quad (4.54)$$

From Eq. (4.48), the effective dielectric constant is determined for the microstrip by applying Eq. (4.54) twice by finding the ratio of $C_{\text{micr}}(\epsilon_r)$ with $\epsilon_r = 2.17$ to $C_{\text{micr}}(\epsilon_r)$ with $\epsilon_r = 1$. This static effective dielectric constant is the value at the zero-frequency limit. Designated $\epsilon_{\text{eff}}(0)$, it is 1.592 for this microstrip.

By inspecting Equations (4.48) and (4.54), it is evident that $\epsilon_r > \epsilon_{\text{eff}} > 1$ for $\epsilon_r > 1$. This implies that a portion of the transverse electric field between the microstrip conductors resides in a region of higher permittivity than air. It is also evident that the value of $C_{\text{micr}}(\epsilon_r)$ increases with the ratio $\frac{W}{h}$, implying that a larger portion of the transverse electric field resides in the substrate as the relative size of W increases. Further confinement of

the electric field in the substrate will promote the propagation of non-TEM modes, resulting in dispersion. In the high frequency limit, the microstrip will resemble a parallel-plate waveguide loaded with the dielectric, so $\epsilon_{\text{eff}} \rightarrow \epsilon_r$ and thus the TEM mode be dominant. Therefore, the effective dielectric constant is frequency dependent, or $\epsilon_{\text{eff}}(f)$. Empirical design formulas giving accurate approximations for the dispersive behavior of open microstrip have been developed by Kobayashi [117]. The frequency dependence is

$$\epsilon_{\text{eff}}(f) = \epsilon_r - \frac{\epsilon_r - \epsilon_{\text{eff}}(0)}{1 + \left(\frac{f}{f_h}\right)^m} \quad (4.55)$$

where

$$f_h = \frac{f_T}{0.75 + \left(0.75 - \frac{0.332}{\epsilon_r^{1.73}}\right) \left(\frac{W}{h}\right)},$$

$$f_T = \frac{c \tan^{-1} \left(\epsilon_r \sqrt{\frac{\epsilon_{\text{eff}}(0) - 1}{\epsilon_r - \epsilon_{\text{eff}}(0)}} \right)}{2\pi h \sqrt{\epsilon_r - \epsilon_{\text{eff}}(0)}},$$

and for $\frac{W}{h} \geq 0.7$,

$$m = 1 + \left(1 + \sqrt{\frac{W}{h}}\right)^{-1} + 0.32 \left(1 + \sqrt{\frac{W}{h}}\right)^{-3}.$$

Here, $\epsilon_{\text{eff}}(0)$ is the static value of the effective dielectric constant.

The effective dielectric constant for the 100 Ω microstrip line as a function of frequency is plotted in Figure 4.9, where a large frequency range chosen to show the low frequency and high frequency limits of $\epsilon_{\text{eff}}(f)$. This formulation for microstrip dispersion has been compared to a numerical model [117] and demonstrates an accuracy of better than 0.6 percent in the range of $0.1 < \frac{W}{h} \leq 10$, $1 < \epsilon_r \leq 128$, and any $\frac{h}{\lambda_0}$. In these limits, $\frac{\partial \epsilon_{\text{eff}}(f)}{\partial f} \rightarrow 0$, indicating that one mode, the quasi-TEM mode, is predominant. The non-zero slope of the plot in mid-band shows the dispersive nature of the medium. The plot for a

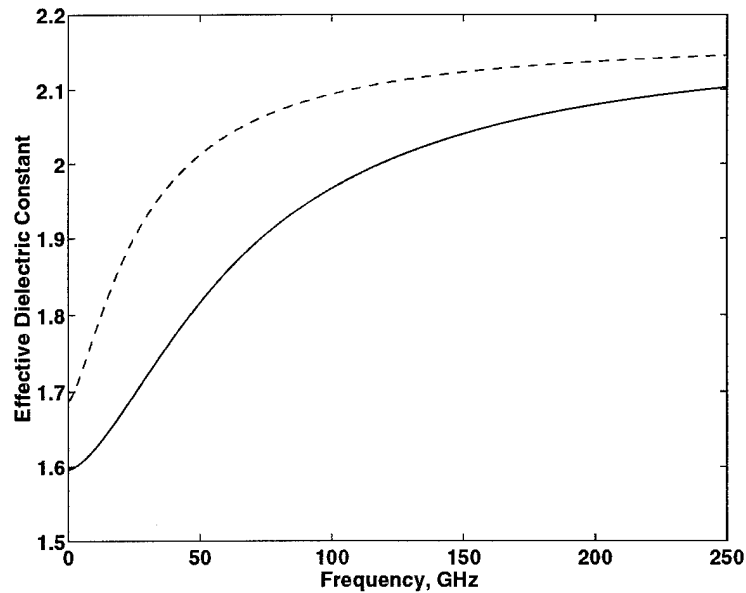


Figure 4.9. The effective dielectric constant of the microstrip transmission line used in the patch-patch constrained lens amplifier array (solid line). The simulation for a 50 Ω microstrip on the same substrate is included for comparison, showing that the effective dielectric constant for the 100 Ω line has a smaller dependence on frequency.

50 Ω on the same substrate is included for comparison, showing that the wider microstrip conductor of the 50 Ω line supports non-TEM modes and approaches the high frequency limit at lower frequencies than the 100 Ω microstrip line. A figure of merit to show how the propagation constant changes as a function of frequency is

$$\frac{f}{\beta} \frac{\partial \epsilon_{\text{eff}}(f)}{\partial f} \quad (4.56)$$

which becomes, for the dispersion formula of Kobayashi, Eq. (4.55),

$$\frac{f}{\beta} \frac{\partial \epsilon_{\text{eff}}(f)}{\partial f} = 1 + \frac{m(\epsilon_r - \epsilon_{\text{eff}}(0))}{2\epsilon_{\text{eff}}(f) \left[1 + \left(\frac{f}{f_h}\right)^m\right]^2} \left(\frac{f}{f_h}\right)^m \quad (4.57)$$

Figure 4.10(b) is a plot of Eq. (4.57) as a function of frequency for the 100- Ω microstrip line. The plot shows that the change in the normalized effective

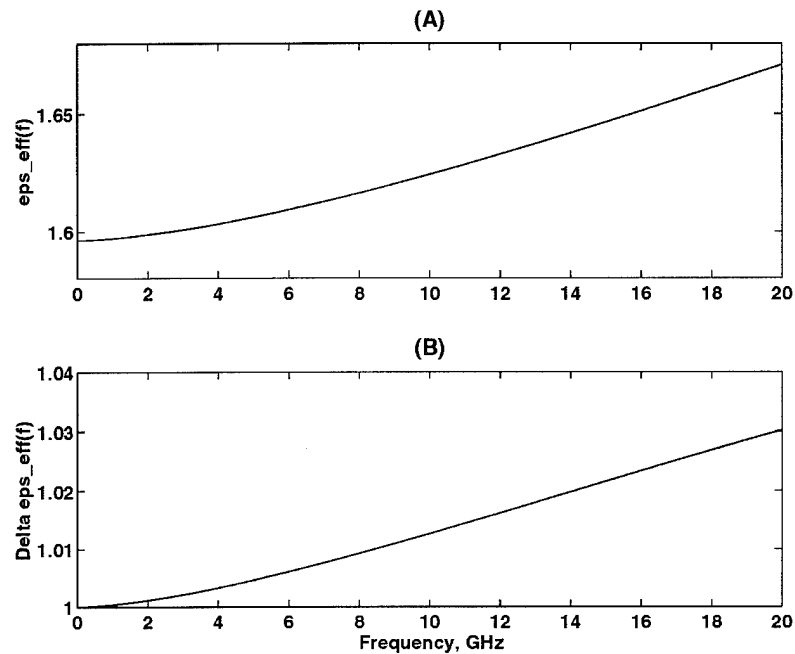


Figure 4.10. (a) Effective dielectric constant detail for the 100 Ω microstrip line. (b) Normalized rate of change in the effective dielectric constant as a function of frequency indicates the dispersion in the microstrip line.

dielectric constant as a function of frequency at 10 GHz is only 0.01, or a 1% decrease in the phase velocity of the line. This decrease in phase velocity translates to a 1% increase in the delay time of the delay lines and thus increase in delay length l . This increase is comparable to the path length error magnitude of the planar constrained lens when scanned [94], so lens bandwidth limitation due to microstrip line dispersion is unlikely.

4.4.2 Coplanar Waveguide

The cross-section of the unshielded CPW transmission line is shown in Figure 4.8(b). As with microstrip, an exact expressions for the characteristic impedance and propagation constant for the quasi-TEM mode are not available. The following quasi-static formula for $C_{\text{CPW}}(\epsilon_r)$ tracks well with

numerically calculated results for a wide range of substrate thicknesses h , particularly if $\epsilon_r \gg 1$ or as $h \rightarrow \infty$ [118]:

$$C_{\text{CPW}}(\epsilon_r) = 4\epsilon_o \left[\frac{K(k)}{K(k')} + \frac{\epsilon_r - 1}{2} \frac{K(k_1)}{K(k'_1)} \right] \quad (4.58)$$

where $K(k)$ is the complete elliptic integral of the first kind, and the moduli k and k_1 appearing in Eq. (4.58) are

$$\begin{aligned} k &= \frac{s}{s + 2w} \\ k_1 &= \frac{\sinh\left(\frac{\pi s}{4h}\right)}{\sinh\left[\frac{s + 2w}{4h}\right]} \end{aligned} \quad (4.59)$$

while the complementary moduli are $k' = \sqrt{1 - k^2}$ and $k'_1 = \sqrt{1 - k_1^2}$. Simple and accurate (to within 3 parts per million) expressions for the elliptic integral ratio $\frac{K(k)}{K(k')}$ developed by Hilberg [119] are, for k real:

$$\begin{aligned} \frac{K(k)}{K(k')} &\simeq \frac{\pi}{\ln \left[2 \frac{1 + \sqrt{k'}}{1 - \sqrt{k'}} \right]} && \text{for } 0 \leq k^2 \leq \frac{1}{2} \\ \frac{K(k)}{K(k')} &\simeq \frac{1}{\pi} \ln \left[2 \frac{1 + \sqrt{k}}{1 - \sqrt{k}} \right] && \text{for } \frac{1}{2} \leq k^2 \leq 1. \end{aligned} \quad (4.60)$$

As $h \rightarrow \infty$, $k_1 \rightarrow k$, and in this limit, as well as $\epsilon_r \rightarrow 1$, Eq. (4.58) becomes exact for the quasi-TEM mode. The quasi-static value of ϵ_{eff} is given by

$$\epsilon_{\text{eff}}(0) = 1 + \frac{\epsilon_r - 1}{2} \frac{K(k')}{K(k)} \frac{K(k_1)}{K(k'_1)}. \quad (4.61)$$

Considering the conductor thickness t of the CPW structure effectively increases the width of the center strip by the amount Δ so that the effective width $s_e = s + \Delta$ and the effective slot width $w_e = w - \Delta$. The expression for Δ is given by Gupta as [120]:

$$\Delta = \frac{1.25t}{\pi} \left[1 + \ln \left(\frac{4\pi s}{t} \right) \right]. \quad (4.62)$$

However Gupta's closed-form expression is based on a similar analysis for microstrip, and may under-estimate the parallel-plate capacitance between the center conductor and ground planes for thick metallization and narrow slotwidth w . To adequately model this additional capacitance, a numerical solution of Laplace's equation for the quasi-static line capacitance (and thus characteristic impedance) was performed by Koshiji [121]. Gupta's closed-form solution, Eqs. (4.62–4.63), closely follows Koshiji's numerical solution when $\frac{t}{w+0.5s} < 0.10$, which is the case for the low noise lens array using CPW in Chapter 7. For thicker metallization in relation to the widths of the center conductor slots, which is the case for low-impedance lines in a GaAs MMIC with plated metal conductors, the numerical solution will be required. Continuing with the closed-form analysis, the static value of the effective dielectric constant considering the conductor thickness is

$$\epsilon_{\text{eff}}^t(0) = \epsilon_{\text{eff}}(0) - \frac{0.7 (\epsilon_{\text{eff}}(0) - 1) \frac{t}{W}}{\frac{K(k)}{K(k')} + 0.7 \frac{t}{W}} \quad (4.63)$$

and the characteristic impedance is determined by

$$Z_c = \frac{30\pi}{\sqrt{\epsilon_{\text{eff}}^t(0)}} \frac{K(k'_e)}{K(k_e)}. \quad (4.64)$$

In applying Eq. (4.64), the effective aspect ratio k_e is found using Eq. (4.59) with the effective dimensions s_e and w_e used in place of the physical dimensions, and calculating the elliptic integral ratio using Eq. (4.60) is subject to the value of k_e . Since the expression for Z_c is not reversible, an iterative process of selecting s and w and calculating the resulting Z_c is employed until the desired characteristic impedance is obtained.

For the low noise lens array of Chapter 7, CPW is selected as the medium in order to use CPW-fed slot antennas as the array elements. The

dielectric selected has dielectric constant $\epsilon_r = 2.17$, is 0.787 mm thick, and has copper-conductor thickness $t = 17 \mu\text{m}$. A ground-to-ground spacing $s + 2w = 1.55$ mm was selected to accommodate placement of the active devices in the CPW medium. The resulting calculations using Eqs.(4.59–4.64) results in a center conductor width $s = 0.65$ mm and slot width $w = 0.45$ mm, and ratio $\frac{s}{s+2w} = 0.42$. A closed-form approximate expression for the frequency dependence of the effective dielectric constant for CPW lines is not present in the literature. A full-wave analysis comparing the dispersion of microstrip and CPW was performed by Jackson [122]. Jackson's analysis shows that for a CPW transmission line simulated at 60 GHz that is roughly 1/6 the dimensions of our line operated at 10 GHz yields a fractional change in effective dielectric constant per fractional change in frequency that is roughly 0.06. Thus, the CPW delay-line dispersion is expected to be higher than that in the microstrip delay lines employed in the constrained lenses.

4.5 Conclusion

Although most QOPC amplifier arrays use rectangular lattices, we have simulated a dramatic reduction in grating-lobe level with triangular lattices. This offers the option of relaxing the element density for a given scan angle performance, or providing additional scan range. We shall use the triangular lattice in our lens amplifiers specifically to improve scan range for our relatively widely-spaced arrays, thereby providing us with another design freedom to accommodate our amplifier circuitry. In addition, the bandwidth on our lens amplifiers is minimally impacted by dispersion, and as shown in Chapter 6, is limited by the input match and element pattern as functions of

frequency. Mutual coupling between array elements will be studied in Chapter 6 to determine if theoretical patterns not accounting for mutual coupling adequately model the lens amplifiers array patterns.

CHAPTER 5

MICROSTRIP PATCH LENS AMPLIFIER ARRAYS

5.1 Motivation

The quasi-optical power-combining amplifiers discussed in Chapter 2 suffered from low (or negative) insertion gain due mainly to the losses in the feed. Constrained lens theory was identified as a method of significantly reducing the feed loss by allowing the feed horn to illuminate the array from its near field. Since our fabrication technique uses planar, copper-clad dielectric, a lens design with planar input and output surfaces is required. The output array of the planar lens is configured for suppressing grating lobes as discussed in Chapter 4 while providing enough area between elements for the amplifiers and delay lines.

In this Chapter, the results of two lens amplifier arrays are presented. The first amplifier is a linear array of seven elements, and was developed to test the concept of embedding amplifiers into a constrained lens structure. The linear lens was limited to beamsteering in one plane only. The second amplifier is a two-dimensional planar array, which enables beamsteering and beam forming in both azimuth and elevation planes. The two-dimensional array uses a triangular-lattice element layout, enabling a relatively wide range of scan angles. Both lens amplifier arrays are microstrip-based and use the alternating-ground plane isolation introduced in Chapter 2. Electrical delay length W calculated from Chapter 3 formulae are realized with low-dispersion microstrip

transmission lines. Both lens amplifiers may be horn-fed. We also demonstrate two-level quasi-optical power combining with a grid oscillator specifically designed for the two-dimensional array.

5.2 Linear 7-Element Lens Amplifier Array

A linear 7-element lens amplifier array was designed for 10 GHz using a 0.787-mm thick Arlon substrate with a relative permittivity of 2.17. The lens amplifier, as shown in Figure 5.1, has an array of receive and transmit patch antennas on opposite sides of the substrate. Each common-source

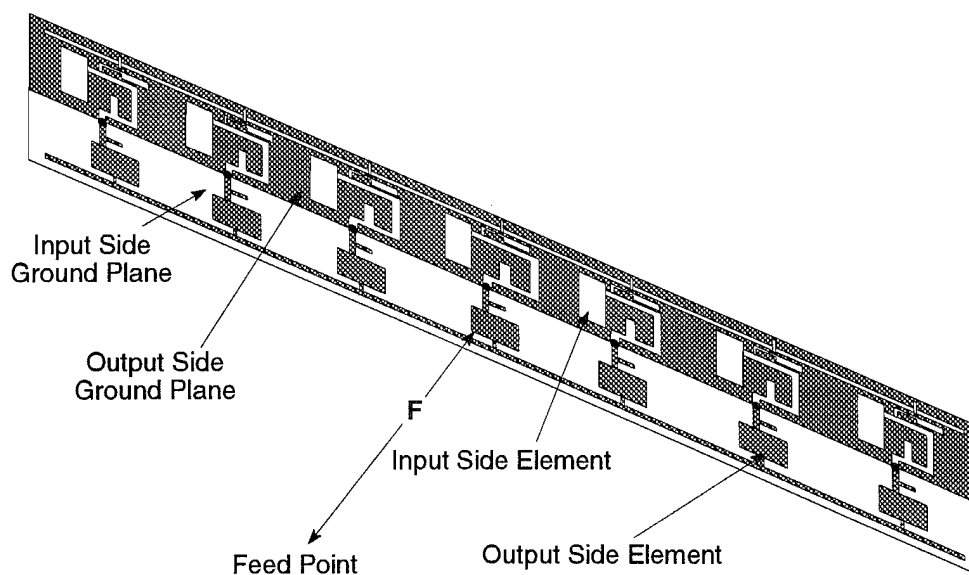


Figure 5.1. The linear 7-element lens amplifier array with a focal-point feed. A horn illuminates the input side of the lens from the focal length $F = 2D$, where D is the lens length.

PHEMT amplifier is coupled and matched to its input and output patch elements with microstrip lines. A substrate via connects each amplifier's output to its transmit-side patch. Alternating ground planes effectively isolate input and output sides of the amplifier structure, allowing input and output wave polarizations to be arbitrarily selected [42]. In the amplifier presented, orthogonal polarizations are chosen to minimize diffraction-path measurement errors.

The lens amplifier element topology is shown in Figure 5.2. Receive and transmit elements are microstrip patch antennas with non-radiating-edge feeds. This is preferable to a radiating-edge feed because the element is more compact and the input impedance may be arbitrarily set. An input impedance of $100\ \Omega$ was chosen for narrower, less dispersive microstrip lines than a $50\text{--}\Omega$ impedance allows. The patches were designed using multi-port network modelling software [93], the details of which will be presented in Chapter 6. Avantek ATF-35576 PHEMTs were selected for their high gain and low bias power requirements. The PHEMTs are impedance matched for gain to $100\text{--}\Omega$

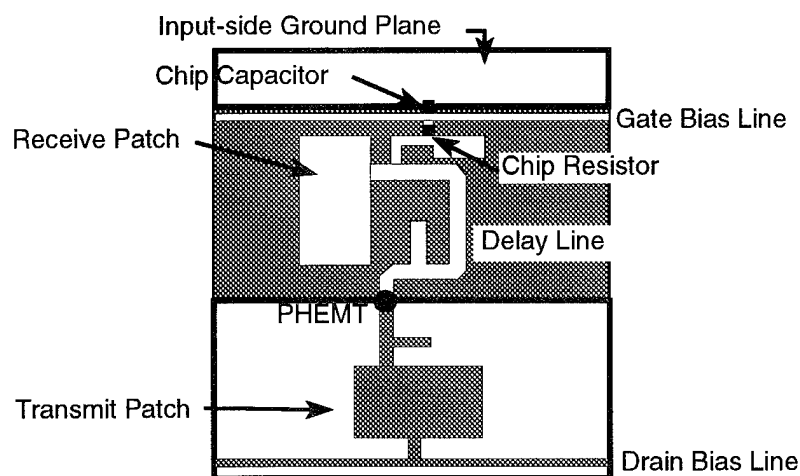


Figure 5.2. Topology of an amplifier unit cell used in the patch-patch linear and two-dimensional lens array.

microstrip delay lines using single-stub matching sections. The gate bias network is similar to that described by Webster [123], and provides unconditional stability for the PHEMTs. The gate bias network consists of a 90° section of $150\text{-}\Omega$ microstrip line, terminated by a $70\text{-}\Omega$, 90° open stub in parallel with a $100\text{-}\Omega$ chip resistor connected to the gate bias line. The 1-pF chip capacitor couples the resistive stability network to the feed-side ground plane. Drain bias is provided through the RF null of the transmit patch. Each microstrip delay line has the same number of discontinuities (mitred bends) for reproducible control of phase delay.

The lens' focal length-to-diameter ratio was chosen to be $F/D = 2.0$ in order to match the radiation pattern of the feed horn. The inter-element spacing is $0.75\lambda_o = 22.5\text{ cm}$ on the output side, and the design focal length F is 27 cm . Since the input and output arrays are planar, the only constrained lens design parameters are the positioning of the input elements ρ in relation to the output elements r , and the electrical line length W connecting them. These equations are

$$\rho = r \left[\frac{F^2 - r^2 \sin^2 \theta_o}{F^2 - r^2} \right]^{\frac{1}{2}}, \quad (5.1)$$

$$W = F + W_o - \frac{1}{2} \left[F^2 + \rho^2 - 2\rho F \sin \theta_o \right]^{\frac{1}{2}} - \frac{1}{2} \left[F^2 + \rho^2 + 2\rho F \sin \theta_o \right]^{\frac{1}{2}}, \quad (5.2)$$

where θ_o is the angle relative to the broadside of the lens input surface that the focal point subtends, and W_o is an arbitrary constant electrical length added to each delay line. The arbitrary length is selected as a matter of practical concern so that the delay lines of all element pairs may connect them. Our design sets $\theta_o = 0$, so that the lens focuses perfectly at one point along the optical axis running perpendicular to the lens array through its center element. Table 5.1 shows the calculated positions of the seven element pairs and the relative

Table 5.1. Element and delay line data for the 7-element linear lens amplifier array

element (m, n)	r (x, y -mm)	ρ (x, y -mm)	W (deg)	Length (mm)
-3,0	-67.5, 0	-69.7, 0	0.0	$W_o + 0.0$
-2,0	-45.0, 0	-45.6, 0	60.3	$W_o + 3.8$
-1,0	-22.5, 0	-22.6, 0	94.9	$W_o + 5.9$
0,0	0.0, 0	0.0, 0	106.3	$W_o + 6.7$
1,0	22.5, 0	22.6, 0	94.9	$W_o + 5.9$
2,0	45.0, 0	45.6, 0	60.3	$W_o + 3.8$
3,0	67.5, 0	69.7, 0	0.0	$W_o + 0.0$

electrical delay length connecting them.

At the design focal point distance of 27 cm, the lens was horn-fed and first tested with the five center elements biased, and then with all seven elements biased. The resulting output power is 3.1 dB higher for 7 elements than for 5 elements biased. This is 0.2 dB above the theoretical increase of 2.9 dB ($20 \log_{10}(7/5)$) expected from a uniformly driven array factor, and indicates that the output of the planar lens has a uniform phase and that its effective area increases linearly with the number of elements. Figure 5.3 shows the array's maximum output power at 9.70 GHz, which is 3% below the design frequency due to the lower than expected resonant frequency of the microstrip patch antennas. The array's isolation, defined as the biased-on to biased-off transmission power ratio, is 29 dB at center frequency. The effect of the feed distance on the radiation pattern of the lens was measured to determine the actual focal length of the lens. In this test, the feed horn was located at broadside and the feed distance was varied between 22 cm to 30 cm. The 22-cm feed location produces about 5 dB more power than at 30 cm, due to the different incident power. The beamwidth is 18° at the 22-cm location, compared to 14° at a feed distance of 26 cm. The wider beamwidth for the

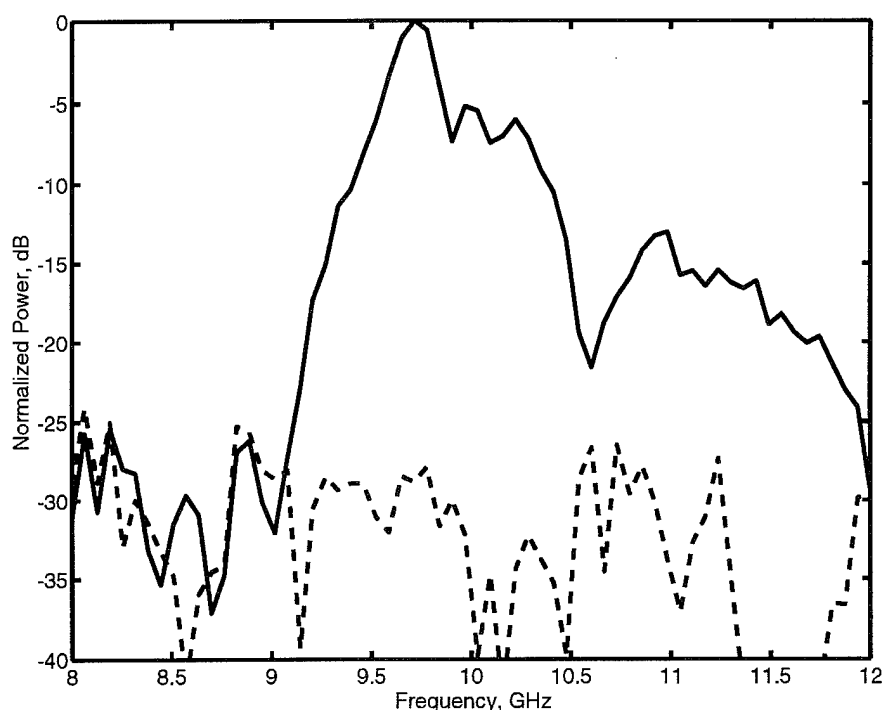


Figure 5.3. Measured frequency response of the linear 7-element lens amplifier in the biased-on (solid line) and biased-off (dashed line) conditions. The on/off isolation is 29 dB.

22-cm feed location indicates that more feed power is illuminating the center elements than the edge elements. The theoretical beamwidth for a 7-element uniformly illuminated array is 14.6° , and its side lobe level is -12.6 dB. The measured side lobe level at a feed distance of 26 cm was -12 dB. Because the lens array pattern displays performance comparable to an array that is uniform in amplitude and phase, it is felt that the lens is properly fed from a distance of 26 cm, which is comparable to the design focal length of 27 cm. The cross-polarization ratio for the lens is 14.0 dB at the experimentally-determined focal length of 26 cm.

The lens preserves the incident phase of the input wave, so it may be

fed with a progressive phase angle for beamsteering. Figure 5.4 shows measured radiation patterns for a feed point distance of 26 cm and feed angles of 0° , 15° , and 30° . Side-lobe levels increase with increased scan angle, as expected, due to non-uniform illumination of the input elements. The main lobe power

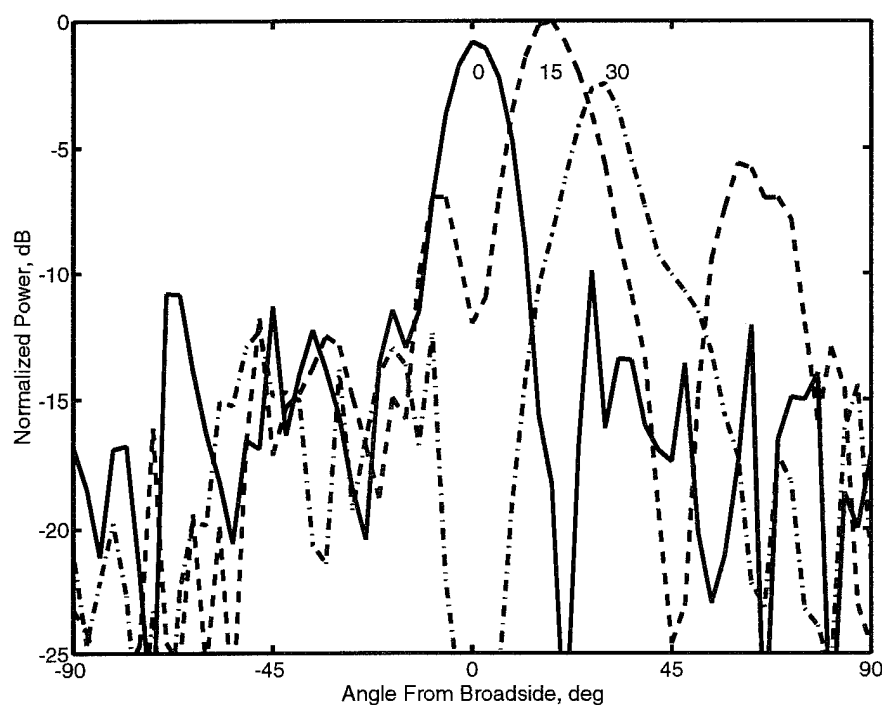


Figure 5.4. Measured beamsteering performance of the linear 7-element lens amplifier array. The lens is fed at $F = 26$ cm and angles 0° , 15° , and 30° . The main lobe beamwidth broadens, the side lobe level increases, and the peak power varies by 2.5 dB as the beam is scanned from 0° to 30° .

decreased by 2.5 dB from the 0° feed angle to the 30° . The difference in power is due to feeding the lens at a constant focal distance of 26 cm, independent of feed angle. Figure 5.5 shows the improved beamforming performance as a result of feeding the lens along the focal arc. The focal arc curve used for this lens is the $F/D = 2.0$ curve shown in Chapter 3, with $F = 26$ cm. The beamwidth of the

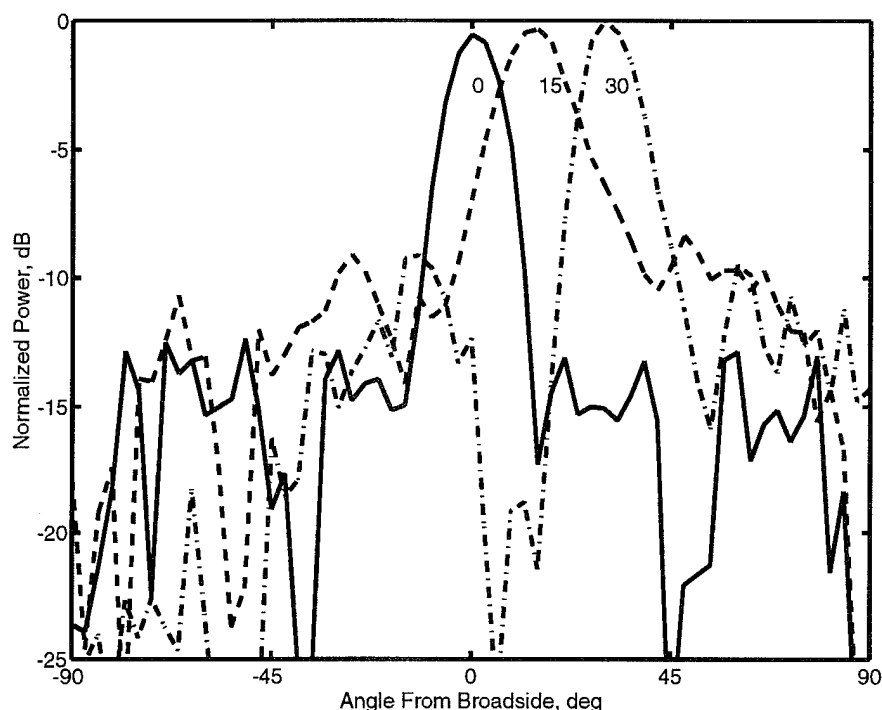


Figure 5.5. Measured beamsteering performance when the lens is fed along the focal arc. The beamwidth of the main lobe remains narrow, side lobe levels are reduced, and peak power variation is less than 1 dB over the 30° scan range.

main lobe remains narrow, the side lobe levels are reduced compared to Figure 5.4, and the peak power variation is less than 1 dB over the 30° scan range. The theoretical radiation pattern of the 7-element linear lens amplifier was simulated based on the passive array theory in Chapter 4. The *E*-plane array factor is multiplied by the output patch element pattern, details of which are given in Chapter 6. Figure 5.6 shows the theoretical radiation pattern at the lens output as the main beam is steered at 9.75 GHz. The simulation assumes all element have equal amplitude and are properly phased. The theoretical radiation patterns are similar to the measured results in that the beam remains narrow and the sidelobes remain below -12 dB. The major difference is the

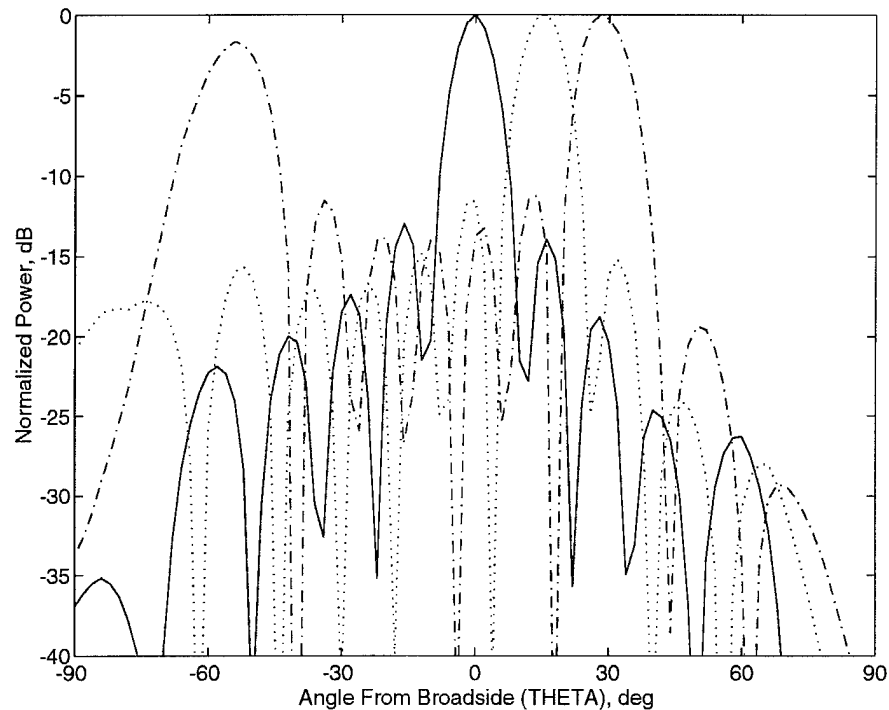


Figure 5.6. Theoretical 7-element linear lens radiation patterns for beamsteering at 0° (solid line), 15° (dotted line), and 30° (dash-dot line).

grating-lobe in the theoretical 30° -beamsteered pattern at -55° which is only 2dB below the main-lobe level, but is a relatively insignificant lobe at -18 dB in the measured pattern. We are unsure of the cause of this discrepancy, but the theoretical beamsteered pattern shows the susceptibility of widely-spaced linear arrays to grating lobe formation. In our development of the two-dimensional array, we use a triangular lattice to improve the beamsteering range, as well as to beamform and beam scan in two dimensions.

5.3 Two-Dimensional Lens Amplifier

Since a linear antenna array has an array factor in only one dimension, the linear transmission amplifier lens does not have absolute power gain. To

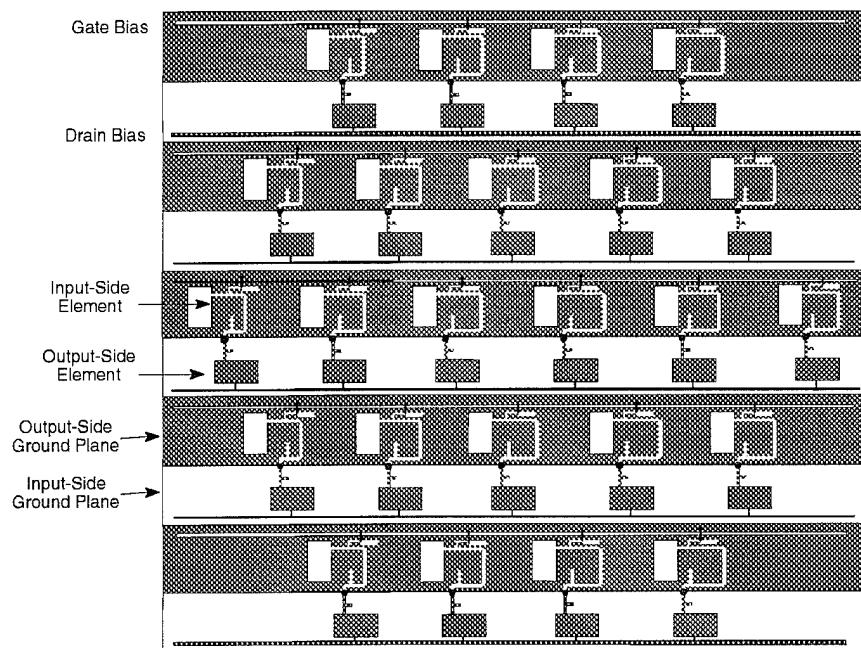


Figure 5.7: The 24-element two-dimensional lens amplifier array.

eliminate diffraction loss, a 24-element two-dimensional array, shown in Figure 5.7, was designed. The lens diameter is $4\lambda_o$, the focal length is 25 cm, and the ratio $F/D = 2$. The output side has uniform inter-element spacing of $0.75\lambda_o$ in the horizontal direction and $0.90\lambda_o$ in the vertical direction. The relatively large spacing in the vertical direction is required to accommodate the via holes connecting the feed-side and output-side ground planes crucial to the isolation and stability of the lens amplifier. A triangular inter-element spacing was selected for improved array scan performance with the large inter-element spacing in the vertical direction. The microstrip patch antennas are fed on the non-radiating edge with $100\ \Omega$ input impedance at resonance.

The design of the single-stage PHEMT amplifier was performed using

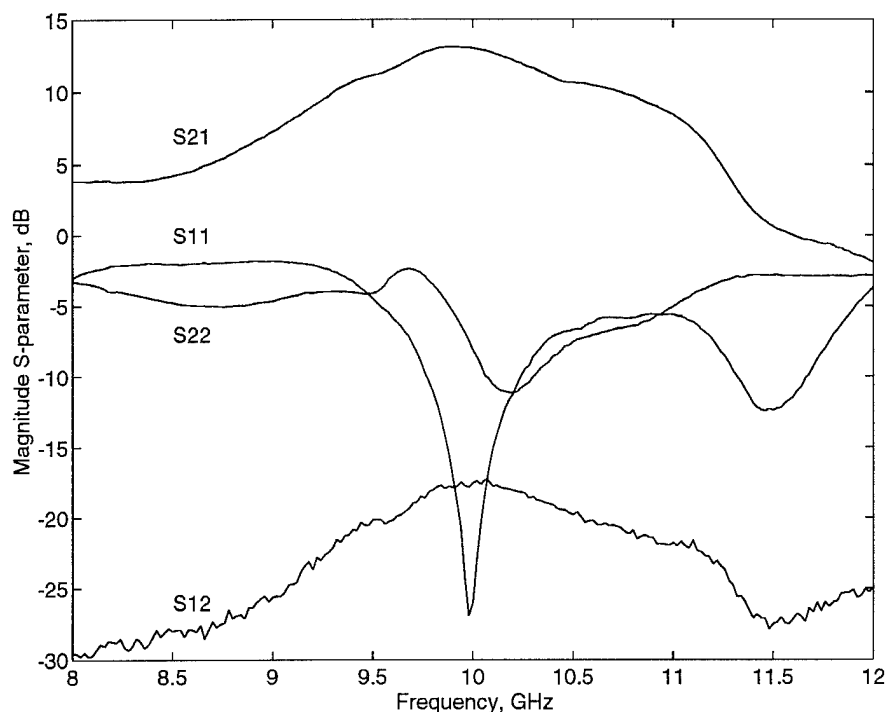


Figure 5.8. Measured s-parameters of the single-stage PHEMT amplifier used in the two-dimensional lens amplifier array.

Hewlett Packard's Microwave Design System (MDS) to account for all discontinuities in the amplifier layout. A microstrip amplifier without antennas as loads was tested on an HP 8510B network analyzer, with results plotted in Figure 5.8. The peak gain is 13.12 dB at 9.92 GHz, and its 3-dB bandwidth is 1.4 GHz. The peak gain of the amplifier used in the two-dimensional lens is 3.3 dB higher than the amplifier used in the linear 7-element lens. With a single element of the lens biased, a free-space gain measurement yielded an amplifier gain of 12.95 dB, indicating good agreement with the network analyzer measurements.

The layout of the two-dimensional lens array is shown above in Figure 5.7. The design equations for the feed-side element locations ρ and delay line

Table 5.2. Element and delay line data for the 24-element two-dimensional lens amplifier array

element (m, n)	r (x, y -mm)	ρ (x, y -mm)	W (deg)	Length (mm)
-3,-2	-33.75, -54.00	-34.90, -55.84	0.0	$W_o + 0.00$
-1,-2	-11.25, -54.00	-11.53, -55.36	26.5	$W_o + 1.67$
+1,-2	+11.25, -54.00	+11.53, -55.36	26.5	$W_o + 1.67$
+3,-2	+33.75, -54.00	+34.90, -55.84	0.0	$W_o + 0.0$
-4,-1	-45.00, -27.00	-46.03, -27.62	34.0	$W_o + 2.14$
-2,-1	-22.50, -27.00	-22.73, -27.27	72.2	$W_o + 4.55$
0,-1	0.00, -27.00	0.00, -27.16	84.7	$W_o + 5.33$
+2,-1	+22.50, -27.00	+22.73, -27.27	72.2	$W_o + 4.55$
+4,-1	+45.00, -27.00	+46.03, -27.62	34.0	$W_o + 2.14$
-5,0	-56.25, 0.00	-57.73, 0.00	23.4	$W_o + 1.47$
-3,0	-33.75, 0.00	-34.06, 0.00	74.6	$W_o + 4.70$
-1,0	-11.25, 0.00	-11.26, 0.00	99.3	$W_o + 6.25$
+1,0	+11.25, 0.00	+11.26, 0.00	99.3	$W_o + 6.25$
+3,0	+33.75, 0.00	+34.06, 0.00	74.6	$W_o + 4.70$
+5,0	+56.25, 0.00	+57.73, 0.00	23.4	$W_o + 1.47$
-4,+1	-45.00, +27.00	-46.03, +27.62	34.0	$W_o + 2.14$
-2,+1	-22.50, +27.00	-22.73, +27.27	72.2	$W_o + 4.55$
0,+1	0.00, +27.00	0.00, +27.16	84.7	$W_o + 5.33$
+2,+1	+22.50, +27.00	+22.73, +27.27	72.2	$W_o + 4.55$
+4,+1	+45.00, +27.00	+46.03, +27.62	34.0	$W_o + 2.14$
-3,+2	-33.75, +54.00	-34.90, +55.84	0.0	$W_o + 0.0$
-1,+2	-11.25, +54.00	-11.53, +55.36	26.5	$W_o + 1.67$
+1,+2	11.25, +54.00	+11.53, +55.36	26.5	$W_o + 1.67$
+3,+2	+33.75, +54.00	+34.90, +55.84	0.0	$W_o + 0.0$

length W are given as

$$\rho = r \left[\frac{F^2 - r^2 \sin^2 \theta_o \cos^2 \phi_e}{F^2 - r^2} \right]^{\frac{1}{2}}, \quad (5.3)$$

$$W = F + W_o - \frac{1}{2} \left[F^2 + \rho^2 - 2\rho F \sin \theta_o \cos \phi_e \right]^{\frac{1}{2}} - \frac{1}{2} \left[F^2 + \rho^2 + 2\rho F \sin \theta_o \cos \phi_e \right]^{\frac{1}{2}}. \quad (5.4)$$

The resulting element positions and delay line lengths are given in Table 5.2

The length W_o was selected to be 10.0 mm so that connection to all elements is possible. We biased several symmetrical configurations of lens

elements to study how the lens insertion gain (or loss) is affected by the number of elements. The results, plotted in Figure 5.9, show a dramatic improvement in absolute power gain as the number of elements increases. The one- and two-element results were obtained by biasing the center two elements of the lens amplifier and feeding them from the far field. These two elements have identical delay line lengths. The free-space measurement established the fact that the PHEMT amplifiers contribute 12.95 dB of gain, but the lens suffers over 15 dB of insertion loss because the feed is located in the far field, and most of the input power is not captured by the lens. A dramatic decrease in the lens insertion loss occurs when the lens is four or more elements are biased, showing

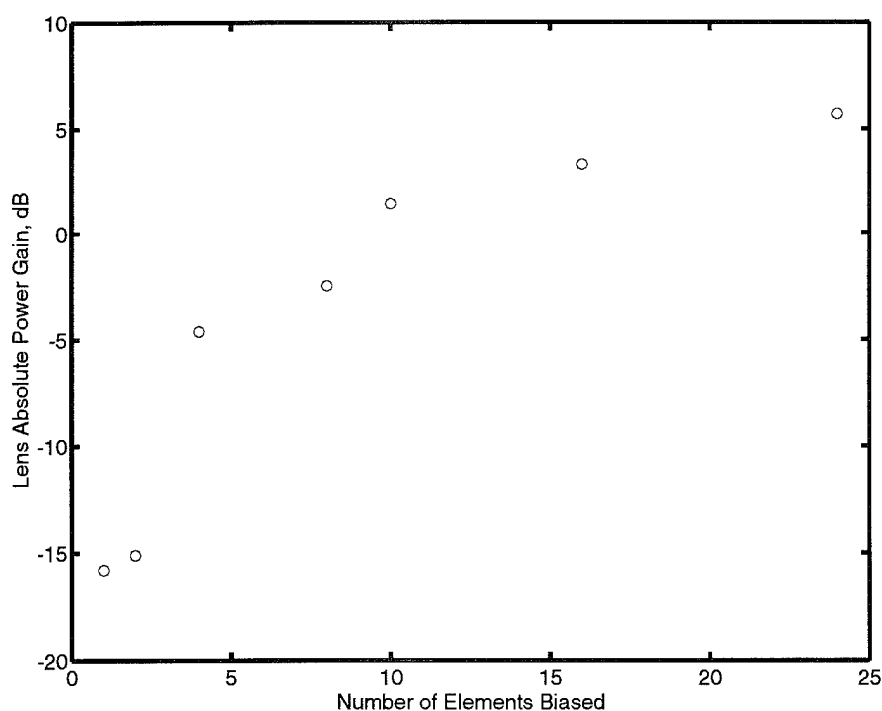


Figure 5.9. Absolute power gain (or loss) of the lens amplifier as a function of the number of elements biased. The one- and two-element cases were fed in the far field, while the other data points were obtained with a focal-point feed.

that feed efficiency of free-space amplifiers is improved when fed as a lens. With all 24 elements biased, the lens delivered 5.7 dB of absolute power gain. The lens frequency response is tested using a Hewlett Packard HP 71500/80200 microwave transition analyzer with a standard-gain horn illuminating the lens at its focal point and another horn receiving the power in the far field of the lens. The resulting frequency plot in Figure 5.10 shows a bandwidth of 320 MHz over which the isolation is at least 17 dB. A peak isolation value of 21 dB occurs at 10.25 GHz. The frequency response of the 24-element lens is broader than that of the 7-element lens and has two peaks. One peak is at 10.25 GHz

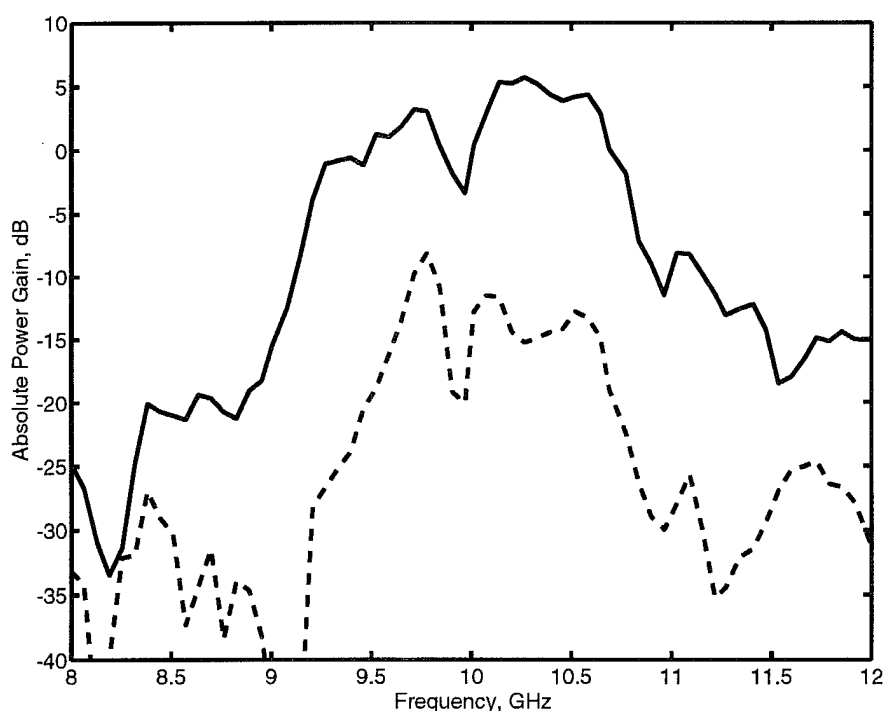


Figure 5.10. Measured absolute power gain as a function of frequency for the 24-element planar lens amplifier in the biased-on (solid line) and biased-off (dashed line) conditions. The isolation is greater than 17 dB over a 320 MHz bandwidth and is 21 dB at 10.25 GHz.

and the other peak, 2.1 dB lower than the first, is at 9.7 GHz. We believe the reason for this is the inadvertent variation in the resonant frequency of the patches. Namely, for some input-side elements, the radiating edges are closer to their neighboring ground planes, altering the effective dielectric constant of these patches. Chapter 6 explores this frequency variation.

An estimate of the feed efficiency of the lens was performed by measuring the peak power reflected by the input side of the biased-on lens, and comparing that power to the peak power reflected off of a metal plate of the same dimensions as the lens. For both measurements, the horn feed was placed on the focal arc at an angle of 30° to avoid blockage by the horn [108]. The peak reflected power was measured at -30° as expected, and 4 dB more power was reflected by the metal plate than by the lens. Therefore, we estimate that about 39% of the power incident on the lens is reflected and not coupled into the amplifiers. Increasing the element density, matching the resonant frequency of all elements, and reducing the reflection due to the isolating ground planes should reduce the reflected power.

5.4 Two-Level Power Combining

The measured results of the linear and two-dimensional lens arrays shown to this point were accomplished with a horn feed located at the focal distance or along the focal arc. A grid oscillator can perform the feed function in a more compact, planar form. The challenge is to design a grid oscillator that will oscillate within the passband of the lens amplifier and provide good illumination of the input side for a good-quality output beam. Beamsteering, beamforming, and beam switching experiments were performed with the two-dimensional lens amplifier array fed with two identical grid oscillators arranged

along the focal surface, demonstrating a two-level QOPC system. The grid oscillators are the primary level of this two-level system in that they generate the source signal. The lens amplifier array is the second level of the system, performing focussing, amplifying, and re-radiating of the primary level.

5.4.1 Grid Oscillator Feed Design

A planar grid oscillator was designed to feed the two-dimensional lens amplifier array. The theory presented in [66],[68] was used, which is based on a full-wave analysis of a single unit cell of the structure. For a given geometry, the metallization is divided into a number of rooftop basis functions and a voltage generator is inserted across the gap in place of a 1-port active device. The moment method is then used to determine the current on the entire structure, and the ratio of the voltage across the gap to the current through the gap is the driving-point impedance seen by the active device. This analysis is extended to a two-port device, such as a transistor, yielding a two-port characterization for the passive part of the grid (the metal geometry, the dielectric, and radiation into free space). An appropriate model for the active device is then connected to this linear network to analyze the behavior of the grid oscillator.

In order to match the narrow-band frequency response of the two-dimensional lens amplifier, a grid oscillator operating at 10 GHz is required. In the design, small-signal *s*-parameters were used to model the Avantek ATF-35576 PHEMTs, the devices selected for fabricating the oscillator. Simulations indicate that a structure with one dipole and one bow-tie radiating element on a 2.54-mm thick Duroid substrate with a relative permittivity of 10.5 results in an oscillation frequency near 10 GHz. The unit cell of the structure is shown in Figure 5.11(a), and the entire grid oscillator is shown in Figure 5.11(b).

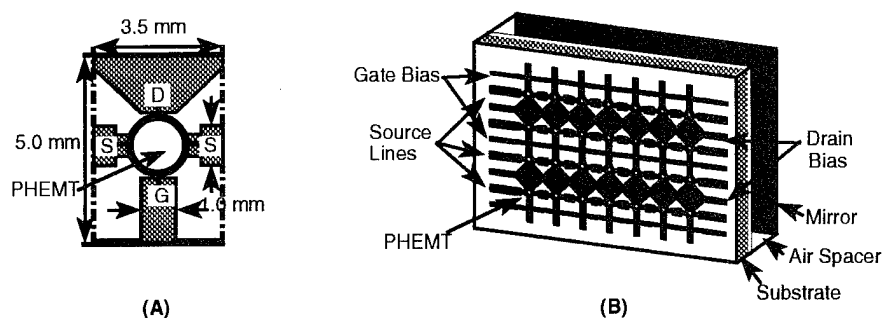


Figure 5.11. A grid oscillator unit cell is shown in (a), where the solid lines are electric walls and the dashed lines are magnetic walls. The 28-element grid oscillator is shown in (b).

According to the simulations, a mirror placed 3 mm behind the dielectric results in an oscillation frequency of 10 GHz. The fabricated grid requires a grid-to-mirror spacing of 5 mm to tune the frequency to 10.0 GHz. We observe a gate-bias tuning bandwidth of 225 MHz with less than 3 dB change in output power. The grid oscillator can be electrically tuned over the operating bandwidth of the lens amplifier array. The 28-element grid oscillator has an effective radiated power of 22 dBm measured in the far field.

5.4.2 Two-Level Power Combiner Performance

For broadside radiation, we mount the grid oscillator along the optical axis of the two-dimensional lens amplifier array in an anechoic chamber. The best output power is produced when the grid oscillator is 15 cm away from the lens. Since the effective size of the grid oscillator is approximately 2.0 cm by 2.5 cm, we expect the optimum feed distance to be closer than the design focal length. The bias of the grid oscillator is $V_{ds} = 2.0$ V, $I_{ds} = 210$ mA, and $V_{gs} = -1.05$ V, and generates 150 mW effective radiated power (ERP) at 10.25 GHz. The lens transistors are biased in parallel at $V_{ds} = 2.5$ V, $I_{ds} = 400$

mA, and $V_{gs} = -0.25$ V. When the oscillator feeds the lens at its optimum feed point, the lens ERP is 525 mW, showing an insertion gain of 5.4 dB. The isolation of the lens is tested by increasing the gate bias to -2.0 V, resulting in 2 mA total drain current. The isolation ratio at 10.25 GHz is 21 dB. A cross-polarization ratio of 23 dB for the lens is found by polarization mismatching the grid oscillator feed and the receive horn with respect to the input and output of the lens, respectively. E -plane and H -plane patterns of the lens fed at broadside are shown in Figure 5.12. The main lobe 3-dB beamwidths of the E - and H -plane patterns are approximately 11° , which is in good agreement with a theoretical value of 11.3° for a uniformly driven array. The H -plane

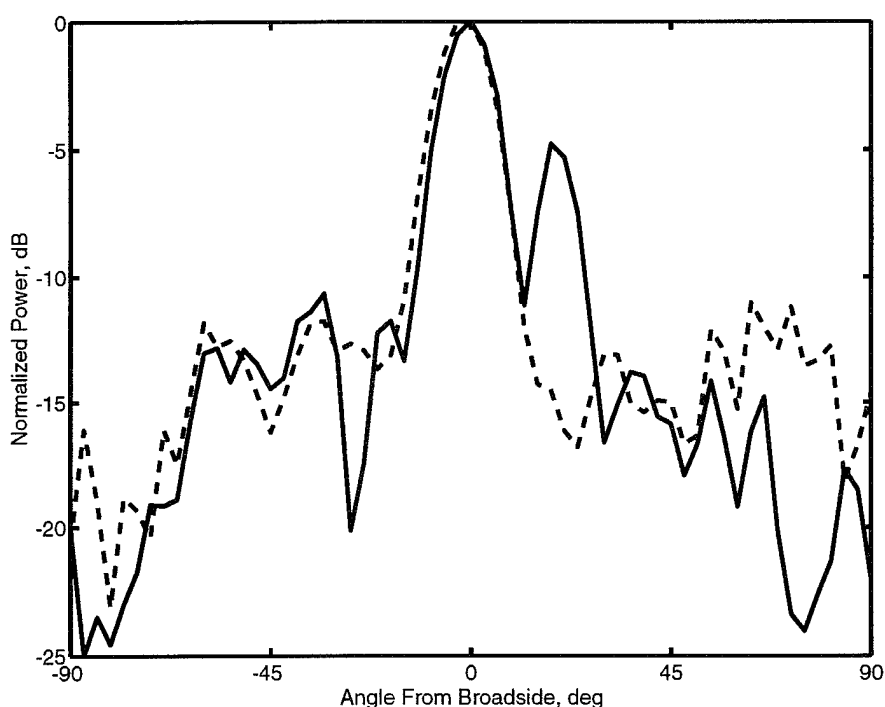


Figure 5.12. Measured antenna patterns for the 24-element lens amplifier array fed by the grid oscillator at the focal point. E -plane (solid line) and H -plane (dashed line) beamwidths are both about 11° .

pattern side lobe level is better than -12 dB, but the E -plane pattern exhibits a significant lobe at $+20^\circ$. We believe the cause of this lobe is an asymmetry in the near field radiation pattern of the grid oscillator, as well as an asymmetry in the output patch pattern at 10.25 GHz. The measured far-field pattern of the grid oscillator shows an asymmetry in the E -plane at around 20° and a symmetrical H -plane pattern, but this does not necessarily indicate the near-field pattern. To check the lens with a symmetrical feed, we replaced the grid oscillator feed with a horn and measured the E -plane radiation patterns of the lens at 10.25 GHz and 9.7 GHz. The resulting patterns, shown in Figure 5.13, indicate that the lobe at $+20^\circ$ is reduced by 5 dB at 10.25 GHz,

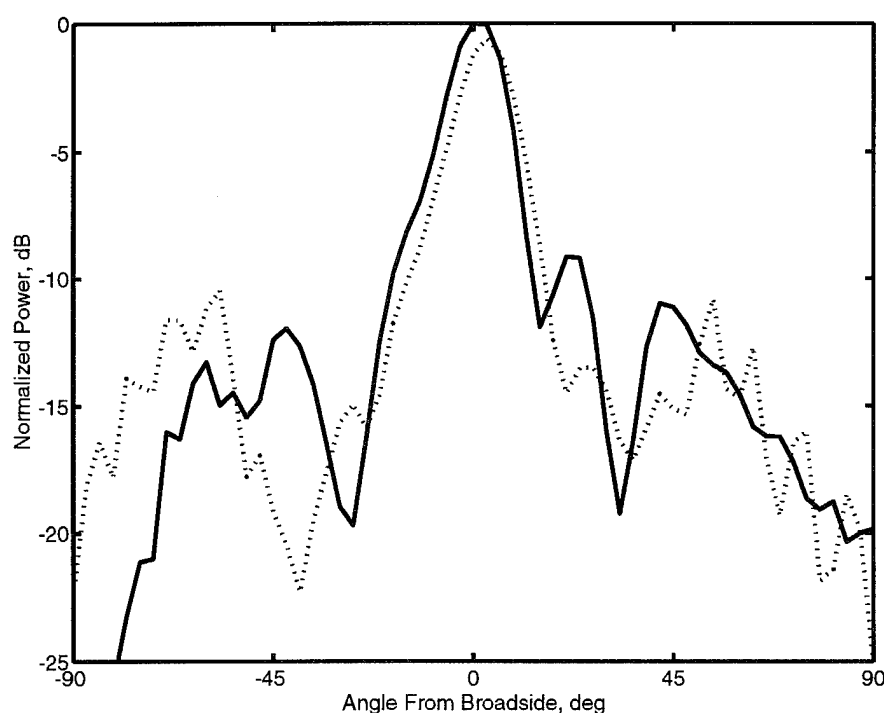


Figure 5.13. Measured E -plane pattern for the 24-element lens amplifier array fed by a horn at the focal point at 10.25 GHz (solid line) and 9.70 GHz (dotted line).

and essentially disappears at 9.7 GHz. Therefore, it appears that there is an asymmetry in the grid oscillator feed that is mostly responsible for the significant side lobe in the patterns. The grid oscillator radiation pattern may be asymmetrical because of a dielectric strip placed across the bias lines on one side of the grid which was required to get the oscillator to reliably lock to the desired mode. To check the frequency dependence of this significant sidelobe being caused by the output patch pattern, we calculated the theoretical array factor multiplied by the output patch pattern (to be explained in Chapter 6). The patch pattern is found to be frequency dependent, with the radiation

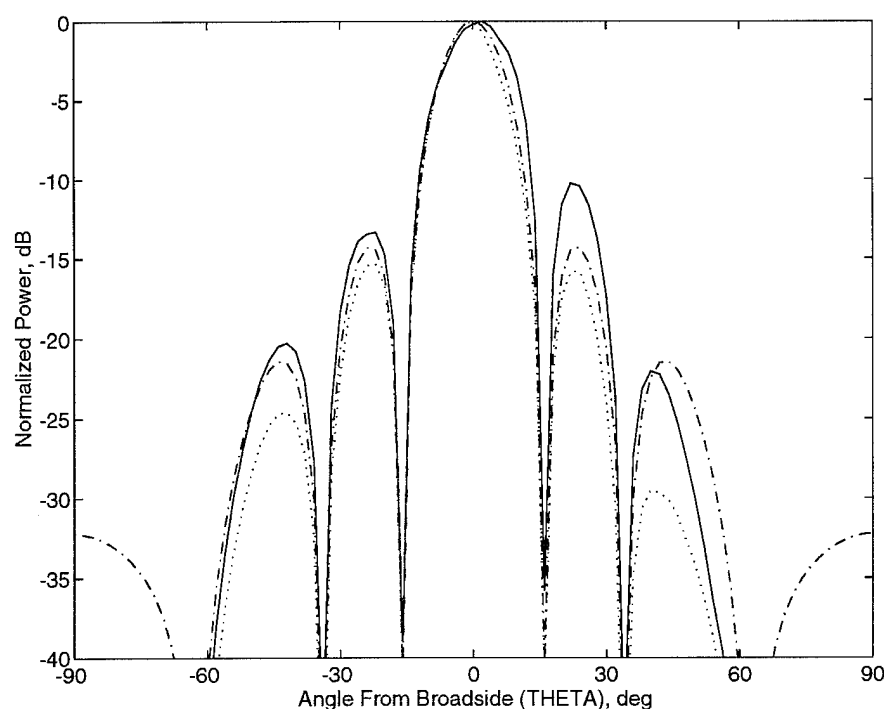


Figure 5.14. Theoretical 24-element lens array factor with frequency-dependent radiation pattern of output patches included to show its effect at 10.25 GHz (solid line) and at 9.75 GHz (dotted line). The array factor is included as the dash-dotted line.

pattern relatively symmetrical at 9.75 GHz but steered to $+20^\circ$ at 10.25 GHz. The theoretical E -plane radiation pattern showing the patch pattern's effect as a function of frequency is shown in Figure 5.14. The simulation assumes uniform amplitude among the elements. The solid line represents the array's pattern at 10.25 GHz, showing the significant sidelobe at $+20^\circ$ and in the asymmetrical pattern. As seen in the measured results, operation at 9.75 GHz (dotted line) reduces the significant sidelobe by 5 dB for a nearly symmetrical pattern. For comparison, the array factor assuming isotropic radiation of all elements is shown as a dash-dot line. This model adequately explains the frequency dependence of the E -plane pattern seen in Figure 5.13 above.

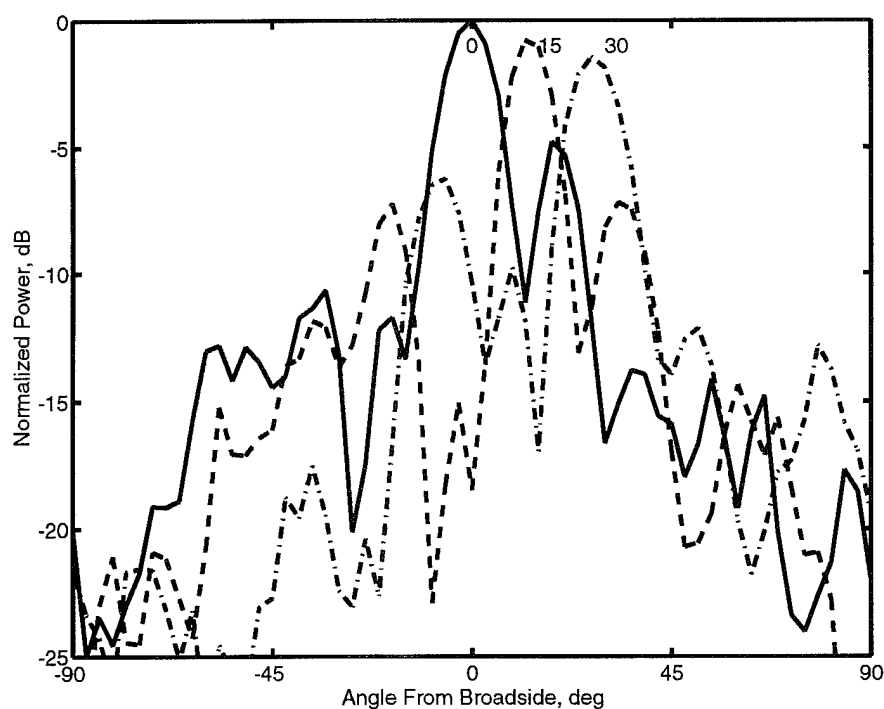


Figure 5.15. Measured beamsteering E -plane pattern for the 24-element lens amplifier fed by the grid oscillator. The main lobe power variation is 2 dB over a 30° scan range.

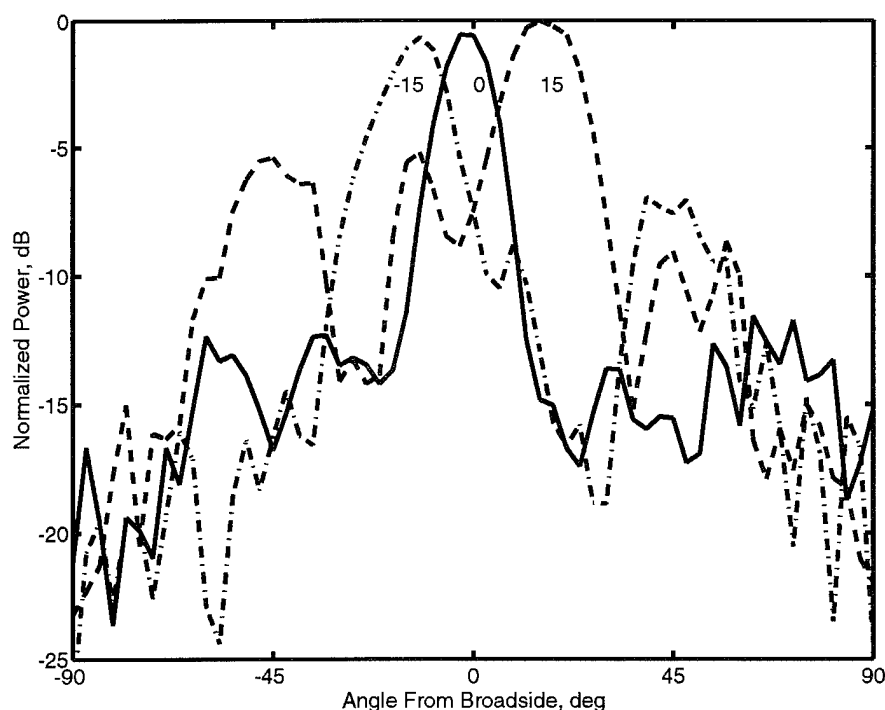


Figure 5.16. Measured beamsteering H -plane pattern for the 24-element lens amplifier fed by the grid oscillator. The main lobe power variation is 1 dB over a $\pm 15^\circ$ scan range.

Beamsteering is performed by positioning the grid oscillator at various angles off of broadside along the focal arc. Figure 5.15 shows the measured beamsteering in the E -plane, and Figure 5.16 shows the measured beamsteering in the H -plane. The beam can be steered in the E -plane by 30° with less than 2 dB power variation. The asymmetric side lobe in the broadside-fed E -plane pattern is reduced when the lens is fed from the $+15^\circ$ and $+30^\circ$ feed points, as expected. Grating lobes are observed for scan angles greater than 24° in the H -plane beamsteering measurement due to the large inter-element spacing. These measured patterns compare favorably with the theoretical patterns for E -plane and H -plane shown in Figure 5.17 and Figure 5.18, respectively. These

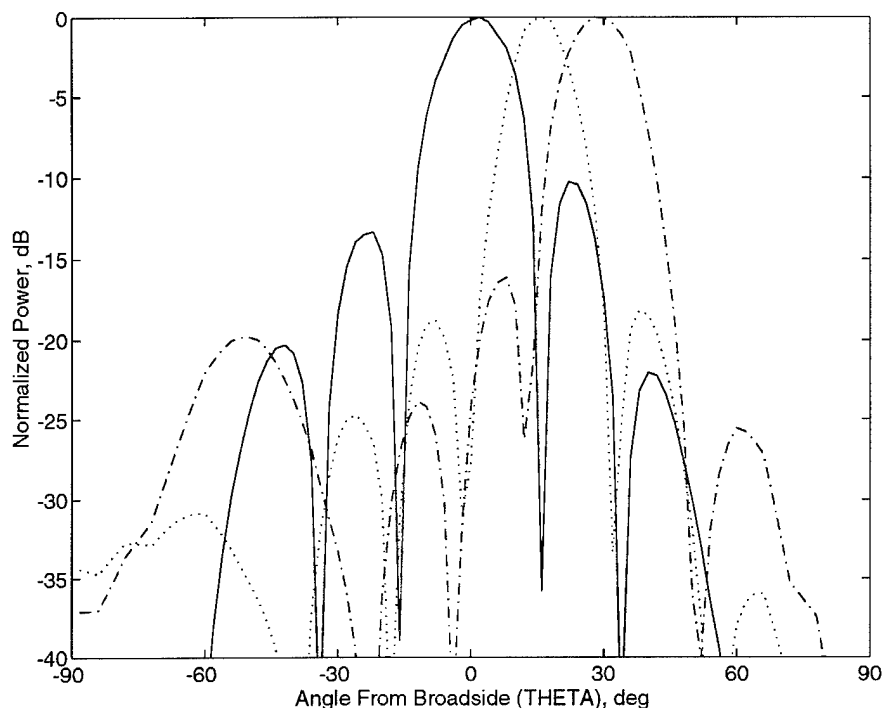


Figure 5.17. Theoretical E -plane beamsteering patterns of the 24-element lens array at 10.25 GHz for scan angles of 0° (solid line), 15° (dotted line), and 30° (dash-dot line).

patterns include the output patch pattern at 10.25 GHz to accurately model the measured patterns made at this frequency. No grating lobes form in the E -plane pattern due to the triangular lattice, unlike the linear array above, even though both arrays have the same inter-element spacing. The H -plane pattern shows grating lobes 7 dB below the peak due to the triangular lattice not suppressing these lobes in the $\phi = 90^\circ$, or H -, plane. Therefore, beam scan range is much more limited in the H -plane than the E -plane.

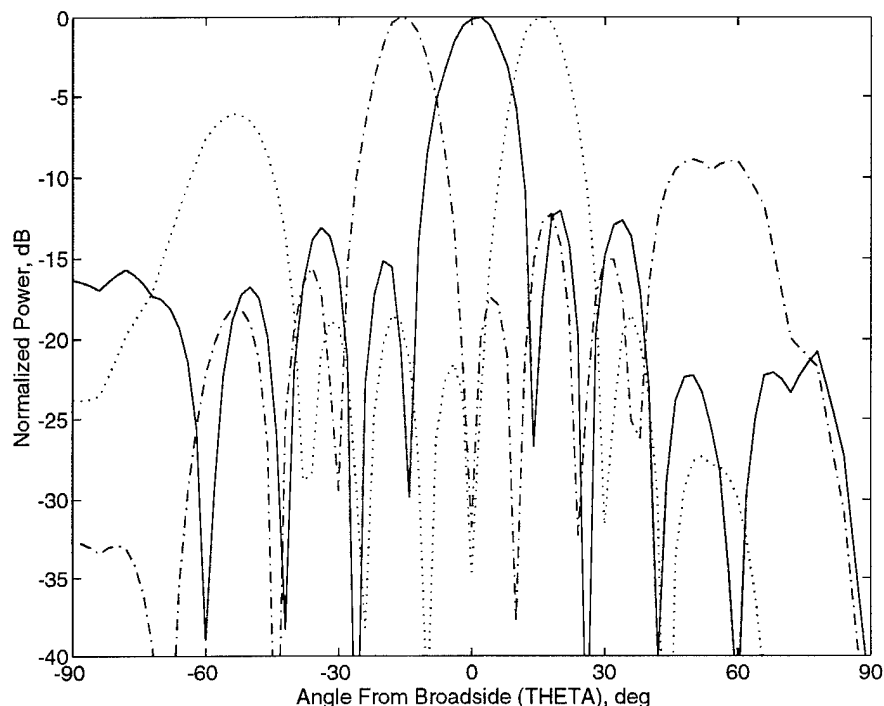


Figure 5.18. Theoretical H -plane beamsteering patterns of the 24-element lens array at 10.25 GHz for scan angles of 0° (solid line), 15° (dotted line), and -15° (dash-dot line).

5.4.3 Beamforming

A second 28-PHEMT grid oscillator was built to the same specifications as the first grid oscillator feed for the amplifier. With two oscillators, beamforming is demonstrated in both E and H planes as the grid oscillators are moved along the focal surface of the lens. Here we present beamforming and beam-switching results with a dual grid-oscillator feed, as shown in Figure 5.19. When both grids are on, the output radiated pattern of the lens amplifier is a superposition of the patterns for the two individual feeds, which makes beamforming possible. Figure 5.20 shows examples of measured dual-beam patterns in the E and H planes of the lens. In the E -plane, the two grids

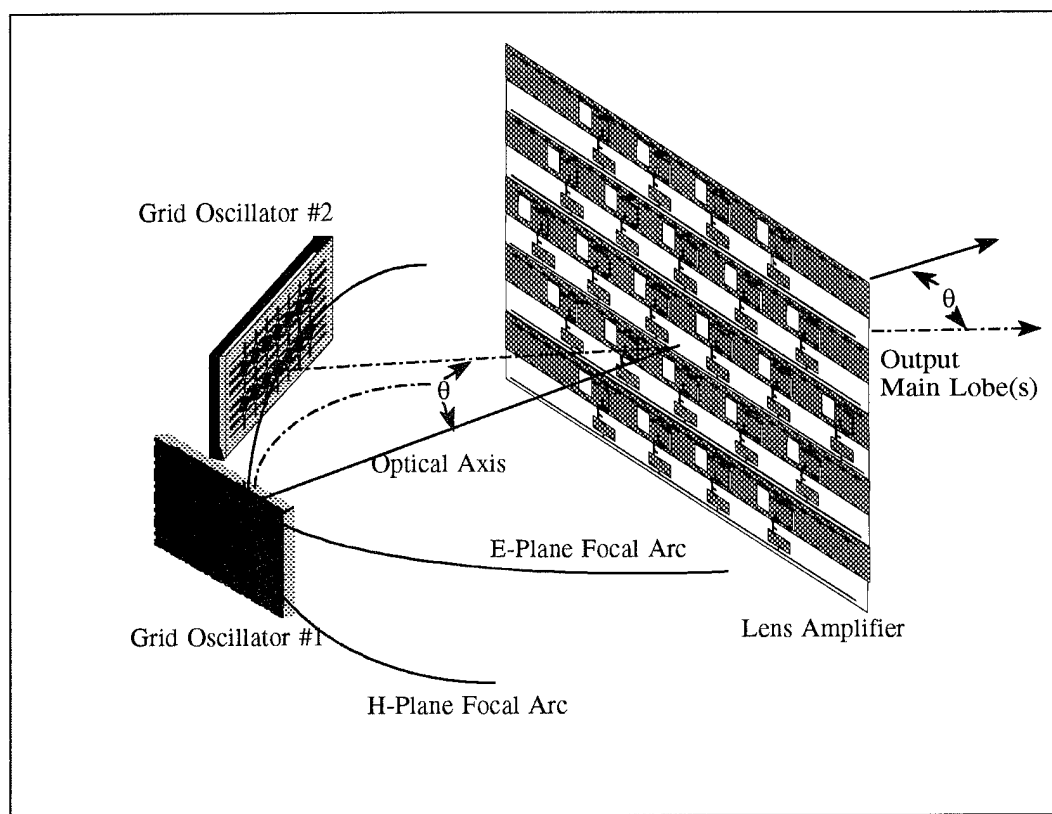


Figure 5.19. A patch antenna lens amplifier with a dual grid-oscillator focal feed point. The shaded patches, microstrip circuits, and ground planes are on the backside of the array.

were placed at 0° and 24° along the focal arc and the amplifier pattern, shown as a solid line, shows equal-power beams at 0° and 24° . Two beams at 21° in the H -plane are shown as a dashed line in Figure 5.20. The individual grid oscillators can also be bias-switched one at a time, and so the amplifier pattern can be switched between a finite number of beams at different angles. In this case, the switching speed is limited by the oscillator settling time. By keeping the oscillators biased at the threshold of oscillation and pulsing the gate bias, a switching frequency of 5 kHz was measured (0.2 msec switching rate). It was verified that the grid oscillator that is off does not affect the pattern of the lens.

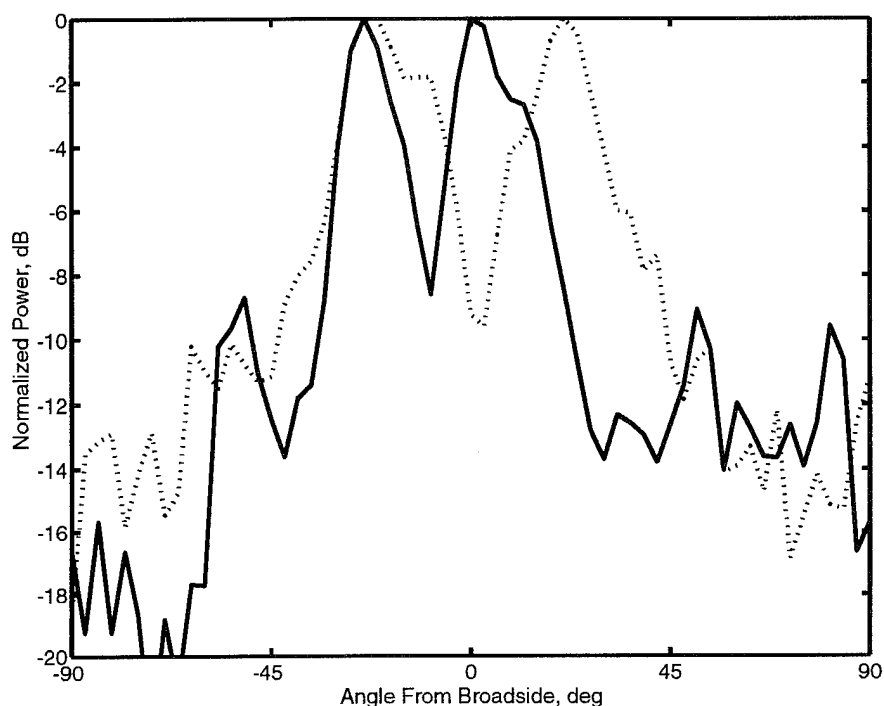


Figure 5.20. Measured normalized beamforming lens amplifier radiation patterns for two different positions of the grid oscillator feeds in E - and H -planes (solid and dashed lines, respectively).

As the input power to the lens amplifier is increased, the center elements saturate first. This makes the saturation curve of the array more gradual than that of a single element. However, as the lens becomes nonuniformly saturated, its radiation pattern changes: the main lobe broadens and the sidelobes are reduced. Figure 5.21(a) shows the measured gain compression curve of the lens using a 1-Watt TWT amplifier at the output port of a HP71500A Transition Analyzer. Figure 5.21(b) shows the pattern broadening corresponding to the 3-dB compression point of the ERP.

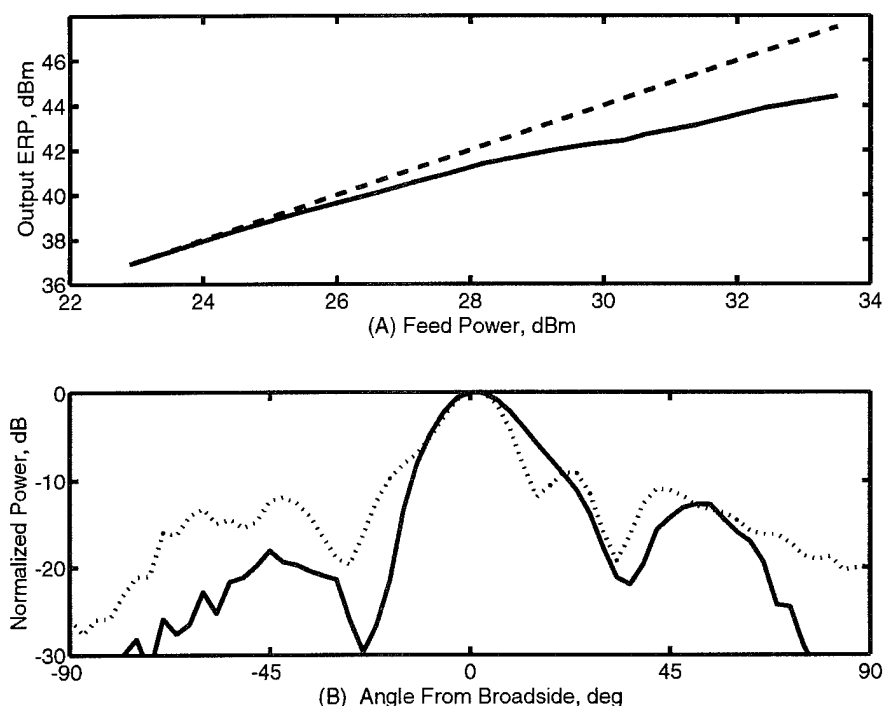


Figure 5.21. (a) Measured gain compression of the lens amplifier effective radiated power (ERP). (b) Radiation pattern corresponding to the amplifier operation in the linear regime (dashed line), and 3-dB into compression (solid line).

5.5 Conclusion

A two-dimensional, 24-element planar lens amplifier and a grid oscillator are integrated into a two-level quasi-optical power combining system. The amplifier demonstrates an isolation (on/off ratio) of 21 dB and a cross-polarization ratio of 23 dB at a center frequency of 10.25 GHz. When fed by a 28-element grid oscillator, an effective radiated power of 525 mW is measured. The grid oscillator is designed using a full-wave theory and is tunable over the pass band of the amplifier. The lens has an insertion power gain of 5.7 dB. The output beam of the two-level free-space combiner can be steered in both E -

and H -planes. E -plane beamsteering to a 30° scan angle is demonstrated with less than 2 dB of main lobe power variation. H -plane beamsteering of up to 24° is measured. Another lens amplifier, a 7-element linear array fed by a horn, has a center frequency is 9.7 GHz and an isolation figure of 29 dB. Scanning angles up to 30° produce less than 1 dB of main lobe power variation when the linear lens array is fed along its focal arc. These lens systems are useful for amplification, focusing and beamsteering applications with solid state power generation.

CHAPTER 6

BROADBAND RADIATORS

6.1 Motivation

The microstrip antennas used in the linear and two-dimensional lens amplifier arrays presented in the last chapter limit the 3-dB bandwidth to three percent of the center frequency. These lens amplifier arrays used non-radiating-edge-fed microstrip patch with an input impedance of $100\ \Omega$ as input and output elements. In addition, the patch-patch plane-wave fed transmission amplifier presented in Chapter 2 has limited bandwidth due to its radiating-edge-fed microstrip patches. However, wideband requirements at millimeter-wave frequencies will require an efficient antenna element that remains well matched to the amplifier and radiates efficiently over a wider bandwidth ($> 10\%$). Typically, the bandwidth of an antenna is defined as the frequency range over which it presents a voltage standing wave ratio (VSWR) below some specified limit into a specified characteristic impedance. A radiation pattern characteristic such as directivity, cross-polarization ratio or axial ratio may also be used to specify an antenna's bandwidth. We use a $\text{VSWR} < 2:1$, or better than a $-9.6\ \text{dB}$ return loss for our bandwidth specifications.

A planar structure is required so that it may be integrated with the amplifier on a planar dielectric metallized on one or both of its sides so that low-cost printed-circuit fabrication techniques can be used. The microstrip patch antenna used in the lens amplifier arrays of Chapter 5 will first be discussed.

Then, a microstrip-based broadbanded antenna will be presented which requires multiple dielectric layers, and may be a good candidate for future wide-band arrays. Finally, broadbanded slot antennas that are operated at their second resonance are presented as a solution to the limited bandwidth experienced in earlier lens arrays, leading to a low noise amplifier lens array discussed in Chapter 7.

6.2 Microstrip Patch

The microstrip patch antenna was selected for our initial lens amplifiers because of its compatibility with microstrip circuitry and the alternating ground-plane isolation. The extensive information and availability of modeling software made the element design relatively straight forward [124],[125]. The layout of the input and output patch antennas is shown in Figure 6.1(a) and (b), respectively. A non-radiating-edge (NRE) microstrip-fed design was selected because an arbitrary impedance can be chosen. An resonant input impedance of $100\ \Omega$ was selected so that the microstrip delay lines connecting the patch with its amplifier circuitry are narrow and exhibit minimal dispersion. The distance x_i from the feed line center to the closer radiating edge is the critical dimension determining the resonant input impedance. The width of the radiating edge b was set to be narrower than its resonant length a for a compact design, and sets the fundamental orthogonal (the radiating-edge-fed) mode at a higher frequency where the amplifier has much lower gain. Using this compact element in the lens array results in an inter-element spacing of $0.75\lambda_o$ compared to the $1.33\lambda_o$ spacing needed for our plane wave-fed QOPC amplifier array in Chapter 2, which uses radiating-edge-fed patches.

Figure 6.1(a) represents the patch layout simulated using multiport

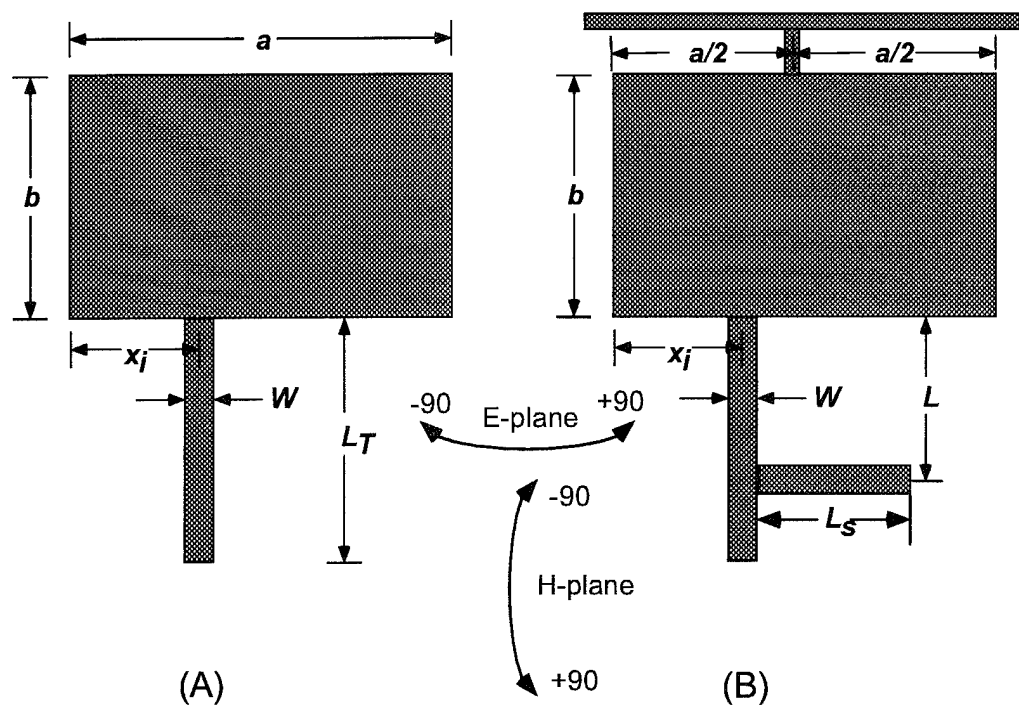


Figure 6.1. Non-Radiating-Edge (NRE) microstrip-fed patch antenna. The resonant length is a and the radiating-edge length is b . In (a), the patch layout as designed and fed for the input side is shown; (b) shows the drain bias line added to the patch, which alters its radiation characteristics.

network model (MNM) analysis [124],[125]. With the patch dimensions given in Table 6.1, the MNM analysis predicts a resonant frequency of 10.07 GHz with a directivity of 6.7 dB and radiation efficiency of 84%.

Table 6.1: Dimensions of the Microstrip Patch Antennas						
a (mm)	b (mm)	x_i (mm)	W (mm)	L_T (mm)	L (mm)	L_s (mm)
9.61	6.00	3.27	0.71	9.00	4.50	3.64

The fabricated patch resonates at 10.01 GHz, a deviation of only 0.6% from the simulation. The measured results are compared to the MNM simulation in Figure 6.2. Also included on the plot is a moment-method simulation of the patch using Hewlett Packard's planar electromagnetic simulator called Momentum, which agrees very well with the MNM solution. The Momentum

simulations use a square mesh with $\lambda/30$ period over the patch surface, with a smaller mesh size of approximately $\lambda/45$ along the radiating edges. The frequency plots show that patches are high-Q circuit elements, which have a 2:1 VSWR bandwidth of only two percent of the resonant frequency. Therefore, it is critical to match the input and output elements' frequency response in order to maximize the gain of the quasi-optical power-combiner (QOPC) array. Otherwise, the elements on the input array may resonate at a different frequency than those on the output array, impairing the gain of the QOPC lens amplifier array.

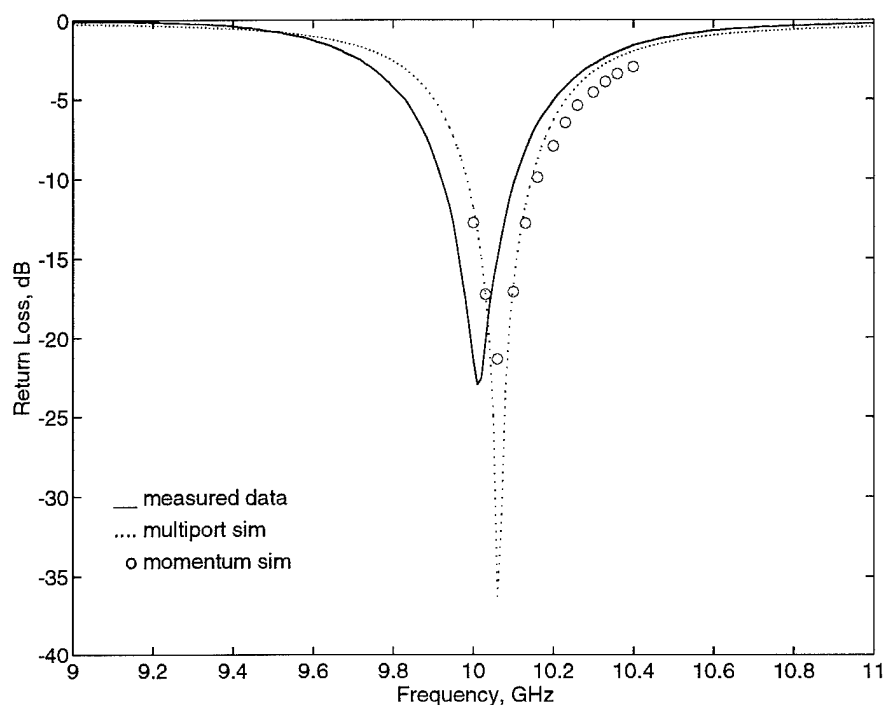


Figure 6.2. The measured return loss of the NRE patch (solid line) compared to the multiport network model (MNM) simulation (dashed line). Symbols represent the method of moments simulation, which compares well with the MNM simulation.

To save space and simplify the amplifier biasing, the output-side patches of the lens amplifier arrays provided the drain bias through the RF null of the patches using a microstrip-type structure shown in Figure 6.1(b). Also attached to the feed line is a single-shunt stub used for optimum gain match to the drain of the PHEMT in the amplifier. In theory, the narrow bias line would not perturb the resonant frequency or antenna pattern of the element since it is connected to the RF null of the patch. However, the drain bias line forms a coplanar stripline (CPS) transmission line with the patch. It is likely that random irregularities and stray coupling could launch waves on this line, resulting in the additional resonances that were measured. In addition, the Q was reduced and the radiation pattern altered. As shown in Figure 6.3, the 10.00 GHz E -plane pattern contains a 5-dB null at broadside and peak lobes at $\pm 60^\circ$, and has considerably less gain than at the other frequencies shown. This is a very undesirable element radiation pattern for inclusion into a power combining array, and explains the poor gain performance of the lens amplifier array at this frequency. However, the 9.75 GHz E -plane pattern was symmetrical with its peak at broadside and exhibits considerably higher gain than at 10.00 GHz and 1.8 dB more gain than at 10.25 GHz. The 10.25 GHz E -plane pattern is asymmetrical, with its peak at $+18^\circ$ and a 2-dB null at broadside. Since the individual element pattern has a multiplicative effect on the output array pattern, the asymmetry in the output patch pattern at 10.25 GHz compared to the symmetry of the pattern at 9.75 GHz explains the prominent side lobe variation in the horn-fed patterns of the two-dimensional lens amplifier at these two frequencies shown in Chapter 5.

On the input side of the two-dimensional lens amplifier array, the

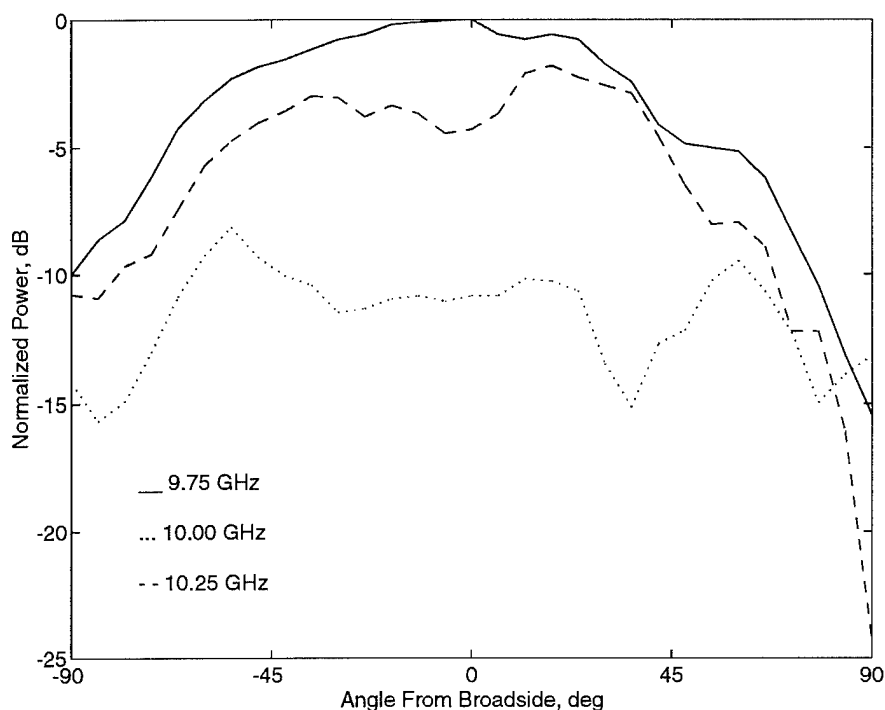


Figure 6.3. Measured radiation patterns of the output patch with matching stub and drain bias line. The radiation patterns are frequency sensitive, with plots at 9.75 GHz (solid line), 10.00 GHz (dotted line), and 10.25 GHz (dashed line) shown.

radiating edges of the patches are very close to the top-side ground planes. This is due to the competing requirements of isolation between the input and output sides of the array, and maximizing power combining efficiency and scan angle. The former is provided by the inter-connected ground planes which take up a large portion of the array area, and the latter is accomplished by reducing the inter-element spacing. In satisfying these requirements, some patches on the input side have radiating edges within one substrate thickness h of the same-side ground plane. To simulate the effect of the ground plane on the input return loss of the patch, a moment-method simulation using the patch

shown in Figure 6.1(a) was performed with top-side ground planes. The ground planes are several wavelengths long, about $0.4\lambda_o$ wide, and are oriented so that their long edges are parallel to both radiating edges of the patch. Therefore, the test structure is very similar to that of the two-dimensional lens amplifier array. The gap between the radiating edge and the ground-plane edge is 0.5 mm, and vias are placed every $\lambda_o/4$ along the ground-plane edge to suppress the generation of slot modes. The moment-method models are compared to measured antennas, resulting in the plots in Figure 6.4. The “control” (dotted

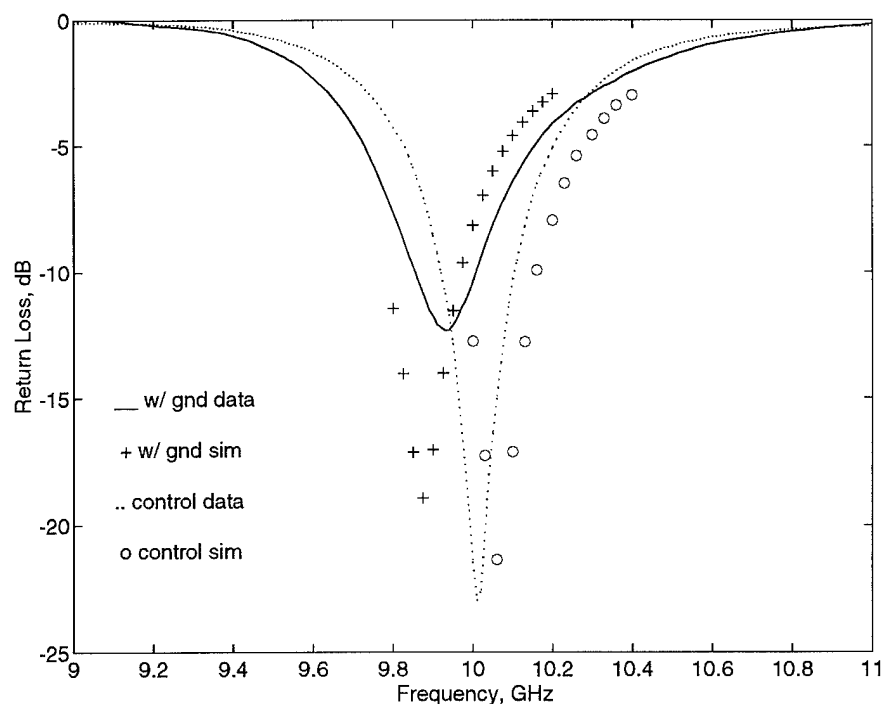


Figure 6.4. Measured and modeled input return loss of the input-side patch to demonstrate the effect the ground-plane edges placed in close proximity ($< h$) away from the radiating edges. The solid line and circle symbols represent the measured and modeled patch without the top-side ground plane, respectively. The dashed line and ‘+’ symbols represent the measured and modelled case with the ground plane.

trace) is the measured patch data without the top-side ground plane, and agrees to within 0.6% to the moment-method simulation ("o" symbols). The solid line is the measured patch data with the top-side ground planes, and agrees to within 0.5% in frequency to the moment-method simulation ("+" symbols). Introducing the ground planes decreases the measured resonant frequency from 10.01 GHz to 9.90 GHz, and from about 10.07 GHz to 9.87 GHz in the moment-method simulations. Although the moment-method simulations do not indicate any degradation in return loss, the measured results show that the top-side ground plane degrades the match and the 2:1 VSWR bandwidth. Therefore, the lens array structure on the input side, with its isolation ground-planes placed very close to the radiating edges of the patches, has the unintentional consequences of lowering the resonant frequency and mismatching the patches with their delay lines. Since the patches in the input and output arrays did not resonate at the same frequency, and the input patch reflection coefficient Γ_{in} was considerably increased, the transmission gain of the lens amplifier was reduced. Figure 6.5 shows these effects on the measured absolute power gain of the two-dimensional lens amplifier array before and after the ground planes were cut away from the radiating edges of the input elements. Before this modification (dotted lines), the amplifier shows two frequency peaks. The minor peak at 9.70 GHz is where the input elements were resonant, and the maximum peak at 10.25 GHz where the output elements radiated best under these conditions. The peak absolute power gain was 5.7 dB. After ground plane metal was removed from around the radiating edges of the input patches, the absolute power gain of the array improved by 2.3 dB to a peak gain of 8.0 dB at 9.75 GHz. The increase in frequency of what was originally the minor peak

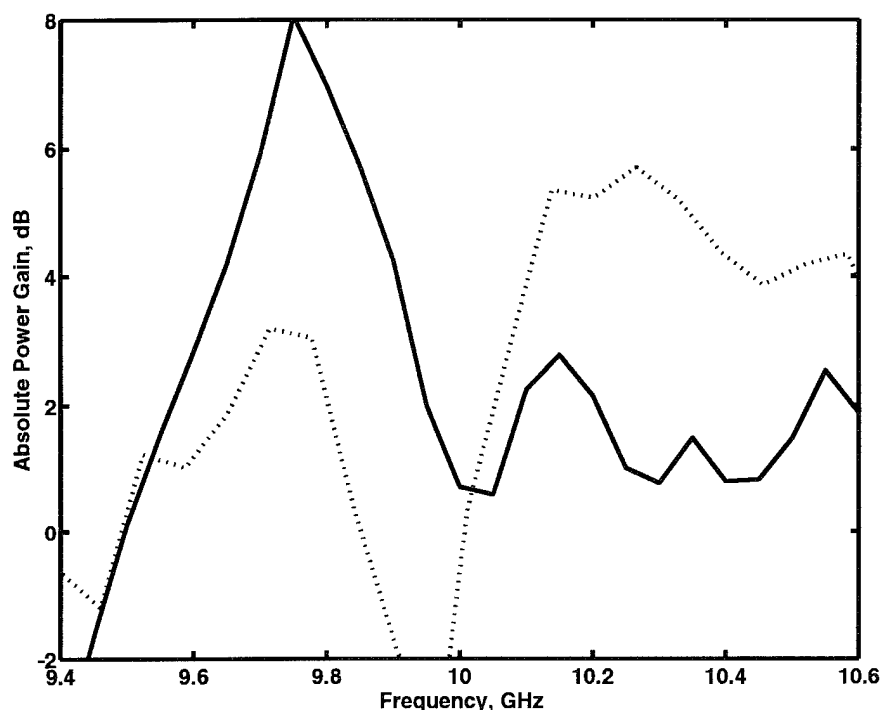


Figure 6.5. Improved two-dimensional lens amplifier gain and change in frequency response after top-side ground plane modification (solid line) compared to before (dotted line).

can be explained from the measurements and simulation in Figure 6.4 above. The input patches are now better matched to their delay lines and amplifier inputs, and the resonant frequency of the elements on the input and output sides is better matched.

Another Momentum simulation was performed to calculate mutual coupling effects on the linear 7-element array shown in Chapter 5. A 7 element linear array of patches identical to the one simulated above with inter-element period of $0.75\lambda_0$ was simulated. A port was defined at the end of the feedline of each patch, and each port is driven with the same amplitude and phase. The simulated magnitude of the s -parameters of the coupled ports are shown

in Figure 6.6 defining port 1 (an edge element) as the excitation port. The S_{11} curve shows the same resonant behavior as that shown in the simulation of an uncoupled patch above. The S_{m1} curves show the magnitude of the coupling between ports, with each patch most strongly coupled at resonance. The strongest coupling is with the neighboring patch, with a maximum coupling of -25 dB, and the minimum coupling is between edge elements at -45 dB. The entire S_{mn} -parameter array was generated and examined and was found to be symmetrical with all $S_{mn} = S_{nm}$. Since the magnitude of the coupling is small between the elements, we feel that simulating the array patterns without mutual coupling effects is a good approximation to the measured results.

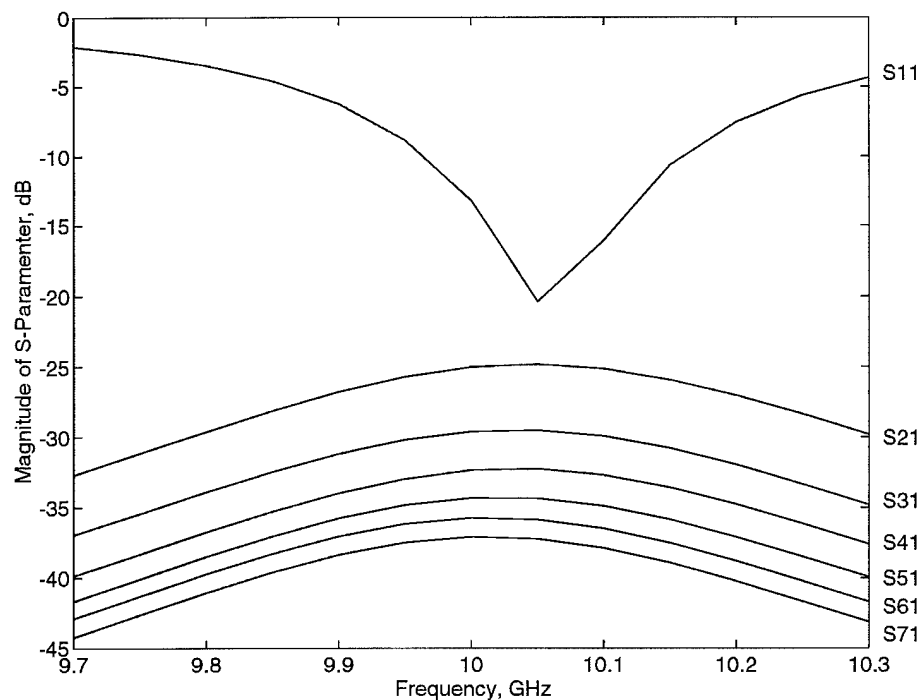


Figure 6.6. Method of moments simulation of a 7-element array of patches showing the magnitude of mutual coupling between elements.

6.3 Broadband Quasi-Microstrip Antenna

The high-Q nature of microstrip patches makes their use in quasi-optical power-combining arrays difficult if the element's proximity to ground planes, amplifier circuitry, or fabrication tolerances alter the resonant frequency or input match. In addition, high data rate communication will require higher bandwidth operation of quasi-optical amplifiers, and since the bandwidth is limited by the antenna elements, new elements need to be employed in the lens amplifier. Various techniques for increasing the bandwidth have been used up to date: reducing the Q of the circuit by reducing the substrate height and/or lowering its dielectric constant [126]; using circular and square ring configurations [127]; using multiple coupled resonators on the same substrate [128]–[130]; using multiple vertically coupled resonators [131]; and using log periodically grating patches [132]. The largest reported bandwidths are around 20%. The disadvantages of the listed techniques include change in the radiation pattern over the bandwidth, complicated multilayer structures and large areas taken up by the antenna.

We presented a new type of planar antenna, which is a combination of a wire antenna array and a microstrip patch antenna [133]. The antenna is slightly smaller in size than the standard resonant patch, and exhibits a 2:1 VSWR bandwidth of about 23%. The radiation pattern does not change appreciably within the bandwidth and the polarization of the radiation field is linear with a measured cross-polarization ratio of 16 dB. The theoretical efficiency of these antennas when properly designed is above 80%. Rather than being resonant at a single frequency, the presented antenna has a broad resonance that can be controlled by proper design with respect to several antenna

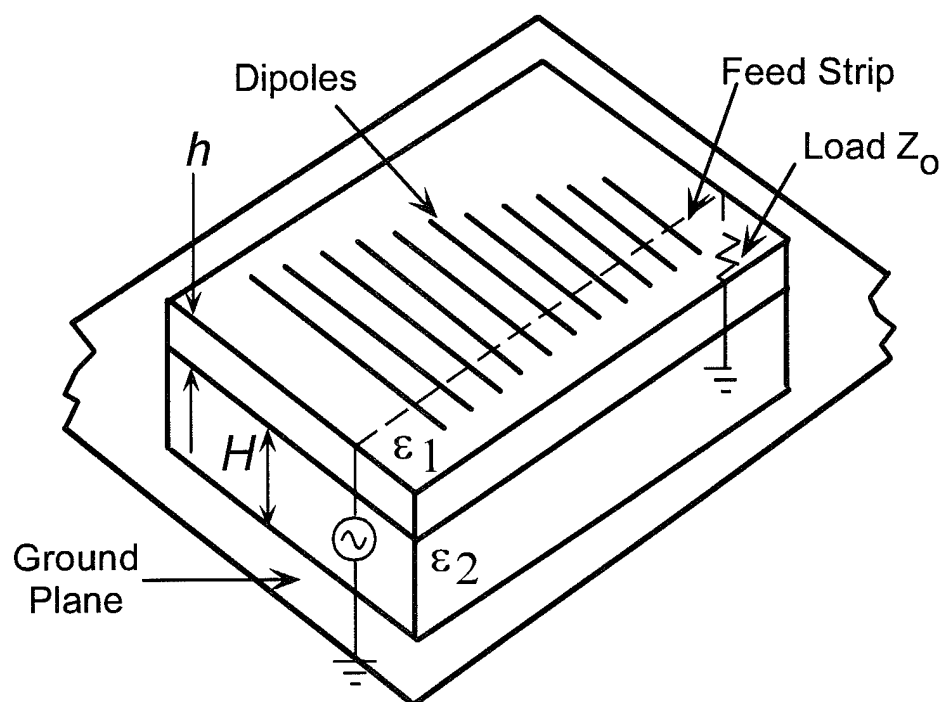


Figure 6.7. The geometry of an N -element quasi-microstrip antenna. The planar array of narrow printed conducting strips is located above a feed strip, itself above an infinite ground plane. The feed line is connected to a generator at one end and terminated in its characteristic impedance at the other end.

parameters. The theoretical impedances, current distributions, efficiencies and far-field patterns of these antennas, as well as measured results obtained for several antenna experimental models have been presented [133],[134].

The antenna geometry is shown in Figure 6.7. A planar array of narrow conductive strips is printed on one side of the top dielectric sheet with thickness h and relative permittivity ϵ_1 . The conductive strips are located above a feed strip printed on the backside of the top dielectric sheet. The feed strip, in turn, is above an infinite ground plane, separated by the bottom dielectric sheet with thickness H and relative permittivity ϵ_2 . The feed line is at a height H , and the strips at a height $H + h$ above the ground plane. The feed strip, dielectric, and ground plane form a transmission line connected

to a generator on one end and terminated in its characteristic impedance Z_0 on the other end. We call this a quasi-microstrip antenna because the planar antenna structure is less than $\lambda_o/10$ above the ground plane, but the antenna is a set of printed narrow strips instead of a metal patch. The antenna has an anisotropic character since the current can flow only along the thin conducting strips. The period between the strips is much smaller than the wavelength and much greater than the width of a strip. There are an arbitrary number of strips, though the resonant frequency and radiation efficiency is dependent on the total number. We used thirteen strips in our measured antennas, resulting in an efficiency of around 90% over a 23% bandwidth.

The antenna was analyzed and designed using the CAD program *WireZeus* [134]. Briefly, the generalized integral equation of Hallén for the current distribution along arbitrarily interconnected straight wire segments is solved by the point matching technique. Entire (or almost entire) domain polynomial basis functions are used for the current distribution. The segments may have at one end concentrated generators and/or impedances. They can also have distributed impedances along their length. Conductive planes are taken into account by the image method. In the case of narrow strips printed on a dielectric, the program uses a cylindrical wire of an equivalent radius with an equivalent magnetic coating [135].

Beside exhibiting 2:1 VSWR bandwidths in excess of 20%, these antennas maintain consistent radiation patterns over this frequency range. Because the current is constrained to flow only along its thin conducting strips, the H -plane pattern is much narrower than for a microstrip patch antenna. The 3-dB beamwidth is approximately 60° in both E - and H -planes, making

this antenna an excellent candidate for array applications with improved side lobe performance compared to one containing microstrip patches. However, we did not pursue an array amplifier using this antenna because of difficulty in maintaining dielectric thickness and flatness across an array surface. Variation in the dielectric thickness of a low dielectric layer and air gaps between layers has been shown to severely alter the return loss and resonant frequency of microstrip patches using a multi-layer structure [136].

6.4 Slot Antennas

6.4.1 Introduction

The difficulty in producing a uniform multi-layer dielectric structure in our laboratory prevented further consideration of the quasi-microstrip patch antenna for QOPC arrays. Also, the numerous through-substrate vias in microstrip-based arrays such as the lens amplifier arrays were required to minimize the source inductance of the common-source amplifiers and prevent slot-mode radiation in the ground planes. The surface area consumed by the isolation ground planes prevented close inter-element spacing for improved beam scanning, power density, and aperture efficiency.

Alternatively, the uniplanar nature of coplanar waveguide (CPW) circuits is attractive for simplifying array fabrication. All devices, circuitry, transmission lines and antenna elements of the array are contained on one side of the dielectric, thus removing the need for vias. Active devices and lumped components are easily connected in series or shunt in CPW, which also provides flexibility in choosing the ground-to-ground spacing for a desired impedance. Slot antennas may use CPW as a compatible feed line in a uniplanar circuit. CPW-fed slot antennas have been demonstrated in a quasi-optical mixer [137]

and amplifier arrays [138],[139], where it was recognized that slots can significantly increase the bandwidth of quasi-optical components.

Analyses of slot antennas defined in a metallic sheet on thin dielectric substrates has been performed with moment method [140] or with a space-domain integral equation (SDIE) solved using the method of moments [137]. These methods are numerically intensive and may take considerable time to generate an s-parameter model over a sizable frequency range for simulation with an amplifier circuit. Below, I will present the theory developed by Popović and Nešić to solve the slot antenna on a thin dielectric using the concept of complementary electromagnetic structures (CES). After a series of conversions using CES and applying the duality principle, the slot antenna may be solved using the CAD program *WireZeus* [134] in a time-efficient manner. Simulations compare closely with measured results of two slot antennas, a center-fed folded slot and an off-center fed slot, both operated at their second resonance. These antenna elements are used in a wideband low noise lens amplifier array presented in Chapter 7.

6.4.2 Motivation

A CPW-fed resonant slot is the dual structure of a comparable resonant dipole antenna, and a folded slot is the dual of a folded dipole. Booker's principle gives the input impedance of an infinitely-thin half-wave resonant slot in an metal sheet of infinite extent and conductivity as

$$Z_{\text{slot}} = \frac{\eta_o^2}{4 \cdot Z_{\text{dipole}}} \quad (6.1)$$

where Z_{dipole} is the impedance of a center-fed half wave resonant dipole in free space. Since the impedance of the dipole at first resonance is $Z_{\text{dipole}} \approx 73\Omega$,

the slot impedance $Z_{\text{slot}} \approx 500\Omega$, which is a difficult impedance to realize in reasonably-sized coplanar waveguide. If the wire of a dipole is “folded” to give two parallel currents of equal magnitude and direction, it becomes a folded dipole whose input impedance is $Z_{\text{in}} \approx 2^2 \cdot Z_{\text{dipole}} \approx 300\Omega$. The dual to this structure is the folded slot antenna, with the resulting input impedance at resonance of $Z_{\text{slot}}/2^2 \approx 125\Omega$, which is a much more reasonable impedance to which to feed or match. York [138],[139] used folded slots to improve the bandwidth of quasi-optical amplifier arrays. In [139], he integrated MMICs with folded slots in a hybrid X -band amplifier array with 4% bandwidth on an alumina substrate. Five-slot elements were required at the input and output to match the 50Ω port impedance of the MMICs. However, as more slots are stacked to reduce the folded slot impedance, its width (non-resonant dimension) becomes comparable or may even exceed its length (resonant dimension). The resulting element area forces the array designer to use a large inter-element spacing, as evident in the $1.0\lambda_o$ spacing in York’s array.

Since it is desirable to minimize the inter-element spacing in an array, an element employing many parallel slots is not desirable. The center-fed folded that is used in our low noise lens amplifier array utilizes only two narrow parallel slots. The impedance is tailored by lumped elements, which are included in the WireZeus simulations once the slot antenna is transformed into its complementary electromagnetic structure.

6.4.3 Theory

The classical concept of complementary electromagnetic structures (CES) described by Booker [141] has been extended by Popović and Nešić [142] to include various complementary, thin planar conductive structures in

the presence of dielectric and/or magnetic media. The distinction between the classical CES approach of Booker and the complementary/dual structures proposed by Popović and Nešić is in the scope of problems each approach may solve. The classical approach considers a given planar antenna, consisting of one or several conductors, immersed in a homogeneous lossless medium. There is just one complementary antenna for this given planar antenna, where the conductor(s) are replaced by the homogeneous medium in the antenna plane and vice-versa. For example, the complement of a dipole made of a thin conductive strip is a slot cut to the same dimensions as the dipole in a conductive sheet. The dipole and slot are said to comprise a complementary electromagnetic pair. Popović and Nešić extended CES to include any number of arbitrary dielectric and/or magnetic material bodies of arbitrary complex permittivities and/or permeabilities, as long as they are symmetrical with respect to the antenna plane. Therefore, an infinite number of complementary/dual antenna pairs may be considered from one classical complementary pair.

A method was developed [143] for analyzing electrically narrow slots. It consists of transforming the slot through a series of transformations into an approximately complementary/dual structure, which is a dipole of circular cross-section with coaxial magnetic cover. This method allows including a CPW feed since it can be transformed, together with the slot antenna, into its complementary/dual structure, which is a magnetically-coated two-wire parallel transmission line. In our modelling, we use a simple delta-function generator since the feed line does not have a large discontinuity in the excitation region of the equivalent dipole. The method enabled us to design CPW-fed input and output slots for the low noise lens amplifier array with a high degree of

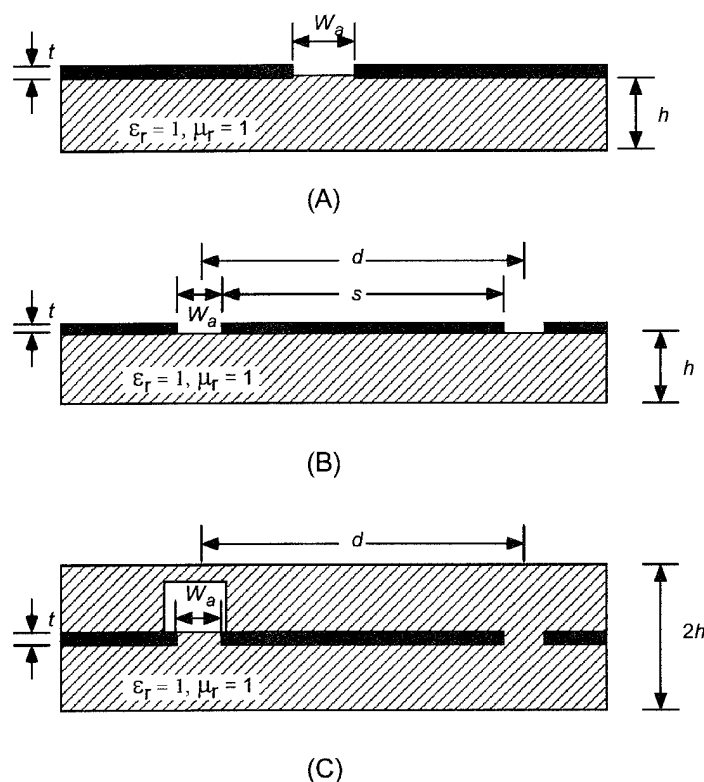


Figure 6.8. The slot antenna analyzed using the quasi-full wave analysis is illustrated in (a). First, it is transformed to its equivalent pair of slots in (b) which is a CPW line, then the TEM-line equivalent is shown in (c).

accuracy in predicting the resonant frequency, impedance and bandwidth of these antennas.

The cross-section of a slot antenna is shown in Figure 6.8(a) with slot width W_a defined in a conductive sheet one side of a non-magnetic thin dielectric sheet of height h and relative permittivity ϵ_r . Using the concept of equivalence, which is relatively similar to that of equivalence of thin cylindrical antennas, we may first consider a pair of parallel, infinitely long slots separated by a large distance d and each of the same width W_a as the slot antenna of interest. The slots are on one side of a non-magnetic dielectric sheet with the same specifications as for the slot antenna. This system represents a coplanar

waveguide as shown in Figure 6.8(b), with capacitance per unit length C_1 and inductance per unit length L_1 . Next, we construct an identical coplanar waveguide conductor geometry, but now centered in a symmetric non-magnetic dielectric sandwich of thickness $2h$ and relative permittivity ϵ_r , as illustrated in Figure 6.8(c). For this line, let the capacitance per unit length be C_2 and inductance per unit length be L_2 . The two waveguides can be considered to be approximately equivalent, in the TEM-mode sense, if their line capacitances and inductances per unit length are equal. Since we are considering the same conducting sheet, with slots of the same width and at the same distance, on or in a non-magnetic sheet, the TEM inductances of the two waveguides are equal, or $L_1 = L_2$. Thus, the capacitances per unit length of the guides must be equal, or $C_1 = C_2$, for approximate TEM-mode equivalence. This implies that the two slot antennas, one on the dielectric sheet in Figure 6.8(b), and the other in a symmetric dielectric sandwich illustrated in Figure 6.8(c), are approximately equivalent.

Using the extended CES theory of Popović and Nešić [142], the system in Figure 6.8(c) is transformed into its complementary/dual structure illustrated in Figure 6.9(a). This is a coplanar-strip (CPS) transmission line in a symmetric sandwich of magnetic material with a value of its relative permeability μ_r equal to the relative permittivity ϵ_r of the CPW dielectric. Finally, the CPS line is transformed into a equivalent two-wire parallel transmission line with conductors of circular cross-section and with coaxial magnetic cover following the theory of equivalent radius [135]. Assuming that the magnetic

materials in the two equivalent structures have the same permeability, the radius of the wire conductors in Figure 6.9(b) is given by

$$a = \frac{W_a}{4}, \quad (6.2)$$

and the outer radius of the coaxial magnetic cover is

$$b = \frac{W_a}{4} \exp \left\{ \frac{1}{\epsilon_r - 1} \left[\frac{\pi}{4\epsilon_o} C_1 - \ln \frac{4d}{W_a} \right] \right\}. \quad (6.3)$$

In Eqs. (6.2–6.3) W_a and ϵ_r are the width and relative permittivity of the original slot antenna, respectively, and C_1 and d are the capacitance per unit length and distance between the slots for the CPW structure in Figure 6.8(b).

The capacitance per unit length C_1 of the CPW structure is given by [118]

$$C_1 = 4\epsilon_o \left[\frac{K(k)}{K(k')} + \frac{\epsilon_r - 1}{2} \frac{K(k_1)}{K(k'_1)} \right] \quad (6.4)$$

where $K(k)$ is the complete elliptic integral of the first kind, and is well approximated by formulae developed by Hilberg [119]. The moduli k and k_1 appearing in Eq. (6.4) are

$$k = \frac{s}{s + 2W_a}, \quad (6.5)$$

$$k_1 = \frac{\sinh \left(\frac{\pi s}{4h} \right)}{\sinh \left(\pi \frac{s + 2W_a}{4h} \right)} \quad (6.6)$$

while the complementary moduli are $k' = \sqrt{1 - k^2}$ and $k'_1 = \sqrt{1 - k_1^2}$. In terms of distance $d = s + W_a$, the modulus k may be expressed as

$$k = \frac{d/W_a - 1}{d/W_a + 1}. \quad (6.7)$$

Since $s \gg W_s$ and $s \gg h$, the expression for k_1 may be approximated as

$$k_1 \approx \frac{\exp \left(\frac{\pi s}{4h} \right)}{\exp \left[\pi \left(\frac{s + 2W_a}{4h} \right) \right]} = \exp \left(-\frac{\pi W_a}{2h} \right). \quad (6.8)$$

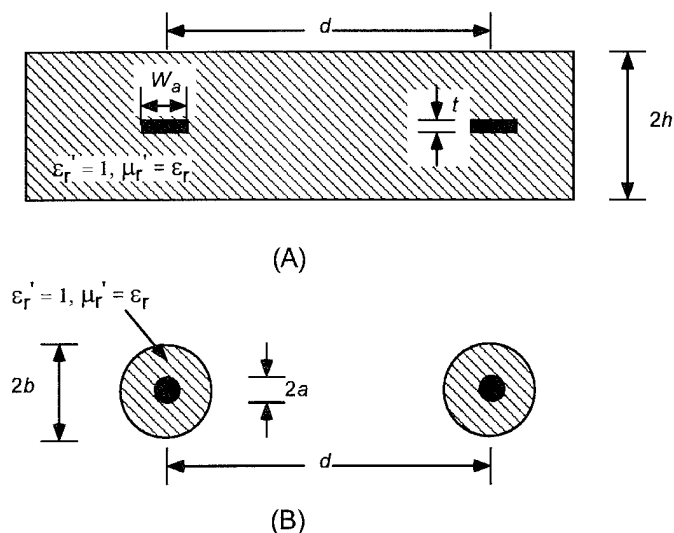


Figure 6.9. The complementary/dual structure of the structure in the sandwich CPW line in (a). A pair of conductors with cylindrical cross-section and coaxial magnetic cover having the equivalent antenna cross-section is shown in (b).

Now we are free to choose the ratio d/W_a which appears in Eqs. (6.3) and (6.7). According to Popović, the ratio d/W_a should be larger than 10 and less than 100, with a value of 40 being reasonable [134]. This approximation is used in our slot simulations.

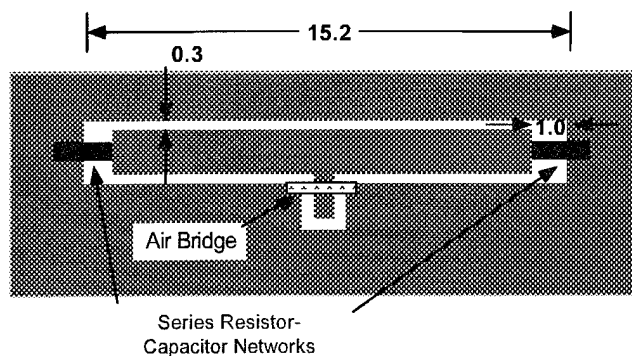
In the case of electrically thin dielectric substrates, the antenna radiation pattern is determined almost entirely by the current distribution on the antenna conductors. Therefore, the equivalent slot antennas in Figure 6.8(b) and (c) have practically the same radiation patterns. Therefore, the final antenna structure (dipole in Figure 6.9(b)) also has very nearly the same radiation pattern, only complementary, as the original slot antenna in Figure 6.8(a). According to Eq. (6.1), the impedance of the original slot antenna may be determined once the impedance of the approximately complementary/dual dipole of Figure 6.9(b) is computed. This cylindrical dipole of circular cross-section with magnetic cover is analyzed using the CAD program *WireZeus* [134], in which

Hallen's equation is extended to model the influence of the magnetic cover as a distributed inductance. The feed is approximated by a δ -function generator, and Hallen's equation is solved by approximating the current distribution along the antenna by a complex polynomial.

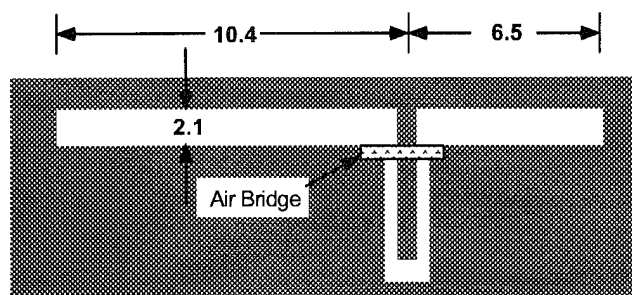
6.4.4 Results

The theory outlined above was used to design two slot antennas for use in the low noise lens amplifier array. The input antenna is a center-fed folded slot loaded with a series-connected $51\text{-}\Omega$ resistor and 10-pF capacitor at each of its ends. The series parasitic inductance of the resistor and capacitor are additive, so a total series inductance of 1.2 nH was added in the simulation model. The folded slot is designed to have a $20\text{-}\Omega$ impedance at the second resonance. This impedance was chosen so that a single series-line match could provide an optimum noise match to the first-stage PHEMT amplifier used in the lens, which is $\Gamma_{opt} = 0.66e^{j148^\circ}$. The output antenna is an asymmetrically-fed slot, designed to have a $100\text{-}\Omega$ impedance at the second resonance. Both slots are defined in a $17\text{-}\mu\text{m}$ thick copper sheet on one side of a non-magnetic dielectric with relative permittivity $\epsilon_r = 2.17$ and dielectric height $h = 0.787\text{ mm}$. The slots are fed with CPW that has a characteristic impedance of $100\text{ }\Omega$, and the design frequency is 10 GHz . These antennas are illustrated in Figure 6.10 with the final dimensions determined from the *WireZeus* simulations.

The final dimension of the folded slot, designed using the procedure outlined above, is illustrated in Figure 6.10(a). The folded slot layout is very compact, with a length of $0.50\lambda_o$ and a width of only $0.077\lambda_o$. The folded slot simulation is compared to the measured data using the Smith chart in Figure 6.11. The simulation data includes the 15° , $100\text{-}\Omega$ series line match required to



(A) Input Folded Slot Antenna



(B) Output Anti-Resonant Slot Antenna

Figure 6.10. The slot antennas designed and simulated using the procedure outlined in the text: (a) Folded slot with lumped series capacitor-resistor loading on its ends; (b) Off-center-fed slot. Both slots are designed to be operated at their second resonance to maximize their bandwidth.

provide an optimum noise match to the first-stage PHEMT amplifier. Without this series line, the simulation indicates a 2:1 VSWR bandwidth of 15% where $Z_o = 20 \Omega$. The measured results were obtained on an HP8510B automatic network analyzer using a 100- Ω through-reflect-line (TRL) calibration for the CPW medium. The reference plane for the measurement was set to match the location of the input port to the first-stage PHEMT amplifier – in other words, the 15° line length used in the input series-line match was added to the input reference plane of the antenna. The input impedance of the measured antenna was higher than predicted in the simulations, but the phase match is relatively good at 10 GHz, and the model predicts the general change in

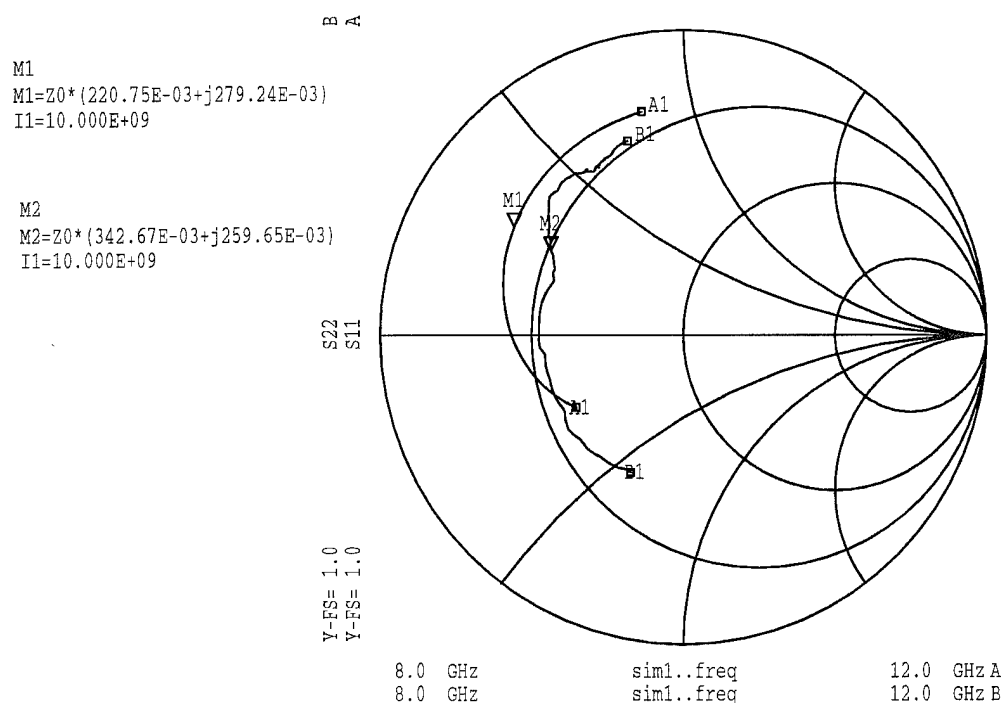


Figure 6.11. Folded slot return loss comparison between simulation (trace a) and measurement (trace b). Both traces include the single series-line match for optimum noise match to the first stage of the low noise amplifier used in the low noise lens amplifier array.

impedance with frequency fairly well. The E - and H -plane patterns are shown in Figure 6.12, exhibiting the bi-directionality of the slot. The antenna plane is oriented along the $90^\circ - 270^\circ$ axis of the plot, angle 0° represents the broadside angle on the air-side of the slot, and 180° represents the broadside angle on the dielectric side. The E - and H -plane patterns are about 1-2 dB higher in magnitude on the dielectric side than on the air side, indicating preferential radiation into the dielectric. The E -plane pattern shows unintended maximum at about $\pm 45^\circ$ from the dielectric broadside direction, and a null of about 5 dB is present at the air-side broadside angle, which will reduce the on-axis gain of the amplifier array. The H -plane pattern clearly shows a significant broadside

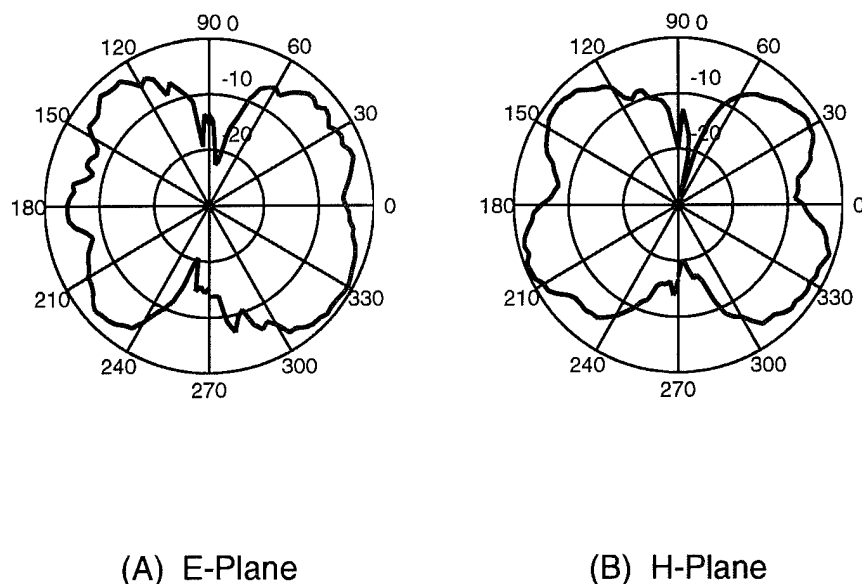


Figure 6.12. Radiation patterns of the center-fed folded slot at 10 GHz in the (a) *E*-plane and (b) *H*-plane.

null of at least 5 dB, and peaks at about $\pm 30^\circ$ from the broadside. The voltage distribution of the folded slot operated at its second resonance indicate that the peak radiation will be away from broadside and symmetrical. A way to achieve the desired voltage distribution for a pattern peak at broadside and operate the slot at its second resonance is to feed it at an off-center location.

The off-center-fed slot antenna is illustrated in Figure 6.10(b) with the dimensions derived from the design procedure above. Its length is $0.57\lambda_0$ and its width is only $0.067\lambda_0$. The off-center feed position is one variable used to tailor the input impedance of the slot to the desired value of $100\ \Omega$, with the other option being the slot width for a given substrate dielectric and metallization. The slot is simulated and compared to its measured data in Figure 6.13,

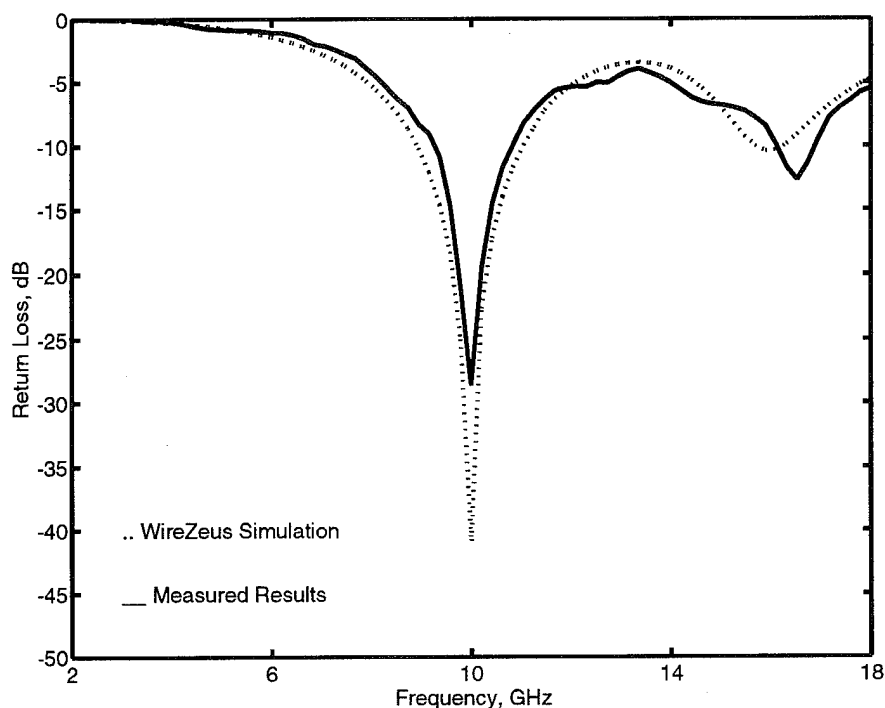


Figure 6.13. Return loss of the $100\text{-}\Omega$ anti-resonant slot used in the low noise amplifier array. Measured results (solid line) and simulated data (dashed line) show excellent agreement. The 2:1 VSWR bandwidth is 18%.

showing excellent prediction of the actual antenna. The measured 2:1 VSWR bandwidth is 18% with a center frequency of 10.0 GHz. The measured resonant impedance is $107\text{ }\Omega$, a deviation of +7% from design, which may be attributed to the measured slot width being slightly wider than design specification. The slot radiation pattern is shown in Figure 6.14, where the angle definitions are the same as for the folded slot patterns above. The improved directionality of this slot is due to the voltage distribution along the slot being maximum at the slot center. The pattern maximum at broadside in both radiation planes makes this element ideal for array applications.

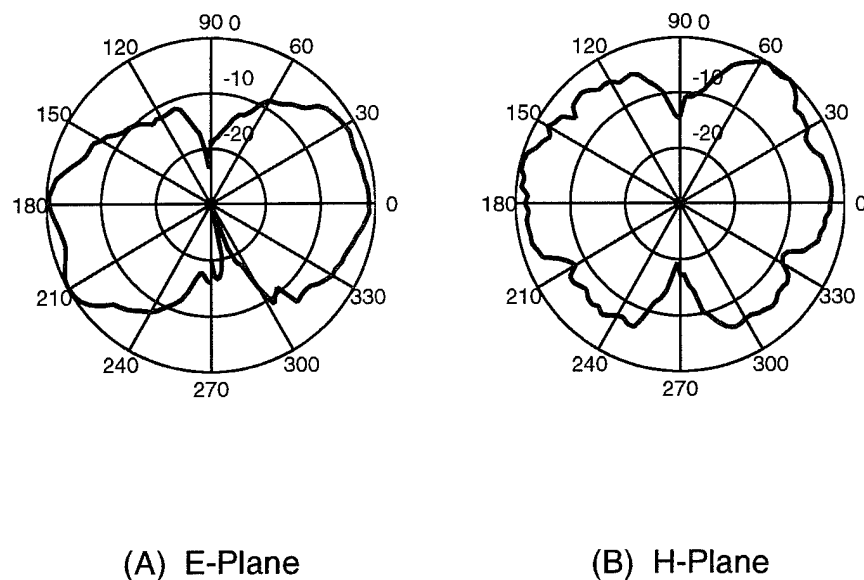


Figure 6.14. Radiation patterns of the off-center-fed slot at 10 GHz in the (a) *E*-plane and (b) *H*-plane.

6.5 Conclusion

The CPW-fed slot antennas operated at their second resonance provide a wide bandwidth radiator for uniplanar quasi-optical power-combining arrays. The element is compact in both length and width for high density inter-element spacing, and the resonant impedance is convenient for the amplifier circuitry of the lens amplifiers without needing impedance transformers. These antenna elements enabled us to develop a wide band lens amplifier array, which is presented in the next chapter.

CHAPTER 7

LOW NOISE CONSTRAINED LENS AMPLIFIER

7.1 Motivation

In Chapter 5, the results of two lens amplifier arrays optimized for gain were presented. The single-stage PHEMT amplifiers in these lenses are capable of $G_{active} = 9.5$ dB at 9.7 GHz. The bandwidth of the lens arrays are only 3% of center frequency because printed microstrip patch antennas are used on an electrically thin substrate. It was shown in Chapter 3 that the bandwidth of the delay network used in constrained lenses is much wider than that of the microstrip patch radiators. In Chapter 6, a broad-bandwidth slot antenna was developed that is compatible with a coplanar waveguide (CPW) feed. Thus a broader bandwidth lens array can be produced using slots.

In addition, we want to explore the use of the lens as a receiver so that an active receive array may be included in a quasi-optical communication system. As such, an amplifier matched for noise is designed. Also, higher gain for each amplifier cell is necessary to improve the receiver performance and also increase the overall insertion gain of the lens amplifier. Also, for a given signal to noise (SNR) criterion, a 1-dB reduction in the amplifier noise figure allows a 20% reduction in the array size.

Before discussing the specific design and results, it is instructive to develop the method used to measure the noise figure. First, the equations governing the analysis the noise added by a free-space amplifier are developed.

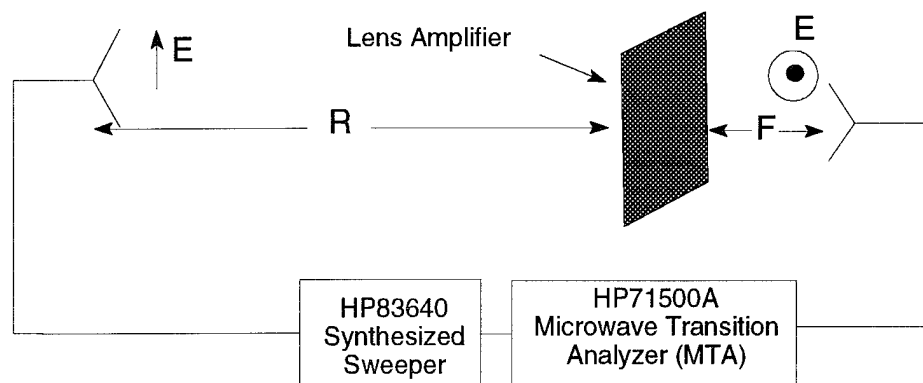


Figure 7.1. Noise figure measurement setup for evaluating the low noise lens amplifier.

Then a description of the experimental procedure for measuring the noise figure in free-space is given. Then, a single amplifier cell is measured and compared to its theoretical added noise. Finally, the results of the free-space noise figure and associated gain of a 24-element, two-stage per element low noise lens amplifier array will be presented.

7.2 Theory of Noise Added by a Linear Amplifier

Since it was our intention to develop a low-noise array for receive applications, the means of evaluating the noise performance of such an array in free-space had to be developed. Important issues include identifying and modeling the sources of noise in a free-space system, and determining the reference planes at which the input and output “ports” of the quasi-optical lens array amplifier are placed. Figure 7.1 illustrates the placement of a quasi-optical lens array amplifier when it is used as a receive array. The input

face of the lens is a periodically-spaced array of elements used to receive a plane wave from a source at a range R the far field. Each element receives a portion of the power incident upon its area and couples it to the input of the low noise amplifier. The amplifiers are designed to have identical gain G and the amplified signal from each amplifier is routed through a delay line to its output element, which re-radiates the signal for free-space power combining. The delay lines of each amplifier cell phase the output elements such that the output array focuses the combined signal at the focal length F , where a horn with gain profile $G_R(\theta, \phi)$ collects the combined power. Various sources of noise must be taken into account in this free-space system to accurately assess the noise contributed by the amplifier array. The sources of noise which we accounted are included in the following list, and a description of each source follows:

- (1) Far-field sources entering the input of the amplifier array, such as background noise and the noise standards used to determine the noise figure.
- (2) Background noise bypassing the amplifier array and going directly to the collection horn.
- (3) Equivalent noise temperature due to losses in the feed.
- (4) Noise generated by the amplifier array itself, which is the quantity of interest.

7.2.1 Noise Received from the Far Field

The noise entering the receive side of the array amplifier from background noise with brightness temperature $B(\theta, \phi)$ contributes to the antenna

noise temperature T_A through the relation

$$T_A = \int_{4\pi} B(\theta, \phi) G_A(\theta, \phi) d\Omega. \quad (7.1)$$

If the amplifier array is evaluated in an ideal anechoic chamber, the antenna noise temperature due to the background will be equal to the ambient room temperature T_o . A feed horn placed in the far-field is used to inject added noise T_S for evaluating the noise generated by the amplifier array itself. The resulting total antenna temperature can be obtained as

$$\begin{aligned} T_A &= \int_{4\pi - \text{horn}} B(\theta, \phi) G_A(\theta, \phi) d\Omega + T_S L_R \\ &\cong T_o(1 - L_R) + T_S L_R \end{aligned} \quad (7.2)$$

where L_R is the free-space loss factor over the range R ,

$$L_R = \left(\frac{\lambda}{4\pi R} \right)^2 G_H G_A \quad (7.3)$$

between the noise-standard horn with gain G_H and the input to the array amplifier, with gain G_A . Eq. (7.2) suggests that the added noise temperature injected by the feed horn needs to be sufficiently high so that it overcomes the free-space path loss.

The method used to evaluate the added noise T_e of the amplifier is the hot-cold or Y -factor test, where the noise standard temperature T_S is periodically switched from a high temperature T_{hot} to a lower temperature T_{cold} . The noise figure measurement determines the ratio

$$Y = \frac{T_{hot} + T_e}{T_{cold} + T_e} \quad (7.4)$$

so that the noise temperature added by the amplifier is determined from Y in Eq. (7.4) as

$$T_e = \frac{T_{hot} - YT_{cold}}{Y - 1}. \quad (7.5)$$

The susceptibility of the measured effective noise temperature to error may be expressed as

$$\Delta T_e = \frac{1}{Y-1} \Delta T_{hot} - \frac{Y}{Y-1} \Delta T_{cold} - \frac{T_{cold} + T_e}{Y-1} \Delta Y \quad (7.6)$$

assuming that the noise standard impedance (presented to the device under test or DUT) does not change between hot and cold states, which is assured in our free-space measurements. The accuracy of the measurement is completely dominated by the uncertainty in the non-ambient standard temperature T_{hot} . This uncertainty is reduced if the value of $Y \gg 1$, so T_{hot} needs to be significantly larger than that of T_{cold} and T_e . The free-space measurement compounds the difficulty to minimize uncertainty because of the path loss between the noise standard and the input to the amplifier, which must be in its far-field. From Eq. (7.2), it is seen that the background noise dominates the antenna noise temperature T_A when the noise standard is at ambient temperature T_o , or $T_A \approx T_o$. In order to make an accurate measurement, the value of $T_A \gg T_o$ when the noise standard is at its non-ambient value T_{hot} . The required value of T_{hot} in terms of the experimental setup is

$$\frac{T_{hot}}{T_o} \gg \frac{1}{G_H G_A} \left(\frac{4\pi R}{\lambda} \right)^2 \quad (7.7)$$

In our experimental measurements, we set $R = 1.2$ m, $\lambda \approx 0.03$ m, $G_H = 15$ dB, and the estimate of G_A from antenna pattern measurements is 20 dB. This yields a required ratio of $\frac{T_{hot}}{T_o} \gg 18.5$ dB. The effective noise ratio (ENR) is used to specify T_{hot} in relation to T_{cold} through the relation

$$ENR \text{ (dB)} = 10 \log_{10} \left(\frac{T_{hot} - T_{cold}}{T_{cold}} \right) = 10 \log_{10} \left(\frac{T_{hot}}{T_o} - 1 \right). \quad (7.8)$$

The noise standard, a Noise Com 3208A, is specified to have an ENR of 29 dB across X-band, or $\frac{T_{hot}}{T_o} = 29.0$ dB. Therefore, our noise standard temperature

is sufficiently high in its non-ambient state to provide a reasonable value of Y that reduces error due to uncertainty in the standard noise temperature at the input to the array in free-space.

The noise power contribution at the collection horn due to the noise at the array input, modelled by the antenna temperature T_A , is

$$N_A = kBT_A G_{AMP} L_F \quad (7.9)$$

where k is Boltzman's constant, B is the spectrum over which the noise power is analyzed, G_{AMP} is the relationship between the total RF power output to the total power input at the output and input array surfaces, respectively, and L_F is the free-space path loss over the focal length F between the output of the array and the collection horn, given as

$$L_F = \left(\frac{\lambda}{4\pi F} \right)^2 G_R G_A \quad (7.10)$$

where G_R is the gain of the collection horn.

7.2.2 Background Noise Bypassing the Array

The background noise arriving directly at the collection horn, thereby bypassing the array, along with noise generated from losses in the collection horn, may be modelled like the noise from an attenuator at some physical temperature. The attenuator losses are the free-space loss L_F over the range F . The attenuator temperature is some mean value of the physical temperatures of the horn, the output array, and the background. If we assume that all of these temperatures are equal to the ambient temperature of the anechoic chamber T_o , then the noise power due to the background noise bypassing the array and arriving at the collection horn is

$$N_F = kBT_o (1 - L_F). \quad (7.11)$$

7.2.3 Noise Contributed by the Amplifiers

The noise-equivalent temperature of the entire amplifier array at its output, T_{AMP} , or that for each amplifier T_i , is the desired quantity to be determined. The value of T_i includes the noise generated by the active device and any losses in the amplifier circuitry. The noise power delivered at the output of each amplifier circuit will be

$$N_i = kBT_i G_{\text{active}_i} \quad (7.12)$$

where G_{active_i} is the overall gain of the i^{th} amplifier circuit, taking any losses of the circuit into account. An overall noise temperature of the entire amplifier array at its output, T_{AMP} , may be defined from the total noise power at the grid amplifier output that is collected by the collection horn. Noise contribution to the collection horn from each individual amplifier will add as independent sources, since the noise generated in one transistor amplifier is uncorrelated from that in any other amplifier. The total noise power contributed by the amplifier array and detected at the collection horn is

$$N_{AMP} = kBT_{AMP} G_{AMP} L_F = kB \sum_{i=1}^N T_i G_{\text{active}_i} \frac{\lambda^2 G_{\text{Ei}}(\theta_i, \phi_i) G_R(\theta_i, \phi_i)}{[4\pi f(\theta_i, \phi_i)]^2} \quad (7.13)$$

where $G_{\text{Ei}}(\theta_i, \phi_i)$ and $G_R(\theta_i, \phi_i)$ are the gains of the i^{th} output element and collection horn, respectively, at the angle (θ_i, ϕ_i) , and $f(\theta_i, \phi_i)$ is the range between them. For the relatively long F/D ratio chosen for the lens array, the angles (θ_i, ϕ_i) are limited to a range where the angular change in the element and horn gains is negligible. If the individual transistor amplifiers have the same gain and same noise temperature, then the overall noise temperature of the array will be the same, assuming $G_{AMP} = N \cdot G_{\text{active}}$.

7.2.4 Noise Measurement Procedure

The total noise power received by the collection horn is the sum of the individual noise sources, which include the noise standard and background noise sources amplified by the array, the background noise that bypasses the amplifier array, and the noise generated by the amplifier circuitry within the array. The expression for the total power received is

$$N_R = N_A + N_F + N_{AMP}, \quad (7.14)$$

or in terms of the noise temperatures of the various sources and loss factors from the equations above, the noise temperature at the collection horn from the reference point of the array position is

$$T_R = T_A G_{AMP} L_F + T_o (1 - L_F) + T_{AMP} G_{AMP} L_F, \quad (7.15)$$

or in a form that shows the reference point of the noise standard, all of the system losses become apparent by

$$T_R = T_{AMP} G_{AMP} L_F + T_S G_{AMP} L_R L_F + T_o \{1 - L_F [1 - G_{AMP} (1 - L_R)]\}. \quad (7.16)$$

Eq. (7.16) is a variation of the equation presented by Rutledge [37] to determine the noise figure of an HBT grid amplifier in free-space. The received noise temperature is dominated by the first two terms when the amplifier gain is high. If the amplifier gain is insufficient, the third term becomes dominant, which represents the background noise contributions. Thus, to measure the quantity desired, T_{AMP} , and to detect the noise standard temperature, T_S , we require the amplifier to have high gain. If the gain is insufficient, as it is for the evaluation of a single cell, then the range between the amplifier and the horns must be decreased to confidently measurement the desired noise contributions.

This can be achieved by using horns with smaller apertures so that the far field condition is satisfied at shorter ranges.

A free-space measurement technique is used to evaluate the noise and gain of the unit cell. A Noise Com 3208A noise source with an effective noise ratio (ENR) of 29 dB, a HP8593E Spectrum Analyzer and a 38-dB preamplifier can provide a Y -factor measurement in free-space. The measurement procedure for evaluating the noise contributed by a single unit cell free-space amplifier is shown in Figure 7.2. First, the noise source is calibrated in a coaxial setup. Then a horn antenna is connected to the noise diode output port and an identical horn is connected to the preamplifier input port as illustrated in Figure 7.2(a). Circulators are connected at the horn ports to prevent unwanted reflections from affecting the noise measurements. Each horn is placed a distance $r_1 = r_2$ away from a passive unit cell. The passive unit cell contains the input and output elements used in the active unit cell, but with a matched CPW line replacing the active circuitry. Illuminating and collection horns are identical and are polarization-matched to their respective passive-cell elements. The noise meter determines the entire path loss present between the two horns, with the resulting total equally attributed to the input-side and output-side losses in this symmetrical system. The loss of this symmetrical system is equally divided between input and output sides of the passive cell and is used to calibrated out free-space losses L_R and L_R , reflective losses from the input and output surfaces, and background sources for the HP8593E spectrum analyzer. This calibration places the reference plane of the noise diode at the transverse plane of the passive cell. Factoring in the losses effectively transfers the standard noise source temperature T_S from its feed horn to the

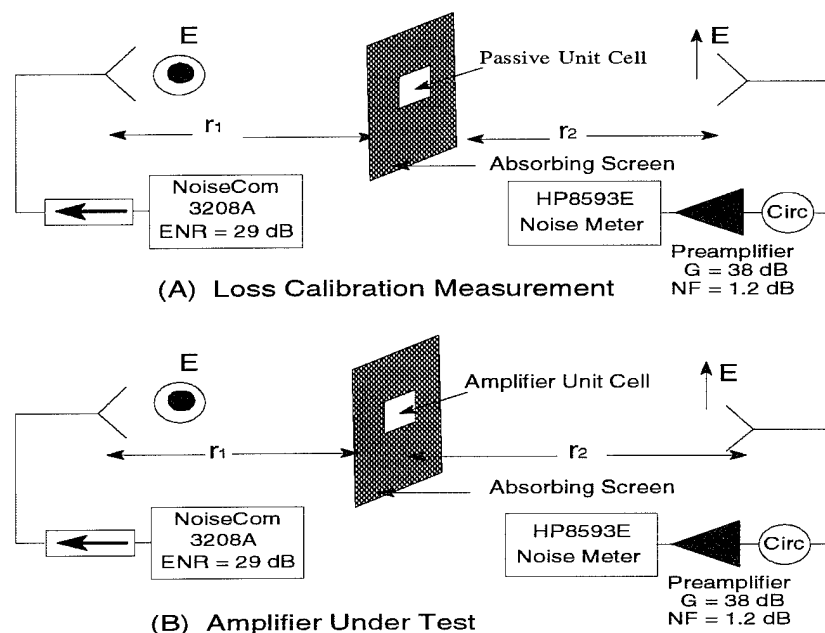


Figure 7.2. Experimental procedure for determining the noise figure of an amplifier unit cell in free space. The calibration measurement in (a) sets the reference plane of the noise standard to the plane of the DUT with a passive unit cell. In (b), the passive unit cell is replaced with the active device to determine the noise added by it.

unit cell's input surface. Likewise, the plane of reference for the collection horn is transferred up to the output surface of the unit cell. With this calibration complete, the passive unit cell is carefully replaced by the active cell, which is positioned at the calibrated reference plane and polarization matched to the horns as illustrated in Figure 7.2(b). This calibration method takes background noise, losses in the horns, and the gain of the input and output elements into account and is used to evaluate the noise figure of an amplifier unit cell used in the array, as shown in the next section.

The calibration and measurement scheme for the entire lens array is illustrated in Figure 7.3. First, the path losses L_F and L_R are each determined

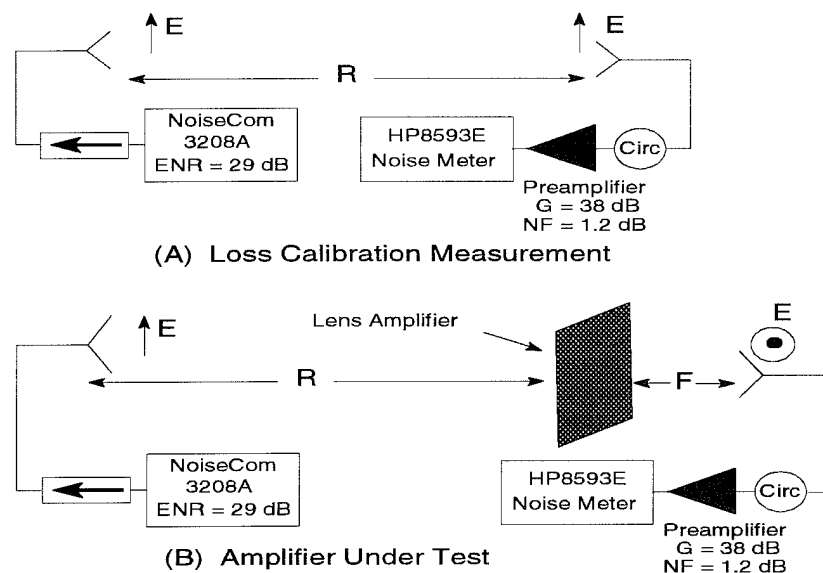


Figure 7.3. Measurement scheme for determining the noise figure of the lens amplifier array. In (a), the path losses L_R and L_F are each determined to define the reference plane up for the array. In (b), the feed horn is rotated for polarization match to the array.

using the free-space calibration measurement between the illumination and collection horns as shown in Figure 7.3(a). The loss factor at the output is then adjusted by the known value of the absolute power gain of the lens amplifier, which is performed through a free-space measurement using the microwave transition analyzer as reported below. The calibration sets the reference plane of the noise standard to the transverse plane containing the input surface of the array. The active array is then placed at the reference plane, and the feed horn is rotated for polarization match to the array input, as illustrated in Figure 7.3(b). This procedure is used to evaluate the noise figure and associated gain of the low-noise lens array amplifier in the next section.

7.3 Slot-Slot Low Noise Lens Amplifier

The lens presented in Chapter 5 was designed for maximum gain. A two-stage coplanar-waveguide (CPW) low-noise amplifier was designed to receive a plane wave and focus it down to a focal point at which a mixer can be placed. The topology of a single cell of the low-noise amplifier is shown in Figure 7.4(a) and its schematic is shown in (b). This two-stage amplifier is

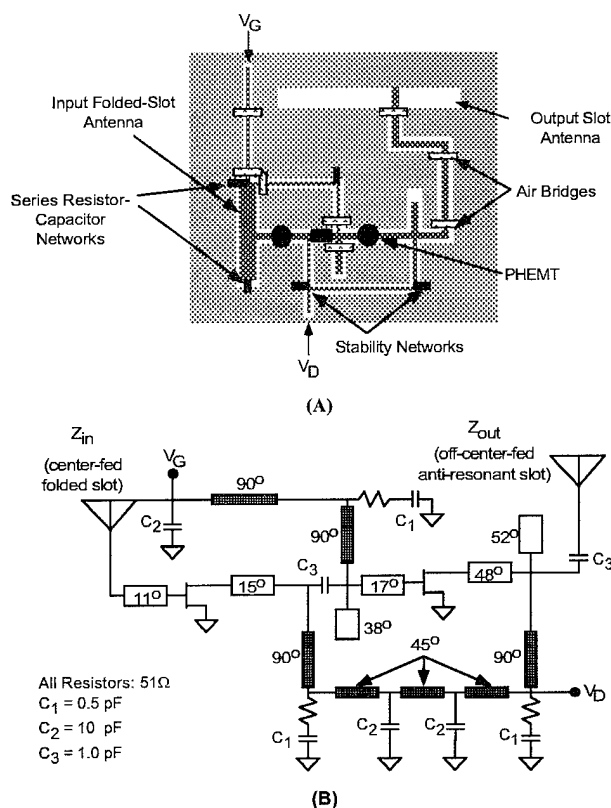


Figure 7.4. A single cell of an X-band slot-slot CPW-based low-noise amplifier array with two-stage low noise amplifier. The topology of the cell is shown in (a), and the circuit schematic is shown in (b).

biased with one drain bias and one gate bias line to simplify its application to an array. Before making a free-space unit cell, the amplifier design was evaluated in a CPW test fixture on an HP 8510B automatic network analyzer (ANA). The amplifier is stable and its measured s -parameters are shown in Figure 7.5

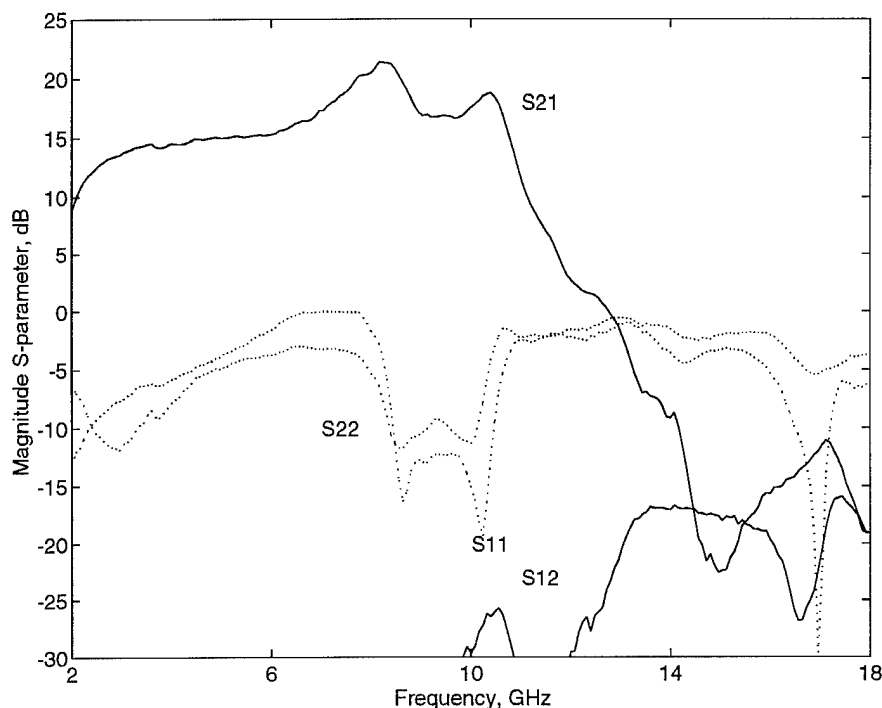


Figure 7.5. Measured s -parameters of the two-stage CPW LNA design for the lens array. The peak gain is over 20 dB and the input and output return losses are better than -10 dB over a 1 GHz bandwidth centered at 10 GHz.

with drain-source voltage $V_{DS} = 1.5$ V and total drain current $I_{DS} = 30$ mA. The Avantek ATF-35376 PHEMT is selected for the low-noise design because of its outstanding noise performance (for a packaged device) and low cost. It exhibits a $NF_{opt} = 0.83$ dB and a noise resistance $R_n = 7 \Omega$ at 10 GHz. The manufacturer's optimum noise match is transformed to a $100\text{-}\Omega$ system, resulting in $\Gamma_{opt} = 0.66 \cdot e^{j148^\circ}$. A single-line input match, employed for its small size and broad bandwidth, requires the input antenna resonant impedance to be either 20Ω or 500Ω for optimum noise match. A center-fed folded-slot antenna is designed to provide an impedance of 20Ω at its second resonance at 10 GHz. This folded slot is CPW-fed and loaded with a series-connected

10-pF capacitor and $51\text{-}\Omega$ resistor at each end (length-wise) of the folded slot. The lumped load enables the folded slots to act as part of the stabilization and biasing network. The folded slot has a 15 % 2:1 VSWR bandwidth. The output antenna is an anti-resonant off-center fed slot with an input impedance of $100\text{ }\Omega$ and a 25 % bandwidth at the 10-GHz second resonance. These slots are fully described in Chapter 6. The amplifier was fabricated on a $\epsilon_r = 2.17$, 0.79-mm thick teflon substrate.

After performing the calibration using the passive unit cell procedure outlined above, the active unit cell is placed at the reference plane, and its noise and gain contribution are evaluated, as shown in Figure 7.6. The free-space

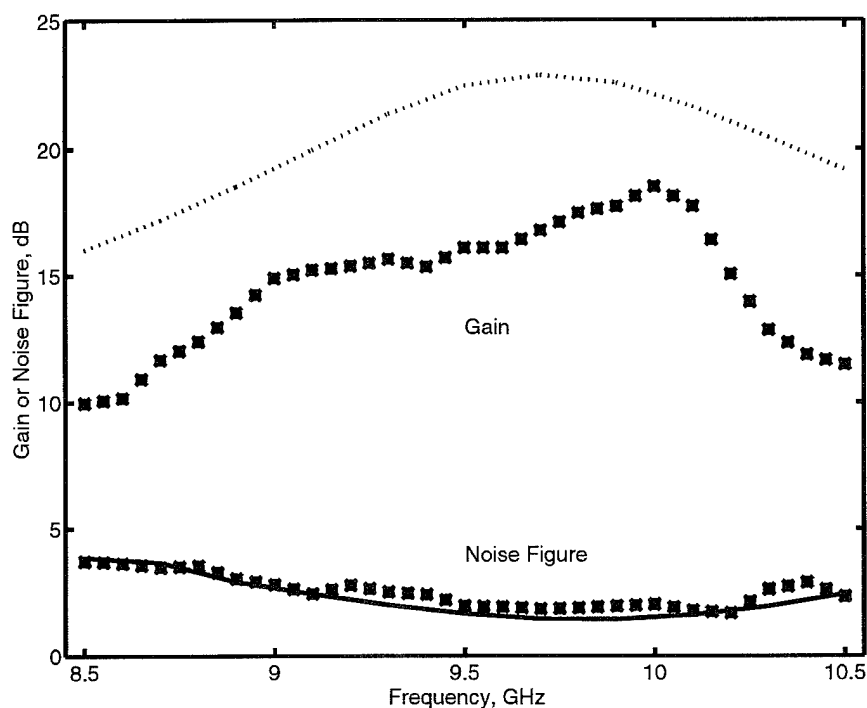


Figure 7.6. Measured noise figure and associated gain (symbols) of a single cell of the low noise amplifier array. Simulated noise and gain performance (lines) using the antenna impedances at input and output ports show excellent prediction of the noise figure and predicts the trend in the gain.

measurements show that the unit-cell two-stage amplifier has a noise figure of 2.0 dB at 10.0 GHz with an associated gain of 18.5 dB. The minimum noise figure is 1.7 dB at 10.2 GHz with an associated gain of 15.1 dB. The noise and gain were simulated using Hewlett-Packard's Microwave Design System (MDS) with the aforementioned noise model data. The frequency-dependent impedances presented by the folded slot and the anti-resonant slot are used as the input and output port impedances, respectively, in the MDS noise modeling. The noise figure simulation shows excellent agreement with the measurement. The gain simulation averages 4 dB higher than measurement, but the measured gain is similar to that observed in ANA-coaxial environment results shown in Figure 7.5 above.

Figure 7.7 shows a 24-element two-dimensional CPW lens array using the 2-stage low-noise amplifier cell. The lens diameter is $6 \lambda_o$, the focal length is 20 cm, and $F/D = 1.2$. Triangular inter-element spacing increases the range of scan without generating grating lobes. The input array of folded slots has a uniform inter-element spacing of $0.9 \lambda_o$. The output anti-resonant slots are connected to delay lines and placed in such a way that the array focuses down to a point and the power is collected by a horn antenna. Inter-element spacing would be significantly reduced using a higher permittivity substrate and monolithic fabrication. Table 7.1 is a list of the element positions and delay line lengths used in the fabrication of this lens. We used a physical line length of $W_o = 22$ mm to enable connection of all element pairs in the array while satisfying delay line and element positioning requirements of the constrained lens design equations.

Figure 7.8 shows the absolute power gain and frequency response of

Table 7.1. Element and delay line data for the 24-element two-dimensional CPW LNA lens amplifier array

element (m, n)	r (x, y -mm)	ρ (x, y -mm)	W (deg)	Length (mm)
-3,-2	-33.75, -54.00	-34.90, -55.84	0.0	$W_o + 0.00$
-1,-2	-11.25, -54.00	-11.53, -55.36	26.5	$W_o + 1.67$
+1,-2	+11.25, -54.00	+11.53, -55.36	26.5	$W_o + 1.67$
+3,-2	+33.75, -54.00	+34.90, -55.84	0.0	$W_o + 0.0$
-4,-1	-45.00, -27.00	-46.03, -27.62	34.0	$W_o + 2.14$
-2,-1	-22.50, -27.00	-22.73, -27.27	72.2	$W_o + 4.55$
0,-1	0.00, -27.00	0.00, -27.16	84.7	$W_o + 5.33$
+2,-1	+22.50, -27.00	+22.73, -27.27	72.2	$W_o + 4.55$
+4,-1	+45.00, -27.00	+46.03, -27.62	34.0	$W_o + 2.14$
-5,0	-56.25, 0.00	-57.73, 0.00	23.4	$W_o + 1.47$
-3,0	-33.75, 0.00	-34.06, 0.00	74.6	$W_o + 4.70$
-1,0	-11.25, 0.00	-11.26, 0.00	99.3	$W_o + 6.25$
+1,0	+11.25, 0.00	+11.26, 0.00	99.3	$W_o + 6.25$
+3,0	+33.75, 0.00	+34.06, 0.00	74.6	$W_o + 4.70$
+5,0	+56.25, 0.00	+57.73, 0.00	23.4	$W_o + 1.47$
-4,+1	-45.00, +27.00	-46.03, +27.62	34.0	$W_o + 2.14$
-2,+1	-22.50, +27.00	-22.73, +27.27	72.2	$W_o + 4.55$
0,+1	0.00, +27.00	0.00, +27.16	84.7	$W_o + 5.33$
+2,+1	+22.50, +27.00	+22.73, +27.27	72.2	$W_o + 4.55$
+4,+1	+45.00, +27.00	+46.03, +27.62	34.0	$W_o + 2.14$
-3,+2	-33.75, +54.00	-34.90, +55.84	0.0	$W_o + 0.0$
-1,+2	-11.25, +54.00	-11.53, +55.36	26.5	$W_o + 1.67$
+1,+2	11.25, +54.00	+11.53, +55.36	26.5	$W_o + 1.67$
+3,+2	+33.75, +54.00	+34.90, +55.84	0.0	$W_o + 0.0$

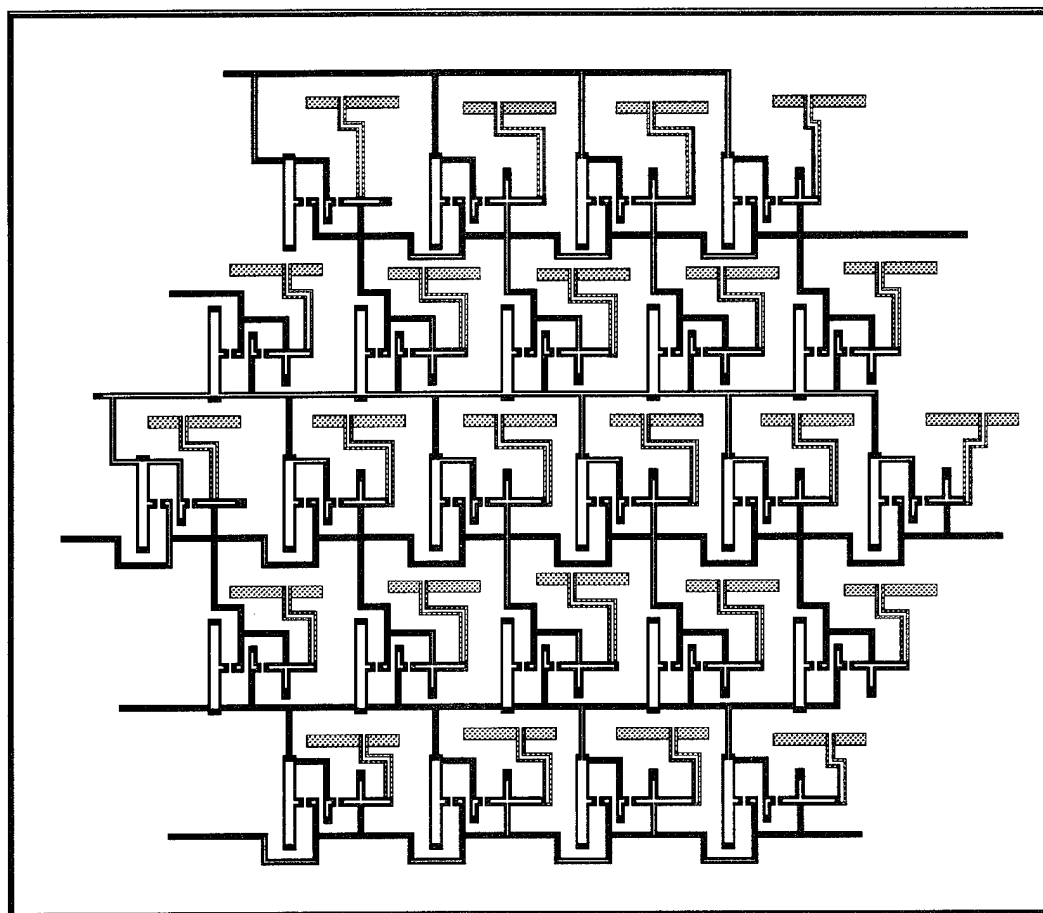


Figure 7.7. A 24-element two-dimensional CPW low noise amplifier lens array. The lens diameter is $6 \lambda_o$, the focal length is 20 cm, and the $F/D = 1.2$. The black lines represent the gaps in CPW, metal is shown in white, and the shaded lines are the output slot elements and CPW delay lines.

the lens with all 24 elements biased on (solid line) and biased off (dotted line). The array demonstrates a peak absolute power gain of 13 dB at 10 GHz and a 3-dB bandwidth of 1.1 GHz over which the absolute power gain is above 10 dB. The on/off ratio is over 30 dB over the bandwidth. These measurements were made with a total drain bias current of 450 mA and drain-source bias voltage of 1.5 V. A free-space noise figure measurement was performed on the array using the procedure outlined above. Minimum noise figure was achieved with a total drain bias current of 330 mA and 1.5 V drain-source bias voltage.

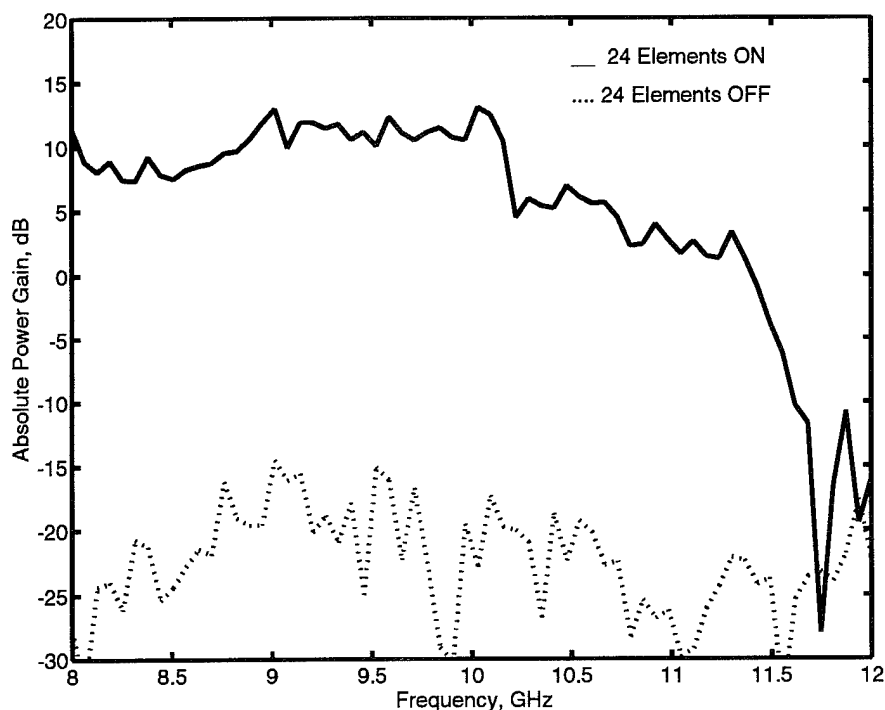


Figure 7.8. Measured absolute power gain as a function of frequency for the low noise amplifier lens array with all 24 elements biased on (solid line) and biased off (dotted line). The on/off ratio is 30 dB over the 1.1 GHz 3-dB bandwidth, where the peak absolute power gain is 13 dB at 10 GHz.

The noise figure and associated gain results are shown in Figure 7.9, showing a minimum noise figure of 1.7 dB at 9.80 GHz and an average noise figure of 2.3 dB across the 11% 3-dB bandwidth. The noise figure of the array is very similar in its frequency response and value to that of the single cell shown in Figure 7.6 above. Therefore, the individual amplifier cells making up the array are producing approximately the same gain and noise temperature, and the lens is focused at the design focal distance.

A measurement of the E - and H -plane patterns of the array was performed with the receive horn placed at broadside. Figure 7.10 shows that

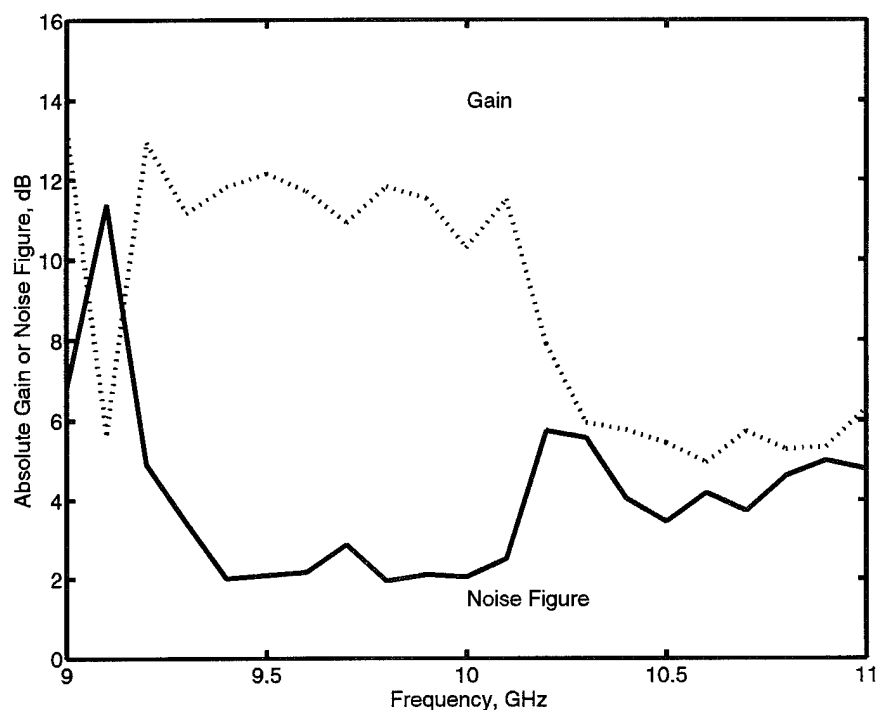


Figure 7.9. Measured gain and noise figure of the 24-element CPW LNA with folded slot input and off-center-fed output slot, both operated at their second resonance for a broad bandwidth.

the resulting measured patterns have relatively high side lobe levels, especially for the H -plane pattern. The high H -plane side lobe level can be explained by considering the H -plane radiation pattern of the folded slot, which is the receiving element, as shown in Chapter 6. The folded slot's H -plane pattern is somewhat asymmetrical, has a 5-dB null at broadside and peaks at about $\pm 30^\circ$. When the element pattern is multiplied by the theoretical array factor, the plots in Figure 7.11 results, showing a maximum side lobe level of -10 dB in the pattern (solid line). The theoretical array factor is shown as the dash-dot line in the figure, illustrating that the side lobes at $\pm 30^\circ$ are elevated by 10 dB due to the folded slot pattern. The asymmetry in the element pattern causes the main

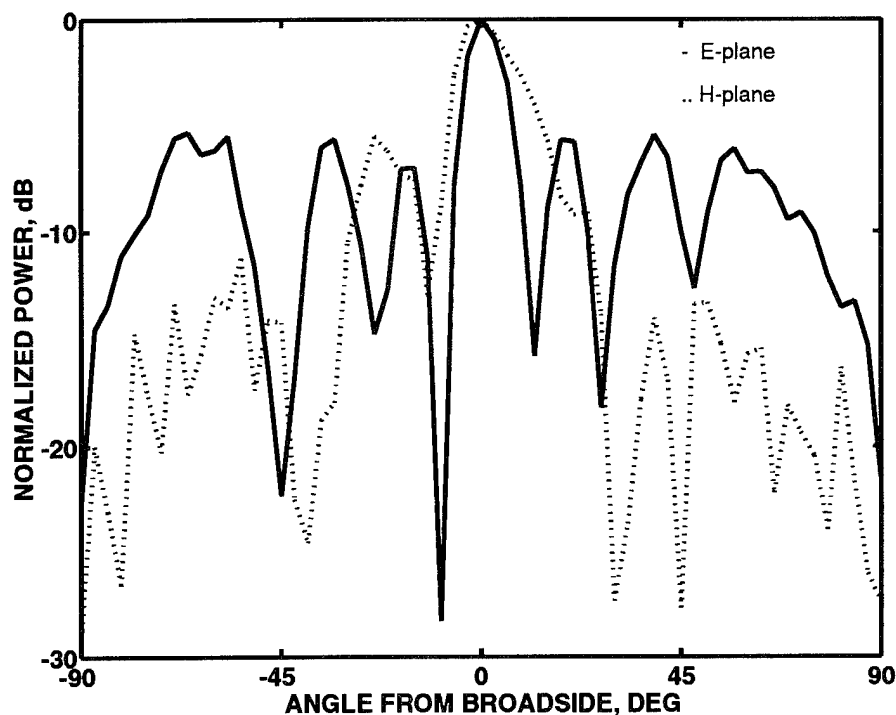


Figure 7.10. Measured radiation patterns for the *E*-plane (solid line) and *H*-plane (dotted line) of the 24-element low noise lens amplifier array with collection horn at broadside.

lobe to be steered by about $+3^\circ$. To provide a more symmetrical array pattern in future array developments using folded slots, one may choose to operate in the fundamental-resonance mode or use an off-center feed if operating in the second-resonance mode. If the fundamental-resonance mode is chosen, the bandwidth will be limited to a few percent. The off-center feed, used with the output slots in this array, allows the element to be operated in the second-resonance mode with little degradation in the antenna pattern.

7.4 Conclusion

A free-space technique for determining the noise figure and associated gain of quasi-optical amplifiers was developed. The free-space measured noise

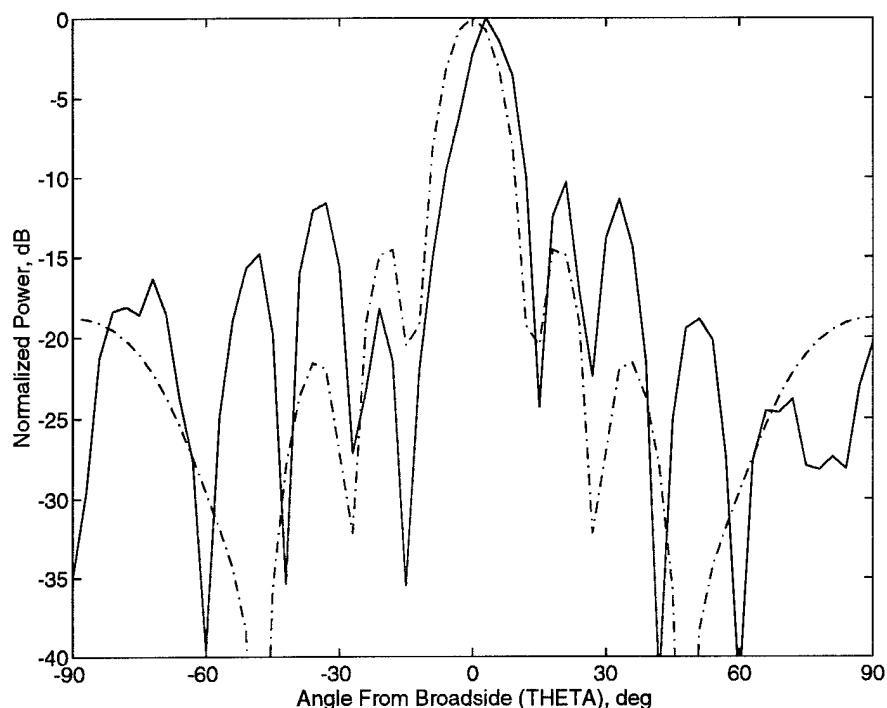


Figure 7.11. The theoretical H -plane array factor multiplied by measured folded slot pattern (solid line) compared to the theoretical array factor (dash-dot lines).

figure of a single amplifier cell is very well predicted by computer simulation. The free-space measured associated gain is very similar to that measured in a coaxial environment on an automatic network analyzer. Therefore, we are confident that the free-space technique yields accurate results. The measured noise figure of the 24-element array shows results very similar to those of the single unit cell, showing that the noise generated in each of the unit cell amplifiers is uncorrelated to each other, and that relatively good uniformity exists among unit cell amplifiers in terms of gain and noise temperature. Thus, the noise figure of a quasi-optical lens amplifier array does not increase as the number of elements increases for uniform gain and noise temperature among the

unit cell amplifiers, and since the gain increases with the number of elements, an improved SNR may be realized. *Since each unit cell amplifier handles only a fraction of the entire signal power at the array input surface, the dynamic range of a receiver is improved by using quasi-optical power combining in a receiver array.* For example, the dynamic range increases by $10\log(10)^2 = 20$ dB for a 100-element array.

CHAPTER 8

QUASI-OPTICAL MILLIMETER-WAVE AMPLIFIER ARRAYS

8.1 Motivation

The antenna array amplifier in Chapter 2, and the lens amplifier arrays in Chapters 5 and 7 have been demonstrated as quasi-optical power combiners in the *X*-band, where simple printed-circuit fabrication techniques and packaged devices may be used for low-cost proof-of-concept development. The goal of our research is to extend these quasi-optical techniques to the millimeter-wave range, where individual solid-state devices generate low power (20 dBm range), and where traditional microwave power combining techniques are no longer practical due to higher circuit losses and smaller physical dimensions. The need for high power millimeter-wave sources may be satisfied with quasi-optical power-combining techniques. The millimeter-wave QOPCs demonstrated in this chapter employ either hybrid or monolithic techniques.

Frequencies around 35 GHz are important for munitions guidance and fusing. Frequencies around 60 GHz are important for certain communications applications because these frequencies are heavily absorbed by oxygen, so the signals cannot propagate very far in the atmosphere. This makes *V*-band ideal for inter-satellite communications whereby the satellites are shielded from interference with ground communication, and also for networks of short-haul wireless local area networks (LANs), where wide bandwidths and boundaries of cells are attainable. Frequencies around 77 GHz have been proposed for

automotive collision avoidance radar. Frequencies around 94 GHz are used for imaging through fog and smoke. These applications will require reliable, high power solid-state sources for generating sufficient power for their respective purposes.

8.2 Slot-Slot Ka-Band Hybrid Array

8.2.1 Introduction

We advised and assisted engineers at the Lockheed-Martin Corporation in the design of a high-power hybrid Ka-band quasi-optical amplifier. The amplifier unit cell consists of a driver amplifier chip followed by a two-stage high power amplifier chip. Input as well as output antennas are anti-resonant slots fabricated on a GaAs chip. A 6×6 array was designed for an output power in excess of 8 Watts. The array allows a variety of amplifier chips to populate any number of cells up to the full array size. A 3×3 subarray achieved a small-signal absolute power gain of 6 dB at 29.0 GHz with 10 % power-added efficiency and a saturated output power of 1 watt. A liquid-cooled test fixture was designed to remove excess heat from the amplifiers.

8.2.2 Amplifier Design

The design goal is to develop a high power quasi-optical Ka-band hybrid amplifier. The amplifier consists of two MMIC chips mounted on a GaAs monolithic antenna array. GaAs is chosen as the antenna array substrate to address issues related to high power amplifier design of a monolithic high power amplifier which will be fabricated in the future. The hybrid amplifier is a uniformly-spaced square 6×6 array. Each of the unit cells is designed for an output power level of 300 mW, small signal gain of 16 dB, and 10%

power-added efficiency.

The unit cell contains a first stage driver amplifier MMIC followed by a two-stage high-power amplifier MMIC, as illustrated in Figure 8.1. The driver consists of a self-biased single-stage power MESFET amplifier that produces 100 mW output power with 6 dB small-signal gain, 4.5 dB large-signal gain and 11.8 % power-added efficiency at a bias point of $V_{DS} = 5$ V and 140 mA drain current. The high power MMIC amplifier chip consists of four combined 400 μm power MESFETs which produce 400 mW output power with 12 dB small-signal gain, 6 dB of large-signal gain, and 11.8% power-added efficiency at a bias point of $V_{DS} = 5$ V and 500 mA total drain current. The 1-dB bandwidth of each MMIC amplifier in the cascade is 5 GHz, centered at 32.5 GHz. The chips were individually probed before being mounted onto the hybrid antenna array to assure their small-signal performance.

Each unit cell has a pair on center-fed anti-resonant slot antennas. The input and output slots are orthogonally polarized, which facilitates free-space measurements and is necessary for amplifier stability. The anti-resonant slots operate in the second resonant mode and offers broader bandwidth and a convenient input impedance compared to resonant slots. The slot dimensions (4220 x 471 μm) are designed to provide a 25- Ω impedance on the 100 μm -thick GaAs substrate at 33 GHz. The slot length is shorter than a half-wave free-space wavelength which is convenient for array design, and are designed using the procedure outlined in Chapter 6. The slot antennas are matched to the 50- Ω amplifier port impedances with quarter-wave transformers. Low-loss CPW-to-microstrip transitions are used at the interface between the CPW-antenna feeds and the microstrip MMICs. Additional hybrid decoupling capacitors are

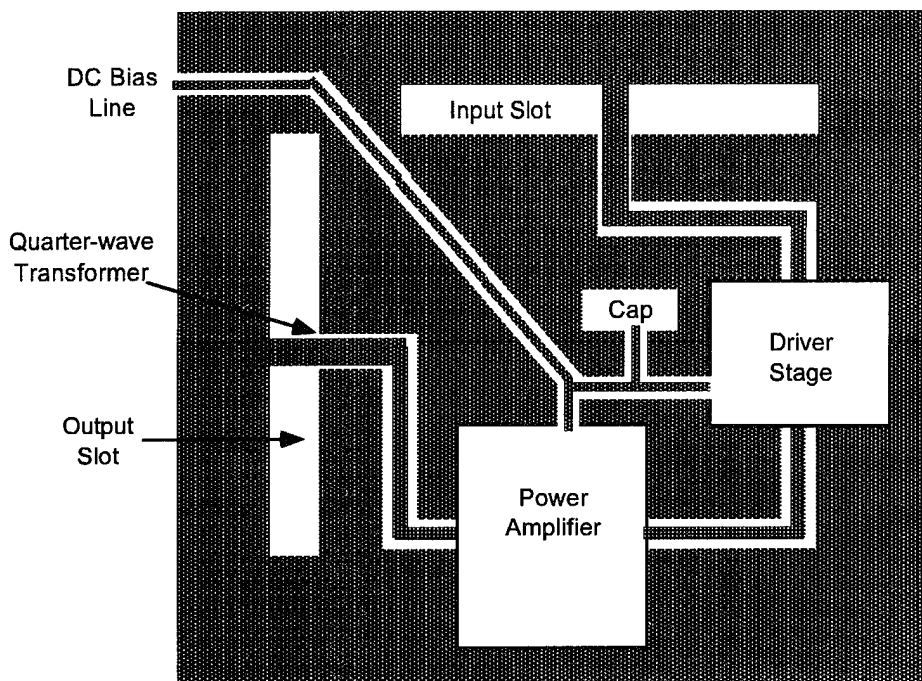


Figure 8.1. Layout of the amplifier unit cell for the V-Band amplifier. Hybrid fabrication with MMIC driver and power amplifier chips is used.

added along the bias lines for stability.

The hybrid array's substrate is a 3.8-cm square GaAs chip. The substrate is thinned to $100\ \mu\text{m}$ which is substantially less than 90 electrical degrees at 30 GHz and therefore is unlikely to support substrate modes. The thin substrate also allows better heat transfer from the amplifier chips to the backside of the substrate, which may be cooled. Input and output polarizers are used to reduce input feed loss and increase transmitted output power. In the array, the gate and drain bias lines are laid out in a square mesh with air bridges at the intersections. The biasing voltage is applied at both ends of each bias line in order to equalize bias conditions across the array.

8.2.3 Measurement and Results

A test fixture capable of removing up to 33 Watts of power dissipated from the array amplifier was designed. Fluorinert FC-43 was chosen as the coolant liquid since it has a low loss tangent of 0.0036 and a reasonable dielectric constant of 1.90 (measured at 8.5 GHz). The liquid directly cools the backside of the array and flows through a plastic channel which covers the entire backside of the array and is 540 electrical degrees thick at 33 GHz. The plastic and the liquid coolant have the same permittivity of 1.9 and represent a second dielectric layer to the transmitted amplified wave. Since the heat generated by the transistors has to propagate through 200 μm of GaAs before it reaches the cooled backside of the substrate, the transistors are 64°C higher in temperature than the coolant. The material of the GaAs chip carrier is Thermcon, which has the same thermal coefficient of expansion as GaAs.

Free-space array measurements were made with a scalar network analyzer with round corrugated waveguide horns. The horns produce a Gaussian transverse-field profile that focus 63% of the power on a 2.5 cm spot size midway between the horns (the power density at the spot edge is $1/e^2$ lower than at the center). Passive array measurements were conducted before the MMIC amplifiers were mounted with no coolant present. The passive array had a peak in its transmission frequency response at 34.5 GHz with a 10% bandwidth. The insertion loss of the passive array is 10 dB. Simulated CPW line loss within the unit cell contributes 1 dB of the loss, indicating that there is 4.5 dB of loss on both the input and output sides of the array.

A 3×3 subarray was populated with the MMIC amplifiers, and the substrate was mounded on the cooling structure. Small-signal measurements

yielded the transmission frequency response of the subarray. The peak absolute power gain was 6 dB, measured at 29.0 GHz, and the 3-dB bandwidth is 440 MHz, or 1.5% of center frequency. The measured frequency is shifted towards lower frequencies as compared to the passive array because the antenna frequency response is changed when it is dielectrically loaded by the cooling liquid. The measured 6 dB agrees well with the expected gain when the aforementioned losses are taken into account and the expected MMIC amplifier small-signal gain is 16 dB. After thirty minutes of continuous operation, the array cleaved and the crack opened a bias line to one of the rows of the subarray. Subsequent measurements were performed on the remaining 2×3 subarray.

Large signal measurements were performed with a TWT amplifier connected to the feed horn and a power meter connected at the output horn. Cooling fluid could no longer be used with the cleaved array, requiring minimum testing times. A power output of 1 Watt was measured with -2 dB absolute power gain. The drop in power gain is due to reduced MMIC gain under saturation, elevated heat levels and the reduced array size. The saturation curve of the 2×3 array demonstrates similar behavior to the lens amplifier array saturation curve in Chapter 5. The center elements of the array saturate first with increased feed power since they receive more of the Gaussian beam power. Therefore, the saturation curve shows two distinct gain slopes as the array feed power is increased. One slope indicates that the center elements saturate (at the lower feed power) and the second when the edge elements saturate at the higher feed power.

8.2.4 Conclusion

This project represents the first quasi-optical millimeter-wave amplifier [144]. The hybrid amplifier is built on a GaAs substrate with CPW passive lines and anti-resonant slot antennas, and microstrip MMIC amplifiers. An absolute power small-signal gain of 6 dB and a saturated output power of 1 Watt were measured at 29 GHz. This amplifier represents the highest power Ka-Band quasi-optical amplifier that has been reported to date.

8.3 Patch-Slot 60-GHz Monolithic Array

An example of a different amplifier with slot antennas on the transmit side of the substrate, and microstrip amplifiers and patch antennas on the receive side, is shown in Figure 8.2. The enhancement-mode PHEMT amplifier is a single-stage design matched for gain with single stubs. Using the manufacture-provided linear equivalent circuit values in a hybrid- π model, the equivalent s -parameters of the 100- μm gate-periphery PHEMT was generated for the amplifier design. The common-source amplifier was designed on MDS and expected to provide 7.1 dB gain at a center frequency of 60 GHz with a 15% 3-dB bandwidth into 75- Ω port impedances. The amplifier is designed and simulated to be unconditionally stable above 100 MHz. Stability is achieved with high-impedance meandered-line bias gate and drain bias lines. Each bias line has alternating 1-pF and 5-pF shunt capacitors, each with 30 pH parasitic inductance, for RF bypass to ground. The gate-bias network consists of a 90° high-impedance line and series 25- Ω resistor connected to parallel network of a 90° low-impedance open stub and a series-connected 150- Ω resistor and 100-fF capacitor to ground. The resistors provide loss out-of-band to stabilize the amplifier. The open-stub enforces an RF short where it connects to the gate

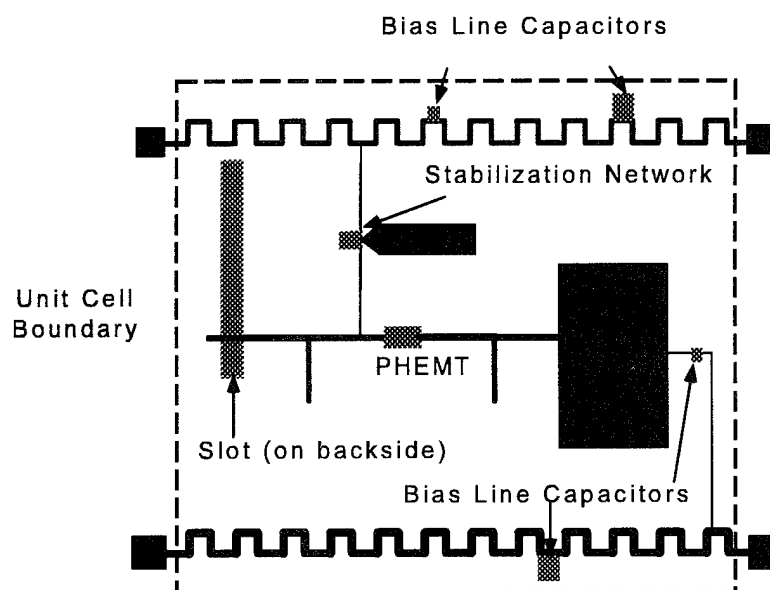


Figure 8.2. A single cell of a V-Band patch-slot amplifier array. The microstrip patch is the receiving antenna, and the microstrip-coupled resonant slot is the transmitting antenna. Meandered bias lines with capacitors prevent low-frequency oscillations.

bias line, thereby minimizing circuit losses in-band. Each amplifier is coupled into free-space by a non-radiating-edge-fed microstrip patch on the circuit-side of the array chip, and a microstrip-coupled off-center-fed resonant slot on the chip's backside. The elements are orthogonally polarized for isolation stability. The resonant impedance of each element is $75\ \Omega$ at 60 GHz with a bandwidth of 1%. The resonant slot measures $1000\ \mu\text{m} \times 25\ \mu\text{m}$ and is fed $75\ \mu\text{m}$ from one end. The open-end of the slots' microstrip feed presents shunt capacitive reactance at the slot feed point, which is resonated by an equal amount of inductive reactance at 60 GHz. The patch was designed using multi-port network analysis and measures $687\ \mu\text{m}$ along its resonant length and $400\ \mu\text{m}$ along the radiating edges. The $22.8\ \mu\text{m}$ -wide $75\text{-}\Omega$ microstrip feedline is located $270\ \mu\text{m}$ away from one of the radiating edges. Each amplifier unit cell in the array measures $\lambda_o/2$ on a side.

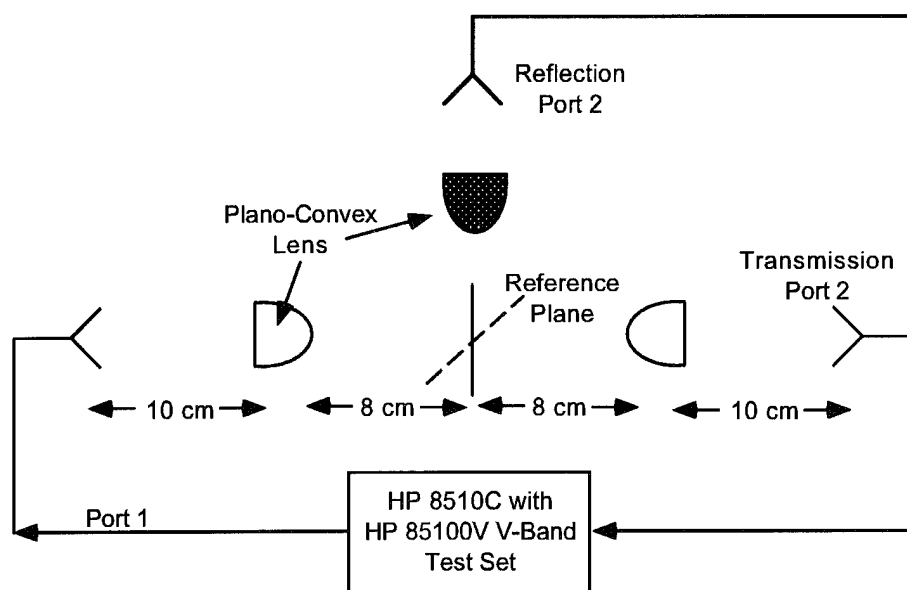


Figure 8.3. Free-space measurement system for evaluating the array at the reference plane (solid line) for return loss and transmission, or as a reflection amplifier (dashed ref plane and shaded lens).

Lockheed-Martin Research Labs (Baltimore) fabricated 16- and 36-PHEMT square-lattice monolithic arrays on 100- μm GaAs. Unfortunately, they inadvertently reversed gate and drain terminals for the PHEMTs, resulting in bias resistor connection to the output circuit and a non-ideal match. This reduced the simulated gain from 7.1 dB to 5.8 dB, but unconditional stability was maintained. A 36-element array chip measuring 1.5 cm on a side was DC-bias tested and found to have all amplifiers functional, or a 100% DC yield. We tested the array as a free-space amplifier using an HP 8510C with an HP85100V V-band source module, as shown in Figure 8.3. The array may be evaluated in transmission as well as reflection for gain or return loss measurements. The lenses are broadband, plano-convex dielectric lenses with a focal length of about 8 cm. The optical system is confocal and provides a beam waist sufficiently large to illuminate the array. The illuminating and receiving horns

have 23.3 dB nominal gain, and are placed 10 cm away from the flat surface of the lenses. Transmission and reflection measurements are taken with the array biased at $V_{DS} = 4$ V and 180 mA total drain current in the biased-on state, and zero bias current in the biased-off state.

8.3.1 Return Loss Measurement

With the lenses and horns configured for a transmission measurement as illustrated above, the return loss of the input surface (array of microstrip patches) was performed to confirm power coupling between the incident field and the array amplifiers. First a metal plate was placed at the reference plane and a reflection measurement was made to calibrate the system for free-space path loss and losses associated with the dielectric lens. The array was then placed at the reference plane and the reflected power was compared to that of the metal plate. As shown in Figure 8.4, the return loss is -10 dB in the biased-on state and -12 dB in the biased-off state. This small difference between on and off states is expected since the PHEMT's gate-source impedance does not change much over the gate bias range we use. The response is narrow-banded due to the highly-resonant nature of the microstrip patches. The measurement is plagued by etalon effects due to longitudinal-cavity-mode reflections between the device under test, the lenses, and the horns. The etalon effect results in the ripple which varies with device position, so care must be exercised in placing the array exactly at the reference plane. This measurement indicates that a significant portion of the incident power is absorbed by the input array of elements at the design frequency of 60 GHz.

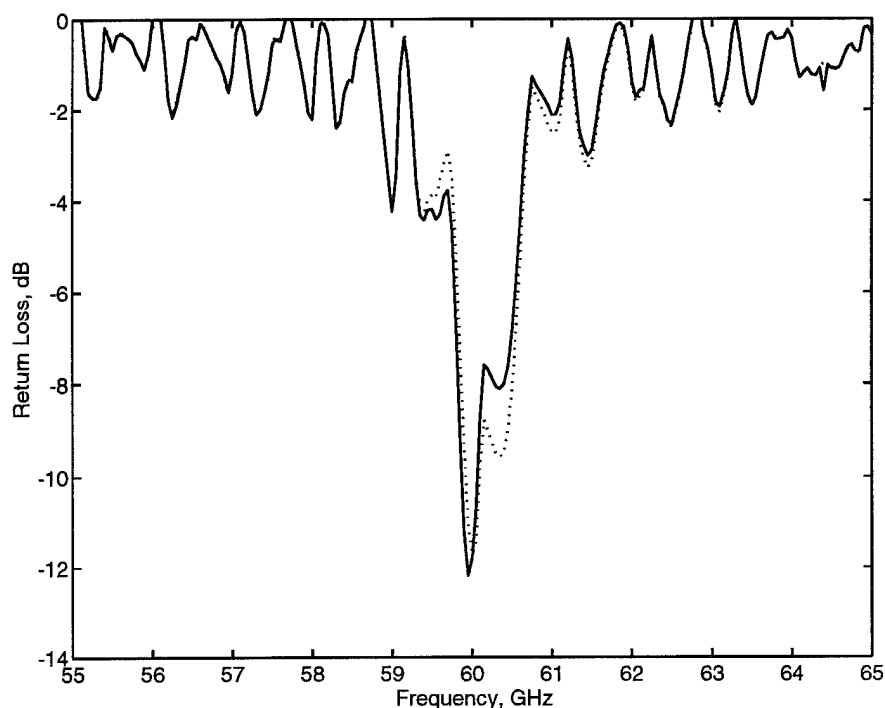


Figure 8.4. Measured input return loss of the V-Band array in the biased-on (solid line) and biased-off (dotted line) states.

8.3.2 Transmission Gain Measurement

With the lenses and horns configured for a transmission measurement as illustrated above, a transmission-through measurement was performed to determine the frequency response, gain, and on/off ratio of the array amplifier. First a power measurement, swept in frequency, was performed between input and output horns with an open aperture with the same physical area as the array placed at the beam waist between the dielectric lenses. This measurement was made to calibrate the system for free-space path loss and losses associated with the dielectric lens. The open aperture also allowed us to confirm the fact that the spot size illuminated the entire aperture. Then the amplifier was placed at the beam waist in place of the open aperture, and the output horn was

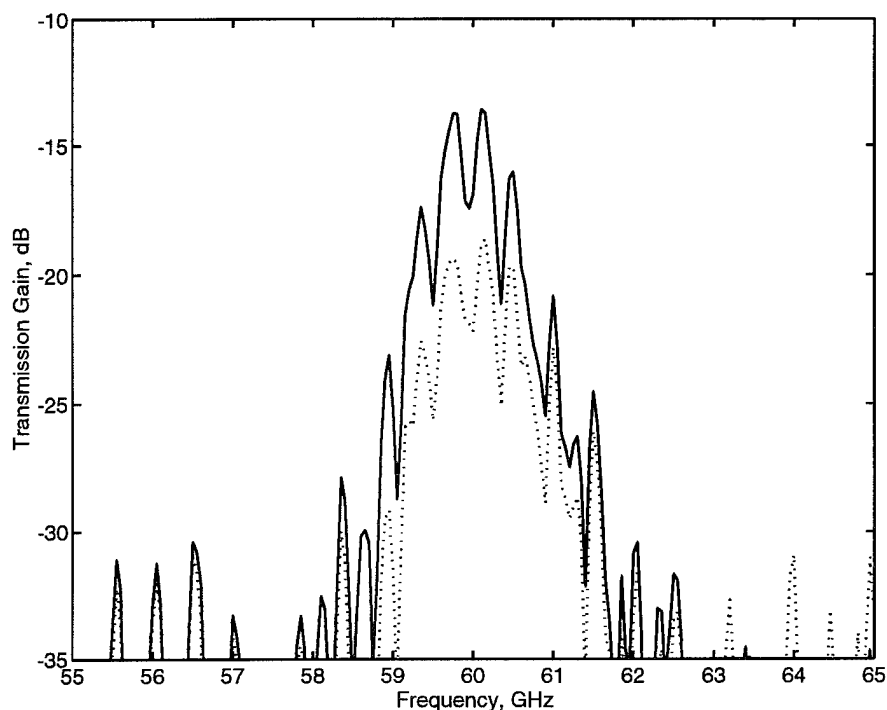


Figure 8.5. Measured transmission-through gain results of the V-Band amplifier array in the biased-on (solid line) and biased-off (dotted line) conditions.

rotated 90° so that it would be polarization-matched to the output slot array. The measured through power in the array's biased-on and biased-off conditions was compared to the calibration through power, as shown in Figure 8.5. The amplifier array was stable, and an on/off ratio of 5 dB at 60 GHz, and this ratio was positive between 58.0 and 62.1 GHz. The 3-dB bandwidth was 1.4 %. The array does not exhibit real power gain, but acts instead as an attenuator, with a peak response of -13.5 dB with respect to the through calibration. This poor performance is due to several factors. The single stage amplifier has low gain, made worse by the reversed gate and drain terminals. The output slots are not well matched to free space, and its output radiation is preferentially directed into the substrate. The slot and patch frequency responses are both

narrow banded, and it is possible that the frequency range over which they are simultaneously matched to the amplifier is narrow or non-existent.

8.3.3 Reflection-Gain Measurement

Next, we evaluated the array as a reflection amplifier by switching the measurement apparatus as shown in Figure 8.3 above. The reflection-amplifier mode of operation is possible due to the bi-directionality of the slot antennas, which radiate preferentially in the direction of the reflection-mode. The array is illuminated at a 45° angle, which is not ideal in terms of array gain, but was the only angle practical with the given measurement apparatus. The calibration was made with polarization-matched horns with a metal plate placed at the plane of reference. Then the array was inserted and the output horn rotated for polarization match, and the array was biased. The resulting reflection-mode power, when compared to the calibration, is shown in Figure 8.6. The etalon effects are much reduced in this mode since experimental setup no longer resembles a cavity, so reflected power is not returned to the feed horn. In this mode, the array amplifier produced an on/off ratio of 4 dB and this ratio was positive between 58.1 GHz and 60.8 GHz. While this is a lower ratio and a smaller bandwidth than the transmission-through mode, the measured absolute power gain in the reflection mode is 2 dB higher. Therefore, the reflection amplifier mode is a viable means of producing power in a quasi-optical amplifier array.

8.3.4 Conclusion

The 60 GHz amplifier is the first fully-monolithic quasi-optical amplifier array operational at V-band. The array is stable and provides an on/off

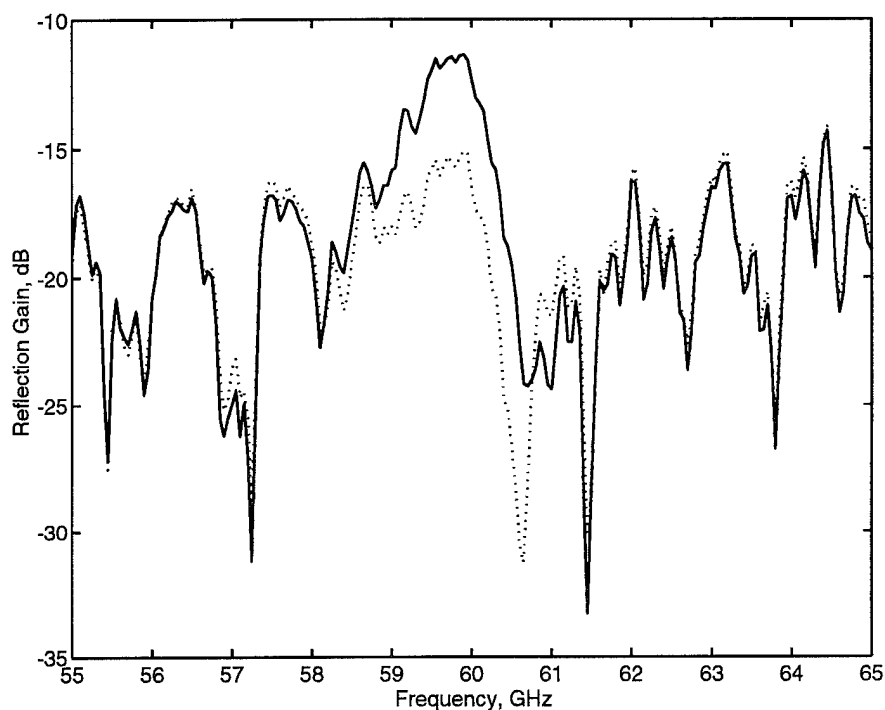


Figure 8.6. Measured reflection-mode frequency response for the V-band amplifier array in the biased-on (solid line) and biased-off (dotted line) states.

ratio of 4-5 dB despite reversed gate and drain terminals. The input array of patches is found to be resonant at the design frequency, and the output array of slots radiate preferentially in the direction of the substrate, as determined by the reflection amplification mode results. This amplifier represents the highest-frequency monolithic quasi-optical amplifier.

CHAPTER 9

CONCLUSION AND FUTURE WORK

A variety of quasi-optical array amplifiers are presented. Combinations of slot and patch antenna elements are used for the input and output arrays. Single- and two-stage microstrip or CPW amplifiers were integrated with the antennas. A feeding technique with on-substrate focusing has enabled absolute power gain in quasi-optical amplifier arrays. Specifically, the following experiments were performed to demonstrate concepts fundamental to quasi-optical array power combining. A two-level power-combining PHEMT patch-antenna lens amplifier with 8 dB of absolute power gain at 9.7 GHz is used for beamforming and beam-switching. An *X*-band low-noise CPW PHEMT amplifier array using anti-resonant slot antennas demonstrates over 10 dB absolute power gain and an average noise figure of 2.3 dB across a 3-dB bandwidth of 1.1 GHz. A saturated class-A polarization-preserving 24-MESFET patch array produces 0.7 Watts at 10 GHz with 21 % power-added efficiency. A *Ka*-Band hybrid amplifier array using anti-resonant slots demonstrated a 6-dB small signal gain and a maximum output power of 1 watt under saturation. A *V*-Band patch-slot amplifier array is used in transmission and reflection modes and found to have an on/off ratio of about 5 dB across a 2-GHz bandwidth. The *Ka*- and *V*-band arrays did not employ constrained lensing on the substrate, but did use external dielectric lenses in their evaluation. The high bandwidth possible at the millimeter wavelengths represents

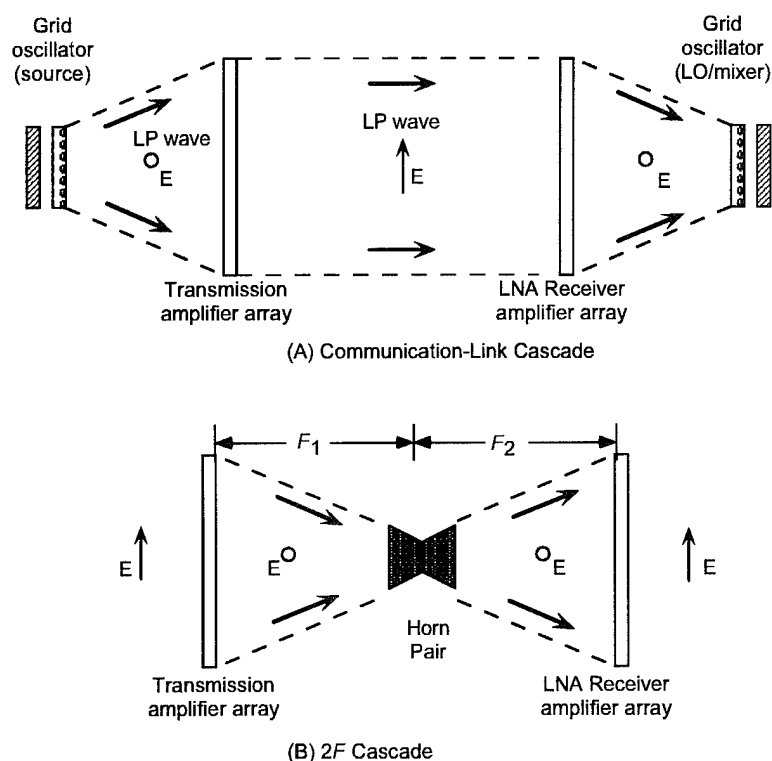


Figure 9.1. Cascaded lens amplifiers in the (a) communication-link and (b) $2F$ configurations.

one opportunity for using constrained lens theory for future millimeter-wave quasi-optical amplifier arrays.

Cascaded amplifier arrays have been proposed and verified as a way of improving the gain of quasi-optical amplifiers [73]. The low-noise receiver lens amplifier and the transmission lens amplifier arrays may be cascaded for improved gain as illustrated in Figure 9.1. The top figure shows a communication-link cascade. A grid oscillator placed at the focal arc of the transmission lens amplifier can be modulated through its gate bias line. The active lens array amplifies and collimates the wave from the grid oscillator, forming a beam in free-space. The low-noise lens receives the signal and focuses the energy down to a quasi-optical mixer. The local oscillator is provided by another grid

oscillator, and the intermediate frequency signal may be extracted from the elements of the mixer via a planar corporate feed network. The lenses must be placed in the far field, making this arrangement large for large arrays. The bottom figure shows a $2F$ cascade, where the lens arrays are placed a distance $2F$ apart. Like its optical analogy of two convex lenses, the cascade is fed with a plane wave, and a collimated beam will emerge from it. A horn pair may be placed at the center to accommodate lenses with different focal lengths and polarization rotation between input and output.

A natural follow-on to the separate development of the transmission and receiver lens arrays is an integrated transmit/receive lens array, as illustrated in Figure 9.2. Passive lenses are reciprocal, but the unidirectional amplifiers embedded in our arrays are not reciprocal. Separate low noise and high power amplifier circuits may be placed in each unit cell, with polarization isolation used for stability and possibly switching between transmit and receive functions. On transmit, the grid oscillator feeds a linearly polarized wave to the feed-side of the transmit amplifier. The lens amplifies and reradiates an orthogonally-polarized wave on the aperture-side, which is converted to right-hand-circular polarization with a polarizer. This polarizer, which acts like a quarter-wave plate, consists of a stack of dipole arrays loaded with capacitors. Upon receive, a right-hand-circularly polarized wave passes through the isolator, converted to a linearly polarized wave by the polarizer, received by the aperture-side of the lens, is amplified by the LNA, and focuses the signal down to the grid oscillator. The grid acts as the local oscillator and mixer, and the intermediate frequency is coupled out of the mixer for information recovery. If a left-hand-circularly polarized signal is incident on the isolator, it will be

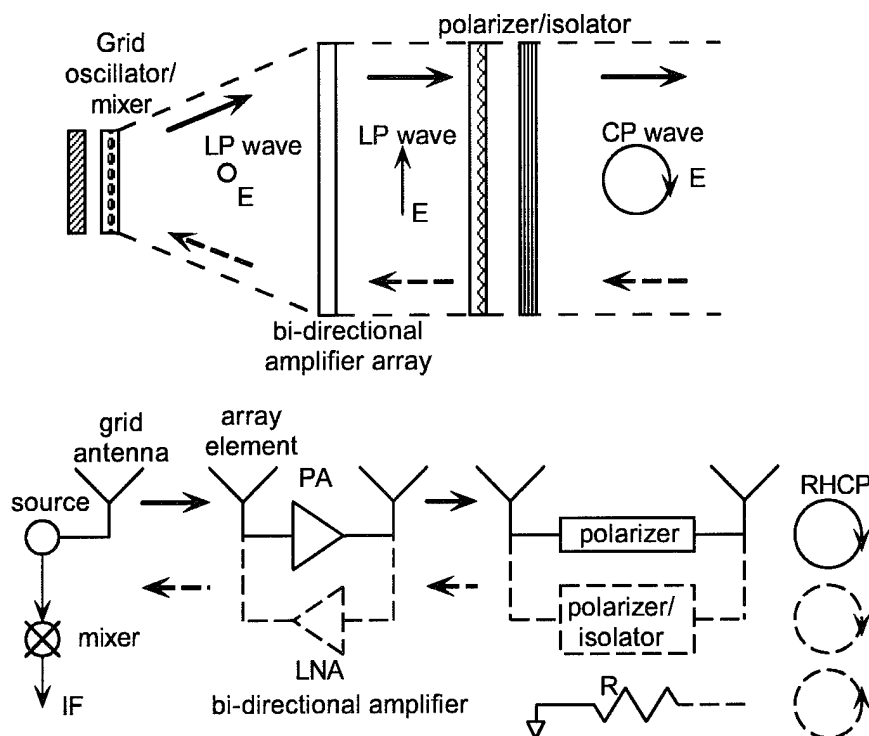


Figure 9.2. Transmit-Receive lens shown with a grid oscillator source/mixer, linear-to-circular polarizer, and isolator in a quasi-optical system.

attenuated. The circuit designer may require monolithic or MMIC amplifier chips in a hybrid structure to minimize the room needed for separate amplifiers and a switch at each unit cell.

Finally, the development of computer models and procedures that accounts for the interaction between the elements and the circuitry will need to be addressed. A recent IEEE workshop on this very subject was recently organized. One of the themes of the workshop it is that at present, active array designers simulate the antenna separate from the circuitry, and design procedures and tools to account for any interaction has not been developed. Planar moment-method codes like Momentum could be used to check interaction between the radiating elements and the passive circuitry in a unit cell to

gain some insight. The desired outcome is to develop some design rules and procedures to minimize these interactions.

BIBLIOGRAPHY

- [1] J.D. Kraus, **Radio Astronomy**, McGraw-Hill, 1966.
- [2] N.C. Luhmann Jr, "Instrumentation and techniques for plasma diagnostics: An overview," in **Infrared and Millimeter Waves**, K. J. Button, Ed., vol. 4, chapter 1. Academic Press, New York, 1979.
- [3] J. C. Wiltse, "Introduction and overview of millimeter waves," in **Infrared and Millimeter Waves**, K. J. Button, Ed., vol. 4, chapter 1, pp. 1-18. Academic Press, New York, 1981.
- [4] T .G. Phillips and D. B. Rutledge, "Superconducting tunnel detectors in radio astronomy," **Scientific American**, vol. 254, pp. 96-102, 1986.
- [5] Takeshi Manabe and Yoji Furuhamma, "Recent propagation studies in japan," **IEEE Antennas and Propagation Magazine**, vol. 36, no. 5, pp. 7-13, October 1994.
- [6] G. Kantorowicz and P. Palluel, "Backward wave oscillators," in **Infrared and Millimeter Waves**, K. J. Button, Ed., vol. 1, chapter 4. Academic Press, New York, 1979.
- [7] H. Bierman, "Microwave tube design efforts yield steady performance improvements," **Microwave J.**, vol. 31, pp. 52-73, June 1988.
- [8] Hans Hieslmair and Others, "State of the art of solid-state and tube transmitters," **Microwave J.**, vol. 26, no. 10, pp. 46-48, October 1983.
- [9] J. W. Hansen, "US TWTs from 1 to 100 GHz," **State of the Art Reference Supplement to Microwave J.**, vol. 32, pp. 179-193, September 1989.
- [10] K. J. Slegler, R. H. Abrams, and R. K. Parker, "Trends in solid-state microwave and millimeter-wave technology," **IEEE MTT-S Newsletter**, pp. 11-15, Fall 1990.
- [11] Y. C. Shih and H. J. Kuno, "Solid-state sources from 1 to 100 GHz," **State of the Art Reference Supplement to Microwave J.**, vol. 32, pp. 145-161, September 1989.

- [12] C. A. Liechti, "High-speed transistors: Directions for the 1990s," **State of the Art Reference Supplement to Microwave J.**, vol. 32, pp. 165-177, September 1989.
- [13] Gary Ferrell, Larry Dickens, John Gipprich, Bob Hayes, and Fred Sacks, "A high efficiency 10 watt HBT power amplifier assembly using combining techniques," in **IEEE 1995 International Microwave Theory and Techniques Symposium Digest**, May 1995, pp. 327-330.
- [14] Doug Teeter, Steve Bouthillette, Lisa Aucoin, Aryeh Platzker, Ciro Alfaro, and Dave Bradford, "High power, high efficiency PHEMTs for use at 8 GHz," in **IEEE 1995 International Microwave Theory and Techniques Symposium Digest**, May 1995, pp. 323-326.
- [15] Kohji Matsunaga, Yasuhiro Okamoto, and Masaaki Kuzuhara, "Ku-Band 10W high efficiency HJFET power amplifier," in **IEEE 1995 International Microwave Theory and Techniques Symposium Digest**, May 1995, pp. 335-338.
- [16] M. Matloubian and Others, "High power V-band AlInAs/GaInAs on InP HEMTs," **IEEE Electron Device Letters**, vol. 14, no. 4, pp. 188-190, April 1993.
- [17] K. J. Russell, "Microwave power combining techniques," **IEEE Transactions Microwave Theory and Techniques Special Issue on Solid-State Microwave/Millimeter-Wave Power Generation, Amplification, and Control**, vol. MTT-27, pp. 472-478, May 1979.
- [18] K. Chang and C. Sun, "Millimeter-wave power-combining techniques," **IEEE Transactions Microwave Theory and Techniques**, vol. MTT-31, pp. 91-107, February 1983.
- [19] K. Kurokawa, "The single-cavity multiple-device oscillator," **IEEE Transactions Microwave Theory and Techniques**, vol. MTT-19, pp. 793-801, October 1971.
- [20] James W. Mink, "Quasi-optical power combining of solid-state millimeter-wave sources," **IEEE Transactions Microwave Theory and Techniques**, vol. MTT-34, no. 2, pp. 273-279, February 1986.
- [21] Robert A. York, "Quasi-optical power combining techniques," **SPIE Critical Reviews of Emerging Technologies**, pp. 101-151, 1994.

- [22] P. F. Goldsmith, "Quasi-optical techniques at millimeter and submillimeter wavelengths," in **Infrared and Millimeter Waves**, K. J. Button, Ed., vol. 6, chapter 5, pp. 277–343. Academic Press Inc., New York, 1982.
- [23] L. Wandinger and V. Nalbandian, "Millimeter-wave power combiner using quasi-optical techniques," **IEEE Transactions Microwave Theory and Techniques**, vol. MTT-31, pp. 189–193, February 1983.
- [24] S. L. Young and K. D. Stephan, "Stabilization and power combining of planar microwave oscillators with an open resonator," in **1987 IEEE International Microwave Theory and Techniques Symposium Digest**, Las Vegas, NV, June 1987, pp. 185–188.
- [25] M. Nakayama, M. Hieda, T. Tanaka, and K. Mizuno, "Millimeter and submillimeter wave quasi-optical oscillator with multi-elements," in **1990 IEEE International Microwave Theory and Techniques Symposium Digest**, Dallas, TX, June 1990, pp. 1209–1212.
- [26] H. Kondo, M. Hieda, M. Nakayama, T. Tanaka, K. Osakabe, and K. Mizuno, "Millimeter and submillimeter wave quasi-optical oscillator with multi-elements," **IEEE Transactions Microwave Theory and Techniques**, vol. MTT-40, pp. 857–863, May 1992.
- [27] P. L. Heron, F. K. Schwing, G. P. Monahan, J. W. Mink, and M. B. Steer, "A dyadic green's function for the plano-concave quasi-optical resonator," **IEEE Microwave and Guided Wave Letters**, vol. 3, pp. 256–258, August 1993.
- [28] P. L. Heron, F. K. Schwing, G. P. Monahan, J. W. Mink, and M. B. Steer, "Impedance matrix of an antenna array in a quasi-optical resonator," **IEEE Transactions Microwave Theory and Techniques Special Issue on Quasi-Optical Techniques**, vol. MTT-41, pp. 1816–1826, October 1993.
- [29] Z. B. Popović, R. M. Weikle, M. Kim, and D. B. Rutledge, "A 100-MESFET planar grid oscillator," **IEEE Transactions Microwave Theory and Techniques**, vol. MTT-39, pp. 193–200, February 1991.
- [30] Z. B. Popović, **Grid Oscillators**, PhD thesis, California Institute of Technology.
- [31] R. M. Weikle II, M. Kim, J. B. Hacker, M. P. De Lisio, and D. B. Rutledge, "Planar MESFET grid oscillators using gate feedback," **IEEE**

- Transactions Microwave Theory and Techniques**, vol. MTT-40, pp. 1997–2003, November.
- [32] R. M. Weikle II, M. Kim, J. B. Hacker, M. P. De Lisio, Z. B. Popović, and D. B. Rutledge, "Transistor oscillator and amplifier grids," **Proceedings of the IEEE**, vol. 80, pp. 1800–1809, November 1992.
 - [33] E. A. Sovero, M. Kim, R. M. Weikle II, D.S. Deakin, W. J. Ho, J. A. Higgins, and D.B. Rutledge, "A monolithic 35 GHz HBT quasi-optical grid oscillator," in **1992 IEEE GaAs IC Symposium Digest**, Miami Beach, FL, October 1992, pp. 305–308.
 - [34] J. B. Hacker, **Grid Mixers and Power Grid Oscillators**, PhD thesis, California Institute of Technology, Pasadena, California, 1994.
 - [35] J. B. Hacker, M. P. De Lisio, M. Kim, C. M. Liu, S. J. Li, S. W. Wedge, and D. B. Rutledge, "A 10-Watt X-Band grid oscillator," in **1994 IEEE International Microwave Theory and Techniques Symposium Digest**, San Diego, CA, May 1994, pp. 823–826.
 - [36] M. Kim, J. J. Rosenberg, R. P. Smith, R. M. Weikle II, J. B. Hacker, M. P. DeLisio, and D. B. Rutledge, "A grid amplifier," **IEEE Microwave and Guided Wave Letters**, vol. 1, pp. 322–324, November 1991.
 - [37] M. Kim, E. A. Sovero, J. B. Hacker, M. P. DeLisio, J. C. Chiao, S. J. Li, D. R. Gagnon, J. J. Rosenberg, and D. B. Rutledge, "A 100-element HBT grid amplifier," **IEEE Transactions Microwave Theory and Techniques**, vol. MTT-41, pp. 1762–1771, November 1993.
 - [38] M. Kim, E. A. Sovero, J. B. Hacker, M. P. De Lisio, J. J. Rosenberg, and D.B. Rutledge, "A 6.5 GHz source using a grid amplifier with a twist reflector," **IEEE Transactions Microwave Theory and Techniques Special Issue on Quasi-Optical Techniques**, vol. MTT-41, pp. 1772–1774, October 1993.
 - [39] W. L. Williams, D. F. Kasilingam, and D. B. Rutledge, "Progress in quasi-optical transistor power amplifiers," in **10th International Infrared and Millimeter Wave Conference Digest**, Lake Buena Vista, FL, December 1985, pp. 50–51.
 - [40] J. Chang, D. H. Schaubert, K. S. Yngvesson, J. Huang, V. Jamnejad, D. Rascoe, and A.L. Riley, "Ka-Band power-combining MMIC array," in **15th International Infrared and Millimeter Wave Conference Digest**, Orlando, FL, December 1990, pp. 532–534.

- [41] J. A. Benet, A. R. Perkons, and S.H. Wong, "Spatial power combining for millimeter-wave solid-state amplifiers," in **1993 IEEE International Microwave Theory and Techniques Symposium Digest**, Atlanta, GA, June 1993, pp. 619-622.
- [42] T. Mader, J. Schoenberg, L. Harmon, and Z. B. Popović, "Planar MES-FET transmission amplifier," **IEE Electronics Letters**, vol. 29, no. 19, pp. 1699-1701, 17 September 1993.
- [43] N. J. Koliass and R. C. Compton, "A microstrip-based unit cell for quasi-optical amplifier arrays," **IEEE Microwave and Guided Wave Letters**, vol. 3, pp. 330-332, September 1993.
- [44] Nilay Sheth, Toni Ivanov, Arul Balasubramaniyan, and Amir Mortazawi, "A nine HEMT spatial amplifier," in **1994 IEEE International Microwave Theory and Techniques Symposium Digest**, May 1994, pp. 1239-1242.
- [45] H. S. Tsai and R. A. York, "Polarization-rotating quasi-optical reflection amplifier cell," **Electronics Letters**, vol. 29, pp. 2125-2127, November 1993.
- [46] H. S. Tsai, M. J. W. Rodwell, and R. A. York, "Planar amplifier array with improved bandwidth using folded-slots," **IEEE Microwave and Guided Wave Letters**, vol. 4, pp. 112-114, April.
- [47] K. D. Stephan, "Inter-injection-locked oscillators for power combining and phased arrays," **IEEE Transactions Microwave Theory and Techniques**, vol. MTT-34, pp. 1017-1025, October.
- [48] R. J. Dinger, D. J. White, and D. R. Bowling, "10 GHz space power combiner with parasitic injection locking," **Electronics Letters**, vol. 23, pp. 397-398, April 1987.
- [49] K. D. Stephan and S. L. Young, "Mode stability of radiation-coupled inter-injection-locked oscillators for integrated phased arrays," **IEEE Transactions Microwave Theory and Techniques**, vol. MTT-36, pp. 921-924, May 1988.
- [50] D. B. Rutledge, Z. B. Popović, R. M. Weikle II, M. Kim, K. A. Potter, R. C. Compton, and R. A. York, "Quasi-optical power-combining arrays," in **1990 IEEE International Microwave Theory and Techniques Symposium Digest**, Dallas, TX, June 1990.

- [51] J. A. Navarro, Y. H. Shu, and K. Chang, "Active endfire antenna elements and power combiners using notch antennas," in **1990 IEEE International Microwave Theory and Techniques Symposium Digest**, Dallas, TX, June 1990, pp. 793-796.
- [52] J. Birkeland and T. Itoh, "Spatial power combining using push-pull FET oscillators with microstrip patch resonators," in **1990 IEEE International Microwave Theory and Techniques Symposium Digest**, Dallas, TX, June, pp. 1217-1220.
- [53] J. Birkeland and Tatsuo Itoh, "A FET oscillator element for spatially injection locked arrays," in **1992 IEEE International Microwave Theory and Techniques Symposium Digest**, June 1992, pp. 1535-1538.
- [54] R. A. York and R. C. Compton, "Mode-locked oscillator arrays," **IEEE Microwave and Guided Wave Letters**, vol. 1, pp. 215-218, 1991.
- [55] P. Liao and R.A. York, "A six-element beam-scanning array," **IEEE Microwave and Guided Wave Letters**, vol. 4, pp. 20-22, January 1994.
- [56] P. Liao and R. A. York, "A 1-Watt X-Band power combining array using coupled VCOs," in **1994 IEEE International Microwave Theory and Techniques Symposium Digest**, San Diego, CA, May 1994, pp. 1235-1238.
- [57] J. A. Navarro, Y. H. Shu, and K. Chang, "Broadband electronically tunable planar active radiating elements and spatial power combiners using notch antennas," **IEEE Transactions Microwave Theory and Techniques**, vol. MTT-40, pp. 323-328, February 1992.
- [58] J. C. Wiltse and J. W. Mink, "Quasi-optical power combining of solid-state sources," **Microwave J.**, vol. 35, pp. 144-156, February 1992.
- [59] A. Mortazawi and B. C. De Loach, "A nine-MESFET two-dimensional power-combining array employing an extended resonance technique," **IEEE Microwave and Guided Wave Letters**, vol. 3, pp. 214-216, July 1993.
- [60] A. Mortazawi, H.D. Foltz, and T. Itoh, "A periodic second harmonic spatial power combining oscillator," **IEEE Transactions Microwave Theory and Techniques**, vol. MTT-40, pp. 851-856, May 1992.

- [61] Z. B. Popović, M. Kim, and D. B. Rutledge, "Grid oscillators," **International Journal of Infrared and Millimeter-waves**, vol. 9, pp. 647–654, July 1988.
- [62] Z. B. Popović, R. M. Weikle II, M. Kim, K. A. Potter, and D. B. Rutledge, "Bar-grid oscillators," **IEEE Transactions Microwave Theory and Techniques**, vol. MTT-38, pp. 225–230, March 1990.
- [63] R. M. Weikle II, **Planar Grid Oscillators for Microwave and Millimeter-Wave Power Combining**, PhD thesis, California Institute of Technology, Pasadena, CA, 1992.
- [64] S. C. Bundy, T. B. Mader, and Z. B. Popović, "Quasi-optical array VCOs," in **1992 IEEE International Microwave Theory and Techniques Symposium Digest**, Albuquerque, NM, June 1992, pp. 1539–1542.
- [65] T. B. Mader, S. C. Bundy, and Z. B. Popović, "Quasi-optical VCOs," **IEEE Transactions Microwave Theory and Techniques Special Issue on Quasi-Optical Techniques**, vol. MTT-41, pp. 1775–1781, October 1993.
- [66] S. C. Bundy, **Analysis and Design of Grid Oscillators**, PhD thesis, University of Colorado at Boulder, Boulder, CO, 1994.
- [67] Scott C. Bundy and Zoya B. Popović, "Analysis of planar grid oscillators," in **Proceedings 1994 IEEE Microwave Theory and Techniques Symposium Digest**, May 1994, pp. 827–830.
- [68] Scott C. Bundy and Zoya B. Popović, "A generalized analysis for grid oscillator design," **IEEE Transactions Microwave Theory and Techniques**, pp. 2486–2491, December 1994.
- [69] Scott C. Bundy, Wayne A. Shiroma, and Zoya B. Popović, "Analysis of cascaded quasi-optical grids," in **1995 IEEE International Microwave Theory and Techniques Symposium Digest**, May 1995, pp. 601–604.
- [70] Wayne Shiroma, Boyd L. Shaw, and Zoya B. Popović, "Three-dimensional power combiners," in **1994 IEEE International Microwave Theory and Techniques Symposium Digest**, May 1994, pp. 831–834.

- [71] W. A. Shiroma, B. L. Shaw, and Z. B. Popović, "A 100-transistor quadruple grid oscillator," **IEEE Microwave and Guided Wave Letters**, vol. 4, pp. 350–351, October 1994.
- [72] Jon S.H. Schoenberg, Scott C. Bundy, and Zoya B. Popović, "Two-level power combining using a lens amplifier," **IEEE Transactions on Microwave Theory and Techniques**, vol. MTT-42, no. 12, pp. 2480–2485, Dec 1994.
- [73] Toni Ivanov and Amir Mortazawi, "Two-stage double layer microstrip spatial amplifiers," in **1995 IEEE International Microwave Theory and Techniques Symposium Digest**, May 1995, pp. 589–592.
- [74] Jon S.H. Schoenberg and Zoya B. Popović, "Planar lens amplifier," in **IEEE 1994 International Microwave Theory and Techniques Symposium Digest**, May 1994, pp. 429–432.
- [75] Jon Schoenberg, Tom Mader, Boyd Shaw, and Zoya B. Popović, "Quasi-optical antenna array amplifiers," in **IEEE 1995 International Microwave Theory and Techniques Symposium Digest**, May 1995, pp. 605–609.
- [76] K. D. Stephan, N. Camilleri, and T. Itoh, "A quasi-optical polarization-duplexed balanced mixer for millimeter-wave applications," **IEEE Transactions Microwave Theory and Techniques**, vol. MTT-31, pp. 164–170, February 1983.
- [77] K. D. Stephan and T. Itoh, "A planar quasi-optical sub-harmonically pumped mixer characterized by isotropic conversion loss," **IEEE Transactions Microwave Theory and Techniques**, vol. MTT-32, pp. 97–102, January 1984.
- [78] V. D. Hwang and T. Itoh, "Quasi-optical HEMT and MESFET self-oscillating mixers," **IEEE Transactions Microwave Theory and Techniques**, vol. MTT-36, pp. 1701–1705, December 1988.
- [79] J. B. Hacker, R. M. Weikle II, M. Kim, M. P. De Lisio, and D. B. Rutledge, "A 100-element planar Schottky diode grid mixer," **IEEE Transactions Microwave Theory and Techniques**, vol. MTT-40, pp. 557–562, March 1992.
- [80] R. M. Weikle II, N. Rorsman, H. Zirath, and E. L. Kollberg, "A subharmonically pumped HFET grid mixer," in **Proceedings of the Fourth**

International Symposium on Space Terahertz Technology, March 1993, pp. 113–122.

- [81] W. W. Lam, C. F. Jou, N. C. Luhmann Jr, and D. B. Rutledge, "Diode grids for electronic beam steering and frequency multiplication," **International Journal of Infrared and Millimeter-waves**, vol. 7, pp. 27–41, January 1986.
- [82] W. W. Lam, C. F. Jou, H. Z. Chen, K. S. Stolt, N. C. Luhmann Jr., and D.B. Rutledge, "Millimeter-wave diode-grid phase shifters," **IEEE Transactions Microwave Theory and Techniques**, vol. MTT-36, pp. 902–907, May 1988.
- [83] L. B. Sjogren, H. X. Liu, X. Qin, C. W. Domier, and N.C. Luhmann Jr., "Phased array operation of a diode grid impedance surface," **IEEE Transactions Microwave Theory and Techniques**, vol. MTT-42, pp. 565–572, April 1994.
- [84] N. Camilleri and T. Itoh, "A quasi-optical multiplying slot array," **IEEE Transactions Microwave Theory and Techniques**, vol. MTT-33, pp. 1189–1195, November 1985.
- [85] C. F. Jou, W. W. Lam, H. Z. Chen, K. S. Stolt, N. C. Luhmann Jr., and D. B. Rutledge, "Millimeter-wave diode-grid frequency doubler," **IEEE Transactions Microwave Theory and Techniques**, vol. MTT-36, pp. 1507–1514, November 1988.
- [86] R. J. Hwu, N. C. Luhmann Jr., D. B. Rutledge, B. Hancock, and U. Lieneweg, "Monolithic watt-level millimeter-wave diode-grid frequency tripler array," **International Journal of Infrared and Millimeter-waves**, vol. 9, pp. 1011–1020, December 1988.
- [87] H. L. Liu, X. H. Qin, L. B. Sjogren, E. Chung, C. W. Domier, and N.C. Luhmann Jr., "Monolithic high power millimeter wave quasi-optical frequency multiplier arrays using quantum barrier devices," in **submitted to the 50th Annual Device Research Conference**, 1994.
- [88] L. B. Sjogren, H. X. Liu, F. Wang, T. Liu, X. H. Qin, W. Wu, E. Chung, C. W. Domier, and N. C. Luhmann Jr, "A monolithic diode array millimeter-wave beam transmittance controller," **IEEE Transactions Microwave Theory and Techniques Special Issue on Quasi-Optical Techniques**, vol. MTT-41, pp. 1782–1790, October 1993.

- [89] K. D. Stephan and P.F. Goldsmith, "W-Band quasioptical integrated PIN diode switch," in **1992 IEEE International Microwave Theory and Techniques Symposium Digest**, Albuquerque, NM, June 1992, pp. 591-594.
- [90] K. D. Stephan, P. H. Spooner, and P. F. Goldsmith, "Quasi-optical millimeter-wave hybrid and monolithic PIN diode switches," **IEEE Transactions Microwave Theory and Techniques Special Issue on Quasi-Optical Techniques**, vol. MTT-41, pp. 1791-1798, October 1993.
- [91] C. Balanis, **Antenna Theory: Analysis and Design**, Harper and Row, New York, 1982.
- [92] R. M. Weikle II, M. Kim, J. B. Hacker, M. P. DeLisio, Zoya B. Popović, and D. B. Rutledge, "Transistor oscillators and amplifier grids," **Proceedings of the IEEE**, pp. 1800-1809, November 1992.
- [93] A. Benalla, C. Thng, and K. C. Gupta, **CAD Of Microstrip Patch Antennas**, Microstrip Designs, Inc., 1993.
- [94] Daniel T. McGrath, "Planar three-dimensional constrained lenses," **IEEE Transactions Antennas and Propagation**, vol. AP-34, no. 1, pp. 46-50, Jan 1986.
- [95] Daniel T. McGrath, "Slot-coupled microstrip constrained lens," **Proceedings of the Antenna Applications Symposium**, Sep 1987.
- [96] Daniel T. McGrath, Paul M. Proudfoot, and Mark A. Mehalic, "The microstrip constrained lens," **Microwave Journal**, pp. 24-37, Jan 1995.
- [97] P. J. B. Clarricoats, A. D. Monk, and Z. Hai, "An array-fed reconfigurable reflector for flexible coverage," in **23rd European Microwave Conference Proceedings**, September 1993, pp. 194-197.
- [98] H. Steyskal, R. J. Mailloux, and J. P. Turtle, "EHF active phased array development in the USA," in **23rd European Microwave Conference Proceedings**, September 1993, pp. 80-83.
- [99] S. Born and J. Wolf, **Geometrical Optics**, Lumierre, New York, 1964.
- [100] R. Johnson and J. Jasik, **The Antenna Engineering Handbook**, chapter 16, pp. 255-259, McGraw-Hill, New York, second edition, 1984.

- [101] R. E. Collin and F. J. Zucker, **Antenna Theory Part II**, McGraw-Hill, New York, 1969.
- [102] S. Cornbleet, **Microwave and Geometrical Optics**, Academic Press, New York, 1994.
- [103] W. E. Koch, "Metal lens antennas," **Proceedings IRE**, vol. 34, pp. 828–836, November 1946.
- [104] John Brown, "Microwave lenses," in **Methuen's Monographs on Physical Subjects**. Methuen, London, 1953.
- [105] J. Ruze, "Wide-angle metal plate optics," **Proceedings IRE**, vol. 38, pp. 53–59, January 1950.
- [106] Carlyle J. Sletton, **Reflector and Lens Antennas**, Artech House, Boston, 1988.
- [107] H. Gent, "The bootlace aerial," **Royal Radar Establishment Journal**, pp. 47–57, October 1957.
- [108] W. Rotman and R. Turner, "Wide angle microwave lens for line source applications," **IEEE Transactions Antennas and Propagation**, vol. AP-11, no. 5, pp. 623–632, Nov 1963.
- [109] D. H. Archer, "Lens-fed multiple beam arrays," **Microwave Journal**, pp. 171–195, September 1984.
- [110] S. Cornbleet, **Microwave and Geometrical Optics**, Academic Press, New York, 1994.
- [111] Jaganmohan B. L. Rao, "Multifocal three-dimensional bootlace lenses," **IEEE Transactions Antennas and Propagation**, vol. AP-30, no. 6, pp. 1050–1056, November 1982.
- [112] Carey M. Rappaport and Amir I. Zaghoul, "Optimized three-dimensional lenses for wide-angle scanning," **IEEE Transactions Antennas and Propagation**, vol. AP-33, no. 11, pp. 1227–1236, November 1985.
- [113] Robert J. Mailloux, **Phased Array Antenna Handbook**, Artech House, Boston, 1994.
- [114] Warren L. Stutzman and Gary A. Thiele, **Antenna Theory and Design**, John Wiley and Sons, New York, 1981.

- [115] Richard C. Johnson and Henry Jasik, **Antenna Engineering Handbook**, McGraw-Hill, New York, second edition, 1984.
- [116] E. F. Kuester, **Waveguides and Transmission Lines**, ECEN 5114, Waveguide and Transmission Lines Class Notes, 1994.
- [117] M. Kobayashi, "A dispersion formula satisfying recent requirements in microstrip CAD," **IEEE Transactions Microwave Theory and Techniques**, vol. MTT-36, pp. 1246-1250, October 1988.
- [118] E. S. Kochanov, "Capacitance of a planar strip line allowing for the dielectric substrate width," **Tel. Rad. Eng.**, vol. 29/30, no. 1, pp. 127-128, 1975.
- [119] Wolfgang Hilberg, "From approximations to exact relations for characteristic impedances," **IEEE Transactions Microwave Theory and Techniques**, vol. MTT-17, pp. 259-265, May 1969.
- [120] K. C. Gupta, R. Garg, and I. J. Bahl, **Microstrip Lines and Slotlines**, Artech House, Inc., Dedham, MA, 1979.
- [121] Kohji Koshiji, Eimei Shu, and Shichiro Miki, "Simplified computation of coplanar waveguide with finite conductor thickness," **IEE Proceedings, Part H**, vol. 130, no. 5, pp. 315-321, August 1983.
- [122] R. W. Jackson, "Considerations in the use of coplanar waveguide for millimeter-wave integrated circuits," **IEEE Transactions Microwave Theory and Techniques**, vol. MTT-34, no. 12, pp. 1450-1456, December 1986.
- [123] R. T. Webster, A. J. Slobodnik, and G. A. Roberts, "Monolithic InP HEMT V-band low noise amplifier," **IEEE Microwave and Guided Wave Letters**, vol. 2, no. 6, pp. 236-238, June 1992.
- [124] K. C. Gupta, "CAD of active microstrip antennas and microstrip arrays," in **1995 Asia-Pacific Microwave Conference Proceedings**, December 1994, pp. 891-895.
- [125] K. C. Gupta, **Computer-Aided Design of Microstrip Antennas**, ECEN 5004-3, Special Topics on Computer Aided Design of Microstrip Antennas Class Notes, 1993.
- [126] A. G. Derneryd and I. Karlsson, "Broadband microstrip antenna element and array," **IEEE Transactions Antennas and Propagation**, vol. AP-29, no. 1, pp. 140-144, January 1981.

- [127] W. C. Chew, "A broadband annular-ring microstrip antenna," **IEEE Transactions Antennas and Propagation**, vol. AP-30, no. 5, pp. 918-922, September 1982.
- [128] K. C. Gupta and G. Kumar, "Directly coupled multiple resonator wide-band microstrip antennas," **IEEE Transactions Antennas and Propagation**, vol. AP-33, pp. 853-855, 1985.
- [129] H. Pues, J. Bogaers, R. Pieck, and A. Van de Capelle, "Wideband quasi-log periodic microstrip antennas," **IEE Proceedings, Part H**, vol. 128, no. 3, pp. 159-1 3, June 1981.
- [130] F. Croq and D. M. Pozar, "Multifrequency operation of microstrip antennas using aperture coupled parallel resonators," **IEEE Transactions Antennas and Propagation**, vol. AP-40, no. 11, pp. 1367-1374, November 1992.
- [131] P. S. Hall, C. Wood, and C. Garrett, "Wide bandwidth microstrip antennas for circuit integration," **IEE Electronics Letters**, vol. 15, pp. 458-459, 1979.
- [132] R. R. DeLyser, D. C. Chang, and E. F. Kuester, "Design of a log periodic strip grating microstrip antenna," **International Journal of Microwave and Millimeter-Wave Computer-Aided Engineering**, vol. 3, no. 2, pp. 143-150, 1993.
- [133] B. D. Popović, Jon Schoenberg, and Z. B. Popović, "Broadband quasi-microstrip antenna," **to be published in IEEE Transactions Antennas and Propagation**, October 1995.
- [134] Branko D. Popović, **CAD of Wire Antennas and Related Radiating Structures**, Wiley, Inc., New York, 1991.
- [135] B. D. Popović and A. Nešić, "Generalisation of the concept of equivalent radius of thin cylindrical antennas," **IEE Proceedings, Part H**, vol. 131, no. 3, pp. 153-158, June 1984.
- [136] M. Sierra and George Jankovic, "Tolerance effects on low-cost printed DBS antennas," in **IEEE Antennas and Propagation Society International Symposium Proceedings 1995**, June 1995, pp. 342-345.
- [137] Steven V. Robertson, Nihad I. Dib, Gyusik Yang, and Linda P. B. Katehi, "A folded slot antenna for planar quasi-optical mixer applications," in

IEEE Antennas and Propagation Society International Symposium Proceedings 1993, May 1993, pp. 600–603.

- [138] H. S. Tsai, M. J. W. Rodwell, and R. A. York, "Planar amplifier array with improved bandwidth using folded slots," **IEEE Microwave and Guided Wave Letters**, vol. 4, no. 4, pp. 112–114, April 1994.
- [139] H. S. Tsai and R. A. York, "Quasi-optical amplifier array using direct integration of MMICs and 50 ohm multi-slot antennas," in **1995 IEEE International Microwave Theory and Techniques Symposium Digest**, May 1995, pp. 593–596.
- [140] H. S. Tsai and R. A. York, "Applications of planar multiple-slot antennas for impedance control, and analysis using FDTD with Berenger's PML method," in **IEEE Antennas and Propagation Society International Symposium Proceedings 1995**, June 1995, pp. 370–373.
- [141] H. G. Booker, "Slot aeriels and their relation to complementary wire aeriels," **Journal of the IEE**, vol. 93, Part 111A, no. 4, pp. 620–626, 1946.
- [142] B. D. Popović and A. Nešić, "Some extensions of the concept of complementary electromagnetic structures," **IEE Proceedings, Part H**, vol. 132, no. 2, pp. 131–137, April 1985.
- [143] B. D. Popović and A. Nešić, "Analysis of slot antenna on dielectric substrate," **IEE Proceedings, Part H**, vol. 132, no. 7, pp. 474–476, December 1985.
- [144] John Hubert, Jon Schoenberg, and Zoya B. Popović, "High-power hybrid quasi-optical Ka-Band amplifier design," in **1995 IEEE International Microwave Theory and Techniques Symposium Digest**, May 1995, pp. 585–588.